DECIPHERING THE FACTORS RELATING SUN-INDUCED FLUORESCENCE TO PHOTOSYNTHESIS AND TRANSPIRATION IN SPACE AND TIME

David Martini

DECIPHERING THE FACTORS RELATING SUN-INDUCED FLUORESCENCE TO PHOTOSYNTHESIS AND TRANSPIRATION IN SPACE AND TIME

DISSERTATION

to obtain
the degree of doctor at the Universiteit Twente,
on the authority of the rector magnificus,
prof. dr. ir. A. Veldkamp,
on account of the decision of the Doctorate Board
to be publicly defended
on Wednesday 6 July 2022 at 12.45 hours

by

David Martini

born on the 30th of July, 1990
in Moncalieri, Italy

This dissertation has been approved by

Prof. dr. ir. C. van der Tol, supervisor

Dr. M. Migliavacca, co-supervisor

ITC dissertation number 415
ITC, P.O. Box 217, 7500 AE Enschede, The Netherlands

ISBN 978-90-365-5414-5
DOI 10.3990/1.9789036554145

Cover design by David Martini
Printed by CTRL P, Hengelo

Graduation Committee:

Chair / secretary:	prof.dr. F.D. van der Meer
Supervisor:	prof.dr.ir. C. van der Tol Universiteit Twente, ITC, Department of Water Resources
Co-supervisor:	dr. M. Migliavacca Joint Research Centre
Committee Members:	prof.dr.ir. A. Stein Universiteit Twente, ITC, Department of Earth Observation Science
	prof.dr. A.K. Skidmore Universiteit Twente, ITC, Department of Natural Resources
	prof. dr. K. Steppe Universiteit Gent
	prof. dr. R. Colombo University of Milano-Bicocca
	prof. dr. A. Damm-Reiser University of Zurich

Acknowledgements

Completing my PhD research has been a very stimulating and enriching experience. It would have not been possible without the supervision and advice of Mirco Migliavacca. I would like to thank you for the great supervision and guidance. I am very grateful to Christiaan van der Tol for excellent supervision and advice and for hosting me at the University of Twente's Faculty of Geo-Information Science and Earth Observation (ITC) for many months. This research was part of the TRuStEE network. I want to thank Micol Rossini for coordinating the project and to all the TRuStEE PhD students for sharing this journey with me and for providing support and friendship.

I am very grateful for my colleagues at the biogeochemical integration department of the Max Planck Institute (MPI) for Biogechemistry; I thank all of you for providing a very stimulating scientific environment that helped me to grow scientifically and personally. A special thank also to Markus Reichstein whose passion for research is very inspiring.

Big thanks to the Biosphere-Atmosphere Interactions and Experimentation group that hosted me and provided me with excellent scientific advice and a great work environment. I want to specifically thank Javier Pacheco-Labrador and Tarek El-Madany for always being available for discussion.

Much of the research has been carried out at the Majadas de Tiétar site, which was set up thanks to the excellent work and expertise of the field experiments and instrumentation group at MPI. Thanks to all of you and especially to Olaf Kolle.

A sincere thanks to Karolina Sakowska for providing the moni-PAM data at both the Majadas and Leinefelde site and for helping with the processing of the data. Many thank also to Jasper Denissen for helping with the translation of the summary.

I also want to thank all the people at ITC that welcomed me and made the research stay an excellent experience.

The biggest thanks goes to my lovely partner, Ingrid Chanca, for the incredible support and love and for being the best companion I could ever ask for.

To my parents, Graciela Peña Alfaro and Claudio Martini, thank you so much for everything, especially for the great positivity and support that you always showed. Many thanks to my grandpa, Attilio Martini, who inspired my love for science.

Table of Contents

1 Introduction 1
  1.1 Photosynthesis and transpiration 2
  1.2 Sun-induced fluorescence (SIF) 3
  1.3 Fluorescence, photochemistry and NPQ at photosystem scale 4
  1.4 Pulse amplitude modulation fluorimetry and photosynthesis 7
  1.5 Effect of leaf and canopy structure on SIF 7
  1.6 Research gaps 8
  1.7 Objectives 9
2 Nitrogen and Phosphorus effect on Sun-Induced Fluorescence and Gross Primary Productivity in Mediterranean grassland[1] 11
  2.1 Introduction 14
  2.2 Materials and Methods 18
  2.3 Results 26
  2.4 Discussion 36
  2.5 Conclusions 40
3 Heatwave breaks down the linearity between sun-induced fluorescence and gross primary production[2] 65
  3.2 Introduction 67
  3.3 Materials and Methods 69
  3.4 Results 74
  3.5 Discussion 82
4 Active and passive fluorescence measurements to interpret the interlink between remote sensing and transpiration 103
  4.2 Introduction 105
  4.3 Materials and methods 107
  4.4 Results 113
  4.5 Discussion 128
5 Synthesis 149
6 Bibliography 155
7 Summary 175
8 Samenvatting 179
9 Author’s biography and publications 183

1 Introduction

1.1 Photosynthesis and transpiration

Terrestrial gross primary production (*GPP*), i.e. the CO_2 assimilated by plants during the photosynthetic process, represents the largest global carbon flux and drives many crucial ecosystem functions, such as plant's growth and the offsetting of anthropogenic CO_2 emissions (Heimann & Reichstein, 2008). Plants' photosynthesis is also the basis for food and wood production and is therefore indispensable for human's survival. Transpiration (*T*) is the water flux constrained by plant's stomata and represents the largest component of the evapotranspiration (*ET*), the total water flux exchanged between atmosphere and biosphere in the majority of terrestrial ecosystems (Jasechko *et al.*, 2013). Plant's physiological activity, especially through stomata regulation, plays therefore a key role globally in the terrestrial carbon and water cycle.

Estimations of *GPP* and *T* at regional and global scale are the subject of ever-evolving research and can be divided between process-based approaches and data-driven methods (Beer *et al.*, 2010). Process-based models explicitly simulate the behavior of ecosystems describing their processes with mathematical simplifications. They rely on many assumptions and usually require large amount of in-situ data to constrain their predictions. Terrestrial biosphere models (Beer *et al.*, 2010) and coupled radiative transfer models and soil-vegetation-atmosphere transfer schemes (van der Tol *et al.*, 2009a) are example of process-based approaches and have been both used to estimate *GPP* and *T*. Other examples which include semi-empirical methods to estimate *GPP* include isotope fractionation (Farquhar *et al.*, 1993) and eddy-covariance partitioning of net ecosystem exchange (*NEE*) (Fig. 1.1) (Reichstein *et al.*, 2005; Lasslop *et al.*, 2010). Data-driven techniques rely instead on statistical relationship to predict *GPP* or *T,* by relating them to meteorological or remote sensing variables.

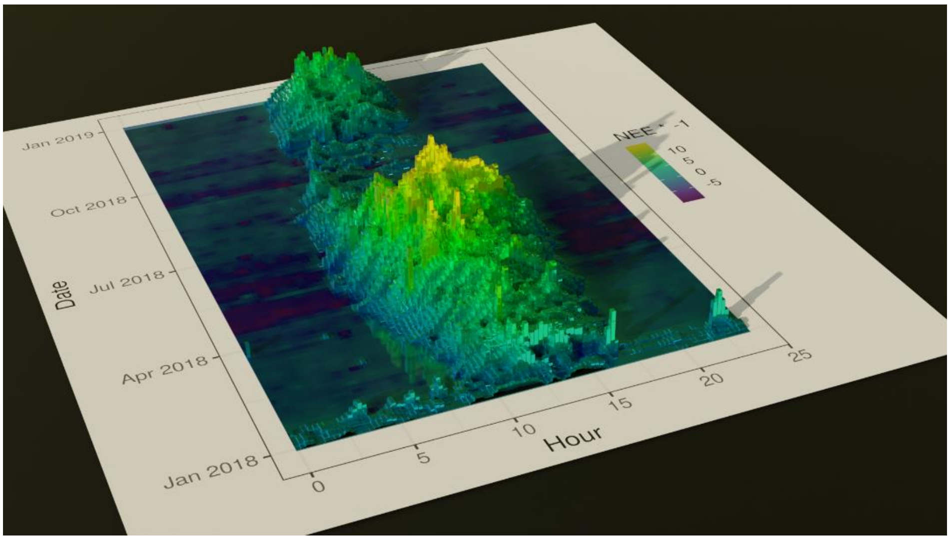

Fig. 1.1. 3d illustration of net ecosystem exchange (NEE) fingerprint at the Majadas site. The x axis represents the hour of the day, the y axis the time of the year. The color and the height of the columns is proportional to NEE * -1. The higher a column the higher is the ecosystem's CO_2 assimilation.

They are free from theoretical assumptions on the underlying processes, but they generally do not extrapolate well their predictions in conditions that significantly differ from the one that have been used to train the model. An example of data-driven GPP extrapolations at global scale is FLUXCOM (Jung *et al.*, 2019). Finally, remote sensing (RS) techniques can be employed both within a process-based framework (Damm *et al.*, 2010), or within a data-driven one (Reichstein *et al.*, 2019). Within the RS approaches, sun-induced fluorescence (*SIF*) has emerged as a very good RS proxy for photosynthesis (Guanter *et al.*, 2014), and recently transpiration (Shan *et al.*, 2019).

1.2 Sun-induced fluorescence (SIF)

SIF is the radiation emitted by chlorophyll containing plants upon sun exposure. *SIF* represents one of the three major pathways of light dissipation by plant's photosystems, the other two being photosynthesis and nonphotochemical quenching (*NPQ*) (Porcar-Castell *et al.*, 2014)(see next paragraph for the physiological link between *SIF* and photosynthesis). The *SIF* emission spans the range between 650 and 800 nm, and therefore contains both visible light (red SIF, wavelength < 700 nm) and near-infrared (NIR) light (NIR *SIF*, wavelength ≥ 700 nm).

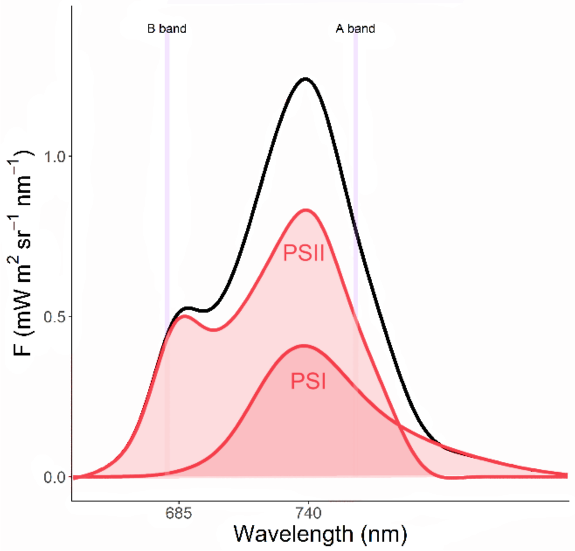

Fig. 1.2. Illustration of the spectral dependency of sun-induced fluorescence (F) and the contribution of photosystem II (PSII) and photosystem I (PSI). The atmospheric oxygen A and B bands are highlighted.

The *SIF* spectrum has two peaks, one at 685 nm and a larger one at 740 nm (Fig. 1.2) and is emitted by both photosystem II (PSII) and photosystem I (PSI), the former contributing to both the red and NIR regions and the latter contributing only to the NIR region (Mohammed *et al.*, 2019). *SIF* represents a small portion of the incoming or reflected radiance (typically less than 1% of reflected radiance) and is generally retrieved by exploiting atmospheric oxygen absorption bands (Fig. 1.2) or solar absorption bands (Frankenberg & Berry, 2018). *SIF* retrievals with atmospheric oxygen absorption bands are performed with a Fraunhofer Line Depth (FLD) approach (Meroni & Colombo, 2006) or through spectra fitting methods (SFM) algorithms (Meroni *et al.*, 2009) and require spectrometers capable of resolving the oxygen absorption bands (Julitta *et al.*, 2017).

1.3 Fluorescence, photochemistry and NPQ at photosystem scale

The reason why *SIF* and photosynthesis correlate is that both processes start with absorption of light by a chlorophyll molecule. The absorption of photons by PSII causes chlorophyll molecules in the reaction center of PSII to transition to an excited state. This energy can be dissipated by three main pathways: (i) it can be used to drive photochemistry by means of linear electron transport (LET); (ii) it can be dissipated non-radiatively as heat; or (iii) it can be emitted as a photon of fluorescence (Porcar-Castell *et al.*, 2014).

(i) The LET chain is the process that allows the transport of electrons from PSII to PSI in order to produce ATP and NADPH to be used in light-independent reactions of photosynthesis for sugar synthesis. During the LET the excited chlorophyll molecule from PSII donates an electron to the quinone A (Q_A) which passes it to a mobile electron carrier, the plastoquinone (Fig. 1.3), reducing it (Porcar-Castell *et al.*, 2014). PSII, which has just lost an electron, is positively charged and is reduced by the oxygen-evolving complex (OEC) (Fig. 1.3), which splits a water molecule in the thylakoid lumen and produces O_2 and a proton. The plastoquinone transfers the electron to the proton pump cytochrome b_6f (Cyt *b6f*) (Fig. 1.3), which has the dual function of transferring an electron to the plastocyanin molecule and transporting a proton to the thylakoid lumen, thereby further decreasing the pH of the lumen (Kramer *et al.*, 2004). Meanwhile PSI also absorbs a photon and uses the energy to reduce the electron acceptor ferrodoxyn (Fd) (Fig. 1.3), which in turns transfers the electron to $NADP^+$ to produce NADPH. Finally, the oxidized PSI receives an electron from the plastocyanin molecule (the electron that was transferred from PSII), thereby concluding the linear electron transport. The proton gradient in the thylakoid lumen is utilized by ATP synthase to produce ATP, concluding the light-dependent reactions of photosynthesis (Fig. 1.3) (Antal *et al.*, 2013).

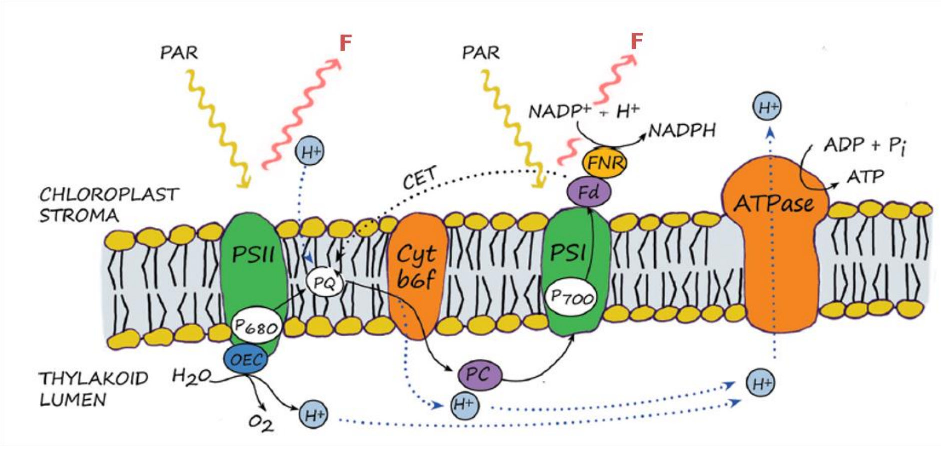

Fig. 1.3. Illustration of linear electron transport (a) and fluorescence emission. Adapted from (Porcar-Castell *et al.*, 2014).

(ii) At high light intensities electron transport and carbon fixation can saturate, thereby causing an accumulation of protons in the lumen and an increase in the lifetime of the charge state of the antenna of PSII (τPSII), which can result in the formation of singlet oxygen, a reactive oxygen species

that can harm the photosystem. In order to avoid the build-up of excessive energy and to decrease the τPSII, plants employ other mechanisms to dissipate the excess quanta as heat; the nonphotochemical quenching (*NPQ*). Low pH in the lumen acts as signal for the *NPQ* mechanism, which works by removing the epoxy group from a violaxanthin molecule, converting it in zeaxanthin (the xanthophyll cycle). Zeaxanthin has a direct role in the quenching process in the form of energy transfer from chlorophyll to zeaxanthin, dissipating the excess energy as heat (Jahns & Holzwarth, 2012).
(iii) Photochemistry can occur only in reaction centers that are open and functional, which means they are paired with an oxidized Q_A. When a reaction center is closed and a chlorophyll molecule is promoted to an excited state by a photon, the energy is dissipated radiatively, through the emission of photon of fluorescence (the *SIF* signal). The fraction of open reaction centers (q) is therefore inversely related to the quantum yield of fluorescence (Kitajima & Butler, 1975). SIF is not physiologically modulated, but both quenching through photochemistry (photochemical quenching, *PQ*) and *NPQ* are controlled by plants. As *SIF*, *PQ* and *NPQ* compete for the same dissipation energy, each dissipation pathway can be quantified as quantum yield, i.e. the efficiency of a certain dissipation pathway compared to the sum all the others. As the pathways are mutually exclusive (van der Tol *et al.*, 2014) they can be defined as follows:

$$\Phi P + \Phi F + \Phi D + \Phi N = 1 \qquad (1)$$

Where *ΦP* is the quantum yield of photochemistry, *ΦF* is the quantum yield of fluorescence emission, *ΦD* is quantum yield of internal conversion (whose rate constant is assumed to be constant and not described here for simplicity) and *ΦN* is the quantum yield of *NPQ*.

In conditions of low light (when *NPQ* is low) *PQ* is the major dissipation pathway and *ΦP* and *ΦF* are negatively correlated, as each reduction in *ΦP* implies a further saturation, increase in lifetime of the excited state, and thus an increase in *ΦF*. Instead in conditions of high light the *NPQ* mechanism becomes dominant, causing a concurrent decrease in both *ΦP* and *ΦF* (Porcar-Castell *et al.*, 2014), establishing therefore the basis for the correlation between *SIF* and photosynthesis.

It should be noted that there are a variety of processes that can decouple the relationship between *SIF* and photosynthesis, such as mitochondrial respiration, photorespiration (Genty *et al.*, 1990), cyclical electron transport and alternative electron sinks, such as chlororespiration (Nixon, 2000) and the Mehler reaction (Asada, 2000).

1.4 Pulse amplitude modulation fluorimetry and photosynthesis

Many of the parameters described in the previous section can be empirically estimated through pulse amplitude modulation (PAM) fluorimetry. The PAM technique employs a weak and pulsed measuring light (ML) which is strong enough to induce a feeble fluorescence emission, but not intense enough to elicit photosynthesis in the dark. The fluorescence emitted in a dark adapted leaf (no *NPQ*) from the ML is defined as F_o. An application of an unmodulated saturating pulse (SP) of light is enough to completely saturate all reactions centers, which causes a spike in fluorescence emission. This maximum fluorescence induced by the SP in a dark adapted leaf is defined as F_m. These two values can be utilized to estimate dark adapted ΦP (ΦP^o) as $(F_m\text{-}F_o)\ /F_m$ (Butler, 1978). If the same method is repeated in a light adapted leaf (with a certain level of NPQ activity) the parameters F'_o and F'_m are derived. These two fluorescence values are of lower magnitude than the ones derived from a dark-adapted leaf because the NPQ process is actives and therefore dissipates some of the additional energy. It is therefore possible to calculate *NPQ* as $(F_m - F'_m)\ /\ F'_m$ (Bilger & Bjorkman, 1991). PAM allows to calculate a large amount of parameters such as *PQ*, *NPQ*, q, ΦP, ΦF, ΦN (Porcar-Castell, 2011) and conductance of Cyt *b6f* (Johnson & Berry, 2021). For details on the practical calculation of these parameters from time series of PAM measurements the reader is referred to the following R package that I wrote. https://github.com/davidmartini90/pam

1.5 Effect of leaf and canopy structure on SIF

Both leaf and canopy structure have a considerable effect on *SIF* emission and *SIF* observed. At leaf scale the chlorophyll content influences not only the amount of absorbed photosynthetic active radiation (*APAR*), and therefore the magnitude of *SIF* emitted, but also the amount *SIF* that escapes the leaf. *SIF* is emitted by chlorophyll molecules, but the same chlorophyll can also re-absorb and scatter *SIF*, as the chlorophyll absorption spectra overlaps with *SIF* emission spectra (Gitelson *et al.*, 1998). Additionally, the wavelength dependency of the chlorophyll absorption spectra causes more *SIF* to be absorbed in the red than in NIR region. Other factors that can affect *SIF* at leaf scale are leaf pubescence, leaf thickness and chloroplast movement. Canopy structure has also a strong influence on the amount of *SIF* observed at top of canopy (TOC), with leaf area index (*LAI*), canopy chlorophyll content, and leaf angle distribution (Migliavacca *et al.*, 2017) having a strong influence on the escape probability of *SIF* (*Fesc*) (Yang & van der Tol, 2018).

Finally, the solar zenith angle (SZA) (Fig. 1.4) has also a considerable effect on canopy interceptance (Liu *et al.*, 2018) and therefore *SIF* emission, and also on the ability to retrieve SIF (Pacheco-Labrador *et al.*, 2019a).

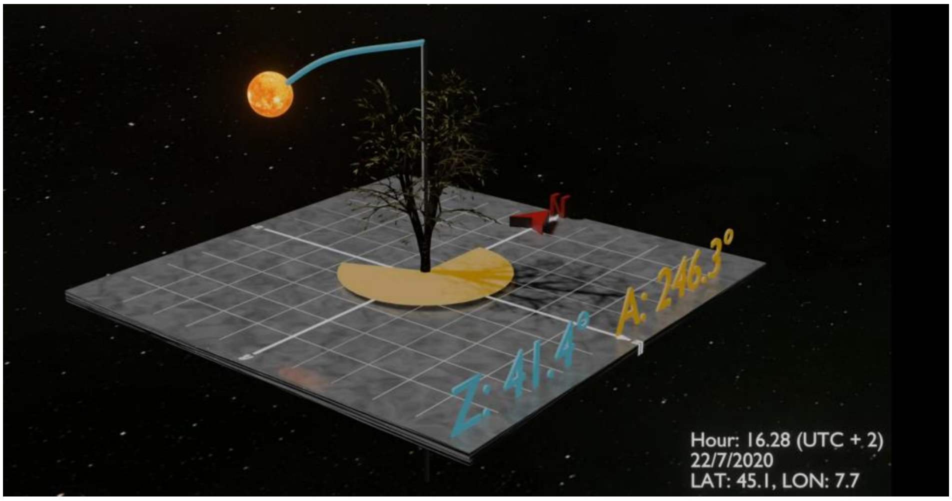

Fig. 1.4. Visualization of the solar azimuth and zenith angle. Frame from the following video that I made as a scientific outreach project and available at: https://www.youtube.com/watch?v=V13njSaPBH8

1.6 Research gaps

The relationship between *SIF* and *GPP* is functional and quite well understood, but complex in nature, as many factors can have a profound influence on their link (Mohammed *et al.*, 2019). Especially when exploring the spatial variability of *SIF* and *GPP* one of the main elements that need to be taken into account besides the species composition, is the nutrient content of the canopy. Leaf nitrogen (*N*) and phosphorus (*P*) content are leaf functional traits and changes in *N* and *P* have the potential to strongly affect both canopy structure (which can result in changes in *APAR* and *Fesc*) and photosynthetic or fluorescence efficiency (Migliavacca *et al.*, 2017). Still, not enough is known with regards to how nutrient contents affect the relationship between *GPP* and *SIF*.

The second research gap relates to the role of extreme heatwave events in shaping the *GPP-SIF* relationship (Wohlfahrt *et al.*, 2018). It is clear that *NPQ* plays a major role in driving the *GPP-SIF* positive relationship, but it is unclear what are the dynamics of *NPQ* at high levels of stress, and how changes in *NPQ* would reflect on the *GPP-SIF* connection at very high temperatures.

Finally the third research gap has to do with understanding the relationship between *SIF* and *T*. In the previous sections much more attention has been put on describing the link between *GPP* and *SIF* than *T* and *SIF*. That is because the practice of using *SIF* to predict *T* is very young and not much is known on how and in which cases *SIF* can be used to predict *T*. *T* and photosynthesis are related via the Fick's law, but it is unclear if *T* is also related to *SIF* via the light reactions. The lack of mechanistic knowledge on the *T-SIF* relationship has not stopped their widespread use in the last 3 years (Lu *et al.*, 2018; Damm *et al.*, 2021), but much more has to be learned in order to accurately obtain *SIF* based *T* predictions; one of the major points is to understand if *SIF* and *T* are indeed mechanistically related, or if their relationship is caused by co-variation with external variables.

1.7 Objectives

The main objectives of this thesis are to understand how nutrient content and extreme events affect the *GPP-SIF* relationship and provide a framework for using *SIF* for *T* predictions. In order to do that a large variety of measurements are employed (SIF retrievals, CO_2 fluxes from chambers, eddy-covariance and PAM measurements) and both empirical and process-based approaches are used. Specifically the following questions are asked:

a) How do the spatial variability, especially in nutrient contents, affect the relationship between *GPP* and *SIF* (chapter 2) ?
b) How do stress events influence the relationship between *GPP* and *SIF* (chapter 3)?
c) How can *SIF* be used to predict *T* (chapter 4)?

2 Nitrogen and Phosphorus effect on Sun-Induced Fluorescence and Gross Primary Productivity in Mediterranean grassland[1]

---

[1] This chapter is based on: Martini, D., Pacheco-Labrador, J., Perez-Priego, O., Van der Tol, C., El-Madany, T. S., Julitta, T., ... & Migliavacca, M. (2019). Nitrogen and phosphorus effect on sun-induced fluorescence and gross primary productivity in mediterranean grassland. *Remote sensing*, *11*(21), 2562.

Abstract:

Sun-Induced Fluorescence at 760 nm (F_{760}) is increasingly being used to predict Gross Primary Production (GPP) through light use efficiency (LUE) modeling, even though the mechanistic processes that link the two are not well understood. We analyzed the effect of nitrogen (N) and phosphorous (P) availability on the processes that link GPP and F_{760} in a Mediterranean grassland manipulated with nutrient addition. To do so, we used a combination of process-based modelling with Soil-Canopy Observation of Photosynthesis and Energy (SCOPE), and statistical analyses such as path modelling. With this study we uncover the mechanisms that link the fertilization-driven changes in canopy Nitrogen concentration (N%) to the observed changes in F_{760} and GPP. N addition changes plant community structure and increase canopy Chlorophyll content, which jointly lead to changes in photosynthetic active radiation (APAR), which ultimately affect both GPP and F_{760}. Changes in plant type abundance (e.g. changes in the abundance of graminoids, %graminoids) driven by N addition lead to changes in structural properties of the canopy such as leaf angle distribution, and ultimately influenced observed F_{760} by controlling the escape probability of F_{760} (Fesc). In particular we found a change in GPP-F_{760} relationship between the first and the second year of the experiment that is largely driven by the effect of plant type composition on Fesc, whose best predictor is %graminoids. The P addition leads to a statistically significant increase on light use efficiency of fluorescence emission (LUE_f), in particular in plots with also N addition, consistent with leaf level studies. The N addition induced changes in the biophysical properties of the canopy that lead to a trade-off between surface temperature (Ts), which decreases, and F_{760} at leaf scale ($F_{760leaf,fw}$) that increases. We found that Ts is an important predictor of the light use efficiency of photosynthesis, indicating the importance of Ts in LUE modelling approaches to predict GPP.

2.1 Introduction

An accurate estimation of gross primary production (GPP) by terrestrial ecosystems is crucial to understand the variability of the global carbon (C) cycle (Beer *et al.*, 2010). One of the most common ways to estimate GPP relies on the use of light use efficiency (LUE) models (Equation 2.1). In the LUE framework (Monteith, 1972), estimates of GPP are based on three variables: i) the fraction of photosynthetically active radiation (fAPAR) absorbed by the vegetation; ii) the actual light use efficiency of photosynthesis (LUEp), i.e. the conversion efficiency of absorbed radiation to fixed carbon; and iii) incident photosynthetically active radiation (PAR).

$$\mathrm{GPP} = \mathrm{fAPAR} \times \mathrm{PAR} \times \mathrm{LUE_p} \tag{2.1}$$

The development and retrieval methods in passive sensing of sun-induced chlorophyll fluorescence (SIF), i.e. the radiation emitted by plants upon sun exposure, opens new possibilities to estimate GPP using remotely sensed data (Guanter *et al.*, 2014; Zhang *et al.*, 2014; Yang *et al.*, 2015). In the last decade several studies have shown that sun-induced fluorescence at 760 nm retrieved from top-of-canopy (TOC) measurements (F_{760}) can track changes in APAR and LUE_p, and therefore can be directly linked to GPP from leaves (Meroni *et al.*, 2009), ecosystem, (Damm *et al.*, 2010; Rossini *et al.*, 2010; Wieneke *et al.*, 2016; Migliavacca *et al.*, 2017) to regional and global scale (Lee *et al.*, 2013; Guanter *et al.*, 2014; Parazoo *et al.*, 2014; Guan *et al.*, 2016).

Although the mechanistic link between GPP and F_{760} is not completely understood, recent advances in the field have contributed to explaining the process under various conditions (Ač *et al.*, 2015; Cendrero-Mateo *et al.*, 2015). The reason why F_{760} and GPP correlate is that both processes start with the absorption of light by a chlorophyll molecule. Once the photon is captured by the antenna and reaches the reaction center of the photosystem II, the chlorophyll molecule can return to the ground state through photochemical quenching (PQ), through the non-photochemical quenching of the excited state (NPQ), as the photon is dissipated non-radiatively as heat (Bilger & Bjorkman, 1991), or it can be re-emitted as a photon of fluorescence (Govindjee, 1995). Fluorescence emission cannot be physiologically regulated, and its quantum yield depends on the efficiency of the PQ and NPQ (Govindjee, 1995). The mechanisms regulating the partitioning of absorbed photosynthetically active radiation (APAR) into the different pathways is therefore fundamental to grasp the connection between GPP-F_{760} (Porcar-Castell *et al.*, 2014; van der Tol *et al.*, 2014).

F_{760} is usually described with a similar approach to the Monteith's LUE framework as shown in Equation 2.2:

$$F_{760} = \text{fAPAR} \times \text{PAR} \times \text{LUE}_\text{f} \times \text{Fesc} \tag{2.2}$$

where F_{760} is equal to the product of fAPAR, PAR, the light use efficiency of fluorescence emission at 760 nm (LUE_f), and the escape probability of chlorophyll fluorescence at 760 nm (Fesc) (Damm *et al.*, 2015).

Equation 2.1 and Equation 2.2 can be combined in Equation 2.3, which shows that the only variables that control the relationship between GPP and F_{760} are LUE_p, LUE_f and Fesc:

$$\text{GPP} = F_{760} \frac{\text{LUE}_\text{p}}{\text{LUE}_\text{f} \times \text{Fesc}} \tag{2.3}$$

Multiple factors can influence the different terms in Equation 2.3, and eventually GPP-F_{760} relationship (Zhang *et al.*, 2014; Migliavacca *et al.*, 2017). Among these, the ones that require more attention because they are not fully understood are i) leaf nutrient content, in particular Nitrogen (N) and Phosphorous (P), and ii) canopy structural parameters such as leaf area index (LAI) and leaf angle distribution (LAD), that in grasslands are often related to the community structure of the canopy (Grime, 2006; Migliavacca *et al.*, 2017). Being able to quantify the effect of nutrients and canopy structure on the partitioning of absorbed radiation and on LUE_p, LUE_f, and Fesc is the first step to shed light on GPP and F_{760} changes under different nutrient availability.

Canopy N concentration (hereafter N%, N mass per gram of leaves of the whole canopy) is often related to the nutritional condition where the plant grows. Nitrogen is a fundamental constituent of leaves that is typically associated with higher LAI, and positively correlated with the amount of chlorophyll a and b (Cab) (Niinemets *et al.*, 1999). Higher LAI and Cab increase APAR, but at the same time should reduce Fesc due to higher absorption and scattering of emitted fluorescence (Ač *et al.*, 2015). Nitrogen is also positively related to the amount of ribulose-l,5-bisphosphate carboxylase and oxygenase (Rubisco) protein content (Evans, 1989; Houborg *et al.*, 2013), and thus the maximum carboxylation rates (Vcmax), that is a key determinant of the maximum photosynthetic rates, and therefore GPP (Farquhar *et al.*, 1980). Therefore nitrogen can influence the partitioning of APAR into PQ, NPQ, and fluorescence emission (Cendrero-Mateo *et al.*, 2015), but different studies, mainly at leaf level, showed contrasting results (Verhoeven *et al.*, 1997; Ač *et al.*, 2015). Moreover, there is lack of studies that investigate at canopy scale how LUE_p, LUE_f, and Fesc are modulated under varying nitrogen availability (Ač *et al.*, 2015). Canopy Phosphorous concentration (hereafter P%) is another critical element for photosynthesis, being involved in the synthesis of Adenosine triphosphate (ATP) (Jiang *et al.*, 2019). Leaf-level studies with active fluorescence measurements showed that P% deficient plants have lower chlorophyll fluorescence emission efficiency

(Singh *et al.*, 2017). However, we are not aware of canopy level studies showing the effect of P% on F_{760} and LUE_f.

Canopy structural variables, such as LAI and LAD, influence the radiative transfer of incoming radiance and emitted SIF within the canopy (van der Tol *et al.*, 2014). LAD can vary on a daily and seasonal basis and is strongly influenced by species composition and plant functional forms (Wohlfahrt *et al.*, 2001). LAI and LAD can have a major influence on the sun/shaded leaf ratio through the canopy. This ratio has the potential to directly influence the level of NPQ in the canopy (Porcar-Castell *et al.*, 2008) (higher in sunlit, lower in shaded leaves) and therefore could indirectly influence the LUE_f. Canopy structure, through absorption and scattering of the fluorescence emitted by the leaves, has a significant influence on observed F_{760}, determining Fesc, the probability of F_{760} to escape the canopy. (Yang & van der Tol, 2018). Absorption by chlorophyll is higher in the red region, whereas multiple scattering in the far red region increases the probability of absorption by soil and woody elements. It has been shown recently with modeling studies that TOC observed F_{760} (canopy scale) is only a fraction of the F_{760} emitted at leaf scale ($F_{760leaf}$) (Liu *et al.*, 2018). The decoupling between $F_{760leaf}$ and F_{760}, mainly mediated by Fesc, can have implications for the GPP-F_{760} relationships. Recently, new methods to estimate Fesc have been developed, potentially allowing to downscaling the F_{760} signal at the leaf level (Yang & van der Tol, 2018; Zeng *et al.*, 2019) (Yang, P *et al.*, 2020). Finally, other variables such as soil moisture or surface temperature (Ts) have also the potential to impact the relationship between GPP-F_{760}. Heat and water stress have been proven to affect photorespiration, but not the PQ in Mediterranean species (Galmés *et al.*, 2007), thus decoupling photochemistry from F_{760} (Porcar-Castell *et al.*, 2014). Ts in particular, contains both information of the activation of NPQ mechanisms, but also other processes related to stomatal closure and sensible heat losses (Alonso *et al.*, 2017).

Therefore, surface temperature might also help to better characterize the seasonal variations of LUE_p and therefore to better predict GPP, in particular under stress conditions (Hilker *et al.*, 2008; Alonso *et al.*, 2017). Fig. 2.1 illustrates a theoretical framework that sums up current knowledge and our hypothesis regarding the interlinks between GPP, F_{760} and their relationship with canopy structural parameters and leaf traits of vegetation. In Fig. 2.1 solid colored lines represent the energy partitioning at both leaf and canopy level and dotted lines represent the hypothesized relationships.

All the factors illustrated in Fig. 2.1 play a role in determining GPP, F_{760}, and their relationship. However, the strength of these influences, and whether leaf nutrient content and canopy structure influence the GPP-F_{760} relationship directly (through LUE_p, LUE_f and Fesc) or occur indirectly (mediated by APAR or by a third variable), is not clear.

In this chapter we aim to fill the gap in understanding on how nutrients and canopy structure control LUE_p, LUE_f and Fesc, and we investigate the mechanisms that drive GPP and F_{760} in a nutrient manipulation experiment. We asked the following questions:

i) How do the treatments (N, NP, P) influence LUE_p, LUE_f, Fesc?

ii) What are the drivers of the light use efficiency equations terms (LUE_p, LUE_f, Fesc) that relate GPP and F_{760}?

iii) What are the direct and indirect effects of nutrients (in particular N%) and canopy structure on GPP and F_{760}?

To answer these questions we use GPP, F_{760}, and additional data on vegetation properties from a nutrient manipulation experiment in Mediterranean grassland with addition of N, P and N and P together (NP). The aim of the fertilization is to induce a change in both plant nutrient content and structural traits (through changes in LAD mediated by plant community and LAI) within the ecosystem.

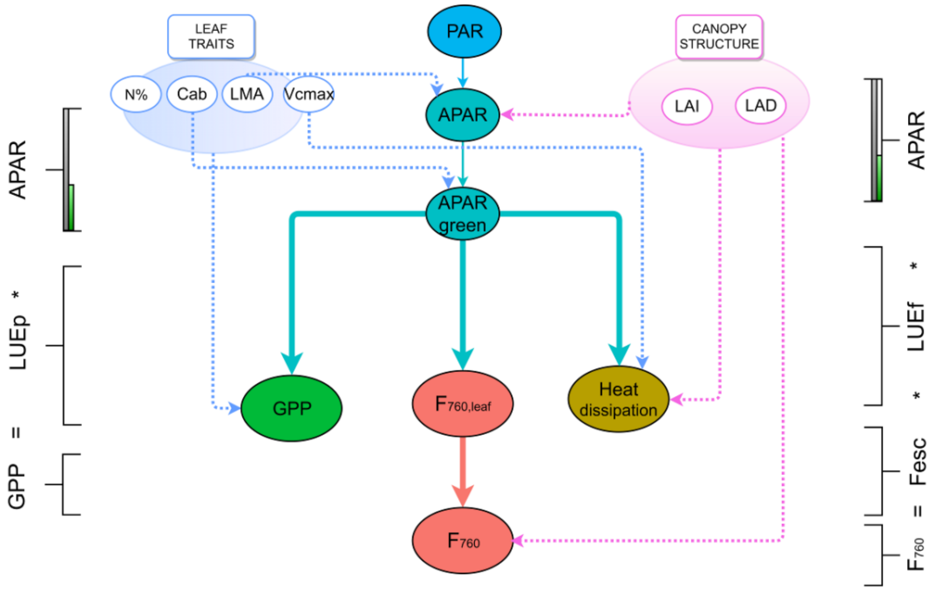

Fig. 2.1. Energy partitioning at the leaf and canopy level representing the processes involved in the photosynthetic light use efficiency model (GPP=APAR * LUE_p) and fluorescence light use efficiency model (F_{760} = APAR *LUE_f * Fesc) are represented with solid arrows. Dotted arrows represent the hypothesized relationship between leaf traits, canopy structure and the various processes related to the allocation of energy and transfer of SIF within the canopy. Photosynthetic active radiation (PAR); absorbed (by vegetation) photosynthetic active radiation (APAR); PAR absorbed by Chlorophyll a and b molecules ($APAR_{green}$), represented as the green bar in the equations on both sides of the figure; gross primary production (GPP); sun-induced fluorescence emitted by all leaves at 760 nm ($F_{760leaf}$); sun-

induced fluorescence at 760 nm observed at top of canopy (F_{760}); Nitrogen concentration on a mass basis (N%); chlorophyll a and b on a mass basis (Cab); leaf mass per area (LMA); maximum carboxylation rate on a mass basis (Vcmax); leaf area index (LAI); leaf angle distribution (LAD).

2.2 Materials and Methods

Experimental site

The study was conducted in a Mediterranean savannah located in Spain (39°56'24.68"N, 5°45'50.27"W; Majadas de Tietar, Caceres) characterized by a continental Mediterranean climate, with temperate winters and warm dry summers: mean annual temperature of 16.7°C, annual precipitation of ~650 mm distributed mainly between September and May (Perez-Priego *et al.*, 2015).

The herbaceous layer is dominated by annual C3 species of the three main functional plant forms: grasses, forbs and legumes that are green and active from October to end May (Luo *et al.*, 2018a). The site is managed as a typical wood pasture (Iberian *Dehesa*) with low intensity grazing by cows (~0.3 cows ha^{-1}) (Perez-Priego *et al.*, 2015).

Nutrient manipulation experiment, Gross Primary Production and ancillary data

A nutrient manipulation experiment focused on the herbaceous layer was established in early spring 2014 and 2015. The set-up consisted of four 20x20 m width randomized blocks. Within each block we established four plots (9x9 m) with 2 m of buffer between treatments (Supplementary Fig. S2.1). We established 4 treatments (for details see Perez-Priego *et al.* (2015)): control (C) with no fertilization, N addition with one application of 100 kg N ha^{-1} as potassium nitrate (KNO_3) and ammonium nitrate (NH_4NO_3), P addition with 50 kg P ha^{-1} as monopotassium phosphate (KH_2PO_4), and nitrogen-phosphorous (NP) addition, 100 kg N ha^{-1} and 50 kg P ha^{-1} as NH4NO3 and KH_2PO_4.

Table 1. Summary of the main meteorological data collected in each field campaign.

Date	Campaign	Fertilization	PAR µmol s^{-1} m^{-2}	VPD hPa	Ta °C	SWC %	SZA °
20-03-14	1	No	**1604.82** ± 11.33	**12.59** ± 0.38	**24.2** ± 0.2	**19.01** ± 0.27	**41.86** ± 0.23
15-04-14	2	Yes	**1842.92** ± 32.63	**15.12** ± 0.59	**30.09** ± 0.55	**22.58** ± 0.58	**31.83** ± 0.85
7-05-	3	Yes	**1342.1** ± 93.73	**22.4** ± 1.98	**32.1** ± 0.91	**4.78** ± 0.09	**25.69** ± 0.6

14							
27-05-14	4	Yes	**1417.15** ± 104.4	**15.83** ± 1.2	**27.89** ± 0.47	**6.57** ± 0.09	**21.4** ± 0.82
04-03-15	5	Yes	**1411.29** ± 18.05	**7.01** ± 0.36	**23.9** ± 0.48	**21.49** ± 1.91	**49.66** ± 0.49
23-04-15	6	Yes	**1842.64** ± 25.23	**16.38** ± 0.84	**29.98** ± 0.37	**6.7** ± 0.11	**31.21** ± 0.98
27-05-15	7	Yes	**1955.21** ± 35.25	**23.2** ± 1.56	**36.33** ± 0.73	**1.14** ± 0.02	**24.26** ± 1.87

PAR is the photosynthetic active radiation. VPD is the Vapor Pressure Deficit, Ta represents the mean air temperature, SWC is the soil water content and SZA is the solar zenith angle. Medians and 1 standard error is shown for each variable.

Carbon Dioxide (CO_2) fluxes between the herbaceous layer and the atmosphere were measured in 32 collars of 60x60 cm for each field campaign around noon local solar time (Table 1). At each collar GPP (µmol $CO_2 m^{-2} s^{-1}$) was estimated as the difference between net ecosystem CO_2 exchange (NEE) measured with transparent chambers and ecosystem respiration (Reco) measured with opaque chambers. Measures CO_2 and water vapor mole fractions (W) were collected at 1 Hz by means of an infrared gas analyzer (IRGA LI-840, Lincoln, NE, USA) connected to the chambers. The flux calculations and corrections were conducted using the self-developed R package *'RespChamberProc'* (https://github.com/bgctw/RespChamberProc). Air temperature (Ta,°C) was measured with a thermistor probe (Campbell Scientific, Logan, UT, USA). Soil moisture content (%) at 5 cm depth was determined with an impedance soil moisture probe (Theta Probe ML2x, Delta-T Devices, Cambridge, UK). Vapor pressure deficit (VPD, hPa) was computed using relative humidity and Ta. Incident PAR (µmol m^{-2} s^{-1}) was measured with a quantum sensor (Li-190, Li-Cor, Lincoln, NE, USA) mounted outside of the chamber. Surface temperature (Ts, °C) was measured with infrared thermometer installed in the chambers (Tc, IRTS-P, Apogee, UT, USA).

The meteorological conditions for each field campaign are reported in Table 1. Destructive sampling of the vegetation in four parcels (0.25x0.25 m each) within each plot was conducted to estimate LAI and green to dry biomass ratio (Perez-Priego *et al.*, 2015). The abundance of each functional group such as fraction of graminoids (%graminoids), forbs (%forbs), and legumes (%legumes) was determined. The Shannon biodiversity index (H) among plant functional types was determined as in (Spellerberg & Fedor, 2003).N% and P% in plant tissues were determined as described in Perez-Priego *et al.* (2015). Carbon isotopic signature ($\delta^{13}C$) for the vegetation was determined from dried samples using a DeltaPlus isotope ratio mass spectrometer (Thermo Fisher, Bremen, Germany) coupled via a ConFlowIII open-split to an elemental analyzer (Carlo Erba 1100 CE analyzer; Thermo Fisher Scientific, Rodano, Italy). δ^{13}C was calculated using the measured ratio between ^{13}C and ^{12}C in the sample and in a calibrated in-house-standard (Acetanilide: -30.06 ± 0.05 ‰) as in (Coplen, 2011; Brand & Coplen, 2012)(Equation 2.4, Supplementary Fig. S2.2):

$$\delta^{13}C = \frac{\left(13R_{sample} - 13R_{standard}\right)}{13R_{standard}} \tag{2.4}$$

where $^{13}R_{sample}$ and 13Rstandard are $^{13}C/^{12}C$ ratio of the sample and of the standard, respectively.

Transpiration estimates

Two independent estimates of transpiration (expresses as latent heat fluxes, LE) have been obtained; one from upscaling the δ^{13}C measurements (LE_{ISO}) and the other from the runs of SCOPE optimized at the experimental site (Pacheco-Labrador Javier 2019) to obtain the LE of canopy component ($LE_{canopy,inv}$).

LE_{ISO} was calculated from δ^{13}C, GPP and VPD according to (Seibt *et al.*, 2008) (Equation 2.5), and then the units were converted from $mmol_{H20}$ m^{-2} s^{-1} to W m^{-2}.

$$LE_{ISO} = \left(\frac{GPP}{WUE_i}\right) \times VPD_{mean} \tag{2.5}$$

where VPD_{mean} is the mean daytime VPD computed over the period between the beginning of the growing season and the plant sampling dates for the isotope measurements, and intrinsic water use efficiency (WUE_i) is calculated according to (Equation 2.6):

$$WUE_i = \frac{Ca}{1.6}\left(\frac{b' - \Delta_{lin}}{b' - a}\right) \tag{2.6}$$

where Ca is the CO_2 mole fraction in ambient air, *b′* is the mean fractionation during carboxylation and internal transfer (0.27%), *a* is the fractionation during diffusion through stomata (0.44 %) and Δ_{lin} is the community weighted mean of δ^{13}C.

Supplementary Fig. S2.3a,b display LE_{ISO} and $LE_{canopy,inv}$ respectively and Supplementary Fig. S2.3c shows the scatterplot of the two estimates. The two independent estimates have a good relationship, with Pearson correlation coefficient (r) of 0.701 and slope of 0.809. In Supplementary Fig. S2.3a there are no significant differences among treatments for each campaign in 2014 or 2015 in LE_{ISO}. According to the ANOVA test, the $LE_{canopy,inv}$ shows significant differences in the campaign 2 in 2014 ($F_{3,11}$= 11.4, p= 0.01) and the Tukey HSD post hoc-test identifies the P treatment as significantly different from the C treatment (p = 0.012). Also, in 2015 in the campaign 7 there is a significant difference ($F_{3,10}$= 5.47, *p*= 0.017) and the Tukey post-hoc identifies a significant decrease for N and P treatments in comparison with the control (*p*= 0.016, *p*= 0.042 respectively).

Field spectroscopy, retrieval of sun-induced fluorescence and biophysical properties

TOC spectral radiances were collected under clear-sky conditions immediately before flux measurements at each collar (Perez-Priego *et al.*, 2015; Migliavacca *et al.*, 2017). The sampling strategy was designed to minimize the differences in solar zenith angle (SZA) between measurements, confirmed by the ANOVA test which reports non-significant differences in SZA between treatments in each campaign (*p* = 0.43, *p* = 0.41, *p* = 0.33, *p* = 0.65, *p* = 0.99, *p* = 0.99, *p* = 0.57, for the campaign 1 to 7 respectively). The ranges of SZA for the spectral measurements are reported in Table 1. Two portable spectrometers (HR4000, OceanOptics, USA) were used to estimate chlorophyll fluorescence at the O_2A band (i.e. F_{760},) and reflectance in the spectral range 400-1000 nm. The measurements protocol was the following: we first measured the incident solar irradiance by nadir observations of a leveled calibrated standard reflectance panel (Spectralon, LabSphere, USA), and second we acquired five measurements of TOC spectral radiances from nadir at 110 cm above the targeted area using bare fiber optics of 25° of field of view (about 43 cm diameter at the ground, Supplementary Fig. S2.4). F_{760} was estimated by exploiting the spectral fitting method (Meroni *et al.*, 2009). The spectral interval used for F_{760} was set to 759.00–767.76 nm.

$Albedo_{400\text{-}900}$ was calculated from TOC spectral radiances as shown in Equation 2.7, assuming a Lambertian behavior of the reflected radiance.

$$Albedo_{400-900} = \frac{\int_{400}^{900} L_r \times \pi}{\int_{400}^{900} E} \tag{2.7}$$

where L_r is the reflected radiance and $E_{400\text{-}900}$ is the Irradiance.

fAPAR was estimated in three different ways;

i) $fAPAR_{SCOPE}$ simulated by the process based SCOPE model (van der Tol *et al.*, 2009b);

ii) $fAPAR_{RENDVI}$ based on the established relationship between measured fAPAR and the red edge NDVI (RENDVI) found in maize, soybean and grasslands (Vina & Gitelson, 2005) (Equation 2.8).

$$fAPAR_{RENDVI} = 1.61 \times RENDVI - 0.03 \tag{2.8}$$

where RENDVI is calculated as show in Equation 2.9:

$$\mathrm{RENDVI} = \frac{(\mathrm{R_{NIR}} - \mathrm{R_{RE}})}{(\mathrm{R_{NIR}} + \mathrm{R_{RE}})} \tag{2.9}$$

where R_{NIR} and R_{RE} are reflectance factors in spectral bands 770-800 nm and 700-710 nm, respectively

iii) $APAR_{Li\&Moreau1996}$ based on subtracting the the integral (between 400 and 700 nm) of the incoming PAR (PAR_{inc}) from the integral (between 400 and 700 nm) of the reflected PAR (PAR_{refl}) measured by the spectrometers (Li & Moreau, 1996; Damm *et al.*, 2010) and then muliplying by the proportion of canopy absorption (RAPAR) (Moreau & Li, 1996) (Equation 2.10).

$$APAR_{Li\&Moreau1996} = (\mathrm{PAR_{inc}} - \mathrm{PAR_{refl}}) \times \mathrm{RAPAR} \tag{10}$$

where RAPAR is calculated as:

$$RAPAR = 0.105 - 0.323 \times NDVI + 1.468 \times NDVI^2 \tag{11}$$

The fAPAR formulations are quite consistent with each other (Supplementary Fig. S2.5), and therefore hereafter we use $fAPAR_{RENDVI}$.

SCOPE model simulations

Forward and inverse simulations with the SCOPE model were conducted to assess the robustness of fAPAR, Fesc, and LE_{ISO} derived from field observations.

The forward runs model was parameterized using the structural and functional traits derived from the field sampling as well as meteorological and chamber data. Vapor pressure deficit (VPD, hPa), air pressure (p, hPa), short wave downwelling radiation (Rin, W m^{-2}), long wave downwelling radiation (Rli, W m^{-2}), air temperature (Ta, °C), wind speed (u, m s^{-1}), soil moisture content (SMC, %), leaf area index (LAI), canopy height (h, m), chlorophyll a and b content (Cab, μg cm^{-2}), dry matter content (Cdm, g cm^{-2}), maximum carboxylation rate (Vcmax, μmol m^{-2} s^{-1}) and the parameters to characterize the leaf angle distribution (LAD), respectively LIDFa and LIDFb, were used to parameterize the model run. SCOPE meteorological drivers were measured along with chamber measurements for the majority, in case not available with the chambers, such as Rin, Rli, p, VPD, wind speed, atmospheric CO_2 concentration (Ca, ppm), atmospheric O_2 concentration (Oa, ppm) were derived by linearly interpolating two consecutive measurements around the chambers measurement time collected at the nearby eddy covariance flux tower at 10 min of temporal resolution. Canopy height was estimated in the field with a meter stick in five positions within the measurement collar. Additional parameters such as leaf equivalent water thickness, leaf width, Ball-Berry stomatal conductance parameter and dark respiration rate at 25°C as fraction of Vcmax were obtained from the literature for C3 grasses (Migliavacca *et al.*, 2017). The SZA at the time of the collection of the spectral measurements was used as model input. Soil reflectance spectra were collected in a dedicated field campaign in April 2015 and used for all the runs. Leaf angle distribution was parametrized in SCOPE as in Migliavacca *et al.* (2017) by assuming grasses to be erectophile, forbs spherical and legumes planophiles.

The accuracy of F_{760} and GPP simulated with SCOPE (F_{760FW} and GPP_{FW}, respectively) was evaluated by root mean-squared error (RMSE), slope, intercept, and the determination coefficient (R^2) of the linear regression between observed and modeled data (Supplementary Fig. S2.6).

Inverse runs of SCOPE against reflectance, F_{760}, GPP and thermal radiance, as described in Pacheco-Labrador Javier (2019) were carried out to obtain $LE_{canopy,inv}$ and Fesc ($Fesc_{inv}$).

Calculation of the Light use efficiency of photosynthesis (LUE_p) ,light use efficiency of fluorescence emission (LUE_f) and escape probability of F_{760} (Fesc).

For each plot and campaign the LUE_p, LUE_f and Fesc were computed. LUE_p was calculated as in Equation 2.12:

$$LUE_p = \frac{GPP}{APAR} \tag{2.12}$$

where GPP is the one measured with the chambers and APAR is calculated as in Equation 2.13:

$$APAR = fAPAR_{RENDVI} \times PAR \tag{2.13}$$

LUE_f, is computed as in Equation 2.14:

$$LUE_f = \frac{F_{760}}{APAR_{radiance} \times Fesc_{fw}} \tag{2.14}$$

where F_{760} is the TOC fluorescence retrieved and $Fesc_{fw}$ is the escape probability calculate from forward runs of SCOPE and $APAR_{radiance}$ (mW m^{-2} nm^{-1} sr^{-1}) is calculated from APAR (μmol m^{-2} s^{-1}) as shown in Equation 2.15. The coefficient 4.6 represents the conversion factor from μmol m^{-2} s^{-1} to W m-2 for radiation from 400 to 700 nm (Sager & McFarlane, 1997) and wl is the wavelength interval (300 nm).

$$APAR_{radiance} = \frac{APAR}{(4.6 \times wl \times \pi)} \times 1000 \tag{2.15}$$

We computed Fesc and $F_{760leaf}$ in three alternative ways to evaluate their consistency:

i) Combination of forward runs of SCOPE and measured F_{760} ($Fesc_{fw}$) as shown in Equation 2.16:

$$Fesc_{fw} = \frac{F_{760} \times \pi}{F_{760leaf,FW}} \tag{2.16}$$

$F_{760leaf,FW}$ and $F_{760leaf,fw}$ are fluorescence emitted by all leaves at 760 nm as calculated by the forward SCOPE run (hemispherical and directional respectively).

ii) An empirical estimate of Fesc ($Fesc_{emp}$) computed according to Zeng *et al.* (2019) (Equation 2.17):

$$Fesc_{emp} = \frac{NIR_v}{fAPAR_{RENDVI}} \tag{2.17}$$

NIR_V is calculated as in Equation 2.18, where NIR_T is the reflectance at 858 nm.

$$NIR_V = NDVI \times NIR_T \tag{2.18}$$

Then empirical F_{leaf} ($F_{760leaf,emp}$) was calculated as in Equation 2.19.

$$F_{760leaf,emp} = \frac{F_{760}}{Fesc_{emp}} \tag{19}$$

iii) An estimation of Fesc using data from a SCOPE inversion ($Fesc_{inv}$) (Equation 2.20).

$Fesc_{inv}$ was obtained from inversion of SCOPE against reflectance, F_{760}, GPP and thermal radiance, as described in Pacheco-Labrador Javier (2019) and was calculated as in Equation 2.20.

$$Fesc_{inv} = \frac{F_{760INV}/\pi}{F_{760lea,INV}} \tag{2.20}$$

Where F_{760INV} and $F_{760leaf,INV}$ are the top-of canopy sun-induced fluorescence at 760 nm and sun-induced fluorescence emitted by all leaves at 760 nm as obtained from SCOPE inversion.

Finally $F_{760leaf,inv}$ was calculated as in Equation 2.21.

$$F_{760leaf,inv} = \frac{F_{760}}{Fesc_{inv}} \tag{2.21}$$

The three alternatives Fesc and F_{leaf} computed ($F_{760leaf,fw}$, $F_{760leaf,emp}$, $F_{760leaf,inv}$) were compared against each other (Supplementary Fig. S2.7) and the analysis presented below were conducted with all the different estimates of Fesc to evaluate the effect on the results presented. Hereafter, we report only the results obtained with $Fesc_{fw}$ and $F_{760leaf,fw}$.

Statistical analysis

Our statistical analysis consisted of three parts. First, to answer research question i), group differences among treatments were analyzed with Analysis of Variance (ANOVA) and differences among groups were tested with Tukey Honest Significant differences (HSD) post-hoc test. In case of violation of the assumption of homoscedasticity of residuals the ANOVA with the Welch's correction (Moder, 2010) and post-hoc analysis with Games-Howell test (Games & Howell, 1976) were used. Also, an analysis of Covariance (ANCOVA) was used to test if the relationship between GPP and F_{760} (canopy scale) and $F_{760leaf,fw}$ (leaf level) is changing with the treatment and in time (Fig. 2.4).

Second, we addressed the research question ii) with the relative importance analysis with "lmg" (Lindeman, Merenda and Gold), a popular approach for quantifying the individual contributions of multiple regressors, assuming linear relationships, as implemented in the R package "relaimpo" (Groemping & Matthias, 2006). Standard errors were computed by means of bootstrapping (n= 1000 realizations). Independent variables (i.e. predictors) used in the relative importance analysis are N%, %graminoids, %legumes, Ts, LAI, Shannon Biodiversity Index (H) and soil moisture. Additional relative importance analyses were carried out the surface-air temperature (Ts - Ta) in place of Ts (Supplementary Fig. S2.8), as Ts -Ta could be a good proxy for water stress (Sumayao *et al.*, 1980).

Third, to answer the research question iii) a path analysis was used. The path analysis assumes linearity among variables and the effects are considered additive and not multiplicative. The structural model is based on expected relationships hypothesized and its model structure is shown in Supplementary Fig. S2.9. The user specifies the model structure, and the method outputs estimates of the path coefficients. The analysis was conducted with the R package "lavaan" (Rosseel, 2012). The individual links among variables were evaluated by means of the p-value and standardized coefficient (β). It should be noted that in the analysis we used Ts in place of the reflectance based indexes because i) Ts contains information on NPQ (Weis & Berry, 1988), ii) Ts is independent from the measurements used to estimate F_{760}.

Chi-squared (χ^2), comparative fit index (CFI), standardized root mean square of residual (SRMR) and Root Mean Square Error of Approximation (RMSEA) were computed to evaluate the overall accuracy of the models. The standard error of β and of the model fit indices were obtained from bootstrapping the dataset (n=100 realizations). Additionally, to assess the stability of the individual paths across treatments and the robustness of the original model, we made intervention on the dataset by removing from the dataset one treatment and evaluating the impact on the individual β coefficients (Supplementary Fig. S2.10-S13).

2.3 Results

Description of fertilization effects on fluxes, optical data, and vegetation characteristics

The effect of the fertilization treatment on GPP, LUE_p, F_{760}, LUE_f and $Fesc_{fw}$ is shown in Fig. 2.2. All these variables show a wide variation in time (campaign) and with treatment. GPP is higher in the N and NP treatments in 2014 and more substantially in 2015 during the campaign 5 ($F_{3,18}$= 15.6, $p <$ 0.01) and campaign 6 ($F_{3,26}$= 13.1, $p < 0.01$). LUE_p in the N treatment is significantly different from the C treatment only during the campaign 6 ($F_{3,26}$= 2.7, $p < 0.05$).

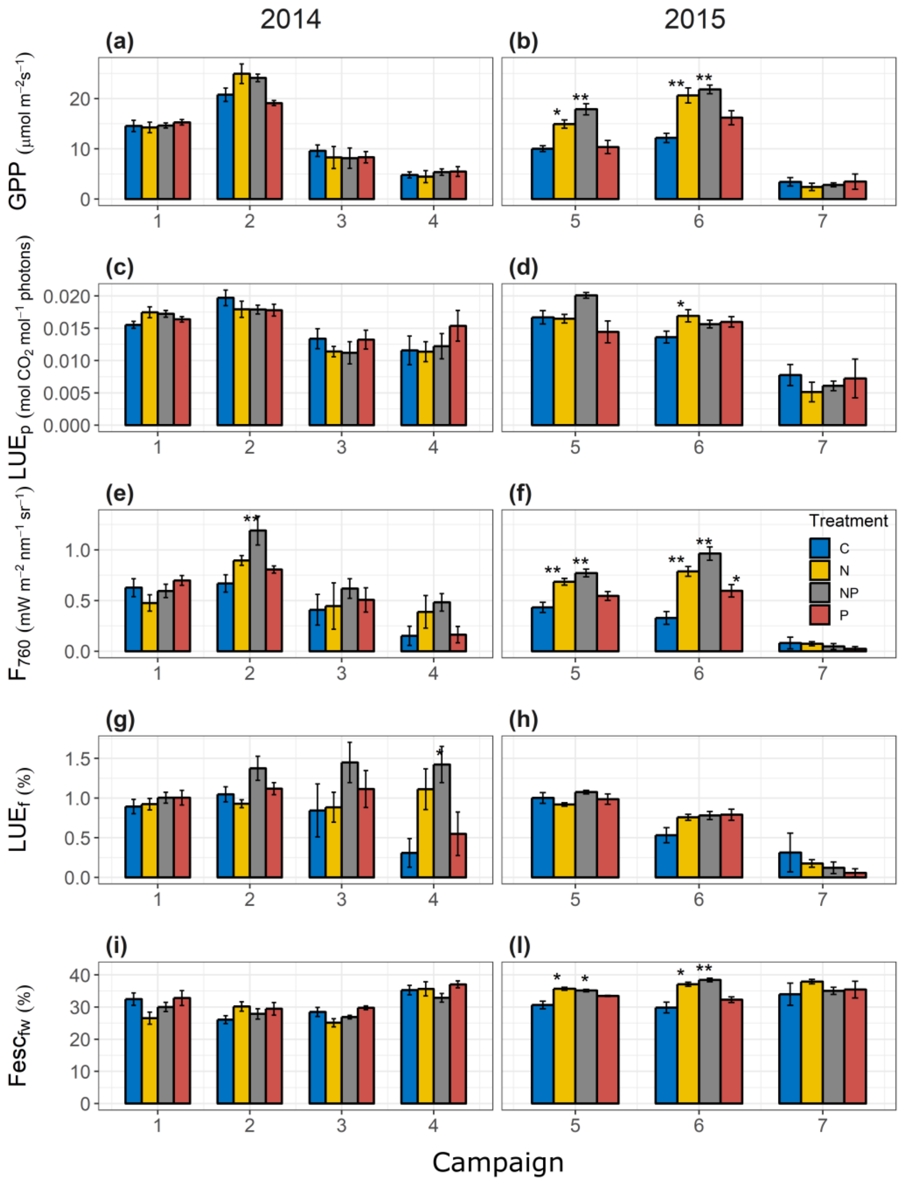

Fig. 2.2. Bar graphs representing differences among treatments (Control Treatment, C; Nitrogen treatment, N; Nitrogen and Phosphorus treatment, NP and Control Treatment, C) of Gross Primary Production (GPP) in 2014 (a) and 2015 (b), light use efficiency of photosynthesis (LUE_p) in 2014 (c) and 2015 (d), Fluorescence at 760 nm (F_{760}) in 2014 (e) and 2015 (f), light use efficiency of fluorescence emission at 760 nm (LUE_f) in 2014 (g) and 2015 (h) and fraction of F_{760} that escapes the canopy ($Fesc_{fw}$) in 2014 (i) and 2015 (l). Data are divided among campaigns. Bar graphs represent means and

error bars represent 1 standard error. Group differences in (a) until (h) were analyzed with ANOVA test and individual differences among groups were evaluated with Tukey HSD post hoc test. Group differences in (i) and (l) were analyzed with ANOVA with the Welch correction and individual differences among groups were evaluated with the Games-Howell post hoc test. “*” refers to a significant difference from the control treatment with p value < 0.05 and “**” refers to a significant difference from the control treatment with p value < 0.01.

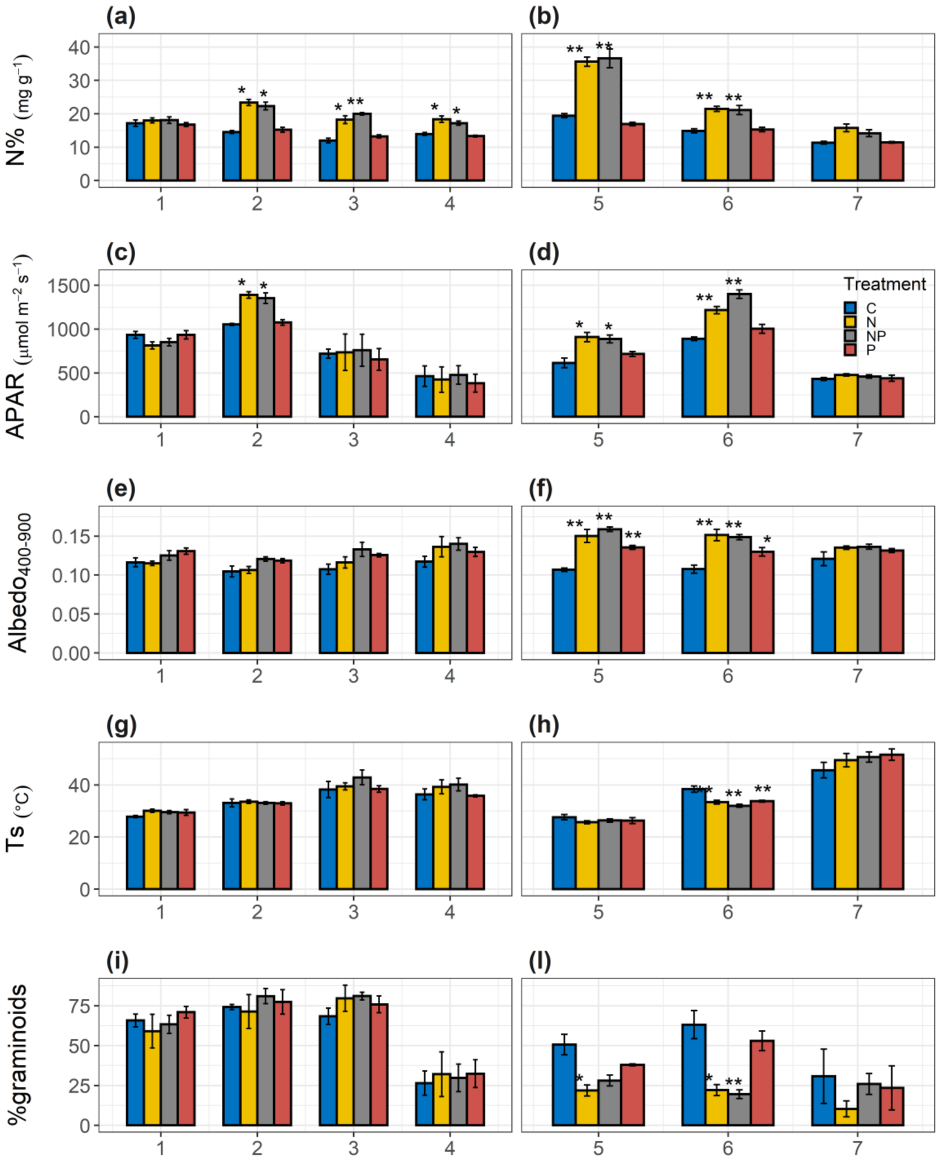

Fig. 2.3. Bar graph representing differences among treatments (Control Treatment, C; Nitrogen treatment, N; Nitrogen and Phosphorus treatment, NP and Control Treatment, C) of Canopy Nitrogen content (N%) in 2014 (a) and 2015 (b), Absorbed Photosynthetic Active Radiation (APAR) in 2014 (c) and 2015 (d), Albedo$_{400\text{-}900}$ in 2014 (e) and 2015 (f), and Surface Temperature (Ts) in 2014 (g) and 2015 (h), and graminoids relative abundance (%graminoids) in 2014 (i) and 2015 (l). Data are divided among campaigns. Bar graphs represent means and error bars represent 1 standard error. Group differences in (e) until (h) were analyzed with Anova test and

individual differences among groups were evaluated with Tukey HSD post hoc test. Group differences in a), b), i), l) were analyzed with ANOVA with the Welch correction and individual differences among groups were evaluated with the Games-Howell post hoc test. "*" refers to a significant difference from the control treatment with p value < 0.05 and "**" refers to a significant difference from the control treatment with p value < 0.01.

F_{760} shows a significant increase during the campaign 2 for the NP treatment ($F_{3,11}$= 5.9, $p < 0.05$) and during the campaign 5 (for N and NP) ($F_{3,18}$= 13.2, $p < 0.01$) and 6 (for N,NP, and P) ($F_{3,26}$= 19.7, $p < 0.01$) of 2015. LUE_f is significantly higher for the NP treatment during the campaign 4 of 2014 ($F_{3,12}$= 4.59, $p < 0.05$), while Fesc shows significant increases for the N and NP treatment of the campaign 5 ($F_{3,18}$= 11.32, $p < 0.05$ and $p < 0.05$ respectively) and 6 ($F_{3,26}$= 15.91, $p < 0.05$ and $p < 0.01$ respectively) of 2015.
Fig. 2.3 displays changes in N%, APAR, $Albedo_{400\text{-}900}$, Ts and plant community (%graminoids) with the fertilization treatment. N% shows a quite consistent increase in the N and NP treatment in 2014 in comparison with the C treatment for the campaign 2 ($F_{3,11}$= 26.8, $p < 0.01$), campaign 3 ($F_{3,12}$= 14.2, $p < 0.01$) and 4 ($F_{3,11}$= 14.2, $p < 0.01$) and in 2015 in the campaign 5 ($F_{3,18}$= 56.2, $p < 0.01$) and 6 ($F_{3,26}$= 18.5, $p < 0.01$). APAR presents significant differences for the N and NP treatment of the campaign 2 ($F_{3,11}$= 24.98, $p < 0.01$) of 2014 and campaign 5 and 6 of 2015 ($F_{3,18}$= 7.37, $p < 0.01$ and $F_{3,26}$= 38.5, $p < 0.01$ respectively).

All treatments show a significant increase in $Albedo_{400\text{-}900}$ during the campaign 5 ($F_{3,18}$= 29.3, $p < 0.01$) and 6 ($F_{3,26}$= 13.6, $p < 0.01$) in 2015, but no significant treatment-induced changes in $Albedo_{400\text{-}900}$ are observed in 2014. Ts shows significant differences in the campaign 6 for the N, NP and P treatments ($F_{3,26}$= 13.5, $p < 0.01$). LE_{ISO} follows the phenological cycle with lower values in 2015 (Supplementary Fig. S2.3a). There are differences in LE_{ISO} among treatments (such as the increase during the campaign 2 of 2014 for N and NP), but these appeared not significant according to the ANOVA. LE_{ISO} estimates are consistent also with independent simulations with SCOPE (Supplementary Fig. S2.3c).
Instead, significant differences in %graminoids among treatment occur mainly in 2015 in the campaign 5 ($F_{3,18}$= 9.4, $p < 0.01$) and 6 ($F_{3,26}$= 13.3, $p < 0.01$) with lower %graminoids in N and NP treatments. %Forbs also present significant differences in 2015 by increasing in the N treatment (in comparison with the C treatment)(($F_{3,18}$= 8.8, $p < 0.01$) and in the campaign 6 in the N and NP treatment ($F_{3,26}$= 11.5, $p < 0.01$) (Supplementary Fig. S2.14d). %Legumes is marginal and does not change significantly among treatments (Supplementary Fig. S2.14e,f).

Temporal variability of GPP-F_{760} and GPP- $F_{760leaf.fw}$ relationship among treatments

The results of the ANCOVA show that in 2014, the intercept of the C treatment is significantly different from the other treatments for both F_{760} (as shown in previous studies (Perez-Priego *et al.*, 2015; Migliavacca *et al.*, 2017) and $F_{760leaf,fw}$ ($p < 0.05$ and $p < 0.05$, respectively) (Fig. 2.4, Supplementary Table S2.1).

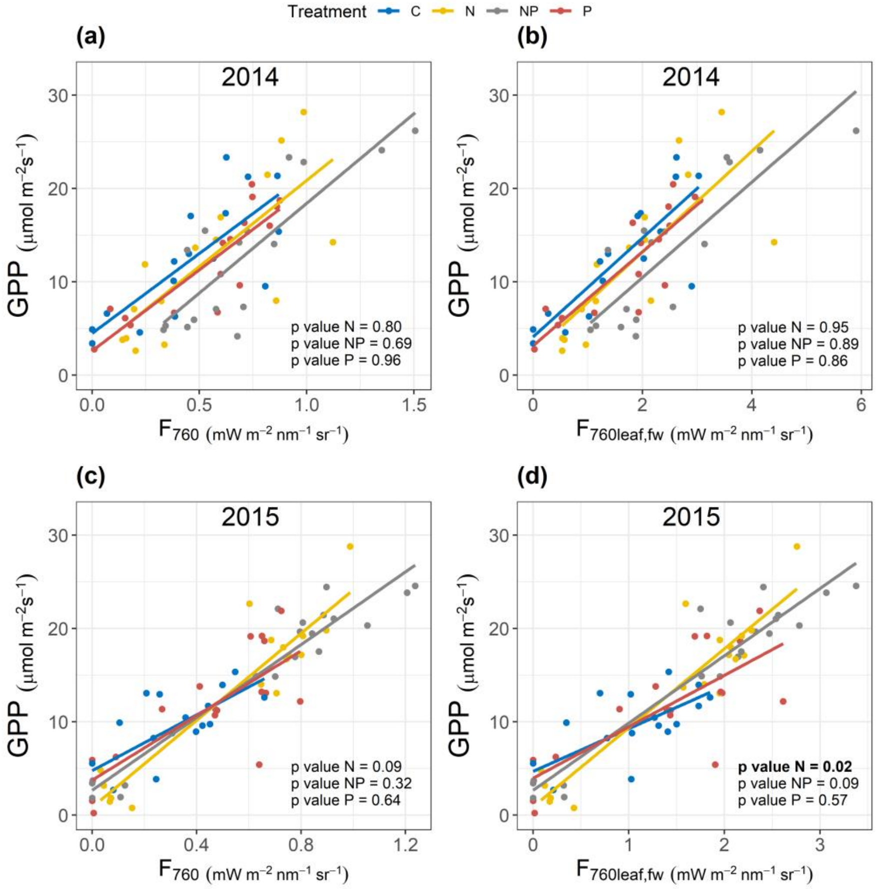

Fig. 2.4. Scatterplot of observed Fluorescence at 760 nm from top of canopy (F_{760}) vs Gross Primary Production (GPP) for 2014 (a) and for 2015 (c) and directional fluorescence emitted by all leaves at 760 nm calculated from forward SCOPE runs ($F_{760leaf,fw}$) vs GPP for 2014 (b) and for 2015 (d). Data are divided for the 4 Treatments; control (C), nitrogen addition (N), nitrogen and phosphorus addition (NP) and Phosphorus addition (P). P values of the interaction Treatment - independent variable (in comparison with the control treatment, C) from an analysis of covariance (ANCOVA) are reported in the

bottom-right of each panel. Colored lines represent the regression from the ordinary least square regression.

In 2015 the intercept is different for the C Treatment for both F_{760} and $F_{760leaf,fw}$ (*p* < 0.01 for both) and for the NP treatment with *p*<0.05 for both F_{760} and $F_{760leaf,fw}$. In 2015 for the N treatment there is no significant interaction between F_{760} and Treatment (Fig. 2.4c), but there is a significant interaction between $F_{760leaf,fw}$ and the N treatment (p < 0.05) (Fig. 2.4d), with significant differences of the relationship GPP- $F_{760leaf,fw}$. There is no significant effect of the year on the relationship between GPP-$F_{760.}$ For each treatment: *p*=0.706, *p*=0.323, *p*=0.927 and *p*=0.992 N, P and NP and C, respectively. Instead when substituting F_{760} with $F_{760leaf,fw}$ the effect of the year is not significant in the treatments C and P (*p*=0.659 and *p*=0.742), but is significant for the NP treatment with *p*<0.05, and barely not significant for the N treatment with *p*=0.057.

Factors controlling the parameters of light use efficiency equation (LUE_p, LUE_f and Fesc)

The relative importance analysis with "lmg" method shows that LUE_p is the variable with the highest explained variance (R^2=0.67 ± 0.054), followed by Fesc (R^2 = 0.62 ± 0.06) and LUE_f (R^2 = 0.46 + 0.06) (Fig. 2.5). The variable that explains the most variance of LUE_p is Ts (R^2 = 0.36 ±0.06), followed by LAI (R^2 = 0.13 ±0.05), Canopy N% (R^2 = 0.06 ± 0.04) and H (R^2 = 0.05 ± 0.04). The main predictor of LUE_f is %graminoids that contributes (R^2 = 0.15 ± 0.07), then Ts (R^2 = 0.13 ± 0.08), LAI (R^2 = 0.07 ± 0.05), and Canopy N% (R^2 = 0.05 ± 0.03).

The main predictor of Fesc is clearly %graminoids (R^2 = 0.52 ± 0.03), followed by soil moisture (R^2 = 0.03 ± 0.04) and Canopy N% (R^2 = 0.02 ± 0.02), the latter contributing only marginally.

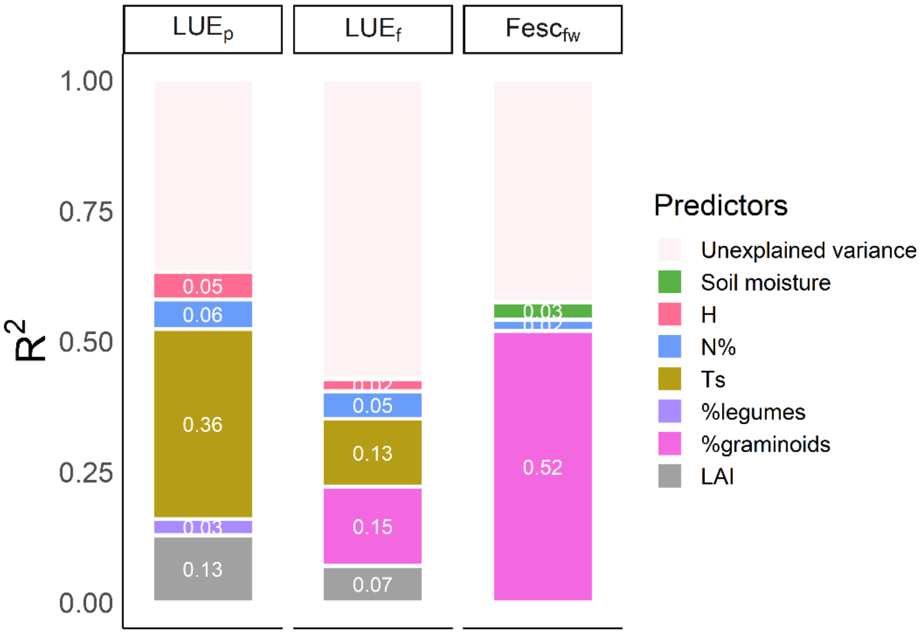

Fig. 2.5. Relative importance analysis with "lmg"(Lindeman, Merenda and Gold) method of Light use efficiency of photosynthesis (LUE$_p$), Light use efficiency of fluorescence emission at 760 nm (LUE$_f$) and escape probability of sun-induced fluorescence at 760 nm obtained from forward runs of SCOPE (Fesc$_{fw}$). Predictors included in the analysis are: soil moisture, Shannon biodiversity index (H), canopy nitrogen content (N%), surface temperature (Ts), relative abundance of legumes (%legumes), relative abundance of graminoids (%graminoids) and leaf are index (LAI). Error bars (1 SE) are calculated through bootstrapping (n= 1000), but are not shown in the figure. They are however reported in the result section.

Results of the relative importance analysis for GPP, F$_{760}$, and F$_{760leaf.fw}$ show the importance of LAI that controls the seasonality of canopy structure and APAR (Supplementary Fig. S2.15).

When substituting as predictor Ts with Ts-Ta we find slightly better results than Ts alone when predicting GPP, F$_{760}$, and F$_{760leaf,fw}$ (Supplementary Fig. S2.8). However, including Ts-Ta does not improve the overall prediction, as the contribution to R^2 of LAI decreases, but the total R^2 remains similar. When predicting LUE$_p$, LUE$_f$, and Fesc, Ts-Ta is a worse predictor of LUE$_p$ than Ts (R^2 = 0.28 ± 0.05).

Mechanisms behind the treatment effect on GPP and F$_{760}$ at leaf and canopy scale

Fig. 2.6 shows the output of the path analysis. The results of the final models are displayed as graphs. The overall model fit is evaluated: χ^2 =129 ± 23, CFI= 0.901 ± 0.03, SRMR= 0.07 ± 0.02 and RMSEA= 0.19 ± 0.02. CFI and SRMR show excellent fit according to (Hu & Bentler, 1999). In contrast, the RMSEA is higher than expected. RMSEA is part of the parsimony-adjusted fit indexes, which reward low model complexity. Our goal is however to represent a holistic model that includes all the relevant processes and we do not use the path analysis *a posteriori* as a mean of model selection. Additionally, according to Iacobucci (2010), "RMSEA over-rejects true models for "small" n (n<250)", which might be the cause of our RMSEA value, as our sample size is 133.

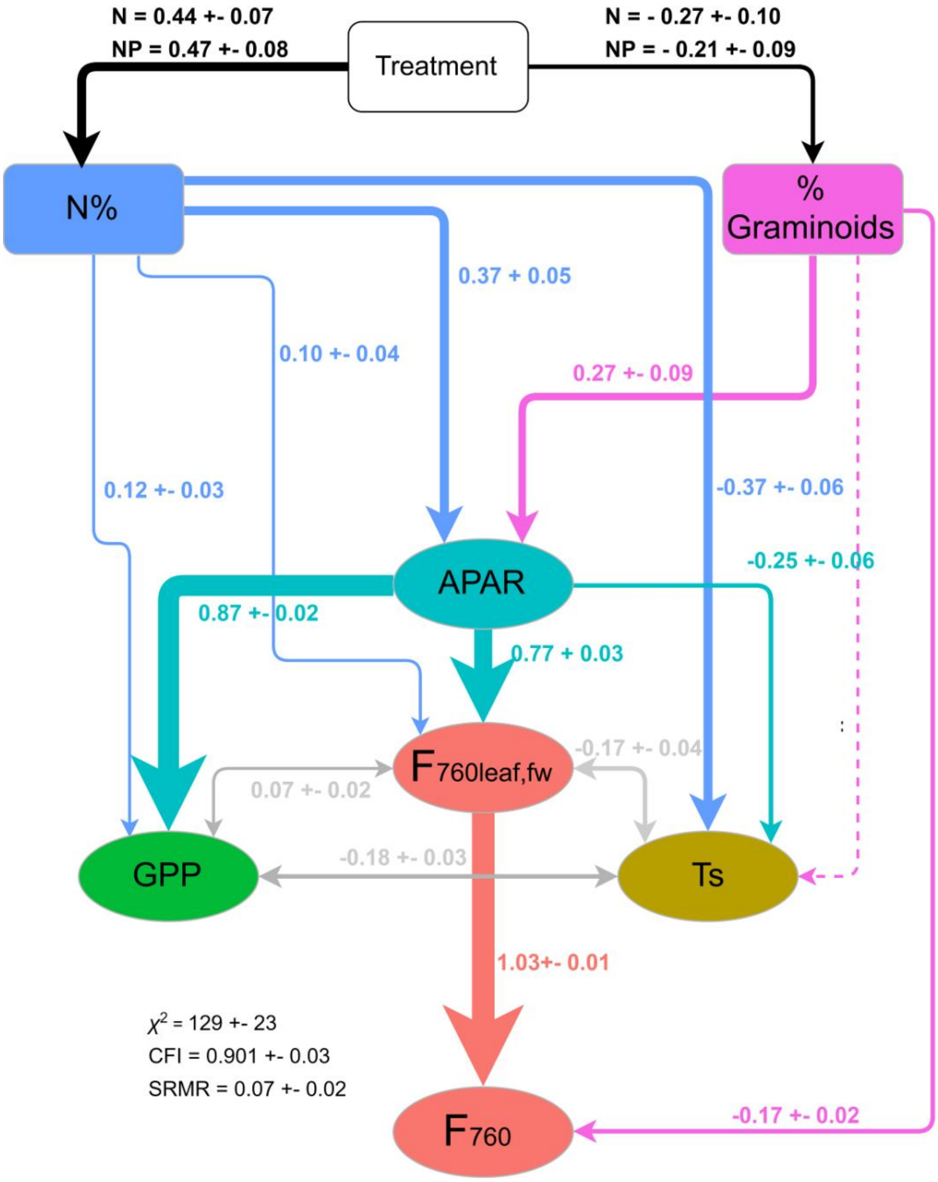

Fig. 2.6. Path analysis displays the role of canopy nitrogen content (Canopy N) and relative graminoids abundance (%graminoids) on the energy partitioning at the leaf and canopy level. Photosynthetic active radiation (PAR); Absorbed by vegetation photosynthetic active radiation (APAR), Fluorescence emission by all leaves at 760 nm calculated by forward runs of SCOPE ($F_{760leaf,fw}$); gross primary production (GPP), Surface temperature (Ts) and observed fluorescence at 760 nm (F_{760}). The strength of the relationship among variables is expressed by the standardized coefficient (β) of the path analysis. Each standardized coefficient has a standard error obtained from

bootstrapping (n=100 times). The width of the arrows is proportional to their standardized coefficient (β). Colored lines (both solid or dotted) represent direct relationships between variables, whereas gray double-headed arrows represent the covariance among variables. Solid and dotted lines indicate significant ($p < 0.05$) and non-significant relationships, respectively. The width of the arrows is proportional to their standardized coefficient (β). The different colors are introduced to increase readability of the standardized path coefficients. The fit by the overall model is measured by means of Chi-squared (χ2), comparative fit index (CFI) and standardized root mean square of residual (SRMR).

Fig. 2.6 shows the clear effect of the %graminoids on F_{760}. The N and NP treatments significantly affect N% with β of 0.44 ± 0.07 and 0.47 ± 0.08 respectively. N and NP treatments also affect significantly %graminoids with β of -0.27 ± 0.1 and -0.21 ± 0.09 respectively. N% has a significant relationship with 4 variables, APAR, Ts, GPP, and $F_{760leaf,fw}$ with β of 0.37 ± 0.05, -0.37 ± 0.06, 0.12 ± 0.03 and 0.10 ± 0.04 respectively. %graminoids significantly affects APAR and F_{760} with β of 0.27 ± 0.09 and -0.17 ± 0.02 respectively. The path between %graminoids and Ts is however not significant. APAR significantly influences GPP, $F_{760leaf,fw}$ and Ts with β of 0.87 ± 0.02, 0.77 ± 0.03 and -0.25 ± 0.06. Finally, $F_{760leaf,fw}$ and Ts have a significant covariance with β of -0.17 ± 0.04 ; $F_{760leaf,fw}$ and GPP have also a significant covariance with β of 0.07 ± 0.02 and so do GPP and Ts with β of - 0.18 ± 0.03.

Alternative models using different estimates of $F_{760leaf}$ were tested and we found that the same paths are selected as significant, and the magnitude of the β coefficients are almost unchanged (Supplementary Fig. S2.16). This suggests that the path analysis model is not strongly dependent by the estimation type of the fluorescence emission. The results of the intervention removing treatments show that the vast majority of the paths remain constant and significant. The only difference can be seen when removing the NP treatment (Supplementary Fig. S2.11), where the links between canopy N and GPP and canopy N and $F_{760leaf,fw}$ become non-significant.

2.4 Discussion

In the following section we first discuss the treatment effects (N, NP, P) on the LUE equation terms, second the predictors of LUE_p, LUE_f and $Fesc_{fw}$, and third how the nutrient fertilization affects GPP and F_{760} through changes in N%, plant community and canopy structure.

Treatment effect on LUE_p, LUE_f, $Fesc_{fw}$

The relative stability among treatments of LUE_p, which is significantly different for the N treatment only in the campaign 6 and shows an increase of

NP in campaign 5 in 2015, suggests that our Mediterranean grasslands is quite constrained in its photosynthetic efficiency, and that any nutrient induced changes in GPP (Fig. 2.2) are mostly modulated by changes in structural parameters such as fAPAR.

The increase in LUE_f in the NP treatment compared to N alone, suggests a co-limitation of nitrogen and phosphorus on fluorescence efficiency. The role of P on the functional modulation of fluorescence efficiency at canopy scale has not yet been shown in the literature. However, a series of studies at leaf level showed a positive relationship between photochemical quenching and P in leaves as well as an effect of P on active fluorescence measurements (Singh & Reddy, 2014), these back the differences in LUE_f observed in our study. Our study suggest that P, and in particular the co-limitation N and P, might have an important role on determining F_{760} but is not conclusive on the mechanism, and more research is needed to understand the mechanism and also to support the current efforts to include P in terrestrial biosphere and photosynthesis models (Jiang *et al.*, 2019).

The fact that the magnitude of increase of $Fesc_{fw}$ is very similar in N and NP treatments support the idea that N addition is the main factor regulating canopy structure ($Fesc_{fw}$, APAR). Other works show that N addition strongly impacts canopy structural parameters such as LAI and plant height in a short-grass prairie (Tatarko & Knops, 2018), though there are no studies focused on the effect of N and NP on Fesc.

Overall the ecosystem responded in the first year to the fertilization, mainly in a functional way (higher LUE_f), whereas in the second year of fertilization we observe structurally mediated increase in GPP and F_{760} (through higher APAR and $Fesc_{fw}$) (Fig. 2.3d, Fig. 2.2l). The structurally mediated changes in 2015, driven by a decrease in abundance of erectophiles plants as the graminoids in the N containing treatments, cause a change in slope in the GPP-F_{760} relationship for the N and NP treatment (Fig. 2.4c) which is almost significantly different from the C for F_{760}, but significantly different from the C for $F_{760leaf,fw}$ in the NP treatment (Fig. 2.4d).

The N treatment has proven to affect plant functioning and canopy structure (APAR and $Fesc_{fw}$), while P has only a marginal role on the LUE_f. For this reason in the next paragraphs more attention will be paid to the role of N%, together with meteorology and canopy structure, as driver of in LUE_p, LUE_f and $Fesc_{fw}$, as well as GPP and F_{760}.

Predictors of the terms of the light use efficiency equation

Understanding the causes of variability of the parameters of LUE equations (LUE_p, LUE_f, and $Fesc_{fw}$ is fundamental to exploit remote sensing information such as F_{760} for modeling spatio-temporal patterns of GPP (Damm *et al.*, 2015). We show that Ts is the main predictor of LUE_p, and together with %graminoids is one of the two main predictors of LUE_f. Ts is a good indicator of water stress and strongly related to phenology and green fraction of vegetation (Jackson *et al.*, 1981; Boulet *et al.*, 2007), which ultimately relates to temporal variability of LUE_p. However, the fact that variables normalized by APAR such as LUE_p and LUE_f are driven by Ts indicates that it is not only a seasonal effect but rather physiological. In fact, Ts contains also information related to the activation of the xanthophyll cycle responsible for NPQ processes (Supplementary Fig. S2.17) that ultimately is related to LUE_p and LUE_f (Porcar-Castell *et al.*, 2014). Finally, many variables that have the potential to influence LUE_p, such as photorespiration and chlororespiration, are influenced by leaf temperature (Diaz *et al.*, 2007), potentially explaining why Ts is being selected. Our results reinforce the idea that Ts should be used as additional input of LUE models aimed at the prediction of GPP (Sims *et al.*, 2008).

The %graminoids is by far the best predictor of $Fesc_{fw}$, independently by the method used for the calculation of Fesc. Graminoids are mainly erectophiles (Wohlfahrt *et al.*, 2001), because of this particular LAD, most of the fluorescence is emitted laterally and therefore scattered by the vegetation (Migliavacca *et al.*, 2017). In this work we tested different formulations of $Fesc_{fw}$ with consistent results, in particular between the model-based ($Fesc_{fw}$) and the data-driven ($Fesc_{emp}$) estimates. The fact that %graminoids is a good proxy for the effect of structure on F_{760} and Fesc also opens interesting perspective to use F_{760} and also Fesc to assess taxonomic diversity, when diversity is somehow represented by changes in canopy architecture (Weisser *et al.*, 2017).

N% is an additional predictor selected for LUE_f and LUE_p, though the additional explained variance seems marginal (Fig. 2.5). N% is positively related to Vcmax (Feng & Dietze, 2013; Houborg *et al.*, 2013), and under light saturated conditions a higher Vcmax leads to an increase of LUE_p and, to less extent to increase of LUE_f (Frankenberg & Berry, 2018). As hypothesized, from this analysis it appears that the effect of N% on F_{760} and LUE equation terms is not direct and in the section 'Mechanisms behind the treatment effect on GPP and F_{760} at leaf and canopy scale' we discuss the relationships between N%, canopy structure, and the observed variables.

Mechanisms behind the treatment effect on GPP and F_{760} at leaf and canopy scale

The effect of canopy structure on F_{760} manifests itself mainly through variation in APAR and $Fesc_{fw}$ (Fig. 2.6 and Fig. 2.2i, respectively). With the path analysis we conclude that %graminoids positively influences APAR that leads to an increase of $F_{760leaf,fw}$ indirectly. Moreover, %graminoids negatively influences $Fesc_{fw}$. The changes of canopy structure mediated by changes in plant community at plot level are the most important factors controlling the pathway between $F_{760leaf,fw}$ and F_{760}, and ultimately GPP-F_{760}.

By analyzing the relationships between different components measured in the manipulative experiment presented here, we were able to disentangle the pathways, mostly unknown (Ač *et al.*, 2015; Damm *et al.*, 2015), through which N% influences the different components of the LUE equations. Our results show that the largest effect of N% on fluorescence emission is not direct, but rather mediated by APAR and Ts (Fig. 2.6), which in turn affect $F_{760leaf,fw}$.

There are two indirect ways in which N% affects $F_{760leaf,fw}$:

i) higher N% in the green fraction of the vegetation is associated to an increase of photosynthetic pigments and in particular Cab in leaves (Feng & Dietze, 2013) and in the canopy (Niinemets *et al.*, 1999), that ultimately has a positive effect on APAR (Peng *et al.*, 2011; Cendrero-Mateo *et al.*, 2015). Increase in APAR causes higher fluorescence emission at leaf and canopy level (Fig. 2.6) (Buschmann, 2007). There are contrasting results in the literature regarding the effect of N% on fluorescence and all the studies conducted at the leaf level (Verhoeven *et al.*, 1997; Ač *et al.*, 2015; Cendrero-Mateo *et al.*, 2015). Our study at canopy level supports the findings from (Cendrero-Mateo *et al.*, 2015), that at varying levels of N availability APAR modulates $F_{760leaf,fw}$ and F_{760}, and its relationship with GPP.

ii) N% influences positively $F_{760leaf,fw}$ through Ts. N% has a negative effect on Ts and $F_{760leaf,fw}$ exhibits a negative relationship with Ts. The first hypothesized mechanism is related with the observed increased in $Albedo_{400-900}$ (Fig. 2.3e,f) associated with the higher N%. The effect of N% on albedo, despite being quite debated in the literature (Ollinger *et al.*, 2008; Knyazikhin *et al.*, 2013), it has been demonstrated both at canopy scale (El-Madany; Ollinger *et al.*, 2009) and at leaf level (Sullivan *et al.*, 2012) and has to do with the increase in near infra-red (NIR) reflectance that is larger than the decrease of the reflectance in the visible region due to higher Cab and light absorption. Therefore, the increase of $Albedo_{400-900}$ with increasing N% results in less available energy in the canopy, that eventually leads to a decrease of Ts if other conditions such as soil moisture and VPD are similar (Ollinger *et al.*, 2008; Sullivan *et al.*, 2012). The second has to do with the modulation of transpiration due to the fertilization (Fig. 2.3g,h), which cools down the canopy, as the leaf surfaces lose heat when water evaporates through the stomata. Our estimate of LE_{ISO} show an increase in N and NP treatments during the peak of the growing season, but it is not significant (Supplementary Fig. S2.3a,b) and lower than the changes in in $Albedo_{400-900}$ for N, NP and P, in particular in 2015 (Fig. 2.3c,d). Given the strong response of GPP in the N and NP treatments in 2015 (Fig. 2.2b), the mild change in LE_{ISO} (Supplementary Fig. S2.3a,b) suggests an increase of water use efficiency, which is backed by $\delta^{13}C$ measurements, which show a significant increase in the N and NP treatment of campaign 6 (Supplementary Fig. S2.2) (where less negative values correspond to higher WUE (Sun *et al.*, 1996)). Therefore, we can conclude that although transpiration might be involved in the regulation of Ts at the peak of the season, biophysical variables such as $Albedo_{400-900}$ are much more affected by N% and contribute to reduce Ts.

Given that a large amount of N is invested in Rubisco protein (Evans, 1989), N can impact directly the carboxylation rates. The direct link between carboxylation rates and $F_{760leaf}$ is not yet clear (Vilfan *et al.*, 2019). However, we found a direct, though weak, relationship between N% and $F_{760leaf,fw}$ (Fig. 2.6) that is mediated likely by the ceiling effect mechanism described in the literature in an elevated CO_2 manipulation experiment (van der Tol *et al.*, 2014; Frankenberg & Berry, 2018), but not yet observed in nutrient manipulation experiments.

2.5 Conclusions

This study analyzed and explained the underlying mechanism responsible for the changes in gross primary productivity (GPP) and sun-induced fluorescence at 760 nm (F_{760}), and their relationship, due to a nutrient fertilization with Nitrogen (N), Phosphorous (P), and the combination of the two nutrients (NP). The Nitrogen additions (N and NP) had an effect mainly through changes in absorbed photosynthetically active radiation (APAR) and escape probability of fluorescence ($Fesc_{fw}$). Changes in APAR are directly related to changes in GPP and F_{760} and are due to the combination of changes in canopy chlorophyll content and in species composition that modifies the canopy structure. Changes in $Fesc_{fw}$ are mainly due to the changes in the abundance of erectophile vs non-erectophile vegetation with N addition. In the treatment with the addition in fact forbs increased (non-erectophile) while graminoids decreased (erectophile), which ultimately leads to changes in leaf angle distribution and modify the F_{760} observed in particular in 2015. This has an effect on GPP-F_{760} relationship both across treatments but also from year to year. Phosphorous addition had a significant effect on the light use efficiency of fluorescence, in particular when combined with high Nitrogen availability. This result points toward the need of better understanding the so far neglected role of phosphorous on modulating sun-induced fluorescence.

With a path analysis we also reveal that N%, not only affects F_{760} indirectly through APAR and $Fesc_{fw}$, but that is also tightly related with surface temperature (Ts). The negative relationship between N% and Ts is biophysically mediated by higher albedo observed after the fertilization, and only marginally physiological mediated by increase in transpiration. We also found a trade-off between F_{760} and Ts (likely mediated by the non-photochemical quenching mechanisms), indicating the importance of measuring simultaneously these two quantities. We finally found that Ts is also the main predictor of the light use efficiency of photosynthesis, which is a fundamental parameter to describe for the improvement of the predictability of GPP. In conclusion our results show that both nutrient availability, and their indirect effect on biodiversity, are fundamental drivers of sun-induced fluorescence, and it relationship with gross primary productivity. Our results also reveal the interlink between fluorescence, surface temperature and GPP, and support the importance of tandem missions such as the FLuorescence EXplorer (FLEX) and Sentinel-3, providing concomitant estimates of sun-induced fluorescence, vegetation related spectral indices, and land surface temperature.

Author Contributions: D.M and M.M designed the study and carried out the majority of the data-analysis. M.M and M.Reichstein designed the experiment. J.P.-L., O.P.-P., M.M., G.M, A.C., M.Rossini and J.G. collected and processed the data and R.G.C. and G.M. contributed with laboratory analysis. O.P.P contribute carried out the analysis of flux data. J.P.-L contributed with SCOPE inversion runs. T.J., M.Rossini contributed with the field calibration of the spectrometers and fluorescence retrieval. C.V.d.T contributed to discussion about SCOPE and the role of transpiration. T.E.M. contributed with the discussion about the role of albedo. R.C. helped to structure the manuscript and provided discussion about the statistical methods used. M. Rossini, M. Reichstein, U.R., G.M., M.P.M., P.Y., A.C., D.M and M.M. contributed to the discussion about the role of nutrients in influencing sun-induced fluorescence. All the authors contributed to the discussion of the results and to the writing of the manuscript.

Funding: The project has received funding from the European Union's Horizon 2020 research and innovation programme under the Marie Sklodowska-Curie grant agreement No 721995. The authors acknowledge the Alexander von Humboldt Foundation for supporting this research with the Max-Planck Prize to Markus Reichstein, and the EUFAR TA project DEHESHyrE (EU FP7 Program), the EnMAP project "MoReDEHESHyReS" (Contract No. 50EE1621, German Aerospace Center (DLR) and German Federal Ministry of Economic Affairs and Energy), SynerTGE (CGL2015-69095-R, Spanish Ministry of Science, Innovation and Universities) and FLUχPEC (CGL2012-34383, Spanish Ministry of Economy and Competitiveness). This work was supported by a research grant (18968) from VILLUM FONDEN.

Acknowledgments: We acknowledge the Majadas de Tiétar city council for its support. We thank Anatoly Gitelson, Tiana Hammer, Kathrin Henkel and Thomas Wutzler for the support

Conflicts of Interest: No conflict of interests

Supporting information

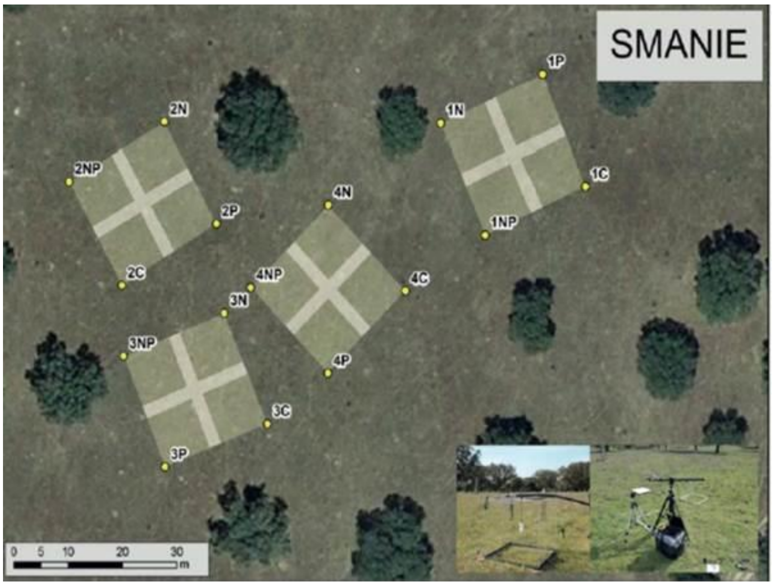

Supplementary Fig. S2.1. Aerial photograph of the experimental site (SMANIE) modified from Migliavacca et al., 2017. The position of the four blocks is indicated in transparent green and the treatment type is indicated at the corners of the blocks. The bands within each block indicate the buffer of 2 m used to separate the different treatments. In the lower right corner the transparent chambers used to measure the CO_2 and water fluxes are shown in the left figure and the manual system used to collect the spectral measurements is shown in the right figure.

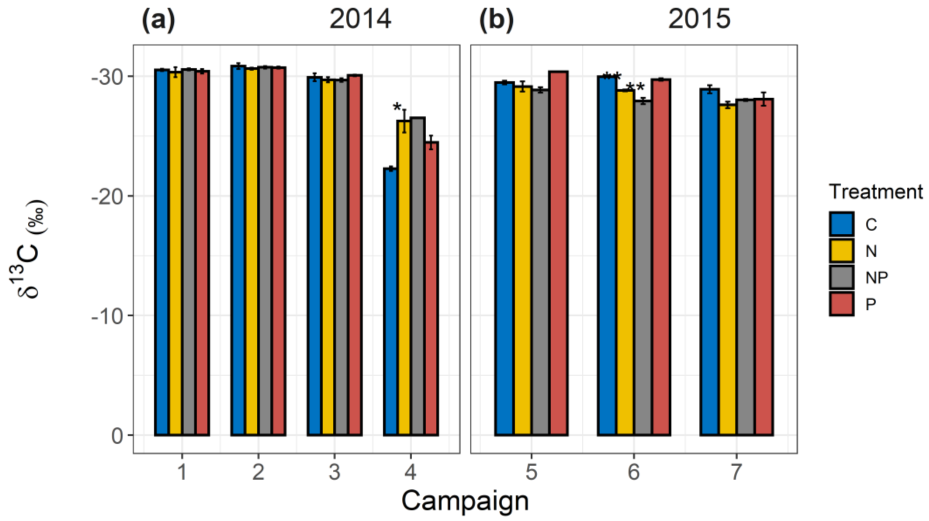

Supplementary Fig. S2.2. Group differences among treatment of carbon isotopic signature ($\delta^{13}C$) in 2014 (a) and 2015 (b). Group differences in (a), (b) were analyzed with ANOVA and Tukey post-hoc test. "*" refers to a significant difference from the control (C) treatment with p value < 0.05 and "**" refers to a significant difference from the C treatment with p value < 0.01.

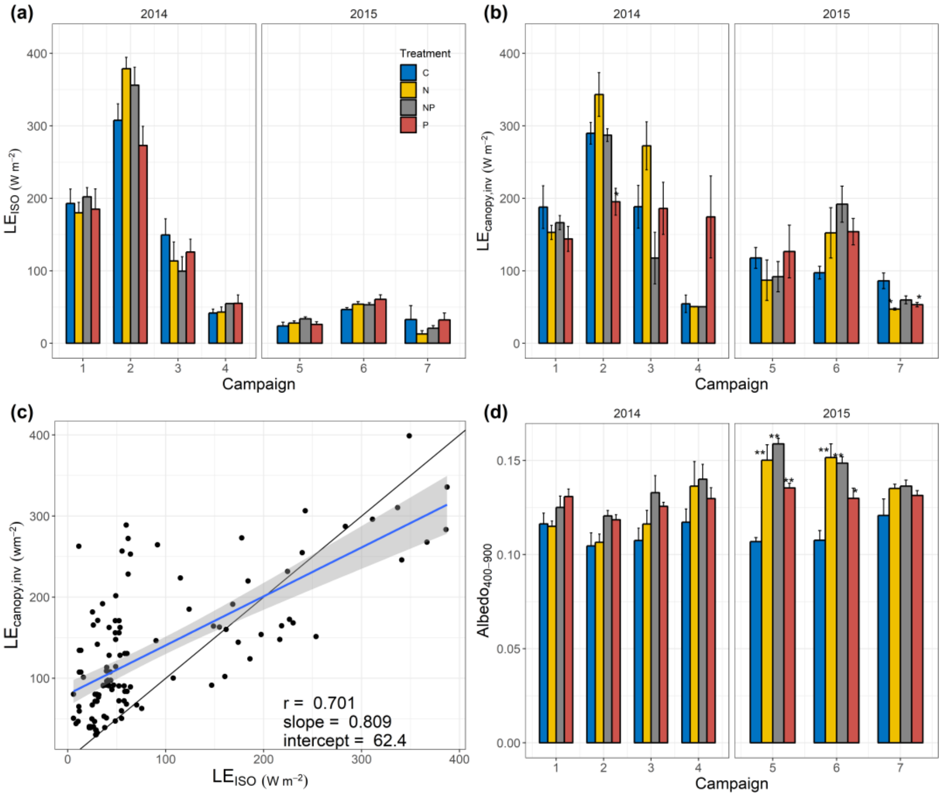

Supplementary Fig. S2.3. Group differences among treatment of transpiration (LE_{ISO}) (a) latent heat flux of the canopy estimated through SCOPE inversion ($Le_{canopy,inv}$) (b) integrated albedo between 400-900 nm($Albedo_{400-900}$) (d) and relation among the two transpiration estimates (c) (note that the LE_{ISO} has been converted to W/m^2). Group differences in (a), (b) and (d) were analyzed with ANOVA and Tukey post-hoc test. "*" refers to a significant difference from the control (C) treatment with p value < 0.05 and "**" refers to a significant difference from the C treatment with p value < 0.01. Dashed lines represent the 1:1 line. Blue lines represent the regression from the total least square regression.

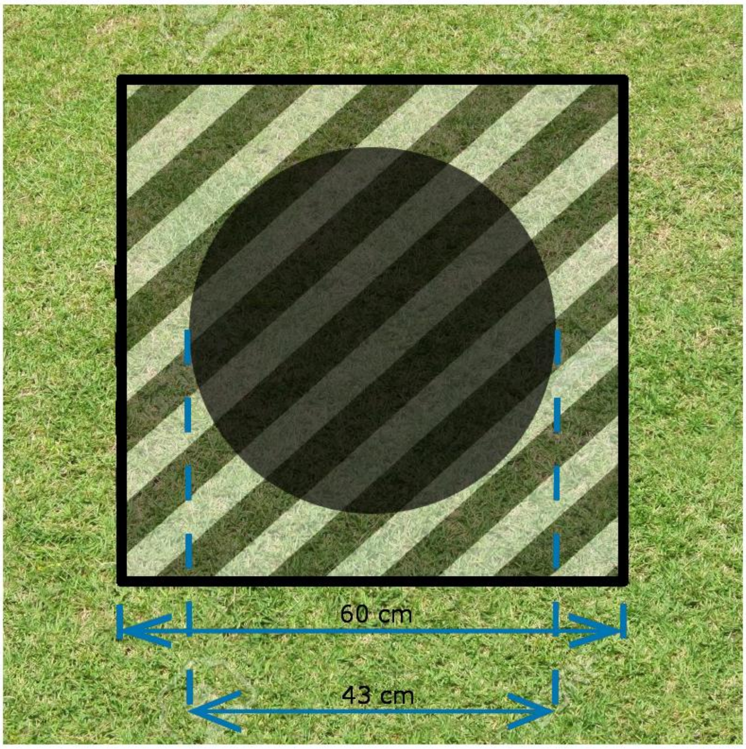

Supplementary Fig. S2.4. Schematic of the radiometric footprint (black circle) and the gas exchange footprint (black diagonal stripes) with the experimental set-up. When performing radiometric measurements, a frame painted with black mat color was put on the edges of the collar to prevent reflections from the metallic collar.

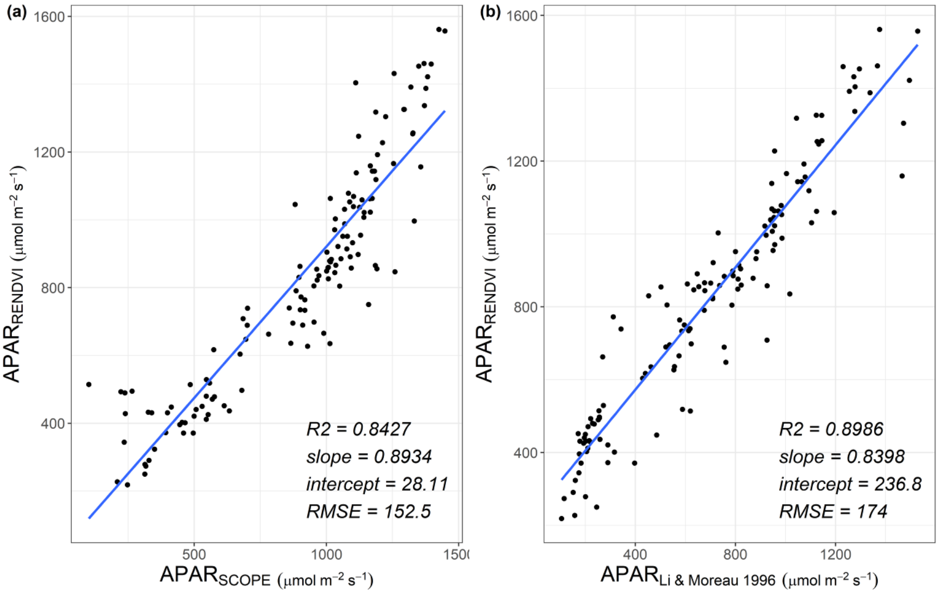

Supplementary Fig. S2.5. Scatterplot of modeled (from forward runs of SCOPE) vs absorbed photosynthetic active radiation (APAR) calculate from the RENDVI index (a), and APAR calculated with method of Li & Moreau 1996 vs $\text{APAR}_{\text{RENDVI}}$. Coefficient of determination (R^2), slope and intercept and Root Mean Square Error (RMSE) of the ordinary least square regression are reported in the bottom right. Blue lines represent the regression from the ordinary least square regression.

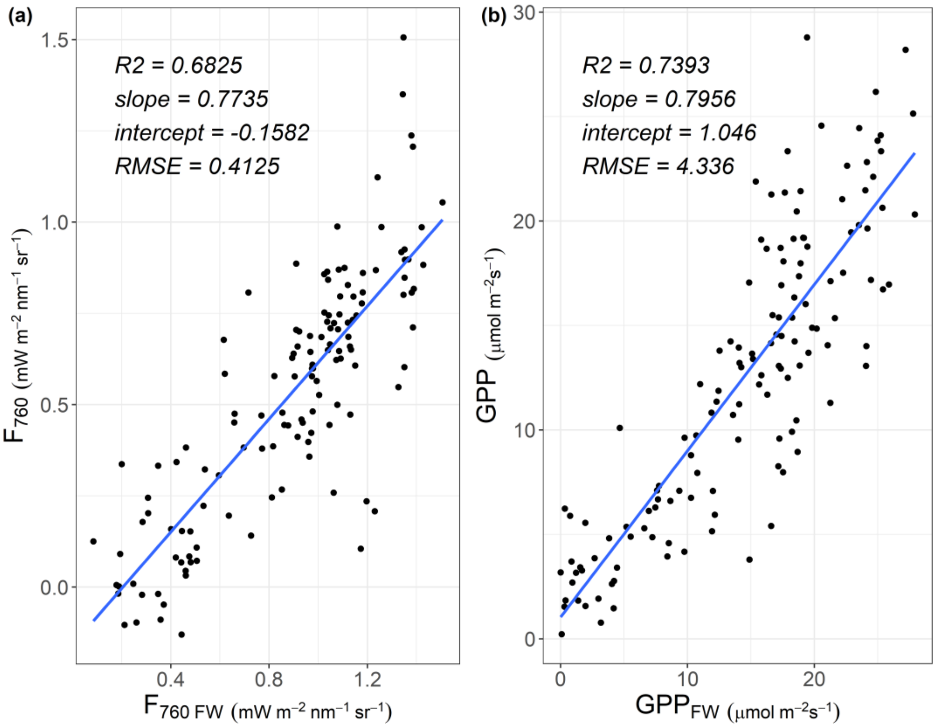

Supplementary Fig. S2.6. Scatterplot of modeled (forward SCOPE runs) vs observed fluorescence at 760 nm (F_{760}) (a) and scatterplot of modelled (from forward SCOPE runs) vs observed gross primary production (GPP) (b). Coefficient of determination (R^2), slope and intercept and Root Mean Square Error (RMSE) of the ordinary least square regression are reported in the top left. Blue lines represent the regression from the ordinary least square regression.

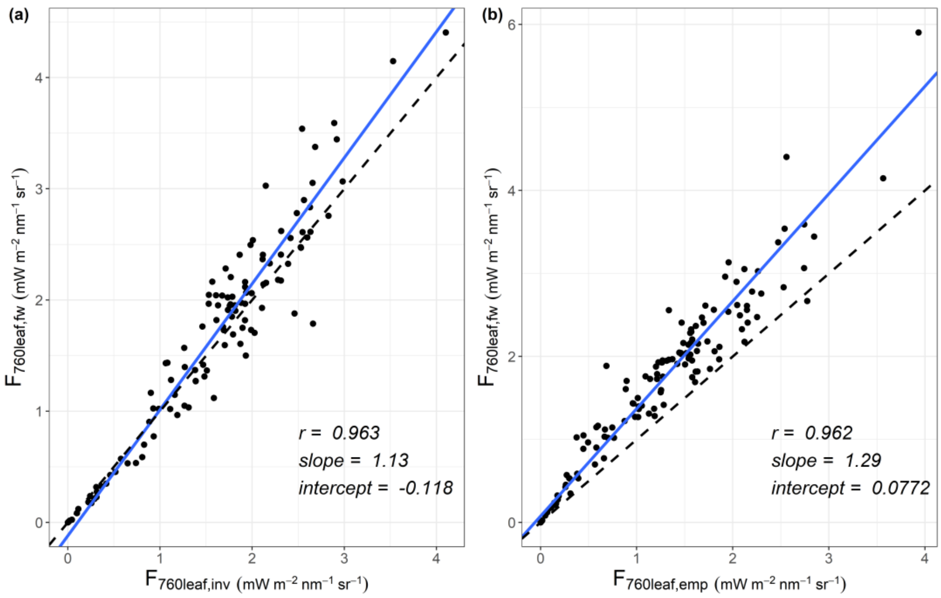

Supplementary Fig. S2.7. Scatterplot of the relationship between Fluorescence emitted by all leaves at 760 nm calculated by forward runs of SCOPE ($F_{760leaf,fw}$) and Fluorescence emitted by all leaves at 760 calculated with the empirical approach ($F_{760leaf,emp}$ (a) and relationship between $F_{760leaf,fw}$ and fluorescence emitted by all leaves at 760 nm calculated from SCOPE inversion ($F_{760leaf,inv}$) (b). Pearson correlation (r), slope and intercept form the Total Least Square regression is provided in the bottom right. Dashed lines represent the 1:1 line. Blue lines represent the regression from the total least square regression.

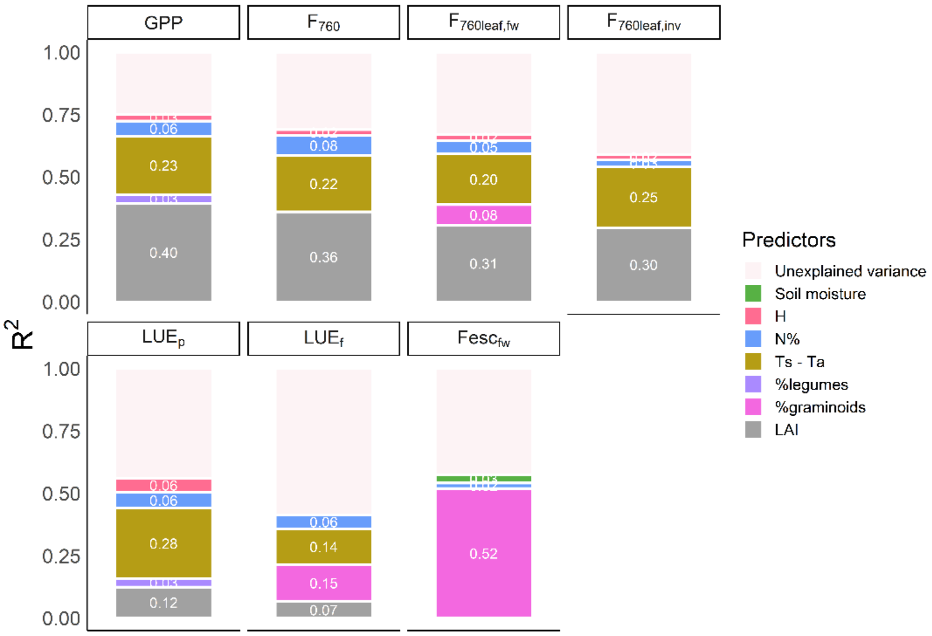

Supplementary Fig. S2.8. Relative importance analysis with LMG (Lindeman, Merenda and Gold) method of gross primary production (GPP), observed fluorescence at 760 nm (F760), Fluorescence emitted at 760 nm calculated by forward runs of SCOPE (F760leaf,fw), Light use efficiency of photosynthesis (LUE_p), light use efficiency of fluorescence emission at 760 nm (LUE_f) ,escape probability of F_{760} calculated from forward runs of SCOPE ($Fesc_{fw}$). Predictors included in the analysis are: soil moisture, Shannon biodiversity index (H), canopy nitrogen content (N%), surface-air temperature (Ts - Ta), relative abundance of legumes (%legumes), relative abundance of graminoids (%graminoids) and leaf are index (LAI).

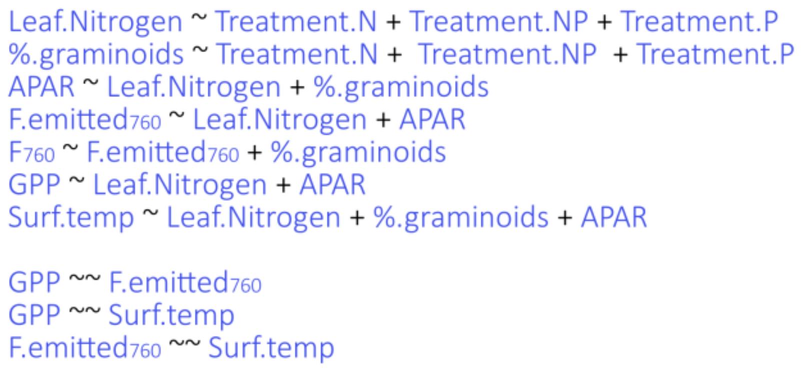

```
Leaf.Nitrogen ~ Treatment.N + Treatment.NP + Treatment.P
%.graminoids ~ Treatment.N +  Treatment.NP  + Treatment.P
APAR ~ Leaf.Nitrogen + %.graminoids
F.emitted760 ~ Leaf.Nitrogen + APAR
F760 ~ F.emitted760 + %.graminoids
GPP ~ Leaf.Nitrogen + APAR
Surf.temp ~ Leaf.Nitrogen + %.graminoids + APAR

GPP ~~ F.emitted760
GPP ~~ Surf.temp
F.emitted760 ~~ Surf.temp
```

Supplementary Fig. S2.9. Set of equations that represent the model structure for the path analysis written as R markdown. Variables are the left are dependent variables and variables to the right of "~"are predictors. "~"denotes direct relationships, whereas "~~" denote covariance.

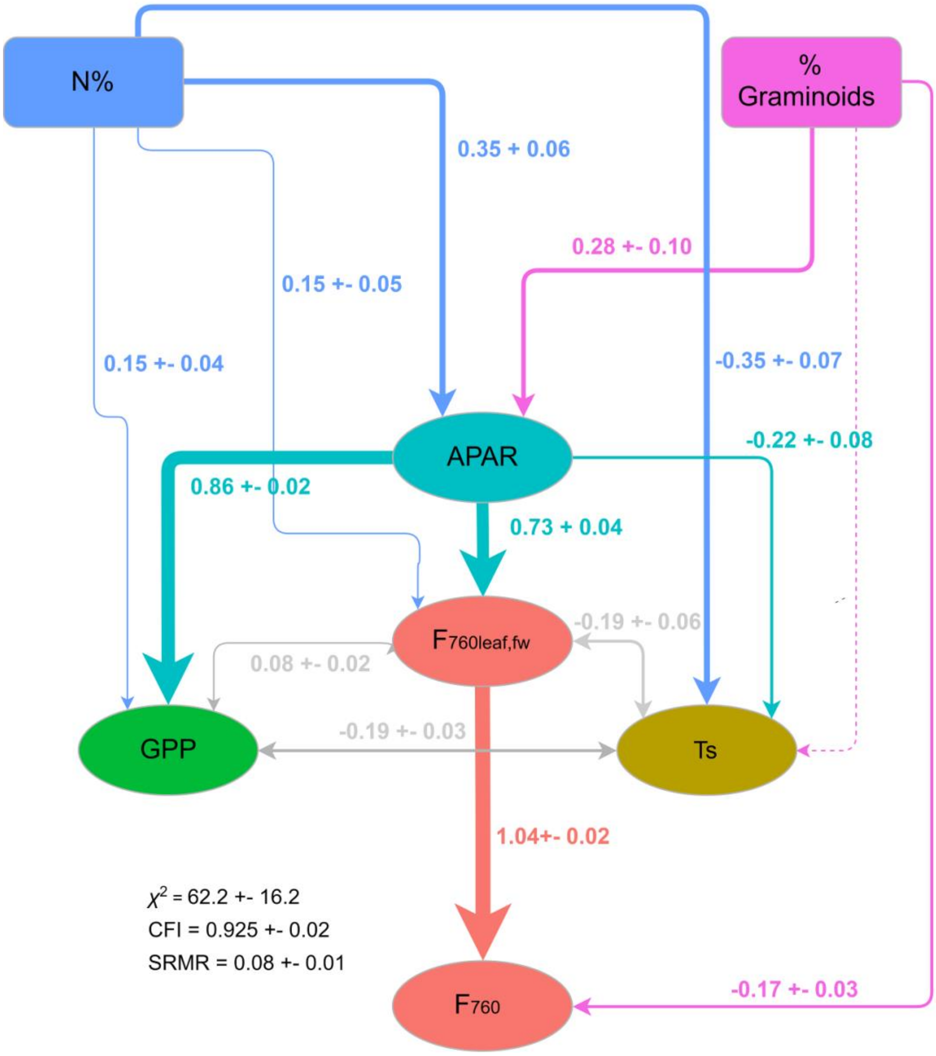

Supplementary Fig. S2.10. Path analysis without the Nitrogen (N) treatment. Path analysis displays the role of canopy nitrogen content (N%) and relative graminoids abundance (%graminoids) on the energy partitioning at the leaf and canopy level. Photosynthetic active radiation (PAR); Absorbed by vegetation photosynthetic active radiation (APAR), Fluorescence emission by all leaves at 760 nm calculated by forward runs of SCOPE ($F_{760leaf,fw}$); gross primary production (GPP), Surface temperature (Ts) and observed fluorescence at 760 nm (F_{760}). The strength of the relationship among variables is expressed by the standardized coefficient (β) of the path analysis. Each standardized coefficient has a standard error obtain from bootstrapping (n=100 times). The width of the arrows is proportional to their standardized coefficient (β). Colored lines (both solid or dotted) represent direct relationships between variables, whereas gray double-headed arrows represent the covariance among variables. Solid and dotted lines indicate significant ($p < 0.05$) and non-significant relationships, respectively. The width of the arrows is proportional to their standardized coefficient (β). The different colors are introduced to increase readability of the standardized path coefficients. The fit by the overall model is measured by means of Chi-squared ($\chi 2$), comparative fit index (CFI) and standardized root mean square of residual (SRMR).

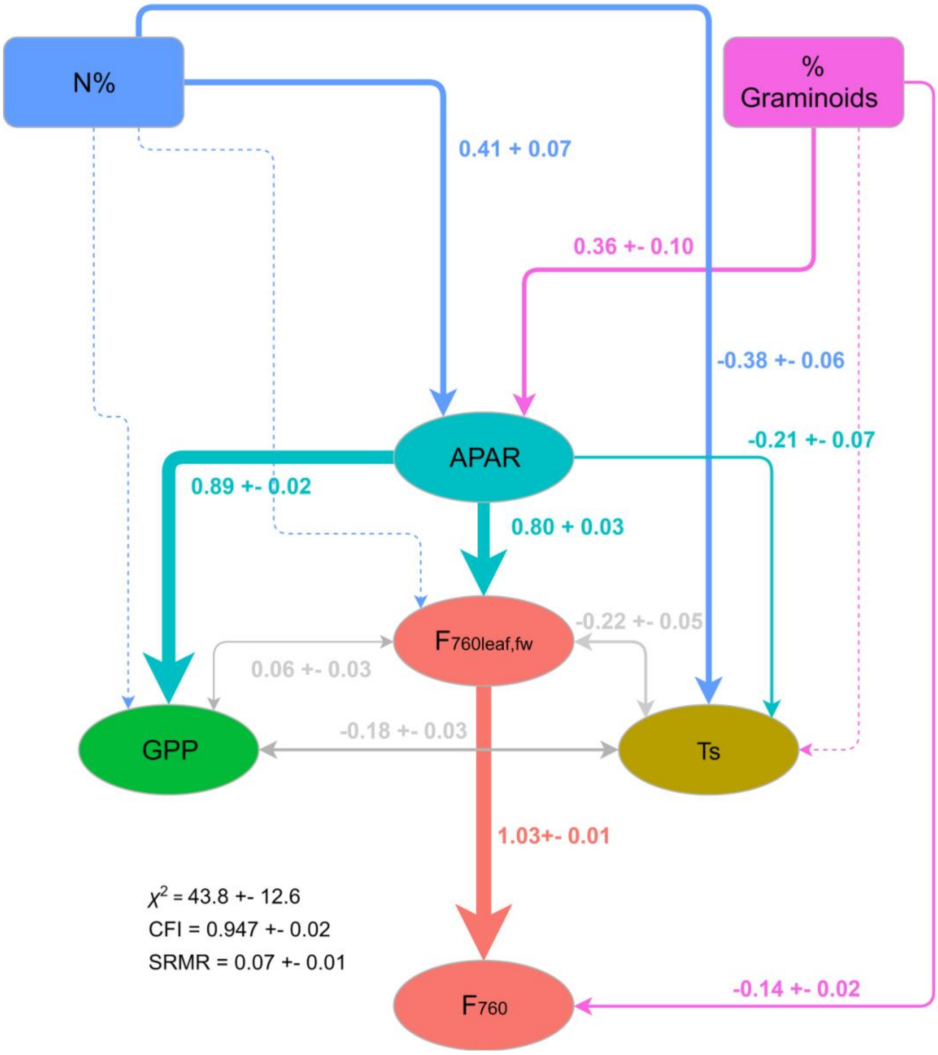

Supplementary Fig. S2.11. Path analysis without the Nitrogen and Phosphorus (NP) treatment. Path analysis displays the role of canopy nitrogen content (N%) and relative graminoids abundance (%graminoids) on the energy partitioning at the leaf and canopy level. Photosynthetic active radiation (PAR); Absorbed by vegetation photosynthetic active radiation (APAR), Fluorescence emission by all leaves at 760 nm calculated by forward runs of SCOPE ($F_{760leaf,fw}$); gross primary production (GPP), Surface temperature (Ts) and observed fluorescence at 760 nm (F_{760}). The strength of the relationship among variables is expressed by the standardized coefficient (β) of the path analysis. Each standardized coefficient has a standard error obtain from bootstrapping (n=100 times). The width of the arrows is proportional to their standardized coefficient (β). Colored lines (both solid or dotted) represent direct relationships between variables, whereas gray double-headed arrows represent the covariance among variables. Solid and dotted lines indicate significant ($p < 0.05$) and non-significant relationships, respectively. The width of the arrows is proportional to their standardized coefficient (β). The different colors are introduced to increase readability of the standardized path coefficients. The fit by the overall model is measured by means of Chi-squared ($\chi 2$), comparative fit index (CFI) and standardized root mean square of residual (SRMR).

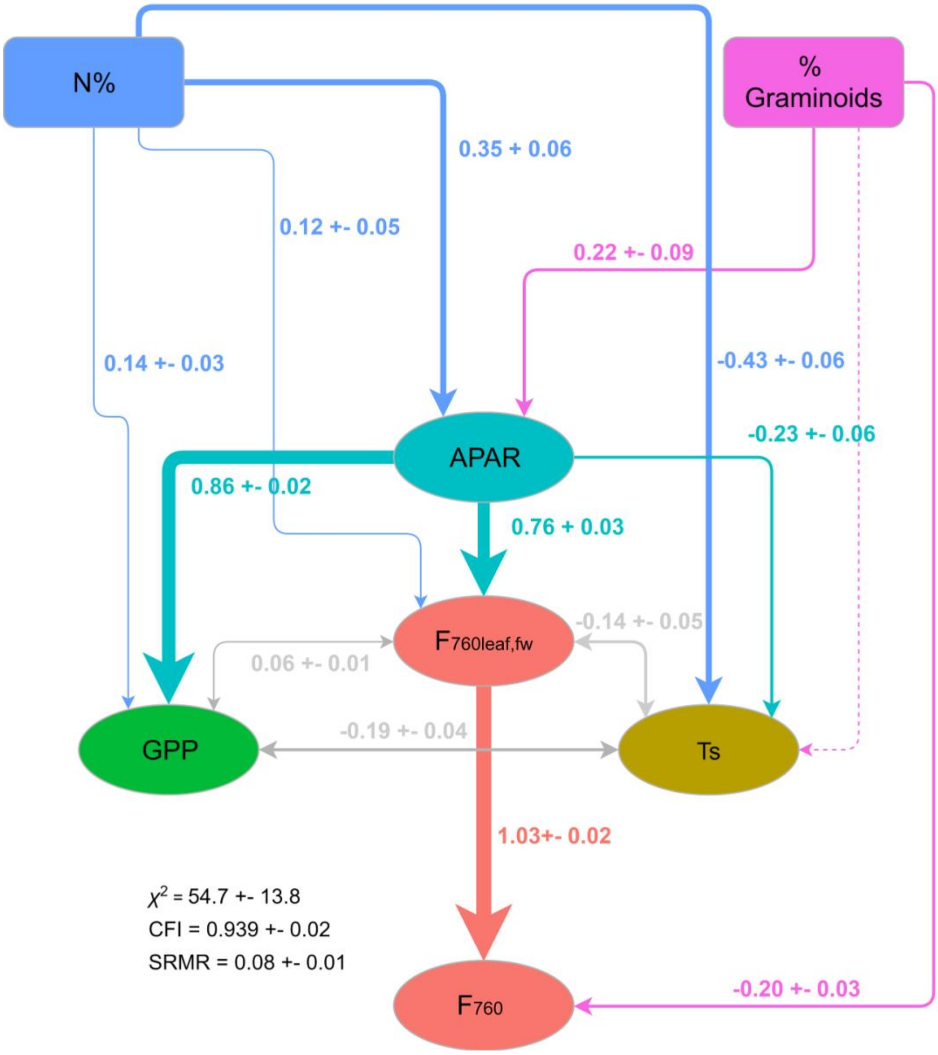

Supplementary Fig. S2.12. Path analysis without the Phosphorus (P) treatment. Path analysis displays the role of canopy nitrogen content (N%) and relative graminoids abundance (%graminoids) on the energy partitioning at the leaf and canopy level. Photosynthetic active radiation (PAR); Absorbed by vegetation photosynthetic active radiation (APAR), Fluorescence emission by all leaves at 760 nm calculated by forward runs of SCOPE ($F_{760leaf,fw}$); gross primary production (GPP), Surface temperature (Ts) and observed fluorescence at 760 nm (F_{760}). The strength of the relationship among variables is expressed by the standardized coefficient (β) of the path analysis. Each standardized coefficient has a standard error obtain from bootstrapping (n=100 times). The width of the arrows is proportional to their standardized coefficient (β). Colored lines (both solid or dotted) represent direct relationships between variables, whereas gray double-headed arrows represent the covariance among variables. Solid and dotted lines indicate significant ($p < 0.05$) and non-significant relationships, respectively. The width of the arrows is proportional to their standardized coefficient (β). The different colors are introduced to increase readability of the standardized path coefficients. The fit by the overall model is measured by means of Chi-squared ($\chi 2$), comparative fit index (CFI) and standardized root mean square of residual (SRMR).

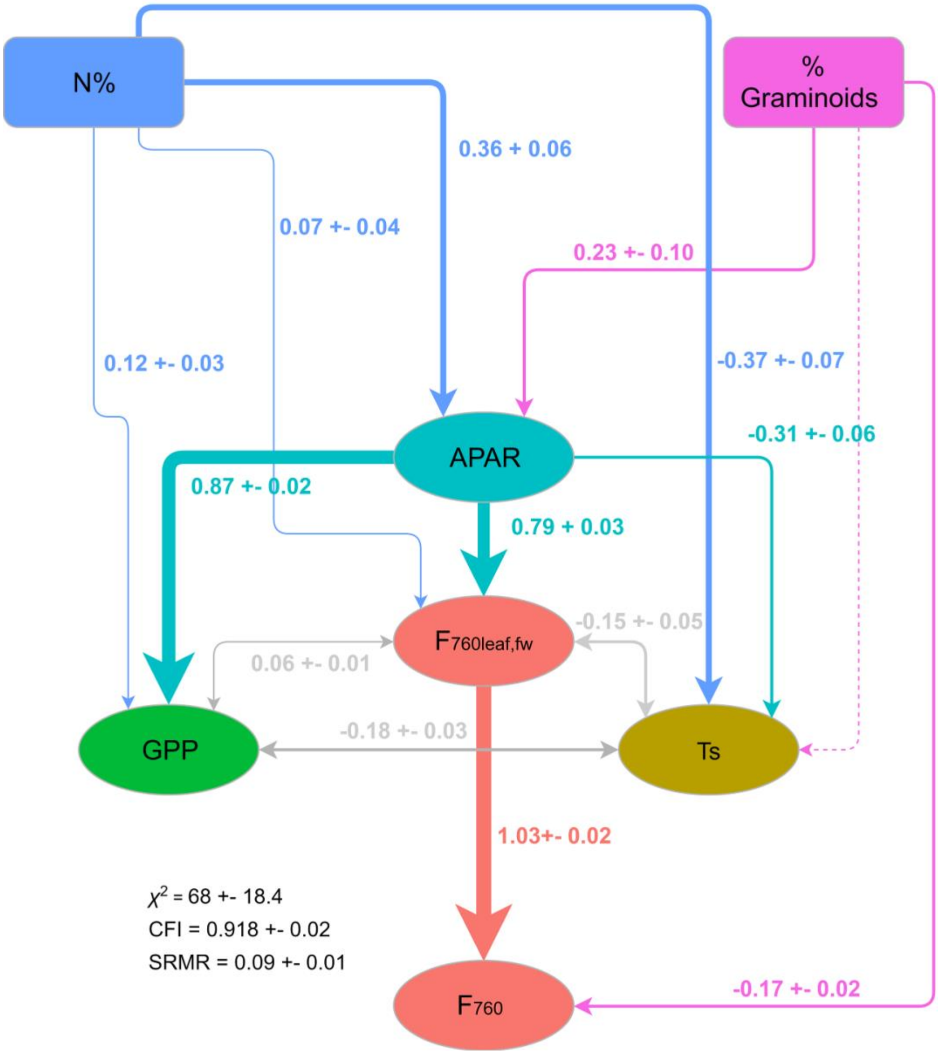

Supplementary Fig. S2.13. Path analysis without the Control treatment(C). Path analysis displays the role of canopy nitrogen content (N%) and relative graminoids abundance (%graminoids) on the energy partitioning at the leaf and canopy level. Photosynthetic active radiation (PAR); Absorbed by vegetation photosynthetic active radiation (APAR), Fluorescence emission by all leaves at 760 nm calculated by forward runs of SCOPE ($F_{760leaf,fw}$); gross primary production (GPP), Surface temperature (Ts) and observed fluorescence at 760 nm (F_{760}). The strength of the relationship among variables is expressed by the standardized coefficient (β) of the path analysis. Each standardized coefficient has a standard error obtain from bootstrapping (n=100 times). The width of the arrows is proportional to their standardized coefficient (β). Colored lines (both solid or dotted) represent direct relationships between variables, whereas gray double-headed arrows represent the covariance among variables. Solid and dotted lines indicate significant ($p < 0.05$) and non-significant relationships, respectively. The width of the arrows is proportional to their standardized coefficient (β). The different colors are introduced to increase readability of the standardized path coefficients. The fit by the overall model is measured by means of Chi-squared ($\chi 2$), comparative fit index (CFI) and standardized root mean square of residual (SRMR).

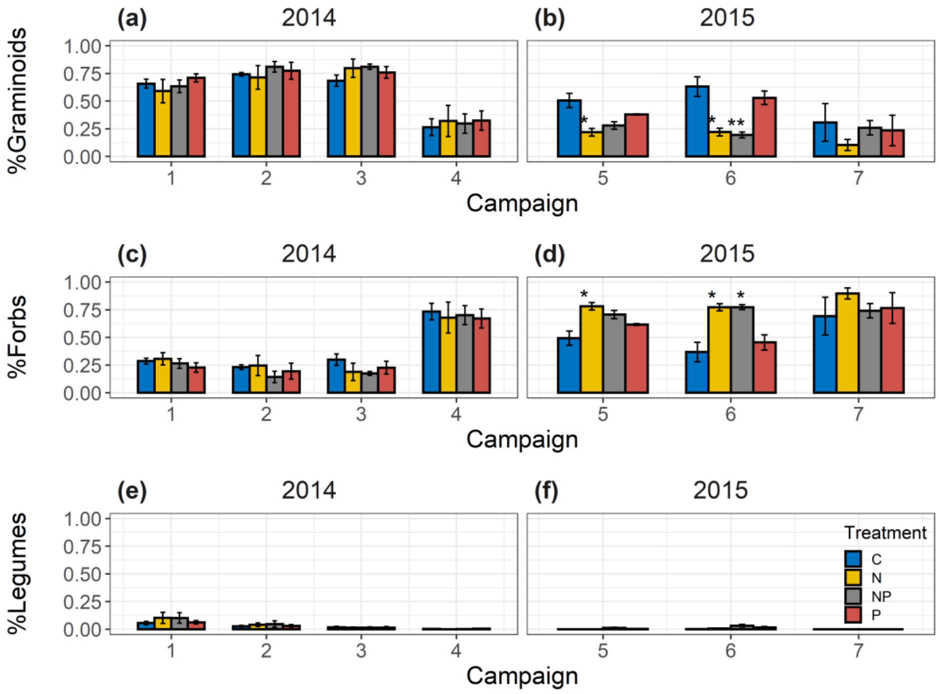

Supplementary Fig. S2.14. Bar graph representing differences among treatments of graminoids relative abundance (%graminoids) in 2014 (a) and 2015 (b), forbs relative abundance (%Forbs) in 2014 (c) and 2015 (d) and legumes relative abundance (%Legumes). Data are divided among campaigns. Bar graphs represent means and error bars represent 1 standard error. Group differences were analyzed with ANOVA with the Welch correction and individual differences among groups were evaluated with the Games-Howell post hoc test. "*" refers to a significant difference from the control (C) treatment with p value < 0.05 and "**" refers to a significant difference from the C treatment with p value < 0.01.

Supplementary Table S2.1. Evaluation of the relationship between Gross Primary Production (GPP) and Fluorescence at 760 nm (F_{760}) and between GPP and Fluorescence at emission level at 760 nm ($F_{760leaf,fw}$) among different treatments.

Year	Treatment	Variable	**Intercept** P value	**Interaction** P value	**Intercept** value	**Slope** value
2014	C	$F_{760leaf,fw}$	**0.03**		4.09	5.30
2014	C	F_{760}	**0.04**		4.48	17.11
2014	N	$F_{760leaf,fw}$	0.38	0.95	2.40	5.39
2014	N	F_{760}	0.39	0.8	2.44	18.42
2014	NP	$F_{760leaf,fw}$	0.92	0.89	0.23	5.11
2014	NP	F_{760}	0.77	0.69	-0.79	19.19
2014	P	$F_{760leaf,fw}$	0.07	0.86	3.14	5.04
2014	P	F_{760}	0.13	0.96	2.60	17.36
2015	C	$F_{760leaf,fw}$	**< 0.01**		4.68	4.57
2015	C	F_{760}	**< 0.01**		4.76	14.93
2015	N	$F_{760leaf,fw}$	0.57	**0.02**	0.89	8.46
2015	N	F_{760}	0.59	0.09	0.84	23.29
2015	NP	$F_{760leaf,fw}$	**0.03**	0.09	2.66	7.21
2015	NP	F_{760}	**0.02**	0.32	2.65	19.50
2015	P	$F_{760leaf,fw}$	0.06	0.57	3.94	5.51
2015	P	F_{760}	0.07	0.64	3.74	17.32

Gross Primary Production (GPP) is the dependent variable. Fluorescence emitted by all leaves at 760 nm calculated from forward SCOPE runs ($F_{760leaf,fw}$) and observed Fluorescence at 760 nm (F_{760}) are the independent variables. The column intercept reports the p values of the intercept from the multiple linear model and the column Interaction reports the p values of the interaction between Independent variable and Treatment factor in relation to the Control (C) treatment from the ANCOVA. Bold p values refer to p values < 0.05. The values of intercept and slope from the linear model GPP ~ F_{760} among treatments and the linear model GPP ~ $F_{760leaf,fw}$ among treatments are reported. N refers to Nitrogen addition treatment, P is the phosphorus addition treatment and NP is the nitrogen and phosphorus addition treatment.

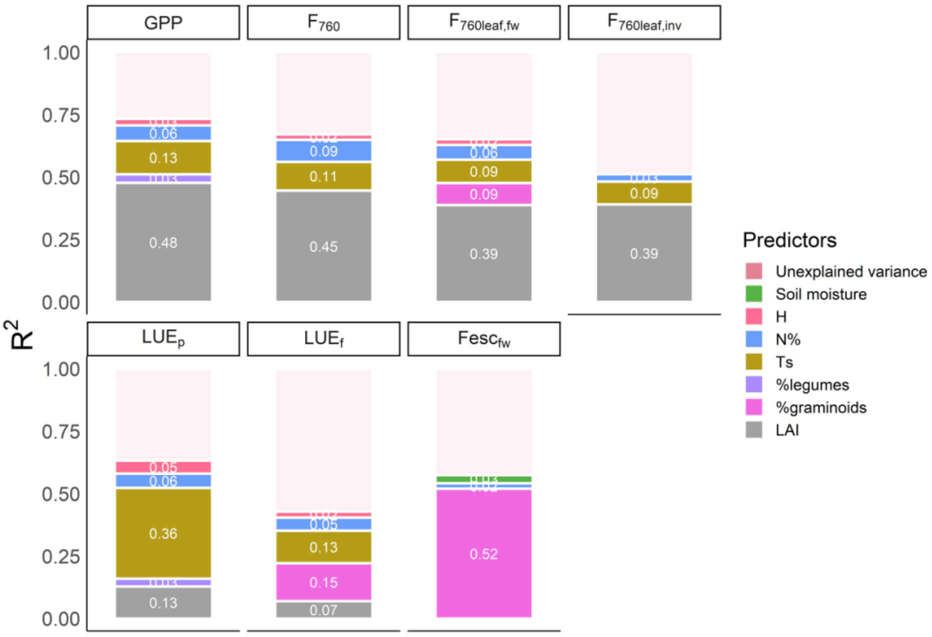

Supplementary Fig. S2.15. Relative importance analysis with LMG (Lindeman, Merenda and Gold) method of Gross Primary Production (GPP), observed fluorescence at 760 nm (F760), Fluorescence emitted at 760 nm calculated by forward runs of SCOPE (F760leaf,fw), Light use efficiency of photosynthesis (LUE_p), light use efficiency of fluorescence emission at 760 nm (LUE_f) ,escape probability of F_{760} calculated from forward runs of SCOPE ($Fesc_{fw}$). Predictors included in the analysis are: soil moisture, Shannon biodiversity index (H), canopy nitrogen content (N%), surface temperature (Ts), relative abundance of legumes (%legumes), relative abundance of graminoids (%graminoids) and leaf are index (LAI).

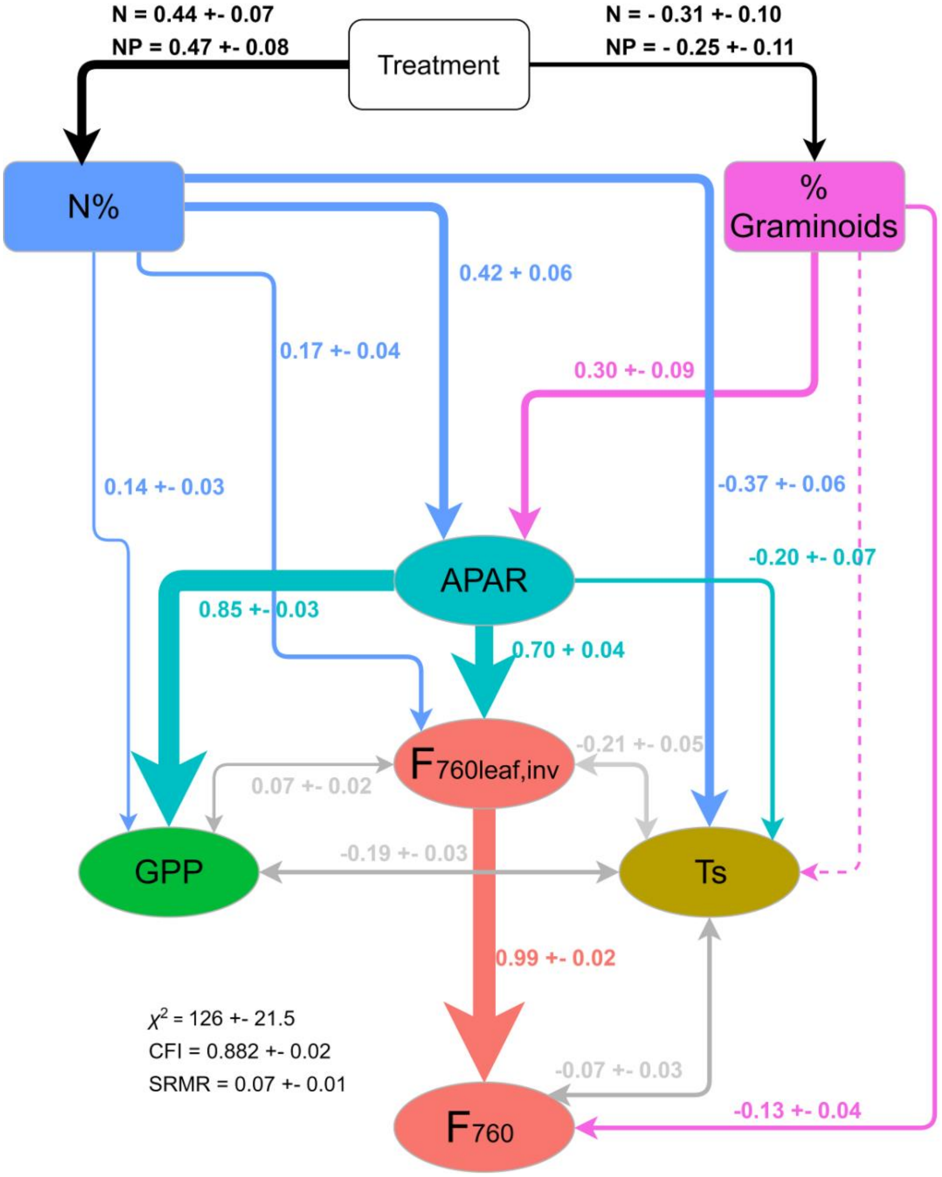

Supplementary Fig. S2.16. Path analysis with Fluorescence emission at 760 nm calculated from SCOPE inversion $F_{760leaf,inv}$. Path analysis displays the role of canopy nitrogen content (N%) and relative graminoids abundance (%graminoids) on the energy partitioning at the leaf and canopy level. Photosynthetic active radiation (PAR); Absorbed by vegetation photosynthetic active radiation (APAR), Fluorescence emission by all leaves at 760 nm calculated by forward runs of SCOPE ($F_{760leaf,fw}$); gross primary production (GPP), Surface temperature (Ts) and observed fluorescence at 760 nm (F_{760}).

The strength of the relationship among variables is expressed by the standardized coefficient (β) of the path analysis. Each standardized coefficient has a standard error obtain from bootstrapping (n=100 times). The width of the arrows is proportional to their standardized coefficient (β). Colored lines (both solid or dotted) represent direct relationships between variables, whereas gray double-headed arrows represent the covariance among variables. Solid and dotted lines indicate significant ($p < 0.05$) and non-significant relationships, respectively. The width of the arrows is proportional to their standardized coefficient (β). The different colors are introduced to increase readability of the standardized path coefficients. The fit by the overall model is measured by means of Chi-squared ($\chi 2$), comparative fit index (CFI) and standardized root mean square of residual (SRMR).

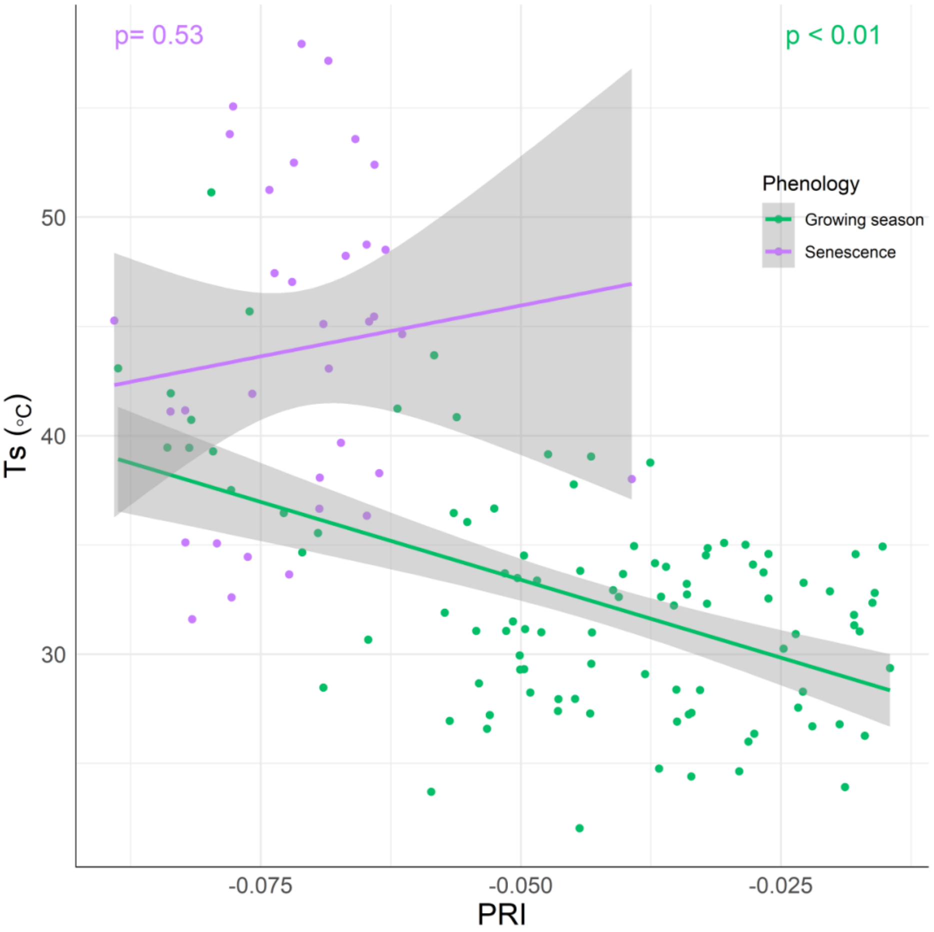

Supplementary Fig. S2.17. Scatterplot of Surface temperature (Ts) vs Photochemical Reflectance Index (PRI). "Growing season" includes the campaigns 1,2,3,5,6 The *p* values of the ordinary least square regressions are reported in the top. Colored lines represent the regression from the ordinary least square regression.

3 Heatwave breaks down the linearity between sun-induced fluorescence and gross primary production[2]

---

[2] This chapter is based on: Martini, D., Sakowska, K., Wohlfahrt, G., Pacheco-Labrador, J., van der Tol, C., Porcar-Castell, A., ... & Migliavacca, M. Heatwave breaks down the linearity between sun-induced fluorescence and gross primary production. *New Phytologist*.

Summary

- Sun-induced fluorescence in the far-red region (*SIF*) is increasingly used as a remote and proximal-sensing tool capable of tracking vegetation gross primary production (*GPP*). However, the use of *SIF* to probe changes in *GPP* is challenged during extreme climatic events, such as heatwaves.

- Here, we examined how the 2018 European heatwave (HW) affected the *GPP*-*SIF* relationship in evergreen broadleaved trees with a relatively invariant canopy structure. To do so, we combined canopy scale *SIF* measurements, *GPP* estimated from an eddy covariance tower, and active PAM fluorescence.

- The HW caused an inversion of the photosynthesis-fluorescence relationship at both the canopy and leaf scales. The highly nonlinear relationship was strongly shaped by nonphotochemical quenching (*NPQ*), i.e., a dissipation mechanism to protect from the adverse effects of high light intensity. During the extreme heat stress, plants experienced a saturation of *NPQ,* causing a change in the allocation of energy dissipation pathways towards *SIF*.

- Our results show the complex modulation of the *NPQ*-*SIF*-*GPP* relationship at an extreme level of heat stress, which is not represented in state-of-the-art coupled radiative transfer and photosynthesis models.

3.2 Introduction

Gross primary production (*GPP*) of terrestrial ecosystems represents the most important flux in the global carbon cycle (Beer *et al.*, 2010), which provides ecosystem services of critical importance for society (Holmberg *et al.*, 2019). Anthropogenic climate change has increased global temperature and the frequency and intensity of climate extremes such as heatwaves and droughts (Bindoff *et al.*, 2014), which have a considerable effect on *GPP* (Reichstein *et al.*, 2013). *GPP* can be estimated by means of proximal and remote sensing (RS), particularly through the use of sun-induced fluorescence in the far-red region (*SIF*) (Damm *et al.*, 2010; Pacheco-Labrador *et al.*, 2019a). Top-of-the-canopy *SIF* measurements contain information on the radiation emitted by plants' chlorophyll when exposed to solar radiation, mediated by canopy architecture through reabsorption and multiple scattering (escape probability of fluorescence, *Fesc*) (Yang & van der Tol, 2018). *SIF* is used to predict *GPP* as it is related to both the amount of absorbed photosynthetic active radiation (*APAR*) and the efficiency with which it is used to drive photosynthesis (light-use efficiency of photosynthesis, LUE_p) (Zhang *et al.*, 2014). Therefore, *SIF* has the potential to quantify the effect of extreme events such as heatwaves on photosynthetic activity (Ač *et al.*, 2015). Nevertheless, it is necessary to explore the mechanistic relationship between *SIF* and *GPP* during rapid extreme heat stress (Wohlfahrt *et al.*, 2018; Magney *et al.*, 2019).

Both the light-dependent reactions of photosynthesis and *SIF* originate at the photosystem level. When a chlorophyll molecule is excited by a photon of light, the available energy can be allocated to photochemistry, emitted as fluorescence (the *SIF* signal), or dissipated as heat through nonphotochemical quenching (*NPQ*) (Kitajima & Butler, 1975), a process involving xanthophyll cycle de-epoxidation. Because photochemistry and *NPQ* are physiologically modulated (Porcar-Castell *et al.*, 2014) and respond to different environmental conditions, it is complicated to find a universal linear relationship between photochemistry and *SIF*, without information about *NPQ*, especially under stress conditions.

Understanding of the trade-offs between these processes can be achieved by combining canopy-scale passive (i.e., *SIF)* with leaf-level active (pulse amplitude modulation, PAM) fluorescence techniques; the latter of which can be used to derive parameters such as yields of photochemistry (φ*P*) (Genty *et al.*, 1989) and fluorescence (φ*F*) (Atherton *et al.*, 2019), and *NPQ* (Cailly, 1996). Active fluorescence data at high temporal resolution (e.g., hourly) suggests that the relationship between φ*F* and φ*P* at the leaf level is highly nonlinear and strongly dependent on illumination conditions and *NPQ* (Porcar-

Castell *et al.*, 2014). Under typical high-radiation conditions, φ*P* decreases in response to *NPQ* increase, driving the positive *SIF*-photochemistry relationship ("*NPQ*-phase") (Porcar-Castell *et al.*, 2014). van der Tol *et al.* (2014) reported that at high light and stress conditions various crops showed a negative φ*F*-φ*P* relationship (the "*NPQ*-saturation phase"). However, to our knowledge there are no observations of the "*NPQ*-saturation phase" for plants experiencing heat stress and it is unclear how this mechanism emerges at the canopy scale. *NPQ* is crucial to understand and model the *GPP*-*SIF* relationship. However, *NPQ* is challenging to measure at the canopy scale from remote sensing platforms because canopy structure can be a confounding factor (Perez-Priego *et al.*, 2015). The integration of leaf and canopy-scale fluorescence has the potential to explain the scale-dependence of trade-offs between *NPQ*, photochemistry, and fluorescence (Magney *et al.*, 2017), and therefore can help to better understand the physiological information contained in *SIF*.

Extreme events such as heatwaves can represent natural experiments, where increases in *NPQ* (Georgieva & Yordanov, 1994) can alter *GPP*-*SIF* dynamics. Generally, deciduous trees, crops, and grasslands react to heatwaves through a combination of physiological (e.g., increase in *NPQ* and/or transpiration (Drake *et al.*, 2018)) and structural changes (reduction in leaf area index (*LAI*), chlorophyll degradation). Evergreen trees, particularly in the Mediterranean and semi-arid regions, can withstand extreme temperatures of short duration without showing significant pigment degradation or changes in canopy structure (Teskey *et al.*, 2015), primarily relying on physiological adaptation for coping with extreme temperatures (Garcia-Plazaola *et al.*, 2008). Evergreen broadleaved trees thus represent an excellent test case to study the effect of extreme heatwaves on the *GPP*-*SIF* relationship independently of the variations of chlorophyll content and *APAR*. Here, we make use of data from the 2018 European heatwave (HW) that resulted in record-breaking temperatures (Bastos *et al.*, 2020) in Western Europe (Barriopedro *et al.*, 2020). During the first week of August, the western side of the Iberian Peninsula experienced daily temperature anomalies compared to long-term observations up to 9°C, caused by a Saharan air intrusion, leading to the most extreme event ever recorded in the region (Sousa *et al.*, 2019; Barriopedro *et al.*, 2020).

This study aims to shed light on the relationship between *GPP* and *SIF* during an extreme HW when changes in canopy structure are minimal. Our goals are twofold: First, we wish to understand the effect of the HW on the *GPP*-*SIF* relationship. In particular, we want to investigate what role NPQ plays in shaping the *GPP*-*SIF* relationship at high heat-stress levels. Second, we investigate if a state-of-the-art radiative transfer and photosynthesis model can reproduce *NPQ*, which is critical to obtain *SIF*, at high heat stress. To do so, we used data from Mediterranean evergreen oak trees (*Quercus ilex*) at the study site Majadas de Tiétar (ES-LMa), where we measured canopy scale *SIF*, *GPP* estimated with the eddy covariance technique, and active PAM fluorescence.

3.3 Materials and Methods

Study site

The study was conducted in a Mediterranean open woodland, a typical "*Iberian Dehesa*" in western Spain (39°56´024.68´´ N, 5°45´50.27´´ W; Majadas de Tiétar, Cáceres, Extremadura, FLUXNET site ES-LMa) (Supplementary Fig. S3.1). The ecosystem is composed of an herbaceous layer and scattered evergreen broadleaved trees, mainly *Quercus ilex L. subsp. ballota* [Desf.] Samp. (Holm Oak). Trees fractional cover was ~20 %, while the average horizontal and vertical crown radius was 4.2 m (σ = 0.9 m) and 2.7 m (σ = 0.9 m), respectively (Pacheco-Labrador *et al.*, 2019b).

The climate is Mediterranean, characterized by a hot and dry summer. The annual precipitation value is about 650 mm (falling mostly from autumn to spring). The mean annual temperature is 16 °C. The study was conducted from June 2018 to August 2018, when the herbaceous layer was senesced (Luo *et al.*, 2018b; Luo *et al.*, 2020), and the trees were the only active vegetation (El-Madany *et al.*, 2020). From August 2 to August 6, 2018, the ecosystem experienced a heatwave (Barriopedro *et al.*, 2020) with a five-day average of daily maximum air temperature (T_{air}) of 43.2 °C and daily maximum vapor pressure deficit (*VPD*) of 76.1 hPa (Supplementary Fig. S3.2)**.** Extensive site details are available in earlier publications (El-Madany *et al.*, 2018). The days considered part of the heatwave are the five days from the 2nd August 2018 to 6th August 2018, according to Sousa *et al.* (2019). The days considered pre-heatwave are the days from the 25th July 2018 to 1st August 2018.

Sun-induced fluorescence observations

The spectral measurements were collected using the FloX (JB Hyperspectral Devices, Düsseldorf, Germany), a field spectrometer designed for continuous high-resolution spectral measurements for *SIF* retrieval with technical specifications in terms of spectral coverage, resolution and signal to noise ratio (SNR) coherent with the FLEX mission instrument specifications (Julitta *et al.*, 2017). The FloX was equipped with two spectrometers: (i) QEPro (Ocean Optics, Largo FL, USA) with high spectral resolution (Full width at half maximum ~0.3 nm) in the fluorescence emission range 650 nm–800 nm; (ii) FLAME S (Ocean Optics, Largo FL, USA) covering the full range of Visible-Near Infrared (Full width at half maximum ~1.7 nm). The spectrometer entrance-slit was split to two optical fibers that led to a cosine receptor measuring the downwelling radiance and a bare fiber measuring the canopy upwelling radiance. The spectrometers were housed in a thermally regulated box, keeping the internal temperature constant at 20 °C in order to avoid dark current drift and spectral shifts related to temperature changes. The thermoelectric cooler (TEC) of the QEPro was set to 20 °C to control the back thinned CCD detector SNR (nominal SNR > 1000:1). Spectrometer integration time was optimized for each channel (down- and up-looking channels) at the beginning of each automatic measurement cycle and two associated dark spectra were systematically recorded.

The FloX system was installed on a 10 m tall optical observation tower located in the vicinity of the eddy covariance (EC) tower. An upward facing fiber cable equipped with a cosine diffuser measured the down-welling irradiance, the up-welling radiance was measured with a bare fiber (25° field of view) pointing roughly North at a Holm Oak crown at about 2 m distance from the tower at a zenith angle of ca. 10°. From the measured spectra we retrieved sun-induced fluorescence in the red (O_2-B band, 687 nm) and far-red (O_2-A band, 760 nm) regions, referred to as SIF_B and *SIF* respectively, using both the improved Fraunhofer Line Depth (iFLD) and the spectral fitting method (SFM) (Meroni *et al.*, 2009). *SIF* and SIF_B retrieved with iFLD and SFM were extremely similar (Supplementary Table S3.1)**,** and therefore in the article we present only the iFLD, as it is less sensitive to noise than other retrieval methods (Cendrero-Mateo *et al.*, 2019). The integrated *SIF* ($SIF_{660\text{-}840}$) was calculated as: $SIF_{660\text{-}840} = 39.2435 * SIF_B + 83.6814 * SIF$ following Moreno *et al.* (2015) who empirically approximated the shape of the fluorescence emission spectra with a double gaussian regression. We applied a filter to remove measurements that were taken at high solar zenith angles ($SZA < 50$), which results in retrieval errors and nonlinear response of the cosine optics (Julitta *et al.*, 2016). We computed a series of additional vegetation indices: the normalized difference vegetation index (*NDVI*), the near infrared reflectance of vegetation index (NIR_V) (Badgley *et al.*, 2017) and the photochemical reflectance index (*PRI*) (Gamon *et al.*, 1997), derived from reflectance at 531 nm and 570 nm**.** Spectral measurements were taken at an interval of about 2 min, and then averaged over 1-hour periods.

In order to reduce the effect of canopy structure on the fluorescence signal and to derive a more physiological proxy of fluorescence we calculated the escape probability of *SIF* (*Fesc*) following Zeng *et al.* (2019) (Equation 3.1). We used the method proposed by Zeng *et al.* (2019) as the assumption of high *LAI* and no contribution from the soil to the reflectance were met given the experimental design.

$$Fesc = \frac{NIR_V}{f_{APAR}} \tag{3.1}$$

Fraction of absorbed photosynthetically active radiation (f_{APAR}) and absorbed photosynthetic active radiation (*APAR*) were estimated from incoming and reflected radiance following Damm *et al.* (2010) and (Li & Moreau, 1996; Moreau & Li, 1996) (Equation 3.2).

$$APAR = (PAR_{inc} - PAR_{refl}) \times RAPAR \tag{3.2}$$

Where PAR_{inc} is the incoming photosynthetic active radiation and PAR_{refl} is the reflected photosynthetic active radiation. *RAPAR*, which is the ratio of *PAR* absorbed by green canopy to the *PAR* absorbed by all surface materials was calculated as shown in Equation 3.3:

$$RAPAR = 0.105 - 0.323 \times NDVI + 1.468 \times NDVI^2 \tag{3.3}$$

Total *SIF* (SIF_{tot}) was calculated as in Equation 3.4:

$$SIF_{tot} = \frac{SIF}{Fesc} \tag{3.4}$$

The light use efficiency of photosynthesis (LUE_p) was calculated as in Equation 3.5:

$$LUE_p = \frac{GPP}{APAR} \tag{3.5}$$

Light use efficiency of fluorescence emission, LUE_f was calculated as in Equation 3.6:

$$LUE_f = \frac{SIF}{(APAR \times Fesc)} \tag{3.6}$$

APAR was estimated in mW m^{-2} nm^{-1} sr^{-1} and was then converted to µmol m^{-2} s^{-1} for the LUE_p calculation in Fig. 3.3B. All data is presented at an hourly scale, except for Fig. 3.1, Fig. 3.2a-d and Supplementary Fig. S3.3 where midday means (between 11 and 13 UTC) are used.

Leaf level active chlorophyll fluorescence and chlorophyll content

Diurnal variation in active chlorophyll fluorescence was measured with a "MONI-PAM Multi-Channel chlorophyll Fluorimeter" (Walz, Effeltrich, Germany) composed of a data acquisition unit and five emitter-detector units. The system was equipped with solar panels as a power supply and operated in stand-alone mode. The five heads of the MONI-PAM were installed on south-facing branches of a *Quercus ilex* tree located within the EC footprint near the tree on which FloX measurements were performed (Supplementary Fig. S3.1e). Branches were accessed using a permanent scaffold, and measurements were performed on leaves flushed in 2018. Active fluorescence signals included instantaneous fluorescence and maximal fluorescence along with incident *PAR* and T_{air}, and were recorded at 10-minute and one-hour frequencies, during the day- and night-time, respectively. For active fluorescence data, the hours from 11 to 16 were considered as the leaves measured by the MONI-PAM were shaded before 11 as shown by the high φP and low *NPQ* values between 8 and 10 UTC

(Supplementary Fig. S3.4d,f). MONI-PAM data was used to derive *NPQ*, the yield of *NPQ* (φNPQ), the reversible component of *NPQ* (NPQ_r), the sustained component of *NPQ* (NPQ_s), and the yield of photochemistry (φP) according to Porcar-Castell (2011). The maximum value at night of quantum yield of photosystem II (ΦP_{max}), corresponding to the widely used Fv/Fm, was calculated according to Porcar-Castell (2011). For the calculation of *NPQ,* a reference maximum fluorescence (F_{mR}) value was obtained during a period in which at night time the ΦP_{max} was 0.81, which is within the range of non-stressed ΦP_{max} in Holm oak (Ogaya & Peñuelas, 2003). The yield of fluorescence (φF) was calculated as in Porcar-Castell *et al.* (2014). Relative light saturation of photosynthesis (x) is a scaling factor that describes the degree of photochemical impairment and was calculated following van der Tol *et al.* (2014). Details regarding the calculation of the MONI-PAM parameters can be found in the following R package developed by us (https://github.com/davidmartini90/pam). For the estimation of the parameters with the PAM we employed the prevailing assumption of perfect connectivity between PSII units (lake model assumption), which is still unclear whether is valid under stress (Porcar-Castell, 2011). The above parameters were obtained for each MONI-head and then averaged across all heads.

A Soil Plant Analysis Development (SPAD) chlorophyll meter was used to estimate leaf chlorophyll status. SPAD measures transmittance of red (650 nm) and infrared (940 nm) radiation through the leaf (Uddling et al. 2007). The SPAD measurements provide an indicator of chlorophyll content in relative units (SPAD values). SPAD values measured in *Quercus ilex* at the Majadas site have been found to strongly correlate ($R^2 = 0.91$) with chlorophyll a+b obtained in the laboratory (Gonzalez-Cascon *et al.*, 2017). SPAD measurements took place on the 20th July, 2018 (before the HW) and the 4th August, 2018 (during the HW), and were carried out on the tree measured with the FloX and the tree measured with the MONI-PAM. In each tree, two branches were measured (12 leaves per branch), dividing between current year leaves (new leaves) and previous year leaves (old leaves).

Biometeorological parameters and carbon fluxes

Biometeorological variables and surface gas exchange were measured at the site in the period June 2018 to July 2018. During this period the herbaceous layer was completely dry. Therefore, the fluxes measured were representative only of the tree functioning as shown by Perez-Priego *et al.* (2017), Perez-Priego *et al.* (2018), and El-Madany *et al.* (2020) where EC derived water fluxes were compared to independent water fluxes of the herbaceous layer obtained with the lysimeters and sap flow measurements of the tree. An EC system consisting of a three-dimensional sonic anemometer (R3-50, Gill LTD, Lymington, UK) and an infrared gas analyzer (LI-7200, Licor Bioscience, Lincoln, USA) was used to measure dry mixing ratios of CO_2 and H_2O at a height of 15.5 m above ground. Shortwave incoming radiation (SW_{in}, W m^{-2}) and long wave outgoing radiation (LW_{out} W m^{-2}) were measured with a ventilated net radiometer (CNR4, Kipp and Zonen, Delft, Netherlands). Air temperature (T_{air}, °C) and relative humidity (*rH*, %) were measured with a combined Pt-100 temperature and capacitive humidity sensor (CPK1-5, MELA Sensortechnik, Germany). Fluxes were computed using EddyPro version 6.2.0 (Fratini & Mauder, 2014) as described in El-Madany *et al.* (2018). Quality check of the fluxes was accomplished according to Mauder and Foken (2011). The storage flux was computed using a vertical profile of CO_2 according to Falge *et al.* (2001). The u*-threshold (~0.13 m s^{-1}) was estimated according to Papale *et al.* (2006). The measured net ecosystem exchange (*NEE*) was partitioned into gross primary production (*GPP*) using both the nighttime partitioning (Reichstein *et al.*, 2005) and daytime partitioning (Lasslop *et al.*, 2010) methods as implemented in the REddyProc 0.7-1 R package (Papale *et al.*, 2006). For the analysis we retained only data coming from measured *NEE* and latent heat data, or gap-filled data with high confidence (i.e., quality flag 0 and 1 (Wutzler *et al.*, 2018)). In the main text only the *GPP* from the daytime partitioning technique is reported. We decided to use the GPP from the day-time partitioning because the *GPP* derived from night-time partitioning is noisier (e.g. (Lasslop *et al.*, 2010)), particularly when measured *NEE* is relatively low as observed during the heat wave*. GPP-SIF* and the *GPP-VPD* relationships were consistent independently to the CO_2 flux partitioning method (Supplementary Table S3.2, Supplementary Table S3.3), as well as the method used for retrieval of *SIF* (Supplementary Table S3.3, Supplementary Table S3.1).

The EC and biometeorological data were averaged at hourly temporal resolution in order to smooth the effect of the random error on the measurements (Damm *et al.*, 2010). Evapotranspiration (*ET*) was obtained from latent heat flux measurements, the surface conductance (*gs*) was obtained by inverting the Penman-Monteith equation (Beven, 1979). Aerodynamic resistance was removed before the calculation of *gs* using Thom (1972) as implemented in the bigleaf R package (Knauer *et al.*, 2018).

Statistical analysis

Significant differences in Fig. 3.2 were calculated with an Analysis of variance (ANOVA) (Girden, 1992). In order to test differences in the slope of the *NPQ-VPD* relationship between the pre-HW period and the HW period (Fig. 3.4c) an analysis of covariance (ANCOVA) was used (Rutherford, 2001). Regressions were performed with linear ordinary least squares and second degree polynomial regression. Selection of the regression method was based on lowest Akaike information criterion.

3.4 Results

Effect of the heatwave on *SIF, NDVI* and *NIR*$_V$

During the HW we observed an increase of 7.2 °C and 22 hPa in daily mean T_{air} and *VPD*, respectively (Fig**. 3.1**a), compared to the pre-heatwave period (pre-HW, i.e., 7 days before the heatwave). The 5-days average of daily maximum T_{air} and *VPD* of 43.2 °C and 76.1 hPa, respectively, showed a substantial positive anomaly compared to what has been measured at the site since 2004 (Supplementary Fig. S3.2). As the HW was caused by a Saharan air intrusion (Sousa *et al.*, 2019), which is usually accompanied by higher than average dust levels, we observed a 4.9% mean decrease in SW_{in} ($p < 0.01$), and therefore also *PAR*. After the HW the SW_{in} returned to the initial values. As a consequence of heat stress, LW_{out} increased by 7.2% ($p < 0.01$) (Fig. 3.1b). The trees responded to the HW by decreasing photosynthesis (32.2% mean decrease of midday – between 11 and 13 UTC - *GPP*, $p < 0.01$) (Fig. 3.1c) and by sharply diminishing midday *SIF* (Fig. 3.1d). *SIF* normalized by *PAR* exhibited a massive decline, with a mean decrease of 64.1% ($p < 0.01$) with respect to the pre-HW (Fig. 3.1d). Evapotranspiration did not significantly vary between the pre-HW and HW period (Fig. 3.1c) ($p = 0.129$), but a gradual decline during the course of the HW was observed. Supplementary Fig. S3.5 shows a strong sensitivity of *gs* to *VPD,* with lower *gs* during the HW. The strong physiological response of the vegetation contrasted with the relative stability of two spectral indices, the *NDVI* and the NIR_V (Fig. 3.1e,f), which can be considered indicators of vegetation canopy greenness. Both indices increased significantly ($p = 0.02$, $p < 0.01$ for *NDVI* and NIR_V, respectively) with the HW, though their increment was modest: 0.7% and 4.7% for *NDVI* and NIR_V, respectively. Simulations with the Soil Canopy Observation, Photochemistry and Energy fluxes (SCOPE), a state-of-the-art radiative transfer-photosynthesis coupled model, showed that this increase can be explained by increased diffuse radiation during the HW (Supplementary Fig. S3.6).

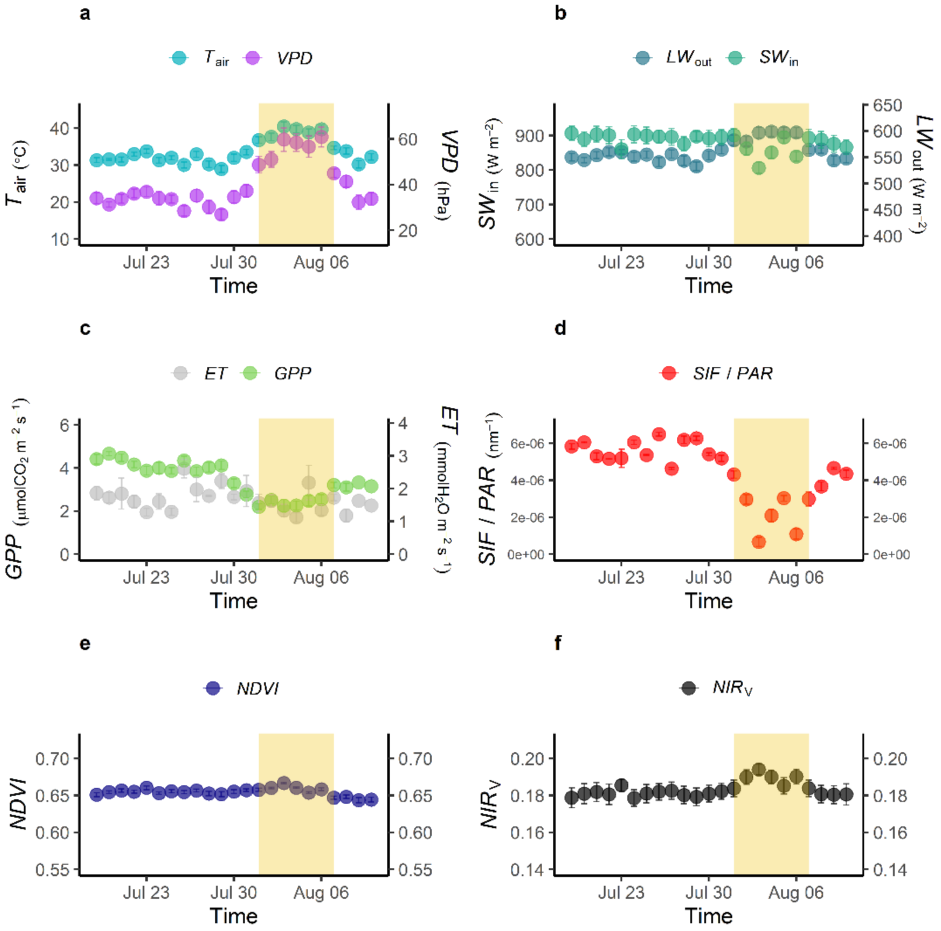

Fig. 3.1. Daily means of (a) air temperature (T_{air}), vapor pressure deficit (*VPD*), (b) shortwave incoming radiation (SW_{in}), longwave outgoing radiation (LW_{out}), (c) gross primary production (*GPP*) and evapotranspiration (*ET*), (d) sun-induced fluorescence at 760 nm (*SIF*) (mW m^{-2} nm^{-1} sr^{-1}) divided by photosynthetic active radiation (*PAR*) (mW m^2 sr^{-1}) (*SIF* / *PAR*), (e) normalized difference vegetation index (*NDVI*), (f) near-infrared reflectance of vegetation (NIR_V). Daily values in (a) to (f) are computed between 11 and 13 UTC. The yellow rectangle represents the heatwave (HW) period.

f_{APAR} and chlorophyll remain unaltered

The HW did not cause statistically significant changes in f_{APAR} ($p = 0.07$) (Fig. 3.2a), which remained stable around 0.49. Likewise, chlorophyll concentration estimated with SPAD (see Methods) did not show significant differences for both the leaves flushed in 2018 ($p = 0.06$) (Fig. 3.2e) and in the previous year (p = 0.052) (Fig. 3.2f). *APAR* decreased (6.9% mean decrease) during the HW due to the reduction in *PAR* (5% mean decrease) (Fig. 3.2a,b). *Fesc* instead showed a modest, yet significant ($p < 0.01$), increase (from a mean value of 0.418 ± 0.011 during the pre-HW to 0.432 ± 0.009 during the HW) (Fig. 3.2d). Due to the small change in *Fesc*, we could not definitively rule out a change in canopy structure during the HW, but it was clear from the negligible changes in vegetation indices and f_{APAR} that the response of *Quercus ilex* to extreme heat was primarily physiological, and only marginally structural.

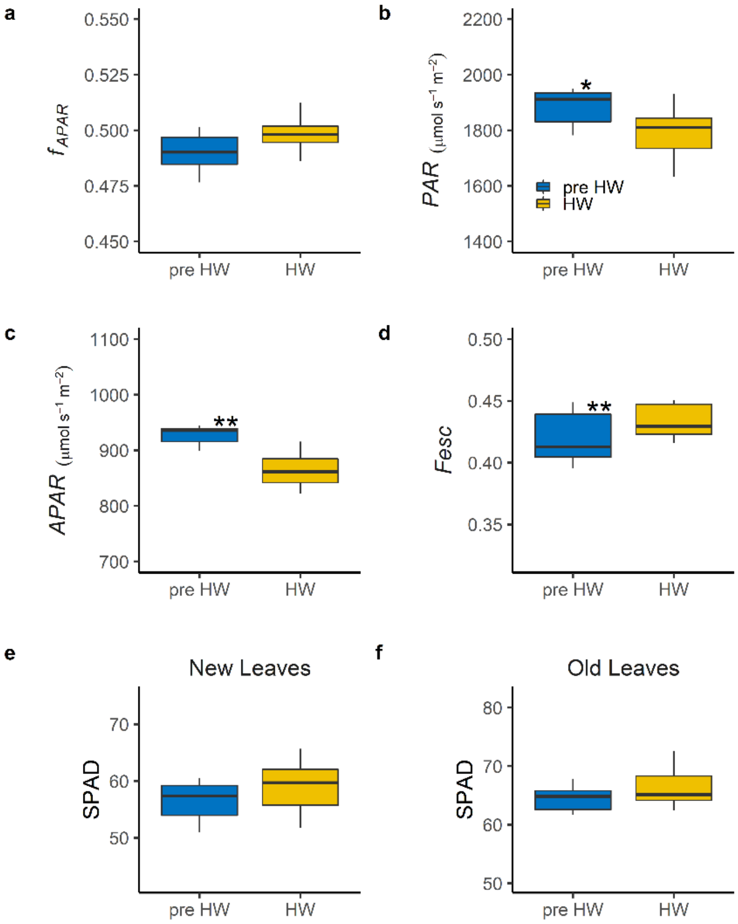

Fig. 3.2. Boxplot of (a) fraction of absorbed photosynthetic active radiation (f_{APAR}); (b) photosynthetic active radiation (*PAR*); (c) absorbed photosynthetic active radiation (*APAR*); (d) escape probability of *SIF* (*Fesc*); and (e), (f) values from Soil Plant Analysis Development (SPAD) chlorophyll

meter for old leaves (i.e. leaves flushed in previous years) and new leaves (i.e., leaves flushed in the 2018), respectively. The pre-heatwave (pre-HW) period values are in blue while heatwave (HW) period values in yellow. Daily values of f_{APAR}, *PAR*, *APAR* and *Fesc* are computed between 11 and 13 UTC. '**' indicates p values $p < 0.01$ and '*' indicates $p < 0.05$ according to an ANOVA test. No significant differences are observed in (a), (e) and (f). In the boxplot the thick lines represents the median and the lower and upper hinges correspond to the 25th and 75th percentiles. The upper/lower whiskers extend from the hinge to the largest/smallest value no further than 1.5 * inter-quantile range.

Nonlinear *GPP-SIF* relationship at hourly time scale during the heatwave

Our study revealed a clearly nonlinear relationship between *GPP* and *SIF*, when considering both the pre-HW and HW period. During the pre-HW period *GPP* and total SIF_{tot} exhibited a positive relationship ($R = 0.52$, $p < 0.01$), while during the HW their relationship was negative ($R = -0.36$, $p = 0.034$) (Fig. 3.3a). This pattern was even more pronounced when the efficiencies of both processes were considered, as shown by the relationship between LUE_{p} and LUE_{f} (Fig. 3.3b, Supplementary Fig. S3.7).

A similar pattern was observed at the leaf level, as the relationship between φP and φF was negative during the HW ($R = -0.61$, $p < 0.01$) and positive during the pre-HW period ($R = 0.64$, $p < 0.01$). During the pre-HW period the φP-φF relationship showed a clear hysteresis (Supplementary Fig. S3.8) as for the same φF, φP showed lower values in the morning and higher values in the afternoon.
The relationship between *GPP* and indices such as *NDVI*, *PRI,* and NIR_{V} (Supplementary Fig. S3.9) differed strongly from the one exhibited by *GPP* and *SIF*. *PRI* showed a strong linear relationship ($R = 0.86$, $p < 0.01$) with *GPP* (Supplementary Fig. S3.9a), which indicated the important role of *NPQ* dissipation during the HW. Moreover, *NPQ* and *PRI* were strongly correlated (Supplementary Fig. S3.10d), suggesting that, given the negligible changes in canopy structure, PRI was a good indicator of NPQ processes despite the different scales at which they were measured (leaf and canopy). *NDVI* showed no significant relationship with *GPP* (Supplementary Fig. S3.9b), while NIR_{V} showed a negative relationship ($R = -0.69$, $p < 0.01$) (Supplementary Fig. S3.9c). The negative relationship could be explained by the fact that *GPP* reached its maximum in the early morning hours, while NIR_{V} is at its minimum (Supplementary Fig. S3.11) due to directional effects under direct illumination.

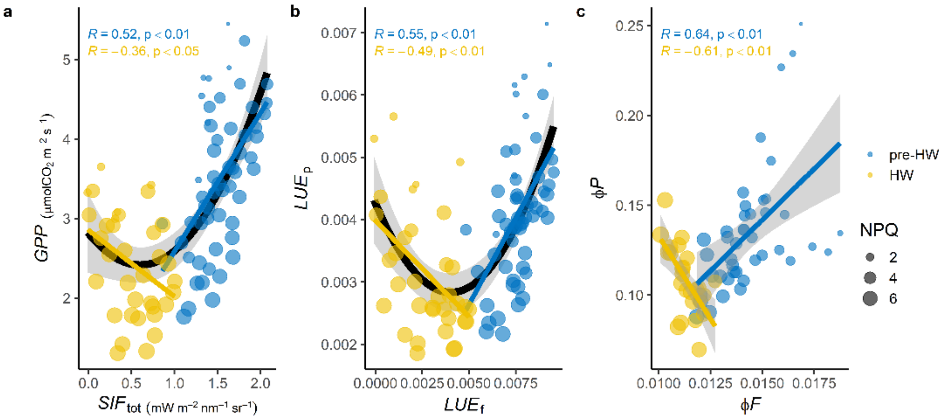

Fig. 3.3. (a) Scatterplot between gross primary production (*GPP*) and fluorescence emission at 760 nm (SIF_{tot}). (b) Scatterplot between light use efficiency of photosynthesis (LUE_p) and light use efficiency of *SIF* emission ($LUEf_f$). In (b) the units of *APAR* for the LUE_p calculation are µmol m^{-2} s^{-1}, and the units of *APAR* for the LUE_f calculation are mW m^{-2} nm^{-1} sr^{-1}. (c) Scatterplot between yield of photochemistry (ΦP) and yield of fluorescence (ΦF). Blue points correspond to the pre-heatwave (pre-HW) period and yellow points correspond to the heatwave (HW) period. Hourly mean values in (a) and (b) are computed from 9 to 16 UTC and from 11 to 16 UTC in (c). The size of each point is proportional to the nonphotochemical quenching (*NPQ*). In each panel the Spearman's rank correlation coefficient (R) and p value are reported for the pre-HW and HW period. The black line is the overall fit from a second degree polynomial. Blue and yellow lines are linear regressions for the pre-HW and HW period respectively. The shaded area represents the 95% confidence interval of the fit.

The overall nonlinear GPP-SIF_{tot} relationship (Fig. 3.3a) was mirrored by a similar NPQ-SIF_{tot} relationship (Fig. 3.4a), with *NPQ* measured at the leaf level. Even though the correlation between NPQ-SIF_{tot} was not significant when the pre-HW and HW periods were considered on a separate basis, the overall nonlinearity departed from the expected negative relationship reported in previous publications which did not account for heat-stress (Magney *et al.*, 2017). *NPQ-GPP* was instead remarkably linear (Fig. 3.4b), and its slope was not altered by the HW (slope pre-HW = -1.2, slope HW = -0.98, p = 0.77), suggesting that the photosynthetic activity of Evergreen oaks was strongly controlled by the activity of the xanthophyll cycle. *NPQ* was correlated with *VPD* (R = 0.82, p < 0.01), but the slope of *NPQ-VPD* showed a decreasing trend during the HW period (Fig. 3.4c) (slope pre-HW =0.064, slope HW = 0.039, p = 0.053). The diurnal cycles of *NPQ* showed in fact marked differences before and after the HW, with *NPQ* reaching a plateau in the afternoon of the HW period (Fig. 3.5a). In the same period

LUE_{f} exhibited a strong increase, highlighting changes in energy allocation during the HW. Additionally, the ΦP_{max} and the LUE_{p} during the HW were strongly downregulated (Supplementary Fig. S3.3a,b, Fig. 3.5b), alongside the accumulation NPQ_{s} (Supplementary Fig. S3.3c,d).

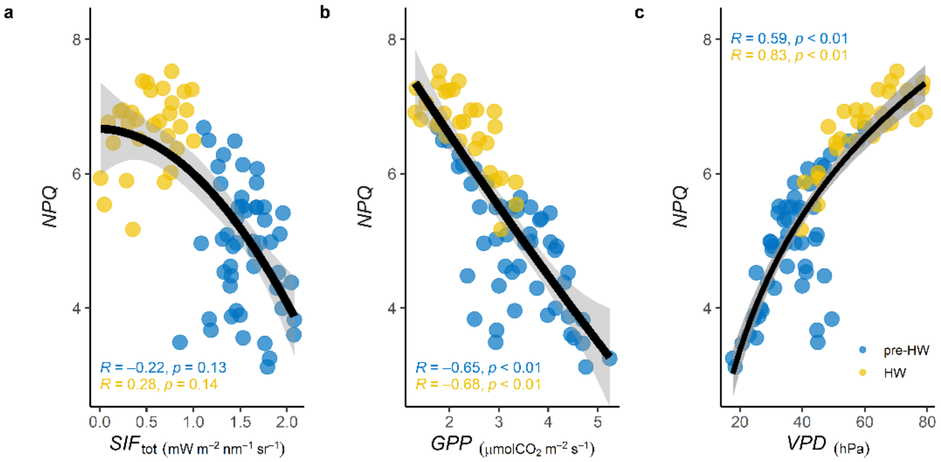

Fig. 3.4. (a) Scatterplot between nonphotochemical quenching (*NPQ*) and fluorescence emission at 760 nm (SIF_{tot}). (b) Scatterplot between *NPQ* and gross primary production (*GPP*). (c) Scatterplot between *NPQ* and vapor pressure deficit (*VPD*). Blue points correspond to the pre-heatwave (pre-HW) period and yellow points correspond to the heatwave (HW) period. Hourly mean values are computed from 10 to 16 UTC. In each panel the Spearman's rank correlation coefficient (R) and p value are reported for the pre-HW and HW period. The black line is the overall fit from a second degree polynomial. The shaded area represents the 95% confidence interval of the fit.

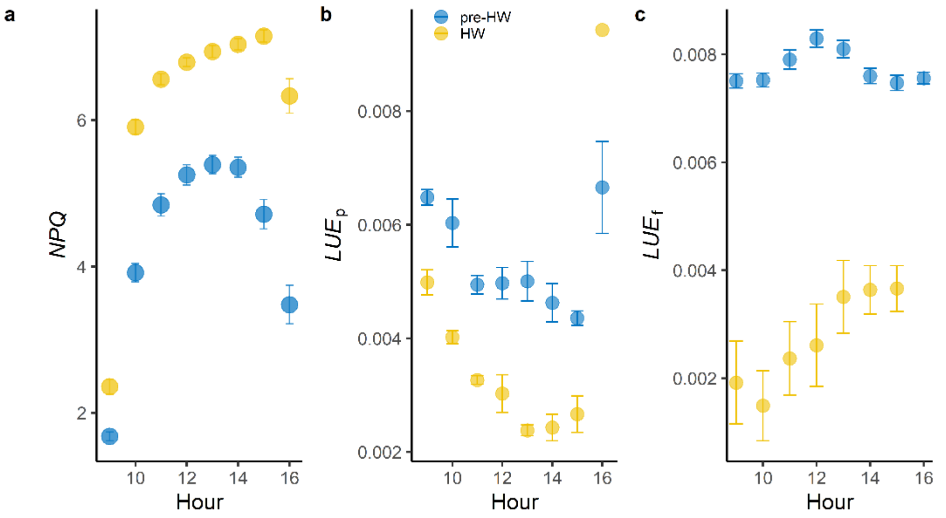

Fig. 3.5. Mean daily cycles for (a) nonphotochemical quenching (*NPQ*) (b) light use efficiency of photosynthesis (LUE_p) and (c) light use efficiency of *SIF* emission (LUE_f). Blue points correspond to the pre-heatwave (pre-HW) period and yellow points correspond to the heatwave (HW) period. Error bars correspond to 1 standard error.

NPQ, φ*P* and φ*F* plotted against *x* showed strong differences between the HW and pre-HW period (Fig. 3.6a,c,e). For *x* values higher than 0.75 *NPQ*-*x* was significantly positive in the pre-HW period (R = 0.61, $p < 0.01$), but showed a negative relationship during the HW (R = -0.32, $p < 0.01$) (Fig. 3.6b). The Φ*NPQ* shows a similar saturation although less extreme than *NPQ* for high levels of *x (*Supplementary Fig. S3.12a,b). φ*P*-*x* presented a consistent negative relationship, but its slope became steeper during the HW (slope of -5.9 and -6.5, for pre-HW and HW respectively, $p < 0.01$) (Fig. 3.6d), meaning that for the same *x*, φ*P* decreases more during the HW. φ*F*-*x* was negative during the pre-HW (R = -0.47, $p < 0.01$), but positive during the HW (R = 0.57, $p < 0.01$) (Fig. 3.6e). Taken together, this means that during the HW at high levels of light saturation, *NPQ* decreased, φ*P* decreased faster than usual and φ*F* increased.

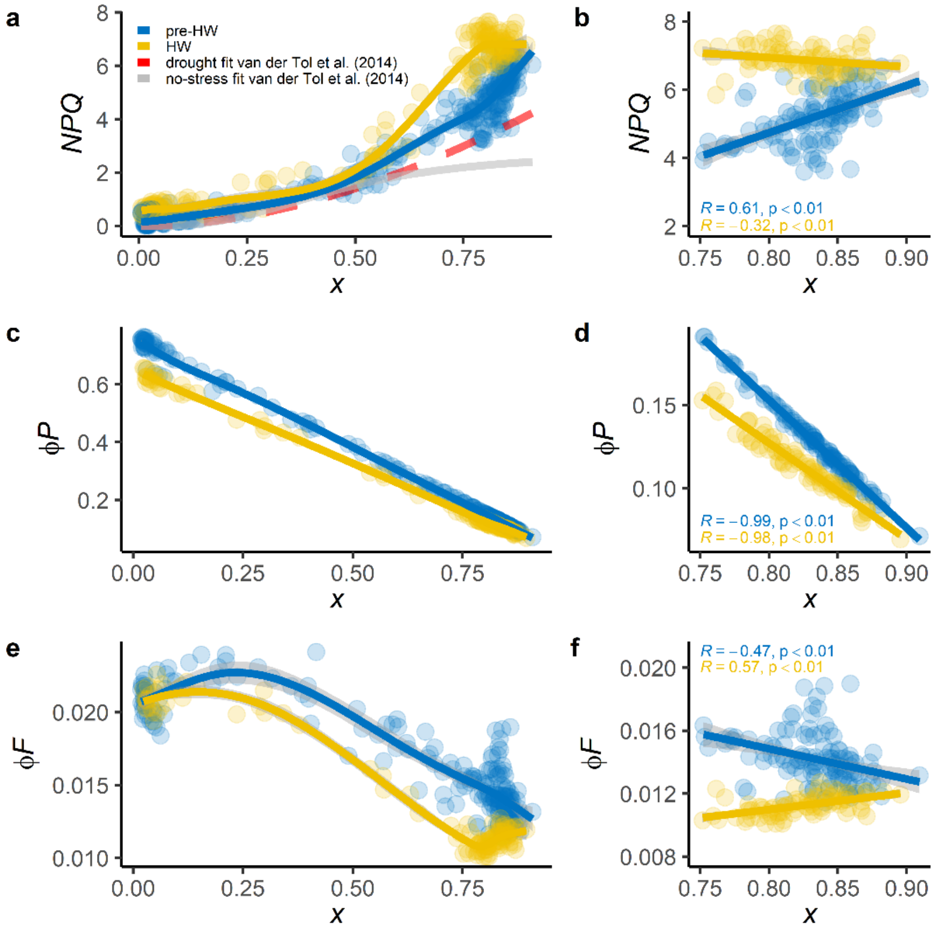

Fig. 3.6. (a,b) Scatterplot between nonphotochemical quenching (*NPQ*) and relative light saturation of photosynthesis (x). The red dashed line and solid gray line represent the *NPQ*-x fit for the drought stressed plants and non-stressed plants, respectively, from van der Tol et al. (2014). (c,d) Scatterplot between yield of photochemistry (ΦP) and x. (e,f) Scatterplot between yield of fluorescence (ΦF) and x. Blue points correspond to the pre-heatwave (pre-HW) period and yellow points correspond to the heatwave (HW) period. Hourly mean values with $x > 0.75$ are shown in (b, d, f). In (a, c, e) the lines are a local polynomial regression. In (b, d, f) the lines represent linear regression and the Spearman's rank correlation coefficient (R) and p value are reported for the pre-HW and HW period. The shaded area represents the 95% confidence interval of the fit.

3.5 Discussion

Previous research has highlighted the need to better understand the relationships between photosynthesis, fluorescence, and *NPQ* under extreme stress conditions, in order to be able to better exploit proximal and/or remote sensing estimates of *SIF* for carbon cycle research (van der Tol *et al.*, 2014; Wohlfahrt *et al.*, 2018). Our study examined the effect of the HW on the *GPP-SIF* relationship in evergreen broadleaved trees, under no major changes in canopy structure. Our results show that the HW caused nonlinearity in the overall relationship (i.e., when considering both the pre-HW and HW period together) between photochemistry and fluorescence at both canopy and leaf scale. We observed a saturation of *NPQ* at high temperatures, and a change in energy allocation towards fluorescence emission, thus leading to the *GPP-SIF* nonlinear relationship when considering both the pre-HW and HW period. Additionally, current state-of-the-art radiative transfer and photosynthesis models such as SCOPE are unable to model *NPQ* at the level of stress experienced in this study, suggesting that improved parametrizations are required to correctly model *NPQ* and *SIF* during extreme events.

Unraveling the mechanism behind *GPP-SIF* nonlinearity in response to heat stress: the role of *NPQ*.

We show that in Mediterranean evergreen broadleaved trees *SIF* responded to the extreme heat stress (Fig. 3.1d), indicating that *SIF* reflects changes in photosynthesis even in absence of large changes in *APAR* and chlorophyll content. There is a current debate on the information content of *SIF* and the GPP-SIF relationship with two different positions (Dechant *et al.*, 2020): the first is that *SIF* contains both information about canopy structure but also physiological modulation of photosynthesis, the second is that *SIF* and GPP-SIF is mainly determined by structural changes. In this study we show that even with minimal changes in canopy structure (*APAR* and chlorophyll content) we observe a relationship between *SIF-GPP*, therefore challenging the studies suggesting that *SIF-GPP* is mainly determined by structure (Yang *et al.*, 2018). For comparison we show that *NDVI* and NIR_V, two vegetation indices that contain information about vegetation structure, are limited at this time scale where both directional effects and diffuse radiation do not allow tracking photosynthesis (Supplementary Fig. S3.9b,c). It is worth noting that we cannot completely rule out subtle changes in canopy architecture, which might be caused by slight changes in leaf angle distribution (Gratani & Bombelli, 2000; Migliavacca *et al.*, 2017) or chloroplast movements (Van Wittenberghe *et al.*, 2019). However, the variations in *Fesc* (Fig. 3.2d) and other structural parameters seem extremely modest (Fig. 3.1e,f). Additionally, more diffuse radiation during the HW could have increased LUE_p or affected the reflectance. Still, reflectance based indices would be only marginally affected by higher diffuse radiation according to simulations with the SCOPE model (Supplementary Fig. S3.6). Moreover, the retrieval of *SIF* is more uncertain during the HW because of the lower signal to noise ratio, which might explain the higher correlation during the HW of the Φ*F*- Φ*P* (leaf scale) relationship than the LUE_f-LUE_p relationship (Fig. 3.3b,c).

This study confirms that *GPP-SIF* is influenced by *NPQ*, which is the dominant dissipation pathway during the progression of the HW. *NPQ*, which is observed with active fluorescence, can also be sensed at top of canopy with PRI (Supplementary Fig. S3.10d); the tight relationship between *GPP* and *PRI* (Supplementary Fig. S3.9a) suggests the need of combining *SIF* and *PRI* for accurate *GPP* predictions under extreme heatwaves.

Leaf- and canopy-level observations agree remarkably well (Fig. 3.3), indicating that some features of the leaf level photosynthesis-fluorescence relationship manifest at the canopy level under the extreme heat stress experienced. This result calls for a more widespread combination of active and passive fluorescence measurements for explaining the partitioning of energy between *NPQ*, φ*P,* and φ*F*, and how this is reflected in the *GPP*-fluorescence relationship. In order to do that, more analysis would be required to understand how the assumptions employed when estimating PAM parameters (such as connectivity between PSII units) are affected at seasonal scale or by stress (Porcar-Castell, 2011).

NPQ exhibits a complex behavior during the HW. *NPQ* shows a strong response to *VPD* (Fig. 3.4c), indicating that stomatal closure may have been a process that triggered an increased dissipation of the excess energy through the *NPQ* mechanism. However, under high *VPD* (e.g., in the afternoon of the hotter days) the response of *NPQ* saturates – indicating that the temporal kinetics of stomata and the light reactions can decouple during heatwave events (Meinzer *et al.*, 2017). The apparent link between NPQ and stomatal conductance, also suggested in previous research (Medrano *et al.*, 2002; van der Tol *et al.*, 2009a) and exploited through remote sensing with the *PRI* (Suárez *et al.*, 2008; Yang, JC *et al.*, 2020) needs to be further investigated. In particular it would be required to establish a process-based understanding of the relationship between stomatal conductance*, NPQ* and *SIF* to correctly use *SIF* as proxy for transpiration. Under typical high illumination conditions φ*P* and φ*F* are positively correlated (Porcar-Castell *et al.*, 2014). This "*NPQ*-phase" is what is generally observed in most studies, which linearly relate *GPP* and *SIF* (Damm *et al.*, 2010; Yang *et al.*, 2015) and is also representative of the pre-HW period. During the HW, plants do not have the capacity to adjust to unfamiliar climatic conditions and *NPQ* saturates, pushing the plant to the "*NPQ*-saturation phase" (van der Tol *et al.*, 2014; Magney *et al.*, 2020). In this phase, *NPQ* saturates early in the day (Fig. 3.5a), leaving the photosystems without sufficient protection to cope with excess energy.

We propose that the mechanisms responsible for the observed *GPP-SIF* overall nonlinearity under high heat stress are shifts in energy allocation towards fluorescence emission (Fig. 3.5c), as the plants are pushed by the extreme stress to the *NPQ*-saturation phase. This would be caused by *NPQ* saturation and sustained photoinhibition. *NPQ* might saturate, if limited by its xanthophyll pool size, which has a turnover time of several days (Demmig *et al.*, 1988). Sustained photoinhibition is clearly demonstrated by decrease in ΦP_{max} and increase in NPQ_s (Supplementary Fig. S3.3) and may be also partly caused by damage of reaction centers (Porcar-Castell *et al.*, 2008).

State-of-the-art radiative transfer and photosynthesis models cannot reproduce *NPQ* at high levels of stress

The fluorescence parameterization in the state-of-the-art radiative transfer and photosynthesis models, such as SCOPE, are based on the relationship between the relative light saturation of photosynthesis and *NPQ* (Fig. 3.6a). van der Tol *et al.* (2014) reported this relationship for a variety of conditions but not for the heat stress described in our study. Magney *et al.* (2020) indicates that there is only sparse evidence that under high stress conditions (high *NPQ*), an increase in ΦF can occur; therefore, more studies are needed to better interpret *GPP-SIF* relationship. With our study we fill this gap and we show that the current parameterization of models such as SCOPE, that are used to derive photosynthesis products from fluorescence measurements, including for current and future satellite missions, do not represent the *NPQ* response at the level of stress observed in our study (Fig. 3.6a,b). In fact, neither the *NPQ* levels reached in this study nor the observed nonlinearity of *NPQ-x* relationship are reproduced by the model (Fig. 3.6a). Hence, the model would not be able to describe the *NPQ*-saturation phase that led to overall nonlinear response between *SIF-GPP*. This lack of description of the *NPQ*-saturation phase under extreme heat stress by SCOPE has to do with the fact that there is shortage of data constraining the process (van der Tol *et al.*, 2014; Magney *et al.*, 2020). The increasing availability of continuous passive and active fluorescence data, alongside *NPQ* estimates in multiple experimental sites will provide the data to constrain the model parameterization under different conditions, including during extreme events. Our results call for an improvement of the parameterization of the relationship between the relative light saturation of photosynthesis and the *NPQ* process in radiative transfer and photosynthesis models. By doing so, we will likely improve the representation of *GPP-SIF* under extreme conditions with important implications for the exploitation of ground based and satellite measurements to monitor photosynthetic performance of the vegetation.

Uncertainties related to footprint mismatch and leaf-canopy scaling.

The difference between the radiometric and the eddy covariance footprint is a common source of uncertainty when analyzing time series of spectral data and eddy covariance flux data. To minimize this uncertainty, the experiment was designed in a way that the FloX system and the MONI-PAM are installed within the eddy covariance footprint climatology (Supplementary Fig. S3.1e), and the selected trees are representative of the trees in the footprint. Moreover, as the herbaceous vegetation in summer was completely senesced, the *GPP* signal is dominated by the photosynthesis of the *Quercus ilex* trees sampled (Perez-Priego *et al.*, 2018; El-Madany *et al.*, 2020). Another source of uncertainty is the mismatch between leaf-scale and canopy-scale measurements. To minimize the scale mismatch we sampled with the MONI-PAM and the FloX similar portions of the canopy of the two trees; that is the southern part of the canopy and external part of the crown. The sunlit leaves at the south side of the tree crown were sampled with the MONI-PAM because representatives of the area of the crown that is in the field of view of the FloX. In this analysis we showed 15 days with stable structure of the canopy (no substantial changes in *NDVI* and SPAD). The stability of vegetation structure guarantees that in the rather short period analyzed there are no artifacts affecting the leaf to canopy scaling due to changes in leaf area or pigments. The good relationship we found between *NPQ* measured at leaf level and the *PRI* (Supplementary Fig. S3.10d) is for instance an indicator of good comparability between leaf level and canopy scale measurements.

Concluding remarks

In sum, the present study shows that under severe heatwaves strong *GPP-SIF* nonlinearities are possible even in the absence of large changes in canopy structure. While a linear *GPP-SIF* relationship is expected in most conditions and driven by *NPQ* at the seasonal scale, under extreme stress a shift in energy allocation can occur. Our results can help improving the parameterization of the response of fluorescence to extreme events and in this way pave the way toward a more robust use of *SIF* for monitoring *GPP* under projected future climatic conditions characterized by increases in both frequency and severity of heatwaves (Bernstein *et al.*, 2008).

Acknowledgments

The project received funding from the European Union’s Horizon 2020 research and innovation program under the Marie Sklodowska-Curie grant agreement No. 721995. The authors acknowledge the Alexander von Humboldt Foundation for supporting this research with the Max-Planck Prize to Markus Reichstein. We also acknowledge the European Space Agency (ESA) in the frame of the FLEXSense campaign (ESA Contract No. 4000125402/18/NL/NA) and the Photoproxy campaign (ESA contract No. 4000125731/19/NL/LF).
MMigliavacca and GWohlfahrt acknowledge funding from the joint FWF-DFG DACH project “Constraining terrestrial gross primary productivity by joint measurements of the carbonyl sulfide exchange and sun-induced fluorescence”. GWohlfahrt further acknowledges financial support by the

AustroSIF project, which is funded by the FFG and BMK within the Austrian Space Applications Program.

Author Contributions

D.M. and M.M. designed the study and carried out the majority of the data-analysis. K.S. provided and processed the MONI-PAM data and contributed to the discussion. G.W. contributed to the discussion and helped to structure the manuscript. J.P.-L. performed SCOPE runs and contributed to the discussion. J.P.-L and D.M. contribute to data sampling. C.v.d.T., A.P.-C. and T.SM. contributed to the discussion of the active fluorescence data. A.C., R.C., T.E.-M., R.G.-C., M.P.M., T.J., G.M., U.R., M.R. (Markus Reichstein), M.R. (Micol Rossini) and M.M. contributed to the discussion and provided crucial feedback. All authors contributed to the discussion of the results and to the writing of the manuscript.

Data availability

Raw data and code are available and provided on an open access Zenodo repository through the DOI: 10.5281/zenodo.5773208.

Supplementary Information

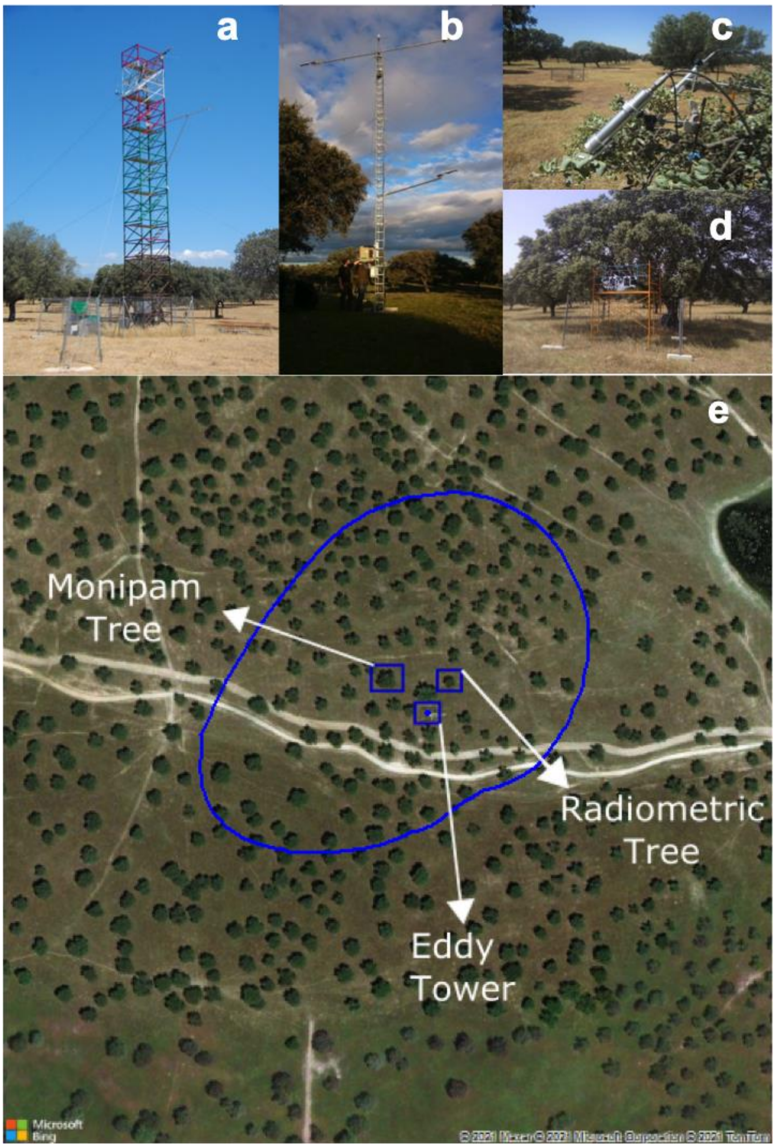

Supplementary Fig. S3.1. (a) Picture of the eddy covariance tower. (b) Picture of the radiometric tower. (c,d) picture of the MONI-PAM system. (e) Satellite picture of the experimental site at Majadas de Tiétar. The eddy-covariance tower, the tree measured by the radiometric tower and the tree measured by the MONI-PAM are highlighted. The blue circle represents the footprint climatology of the eddy covariance tower, here defined as the isoline corresponding to 80% of the total flux footprint contributions.

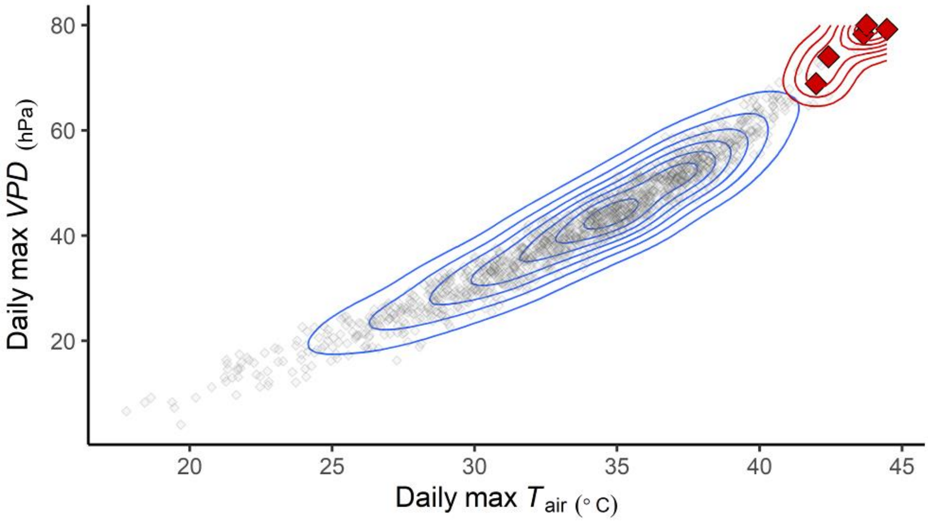

Supplementary Fig. S3.2. 2D kernel density estimation of daily maximum air temperature (T_{air}) and daily maximum vapor pressure deficit (*VPD*) from 2004 to 2018 in the months of June, July and August at the Majadas de Tiétar site in blue, and in red for the 2018 heatwave. The red dots correspond to the daily maximum T_{air} and *VPD* during the 2018 heatwave.

Supplementary Table S3.1. Spearman's rank correlation coefficient (R) and p value between compared variables. Slope and intercept are obtained with total least square regression. SIF_{ifld} is obtained from the Improved Fraunhofer Line Discrimination Method (ifld) and SIF_{sfm} is obtained with the spectral fitting method (SFM).

Compared variables (Y - X)	R	Slope	Intercept	p value
*SIF*ifld - *SIF*sfm	0.988	0.723	0.22	< 0.01

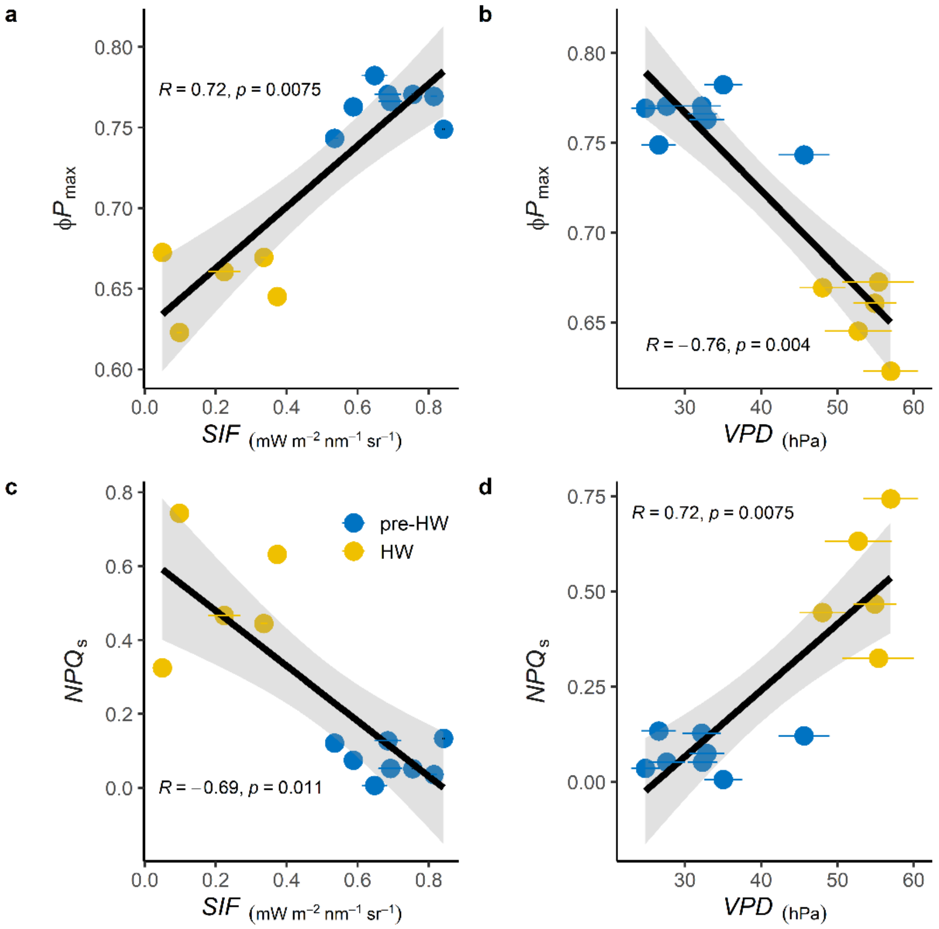

Supplementary Fig. S3.3. (a) Scatterplot between the maximum value at night of quantum yield of photosystem II (ΦP_{max}) (correspondent to the widely used Fv/Fm) and daily means of SIF. (b) Scatterplot between ΦP_{max} and daily means of *VPD*. (c) Scatterplot between daily means of the sustained component of the nonphotochemical quenching (NPQ_s) and sun-induced fluorescence at 760 nm (*SIF*). (d) Scatterplot between daily means of NPQ_s and vapor pressure deficit (VPD). Yellow points correspond to the pre-heatwave (pre-HW) period and blue points correspond to the heatwave (HW) period. Daily mean values in (a) to (d) are computed between 11 and 13 UTC. In each panel the Spearman's rank correlation coefficient (R) and p value are reported for the overall data. The black line is the overall fit from a linear regression. The shaded area represents the 95% confidence interval of the fit.

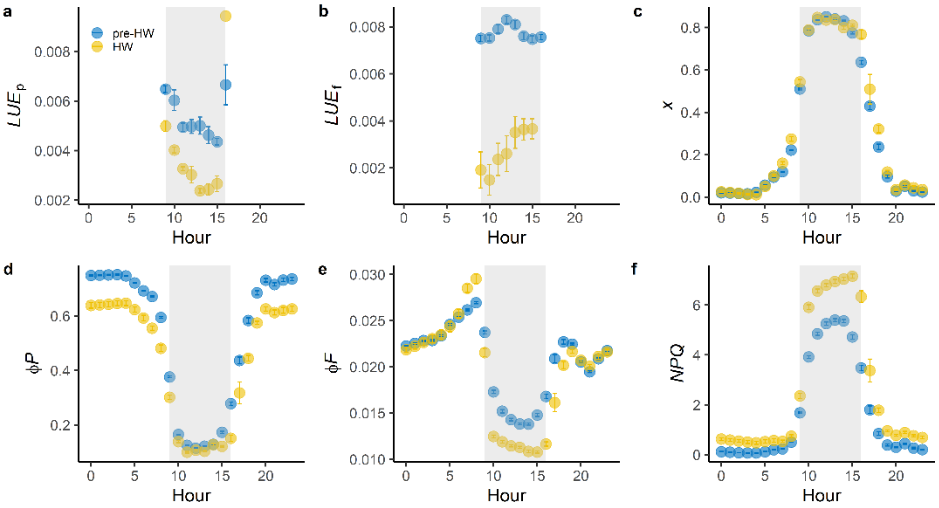

Supplementary Fig. S3.4. Mean daily cycles for (a) light use efficiency of photosynthesis (*LUE*$_p$), (b) light use efficiency of *SIF* emission (*LUE*$_f$), (c) relative light saturation of photosynthesis (*x*), (d) yield of photochemistry (Φ*P*), (e) yield of fluorescence (Φ*F*) and (f) nonphotochemical quenching (*NPQ*). Blue points correspond to the pre-heatwave (pre-HW) period and yellow points correspond to the heatwave (HW) period. Error bars correspond to 1 standard error. The shaded gray bar highlights the hours (UTC + 0) between 9 and 16.

Supplementary Table S3.2. Spearman's rank correlation coefficient (R) and p value between compared variables. Gross primary production from day time partitioning (GPP_{DT}) is obtained according to Lasslop *et al.* (2010) and GPP from night time partitioning (GPP_{NT}) is obtained according to Reichstein *et al.* (2005). HW refers to the heatwave period and pre-HW refers to the days before the HW.

Compared variables (Y - X)	Period	R	p value
*GPP*DT - *SIF*tot	HW	-0.36	0.0342
*GPP*DT - *SIF*tot	pre-HW	0.522	< 0.01
*GPP*NT - *SIF*tot	HW	0.075	0.672
*GPP*NT - *SIF*tot	pre-HW	0.314	0.0176

Supplementary Table S3.3. Spearman's rank correlation coefficient (R) and p value between compared variables. Slope and intercept are obtained with total least square regression. Gross primary production from day time partitioning (GPP_{DT}) is obtained according to Lasslop *et al.* (2010) and GPP from night time partitioning (GPP_{NT}) is obtained according to Reichstein *et al.* (2005).

Compared variables (Y - X)	R	Slope	Intercept	p value
*GPP*DT - *VPD*	-0.928	-0.0549	5.45	< 0.01
*GPP*NT - *VPD*	-0.766	-0.0546	6.28	< 0.01

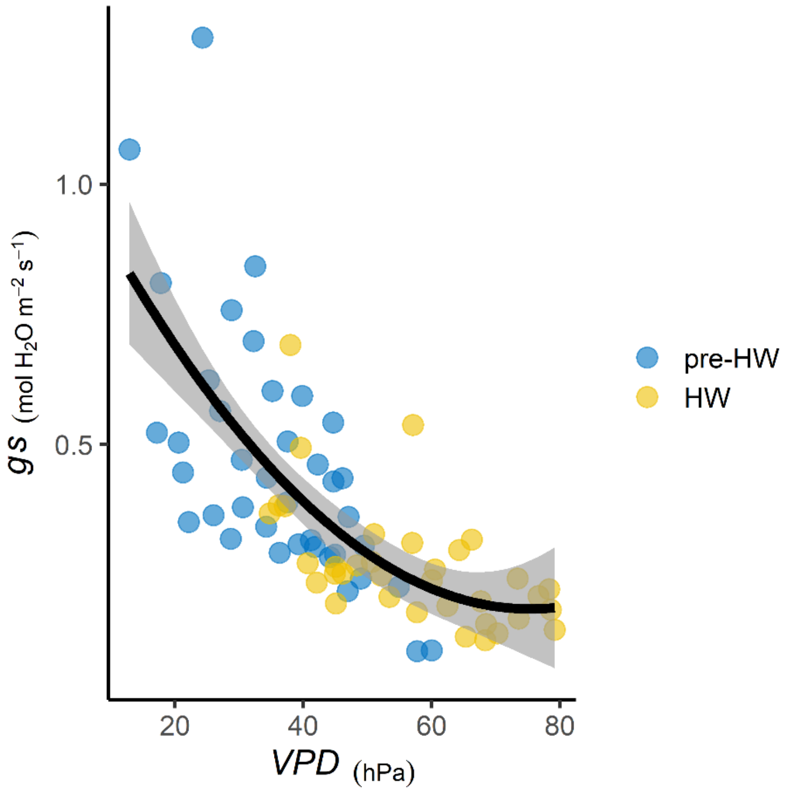

Supplementary Fig. S3.5. Scatterplot between surface conductance (*gs*) and vapor pressure deficit (*VPD*). Blue points correspond to the pre-heatwave (pre-HW) period and yellow points correspond to the heatwave (HW) period. Hourly mean values are computed from 9 to 16 UTC. The black line is the overall fit from a second degree polynomial. The shaded area represents the 95% confidence interval of the fit.

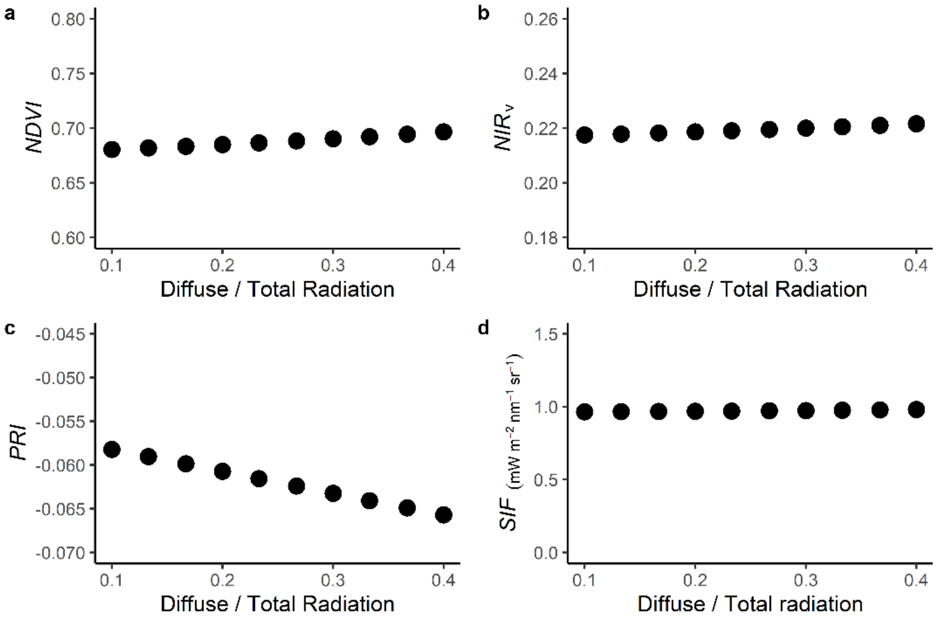

Supplementary Fig. S3.6: Simulations with the Soil Canopy Observation, Photochemistry and Energy fluxes (SCOPE) model on the effect of diffuse to total radiation on normalized difference vegetation index (*NDVI*) in (a), near-infrared reflectance of vegetation (NIR_V) in (b), photochemical reflectance index (*PRI*) in (c) and sun-induced fluorescence at 760 nm (*SIF*) in (d). The range of diffuse to global radiation is consistent with what was observed at the Majadas de Tiétar site during the 2018 heatwave (HW). Simulations were performed with an air temperature (T_{air}) of 43°C.

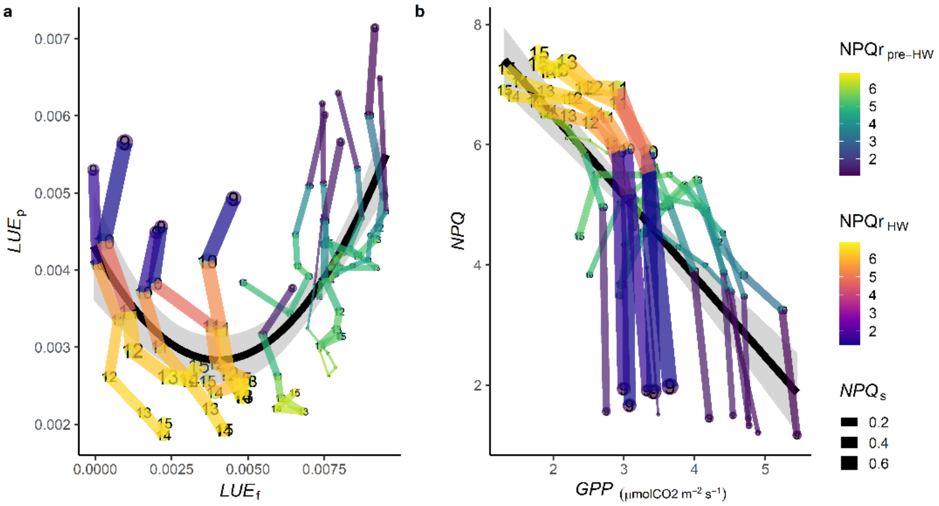

Supplementary Fig. S3.7. (a) Scatterplot between light use efficiency of photosynthesis (*LUE*$_p$) and light use efficiency of *SIF* emission (*LUE*$_f$). (b) Scatterplot between nonphotochemical quenching (*NPQ*) and gross primary production (*GPP*). The days before the heatwave (pre-HW) and the days during the heatwave (HW) are differentiated by different color gradients. Paths connect consecutive observation in a given day. The color of the points and paths refers to the reversible component of the nonphotochemical quenching (*NPQ*$_r$). The size of the paths is proportional to the sustained component of the nonphotochemical quenching (*NPQ*$_s$). The hour (UTC) of the observations is also displayed. Hourly mean values are computed from 9 to 16 UTC. The black line is the overall fit from a second degree polynomial in (a) and a linear regression in (b). The shaded area represents the 95% confidence interval of the fit.

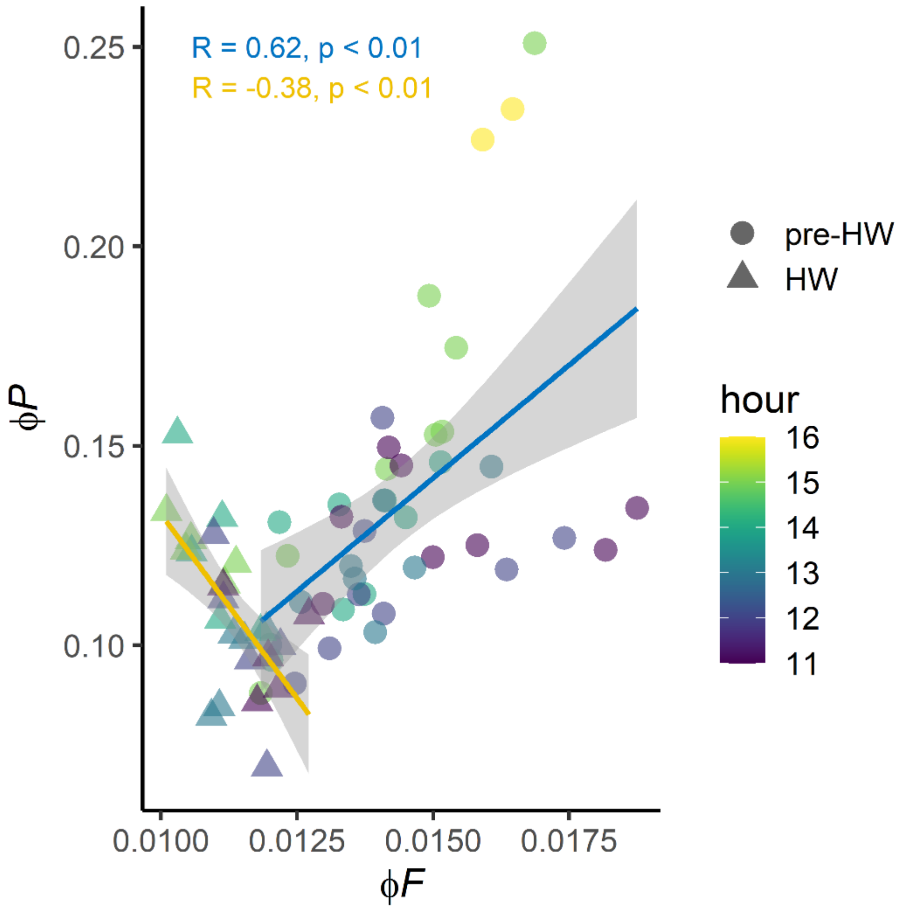

Supplementary Fig. S3.8. Relationship between yield of photochemistry (φ*P*) and yield of fluorescence (φ*F*) for the pre-heatwave (pre-HW) period (circles) and for the heatwave (HW) period (triangles) between 11 to 16 UTC. Points are colored by the hour of the day (UTC). Linear regressions for the HW (yellow line) and pre-HW (blue line) is displayed. Spearman's rank correlation coefficient (R) and p value are reported for the pre-HW and HW period. The shaded area represents the 95% confidence interval of the fit.

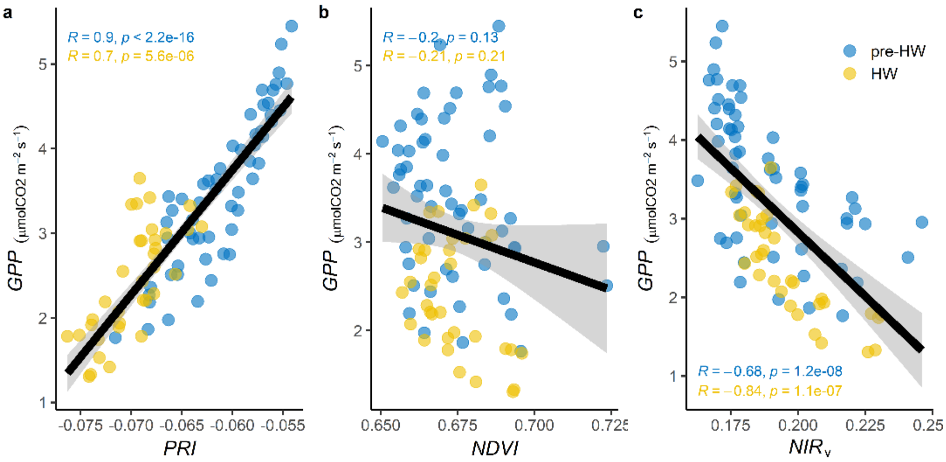

Supplementary Fig. S3.9. (a) Scatterplot between gross primary production (*GPP)* and photochemical reflectance index (*PRI*). (b) Scatterplot between *GPP* and normalized vegetation index (*NDVI*). (c) Scatterplot between *GPP* and near-infrared reflectance of vegetation (*NIR*$_V$). Blue points correspond to the pre-heatwave (pre-HW) period and yellow points correspond to the heatwave (HW) period. Hourly mean values are computed from 9 to 16 UTC. In each panel the Spearman's rank correlation coefficient (R) and p value are reported for the pre-HW and HW period. The black line is the overall fit from a linear regression. The shaded area represents the 95% confidence interval of the fit.

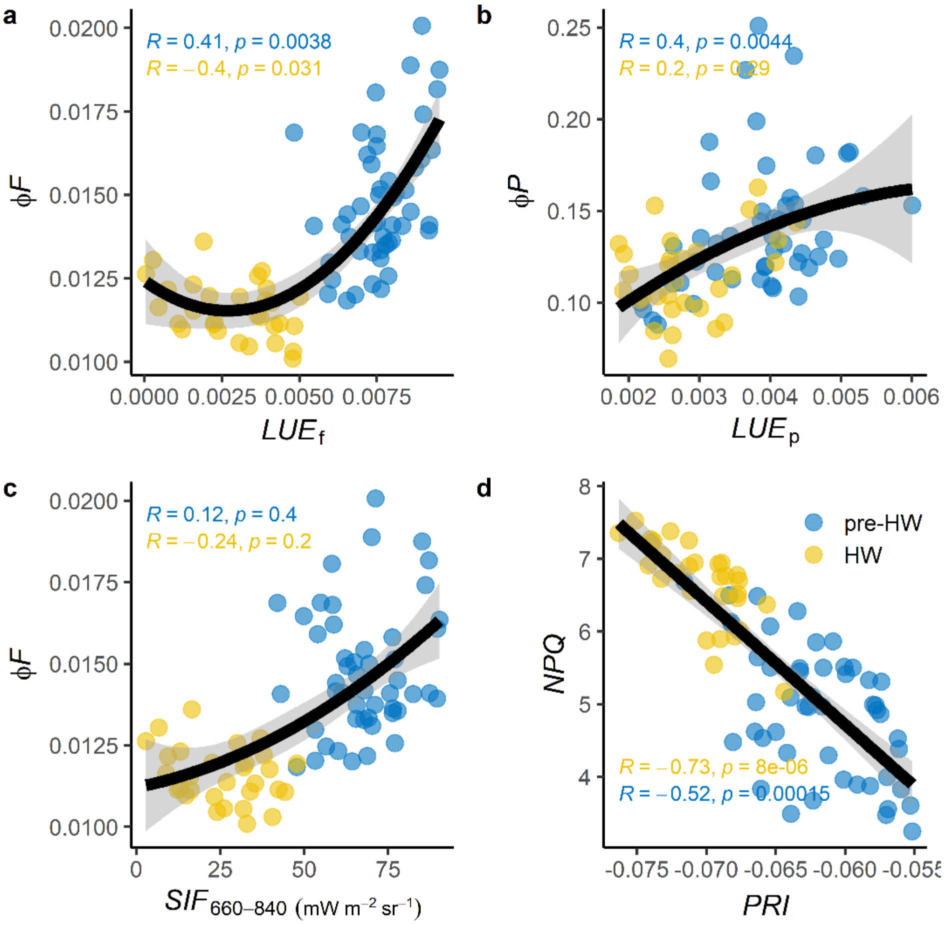

Supplementary Fig. S3.10. (a) Scatterplot between yield of fluorescence (Φ*F*) and light use efficiency of *SIF* emission (*LUE*$_f$). (b) Scatterplot between yield of photochemistry (Φ*P*) and light use efficiency of photosynthesis (*LUE*$_p$). (c) Scatterplot between Φ*F* and sun-induced fluorescence integrated between 660 and 840 nm (*SIF*$_{660\text{-}840}$). (d) Scatterplot between nonphotochemical quenching (*NPQ*) and the photochemical reflectance index (*PRI*). Blue points correspond to the pre-heatwave (pre-HW) period and yellow points correspond to the heatwave (HW) period. Hourly mean values are computed from 10 to 16 UTC. In each panel the Spearman's rank correlation coefficient (R) and p value are reported for the pre-HW and HW period. The black line is the overall fit from a second degree polynomial in (a) and a linear regression in (b,c,d). The shaded area represents the 95% confidence interval of the fit.

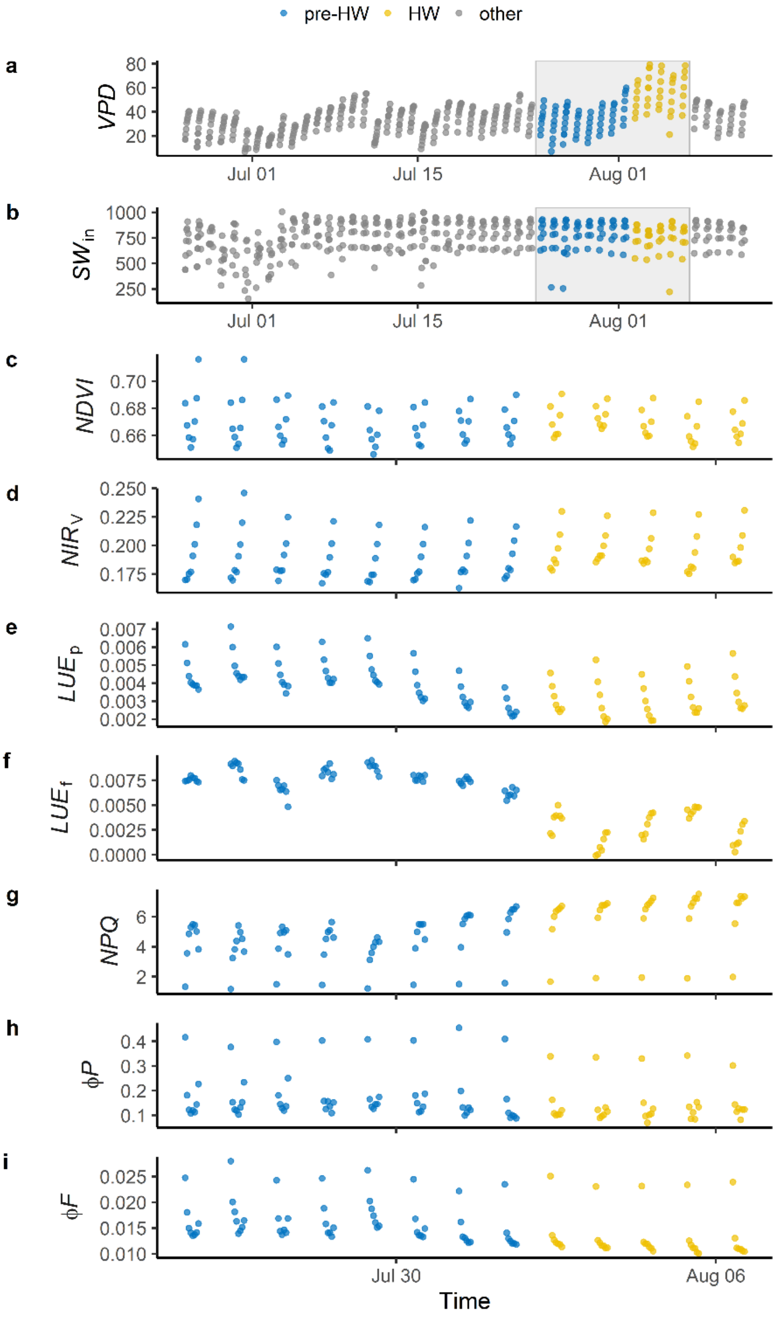

Supplementary Fig. S3.11. Hourly means of (a) vapor pressure deficit (*VPD*), (b) shortwave incoming radiation (SW_{in}), (c) normalized difference vegetation index (*NDVI*), (d) near-infrared reflectance of vegetation (NIR_V)

(e) light use efficiency of photosynthesis (LUE_{p}), (f) light use efficiency of SIF emission ($LUEf_{\mathrm{f}}$), (g) nonphotochemical quenching (NPQ), (h) yield of photochemistry (ΦP) and (i) yield of fluorescence (ΦF).

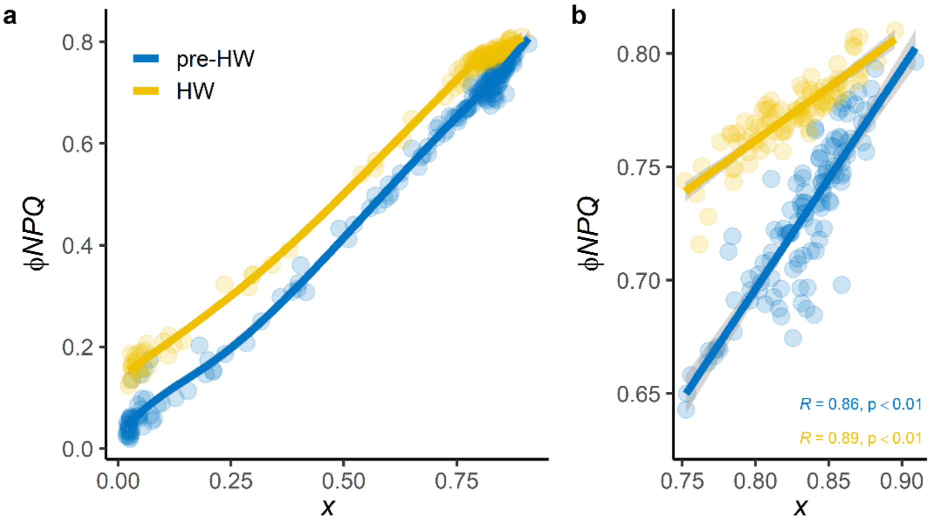

Supplementary Fig. S3.12. (a,b) Scatterplot between yield of nonphotochemical quenching (Φ*NPQ*) and relative light saturation of photosynthesis (*x*). Blue points correspond to the pre-heatwave (pre-HW) period and yellow points correspond to the heatwave (HW) period. Hourly mean values with *x* > 0.75 are shown in (B). In (a) the lines are a local polynomial regression. In (b) the lines represent linear regression and the Spearman's rank correlation coefficient (R) and *p* value are reported for the pre-HW and HW period. The shaded area represents the 95% confidence interval of the fit.

4 Active and passive fluorescence measurements to interpret the interlink between remote sensing and transpiration

ABSTRACT

Plant Transpiration (*T*), the water flux mediated by plant's stomata, plays a pivotal role in the global water cycle and land-surface energy balance and represents a large fraction of evapotranspiration (*ET*), which contains also soil evaporation. Sun-Induced fluorescence (*SIF*), especially in far-red region (F_{760}) has been proposed as a new remote sensing (RS) tool to estimate the latent heat flux related to plant's transpiration (*LEt)* at ecosystem scale. The rationale used to justify *SIF* as a predictor of *LEt* is that stomatal opening is mediating both the photosynthetic and transpiration processes and *SIF* contains information on photosynthetic activity. Although *SIF* has been used to a) predict *LEt*, b) surface conductance (*gs*) and c) water use efficiency (*WUE)*, the mechanistic relationship between *SIF* and *LEt*, *gs* and *WUE* is not clear and it is an active topic of research. Our objectives are twofold: 1) Establishing a framework for RS based (especially through *SIF*) predictions of *LEt* and 2) understanding the mechanism behind this relationship. For the latter point we used not only *SIF*, but also pulse amplitude modulation (PAM) which provides additional information about the electron transport rate (*ETR*), nonphotochemical quenching (*NPQ)* and normalized steady state fluorescence (*Fs/Fo*) which are required to understand the physiological regulation of *LEt* and how it may be reflected at canopy scale on *SIF*.

With a random forest approach, in which RS based and PAM derived predictors are included, we compare *LEt* predictions performed with three methods:

a) Fully empirical approach; direct prediction of *LEt*.
b) A semi-mechanistic hybrid modeling approach in which predictions of canopy conductance (*gc*) are used to reconstruct *LEt* through the Penman-Monteith approach.
c) An efficiency based approach in which predictions of underlying water use efficiency (*uWUE*) are then applied to re-calculate *LEt*.

We find that total F_{760} ($F_{760,\mathrm{tot}}$) has a stronger correlation with *T* than *GPP* across sites, as both $\mathrm{F}_{760,\mathrm{tot}}$ and *LEt* are driven to larger extent by *APAR* than *GPP*. Additionally, we find approach (a) and (b) to have similar predictive power across sites. Finally, the WUE approach had the lowest performance out of the three. In order to better understand the mechanistic relationship between *SIF* and *LEt* we highlight the importance of separating periods in which photosynthesis is stomatal or non-stomatically (i.e. carboxylation) limited from periods of low or no stress. Overall, we find that during periods of photosynthetic limitations *LEt* is mostly predicted by *NPQ* and *SIF*, whereas during periods of no stress we found *LEt* to be more energy driven and therefore more strongly predicted by *APAR* or surface temperature.

4.2 Introduction

Plant Transpiration (*T*), the water flux mediated by plant's stomata, plays a pivotal role in the global water cycle and land-surface energy balance and represents a large fraction of evapotranspiration (*ET*), which contains also evaporation of water from vegetation surfaces and soil evaporation (Jasechko *et al.*, 2013). Plants transpire in order to lower leaf temperature through evaporative cooling, to access nutrients from the soil, to uptake water necessary to the metabolism and to uptake carbon dioxide (CO_2), as the stomata allow for water vapor loss and CO_2 uptake (Farquhar *et al.*, 1980; Sterling, 2005). As stomata mediate both vegetation's water and carbon fluxes, the processes of photosynthesis and transpiration are closely linked and the ratio of the latter and the former can be defined as water use efficiency (*WUE*) (Bonan *et al.*, 2014). *T* and *ET* can also be expressed in terms of energy flux as latent heat flux of transpiration (*LEt*) and latent heat flux of evapotranspiration (*LE*), respectively, which is the notation used in this chapter. *LE* is limited by soil moisture and driven by meteorological variables such as air temperature (T_{air}), surface temperature (T_{surf}), vapor pressure deficit (*VPD*) and solar radiation. Hydro-meteorological models, such as the Penman–Monteith (PM) approach (Beven, 1979), therefore approximate *LE* from T_{air}, wind speed, relative humidity, solar radiation and aerodynamic resistance, by estimating the evaporative demand by the atmosphere. The inversion of the PM equation can allow the calculation of the surface conductance (*gs*) e.g., the conductance of the surface (canopy and soil) to *LE*. By instead inverting the PM equation using *LEt* instead of *LE* it is possible to obtain the canopy conductance (*gc*) e.g., the conductance of the canopy to *LEt*.

LEt estimates at ecosystem scale can be obtained with various methods which include partitioning eddy covariance derived water fluxes (Nelson *et al.*, 2018; Perez-Priego *et al.*, 2018), isotope mass budget measurements (Gibson & Edwards, 2002), and remote sensing (RS) estimates. RS estimates of *LEt* are often based on estimation of the evaporative cooling effect and use remotely sensed surface temperature and meteorological data to constrain transpiration with two-sources energy balance approaches e.g. (Burchard-Levine *et al.*, 2020). Sun-Induced fluorescence (*SIF*), especially in far-red region (F_{760}) has been proposed as a new RS tool to estimate *LEt* at ecosystem scale (Lu *et al.*, 2018; Damm *et al.*, 2021). *SIF* is the radiation emitted by chlorophyll containing plants upon sun's exposure and it is generally considered a good proxy of gross primary production (*GPP*) (Porcar-Castell *et al.*, 2014). Importantly, the relationship between *GPP* and *SIF* is not universal, and it is highly influenced by nonphotochemcal quenching (*NPQ*) (Martini et al. 2021), which represents the third major pathway of allocation of absorbed photosynthetic active radiation (*APAR*), besides photosynthesis and fluorescence emission. The rationale used to justify *SIF* as a predictor of *LEt* is that stomatal opening is mediating both the photosynthetic and transpiration processes and *SIF* contains information on photosynthetic activity (Maes *et al.*, 2020). Although *SIF* has been used to a) predict *LEt* (Lu *et al.*, 2018), b) *gs* (Shan *et al.*, 2019) and c) *WUE* (Pagán *et al.*, 2019), the mechanistic relationship between *SIF* and *LEt*, *gs* and *WUE* is not clear (Damm *et al.*, 2021) and it is an active topic of research.

Our objectives are twofold: 1) develop a framework for RS based (especially through *SIF*) predictions of *LEt* using site-level data, and 2) understanding the mechanism behind this relationship using jointly passive proximal sensing and active fluorescence measurements. For the latter point we make use of *SIF* based and pulse amplitude modulation (PAM) based metrics such as the electron transport rate (*ETR*), *NPQ* and normalized steady state fluorescence (*Fs/Fo*) (Flexas & Medrano, 2002) which are crucial to understand the physiological regulation of *LEt* and how it may be reflected at canopy scale on *SIF*. We propose hypotheses related to mechanistic processes behind each of the approaches used in the literature to predict *LEt* from *SIF* and we test them in two different sites: first a temperate beech forest, and second a Mediterranean Savannah.

a) *LEt-SIF*; predicting *LEt* directly from *SIF* has proven successful at coarse temporal and spatial scales (Maes *et al.*, 2020). Spatially integrated retrievals of *SIF* every 16 days generally correlate well with *APAR*, as the changes in light use efficiency of fluorescence emission (LUE_f) are smoothed out. *We therefore hypothesize that* F_{760}*, which generally correlates well with APAR, might be able to predict T well especially in ecosystems in which T is strongly energy driven.*

b) stomatal conductance-*SIF*; *SIF* may be used to predict *gs* (Shan *et al.*, 2021) or *gc*. As *gc* does not contain information on soil evaporation, and is physiologically controlled by plants, we expect a stronger relationship between *SIF* and *gc* than *SIF* and *gs*. Stomatal conductance is influenced by solar radiation, T_{surf}, *VPD* (Katul *et al.*, 2009) and hormones produced at the root level in response to soil drying, such as abscisic acid (*ABA*) (Omasa & Takayama, 2003). Many parameters obtained from PAM fluorimetry have been found to correlate with *gc*. Among these are *ETR*, *NPQ*, and normalized steady-state chlorophyll fluorescence (*Fs/Fo*) (Flexas *et al.*, 2002). In particular, PAM related parameters can predict *gc* well only when stomatal limitations to photosynthesis or metabolic limitations to photosynthesis (non-stomatal) are present (Medrano *et al.*, 2002). According to Medrano *et al.* (2002) the value of *gc* can give insights into the level of photosynthesis limitation. In particular, $gc > 0.4$ mol H_2O m^{-2} s^{-1} corresponds to periods of no stress. In the *gc* range between 0.4-0.15 mol H_2O m^{-2} s^{-1} (correspondent to mild-water stress) there are reductions in photosynthesis, but not in photorespiration. As the photorespiration process is also powered by electron transport (Flexas & Medrano, 2002), during water stress the reduction in *ETR* is comparably less than in photosynthesis. Metabolic limitations become more important at *gc* values lower than 0.15 mol H_2O m^{-2} s^{-1}, especially if the stomata closure is also caused by high solar irradiance. The feedback mechanism from stress-induced stomata closure to metabolic limitation is mostly mediated by low internal CO_2 concentration (*Ci*). Low *Ci* and the consequent relatively higher photorespiration increase transthylakoid pH, which in turn leads to increased *NPQ* and decreased fluorescence emission. *We therefore expect that gc might be explained by* T_{surf} *and PAM derived parameters (such as Fs/Fo, ETR and NPQ)*.

c) *WUE-SIF*; Multiple works claim that *SIF* can predict several metrics of WUE including Transpiration efficiency (ratio of *T* and potential evaporation), Intrinsic WUE (WUE_i), inherent WUE (*IWUE*) and underlying WUE (u*WUE*) (Lu, X *et al.*, 2018; Pagán *et al.*, 2019). In this work we investigate the *SIF*-u*WUE* relationship as the u*WUE* metric is more related to physiological regulation of carbon uptake and water loss at sub-daily scale than other metrics (Zhou *et al.*, 2014). As u*WUE* takes into account *VPD* driven changes in ratio of internal CO_2 concentration to atmospheric CO_2 concentration (*Ci/Ca)*, which in turn can impact *ETR*, *NPQ* and fluorescence emission (LUE_f) *we expect uWUE to be explained by ETR, NPQ, LUEf and* T_{surf}. This hypothesis is rather speculative, because not many works have linked canopy *uWUE* to *ETR* or *NPQ* and the link between *SIF* and *uWUE* has been so far analyzed empirically, without proposing a solid mechanistic basis for the found correlation (Lu, X *et al.*, 2018).

We believe that the inclusion of 2 different sites with distinct climatic conditions will allow us to test these hypotheses in a robust way, as we want to avoid to draw site-specific conclusions, but rather we are interested in understanding the SIF-*LEt* dynamics that emerge across sites.

4.3 Materials and methods

Study sites

The study was conducted in two sites referred to as Majadas and Leinefelde. The Majadas site is a Mediterranean open woodland, a typical "*Iberian Dehesa*" in western Spain (39°56´024.68´´ N, 5°45´50.27´´ W; Majadas de Tiétar, Cáceres, Extremadura, FLUXNET site ES-LMa). The ecosystem is composed by an herbaceous layer and scattered evergreen broadleaved trees, mainly *Quercus ilex L. subsp. ballota* [Desf.] Samp. (Holm Oak). Trees fractional cover is ~20 %, while the average horizontal and vertical crown radius is 4.2 m (σ = 0.9 m) and 2.7 m (σ = 0.9 m), respectively (Pacheco-Labrador *et al.*, 2019b).

The climate is Mediterranean, characterized by a hot and dry summer. The annual precipitation value is about 650 mm (falling mostly from autumn to spring), and mean annual temperature is 16 °C.

The study was conducted over the period June 2018 to August 2018, when the herbaceous layer is dry (Luo *et al.*, 2018b; Luo *et al.*, 2020) and the trees are the only active vegetation. From August 2 to August 6, 2018, the ecosystem experienced a heatwave (Barriopedro *et al.*, 2020) with a 5 day average of daily maximum air temperature (T_{air}) of 43.2 °C and daily maximum vapor pressure deficit (*VPD*) of 76.1 hPa**.** Extensive site details are available in earlier publications (El-Madany *et al.*, 2018). The days considered part of the heatwave are the 5 days from the 02-08-2018 to 06-08-2018 according to (Sousa *et al.*, 2019). The days considered pre-heatwave are the days from the 25-07-2018 to 01-08-2018.

The Leinefelde site is a 130 year-old even-aged, pure Beech (*Fagus sylvatica*) stand, bordered by other even-aged Beech stands. It sits at an altitude of 450 m, with an annual air temperature of 8°C for and an annual precipitation of 750 mm. It is managed as a shelterwood system for maximum wood production and has been thinned regularly every 10–20 years (Anthoni *et al.*, 2004). The soil is characterised by a slightly thick loess cover, associated with a dominance of Luvisols. The maximum annual effective leaf area index as measured with an LAI-2000 plant canopy analyser (LI-COR Inc., Lincoln, NE, USA) was on average 4.2. The stand density is 224 m^2, and the wood biomass (above and belowground is 237 t C ha^{-1}). The maximum canopy height was about 35 m.

Sun-induced fluorescence observations

At both sites the spectral measurements were collected using the FloX (JB Hyperspectral Devices, Düsseldorf, Germany), a field spectrometer designed for continuous high-resolution spectral measurements for *SIF* retrieval with technical specifications in terms of spectral coverage, resolution and signal to noise ratio (SNR) coherent with the FLEX mission instrument specifications (Julitta *et al.*, 2017). The FloX is equipped with two spectrometers: (i) QEPro (Ocean Optics, Largo FL, USA) with high spectral resolution (Full width at half maximum ~0.3 nm) in the fluorescence emission range 650 nm–800 nm; (ii) FLAME S (Ocean Optics, Largo FL, USA) covering the full range of Visible-Near Infrared (Full width at half maximum ~1.7 nm). The spectrometer entrance-slit is split to two optical fibers that lead to a cosine receptor measuring the downwelling radiance and a bare fiber measuring the canopy upwelling radiance. The spectrometers are housed in a thermally regulated box, keeping the internal temperature constant at 20 °C in order to avoid dark current drift and spectral shifts related to temperature changes. The thermoelectric cooler (TEC) of the QEPro is set to 20 °C to control the back thinned CCD detector SNR (nominal SNR > 1000:1). The spectrometer integration time is optimized for each channel (down- and up-looking channels) at the beginning of each automatic measurement cycle and two associated dark spectra are systematically recorded.

The FloX system at the Majadas site was installed on a 10 m tall optical observation tower located in the vicinity of the eddy covariance (EC) tower. An upward facing fiber cable equipped with a cosine diffuser measured the down-welling irradiance, the up-welling radiance was measured with a bare fiber (25° FOV) pointing roughly North at a Holm Oak crown at about 2 m distance from the tower at a zenith angle of ca. 10°. The FloX system in the Leinefelde site was installed at the height of 43 m on the eddy covariance tower (8 m from the top of the vegetation). The upwelling radiance was measured by bare fibers installed on an arm at about 2m horizontal distance from the tower, pointing south at a zenith angle of about 10° at a single crown of Beech. Due to the close nature of the canopy, no contribution from the understory to the upwelling radiance measured by the FloX is considered. The down-welling radiance was measured with a cosine diffuser.

From the measured spectra we retrieved *SIF* in the red (O_2-B band, 687 nm) and far-red (O_2-A band, 760 nm) regions, referred to as F_{687} and F_{760} respectively, using both the improved Fraunhofer Line Depth (iFLD) and the spectral fitting method (SFM) (Meroni *et al.*, 2009). F_{760} and F_{687} retrieved with iFLD and SFM are extremely similar**,** and therefore in the article we present only the iFLD, as it is less sensible to noise than other retrieval methods (Cendrero-Mateo *et al.*, 2019). The integrated *SIF* (mW m^{-2} sr^{-1}) ($SIF_{660\text{-}840}$) was calculated as: $SIF_{660\text{-}840} = 39.2435 * F_{687} + 83.6814 * F_{760}$ following Moreno *et al.* (2015). We applied a filter to remove measurements that were taken at high solar zenith angles ($SZA < 50$), which results in retrieval errors and nonlinear response of the cosine optics (Julitta *et al.*, 2016). We computed a series of additional vegetation indices: the normalized difference vegetation index (*NDVI*), the near infrared reflectance of vegetation index (NIR_V) (Badgley *et al.*, 2017) and the photochemical reflectance index (*PRI*) (Gamon *et al.*, 1997), derived from reflectance at 531 nm and 570 nm**.** Spectral measurements were taken at an interval of about 2 min, and then averaged over 1-hour periods.

In order to reduce the effect of canopy structure on the fluorescence signal and to derive a more physiological proxy of fluorescence we calculated the escape probability of F_{760} (*Fesc*) following Zeng *et al.* (2019). The fraction of absorbed photosynthetically active radiation (f_{APAR}) and absorbed *PAR* (*APAR*) were estimated from incoming and reflected radiance following Damm *et al.* (2010), Li and Moreau (1996) and Moreau and Li (1996). Total F_{760}, $F_{760,\text{tot}}$ (F_{760} / *Fesc*), light use efficiency of photosynthesis, LUE_{p} (*GPP* / *APAR*) and light use efficiency of fluorescence emission, $LUE_{\text{f},760}$ (F_{760} / (*APAR* * *Fesc*)) were additionally calculated. *APAR* was estimated in mW m^{-2} nm^{-1} sr^{-1} and was then converted to µmol m^{-2} s^{-1} for the LUE_{p} calculation. All data is presented at hourly scale.

Leaf level active chlorophyll fluorescence and chlorophyll content

Diurnal variation in active chlorophyll fluorescence was measured by means of a MONITORING-PAM Multi-Channel chlorophyll Fluorimeter (MoniPam; Walz, Effeltrich, Germany) composed of a data acquisition unit (MONI-DA) and five emitter-detector units (MONI-head/485). The system was equipped with solar panels as power supply and operated in stand-alone mode. At the Majadas site five MONI-Heads were installed on south-facing branches of a *Q. ilex* tree located within the EC footprint and in close proximity to the tree on which FloX measurements were performed. Branches were accessed using a permanent scaffold, and measurements were performed on leaves flushed in 2018. Active fluorescence signals included instantaneous fluorescence and maximal fluorescence along with incident *PAR* and T_{air}, and were recorded at 10-minute and one-hour frequencies, during day- and nighttime, respectively. For active fluorescence data the hours from 11 to 16 were considered as the leaves measured by the MONI-PAM were shaded before 11 as shown by the high ϕP and low *NPQ* values between 8 and 10 UTC. At the Leinefelde site 5 MONI-heads were placed on a platform attached to the eddy covariance tower at about 30 m. The MONI-head measured active fluorescence from 5 leaves that received direct light for the majority of the day (sunlit leaves). Data were used to derive *NPQ*, the reversible component of *NPQ* (NPQ_{r}), the sustained component of *NPQ* (NPQ_{s}), and the yield of photochemistry (ϕP) according to Porcar-Castell (2011). The yield of fluorescence (ϕF) was calculated as in Porcar-Castell *et al.* (2014). The maximum value at night of quantum yield of photosystem II (ΦP_{max}), corresponding to the widely used Fv/Fm, was calculated according to Porcar-Castell (2011). Relative light saturation of photosynthesis (x) is a scaling factor that describes the degree of photochemical impairment and was calculated following van der Tol *et al.* (2014). The above parameters were obtained for each MONI-head and then averaged across all heads.

A Soil Plant Analysis Development (SPAD) chlorophyll meter was used to estimate leaf chlorophyll status at the Majadas site. SPAD measurements took place on 20/07/2018 and 04/08/2018 and were carried out on the tree measured with the FloX and the tree measured with the MONITORING-PAM. In each tree, two branches were measured (12 leaves per branch), dividing between current year leaves (new leaves) and previous year leaves (old leaves). In Leinefelde a Dualex (Force-A, Orsay, France) was used to infer chlorophyll content of sunlit (at about 30 m height) and shaded leaves (at about 20 m height). Sixty leaves were measured on each field campaign which occurred on the following dates: 2019-07-12, 2019-07-31, 2019-08-14, 2019-09-05, 2019-10-03. On the same dates CO_2 response curves were performed with a LI-6800 Photosynthesis System on sunlit leaves. Maximum carboxylation rate (V_{cmax}) and maximum electron transport rate (J_{max}) were obtained from the CO_2 response curves with the R package "plantecophys".

Biometeorological parameters, and carbon, water, and energy fluxes measurements

Biometeorological variables and surface-atmosphere gas exchange were measured at the Majadas site in the period June 2018 to July 2018. During this period the herbaceous layer is completely dry. Therefore, the fluxes measured are representative only of the tree functioning (Perez-Priego *et al.*, 2017). An EC system consisted of a three-dimensional sonic anemometer (R3-50, Gill LTD, Lymington, UK) and an infrared gas analyzer (LI-7200, Licor Bioscience, Lincoln, USA) was used to measure dry mixing ratios of CO_2 and H_2O at a height of 15.5 m above ground. Shortwave incoming radiation (Rg, W m^{-2}) was measured with a ventilated net radiometer (CNR4, Kipp and Zonen, Delft, Netherlands). Air temperature (T_{air}, °C) and relative humidity (rH, %) were measured with a combined Pt-100 temperature and capacitive humidity sensor (CPK1-5, MELA Sensortechnik, Germany).

The eddy covariance measurements at the Leinefelde site were carried out at 44 m above the ground. The measurement system consisted of a three-dimensional sonic anemometer (Solent R3, Gill Instruments Ltd., Lymington, UK) and a closed-path CO_2/H_2O infrared gas analyzer (LI-6262, LI-COR Inc., Lincoln, NE, USA) placed at the bottom of the instrument tower and connected to the gas inlet close to the anemometer by a 50 m long tube (Knohl *et al.*, 2003). Data were synchronized and stored on a field computer using the ''EddySoft'' data acquisition software by O. Kolle (Max-Planck-Institute for Biogeochemistry, Jena, Germany). The turbulent fluxes were recalculated in 2013 with version 4.1 of the ''EddyPro'' software (LI-COR Inc., Lincoln, NE, USA).

Fluxes were computed using EddyPro version 6.2.0 (Fratini & Mauder, 2014) as described in El-Madany *et al.* (2018). Quality check of the fluxes was accomplished according to Mauder and Foken (2011). The storage flux was computed using a vertical profile of CO_2 according to Falge *et al.* (2001). The u*-threshold (~0.13 m s^{-1}) was estimated according to Papale *et al.* (2006). The measured net ecosystem exchange (*NEE*) was partitioned into gross primary production (*GPP*) using both the nighttime partitioning (Reichstein *et al.*, 2005) and daytime partitioning (Lasslop *et al.*, 2010) methods as implemented in the REddyProc 0.7-1 R package (Wutzler *et al.*, 2018). In the main text only the *GPP* from the daytime partitioning technique is reported. For the analysis we retained only data coming from measured *NEE* data without any gap filling. The EC and biometeorological data were averaged at hourly temporal resolution in order to smooth the effect of the random error on the measurements (Damm *et al.*, 2010) and to match the temporal aggregation of the FLoX measurements.

SCOPE modelling

Simulations of carbon and water fluxes, *SIF* and PAM related parameters were performed with the SCOPE (Soil Canopy Observation, Photochemistry and Energy fluxes) model at both the Majadas and Leinefelde site (van der Tol *et al.*, 2014). SCOPE is a vertical (1-D) integrated radiative transfer and energy balance model. Forward simulations were carried out at both the Majadas and Leinefelde site by providing time series of chlorophyll a+b content (*cab*), atmospheric vapor pressure (*ea*), V_{cmax}, J_{max}, short and long wave incoming radiation (SW_{in} and LW_{in} respectively), leaf area index (*LAI*), atmospheric pressure (*Pres*), air temperature (T_{air}), horizontal wind speed (*u*) and solar zenith angle. At both the Leinefelde and Majadas sites *ea*, SW_{in}, LW_{in}, *Pres*, T_{air} and *u* were measured as described above and averaged at hourly scale. At the Majadas site *cab* was estimated from SPAD data, using a regression model calibrated at the site found to strongly correlate ($R^2 = 0.91$) with chlorophyll a+b obtained in the laboratory (Gonzalez-Cascon *et al.*, 2017). V_{cmax} and J_{max} were obtained by performing CO_2 response curves on the 2018-07-20 with the LI-6800 Photosynthesis System and kept fixed at 31.5 and 51.9 μmol m^{-2} s^{-1} respectively. At the Leinefelde site the *cab* and V_{cmax} time series was obtained by fitting the values measured at the 5 campaigns (described above) with a local regression. For each site 2 simulations were carried out. One with the default Kn-x parametrization (rate constant of nonphotochemical quenching to relative light saturation of photosynthesis) (van der Tol *et al.*, 2014), and another one with a site specific Kn-x relationship parametrized at each site.

Transpiration, conductance and uWUE

LEt was obtained by partitioning total *LE* with the TEA algorithm (Nelson *et al.*, 2018). *gc* was obtained by inverting the Penman-Monteith equation by using *LEt* instead of *LE*, therefore obtaining a measure of canopy conductance which is not influenced by soil evaporation. Aerodynamic resistance was removed before the calculation of *gc* using Thom et al., (1972) implemented in the bigleaf R package (Knauer et al., 2018). *gs* was obtained by inverting the Penman-Monteith equation using *LE*. *uWUE* was obtained as specified in Zhou *et al.* (2014) (Equation 4.1).

$$uWUE = \frac{GPP \times \sqrt{VPD}}{T} \tag{4.1}$$

LEt_{gc} was obtained by applying the Penman-Monteith approach using the predicted *gc*, whereas LEt_{gs} was obtained by applying the Penman-Monteith approach using the predicted gs. Finally, LEt_{uWUE} was obtained by inverting the *uWUE* calculation using the predicted *uWUE*. Internal leaf CO_2 concentration was obtained by inverting the Fick's law (Lommen *et al.*, 1975). In the calculation of *LEt*, *gs*, *gc* and *uWUE* all rainy days, as well 2 days following the rain events were removed. Following Medrano *et al.* (2002), we define photosynthesis to be metabolically limited when $gc < 0.05$ mol H_20 m^{-2} s^{-1}. Stomatal and metabolic limitations to photosynthesis correspond to $gc < 0.15$ mol H_20 m^{-2} s^{-1} and $gc > 0.05$ mol H_20 m^{-2} s^{-1}. Mild stress is defined as *gc* > 0.15 mol H_20 m^{-2} s^{-1} and *gc* < 0.4 mol H_20 m^{-2} s^{-1}. Finally values of *gc* > 0.4 mol H_20 m^{-2} s^{-1} are considered as periods of no stress.

Statistical analysis

We use a Random Forest model to predict hourly *LEt*, *gc*, *gs*, and *uWUE*. We used two sets of predictors: remote sensing only (RS) and RS + variables derived from PAM. RS predictors include $F_{760,\mathrm{tot}}$, *APAR*, LUE_{f}, T_{surf} and F_{687}. PAM predictors include *ETR*, *Fs/Fo* and *NPQ*. These variables were selected to test the hypotheses described in the introduction. The predictive performance of the models was tested using a 10-fold cross-validation. The random forest was parametrized with 1000 trees, and the number of predictors randomly sampled at each tree (mytry) and the minimum number of data points in a node (min_n) were tuned according to the data within 10-fold cross validation framework. Variable importance of the predictors (VIP) was established by means of permutation random forest feature importance (Li *et al.*, 2016). Importance values were scaled between 0 and 100. Note that the sum of the variables selected in permutation random forest feature importance is always higher than 100. The variable importance allows for ranking the most important predictors use in the regression analysis. Partial dependance plots (pdp) (Cutler *et al.*, 2007) were performed for each random forest model. A pdp allows to visualize the marginal contribution (yhat) of each predictor to the outcome of the machine learning model and were computer using the DALEXtra R package (Maksymiuk *et al.*, 2020).

4.4 Results

$F_{760,\mathrm{tot}}$ presented a similar correlation with *GPP* in the Majadas site (R = 0.53, $p < 0.01$) and in the Leinefelde site (R = 0.55, $p < 0.01$) (Fig. 4.1). Instead red SIF (F_{687}) performed better at the Leinefelde site (R = 0.75, $p < 0.01$), than at the Majadas site (R = 0.38, $p < 0.01$). The slopes of the linear regressions are very different for the two different sites, with Leinefelde showing higher slope compared to the Majadas sites, where measurements were collected during the dry period. The relationship between *SIF* and *LE* was more similar among sites than the relationship with *GPP*, but $F_{760,\mathrm{tot}}$ showed higher total correlation (R = 0.68, $p < 0.01$) than F_{687} (R = 0.57, $p < 0.01$) (Fig. 4.1). Finally, *LEt* presented a higher correlation than *LE* or *GPP* with $F_{760,\mathrm{tot}}$ (R = 0.71, $p < 0.01$), and with F_{687} (R = 0.59, $p < 0.01$) (Fig. 4.1). Overall $F_{760,\mathrm{tot}}$ showed to be better correlated with water fluxes (*LE*, *T*) than with gross carbon fluxes (*GPP*), especially at the Leinefelde site, which is characterized by higher variation in *APAR* and *LAI*. F_{687} is instead better correlated to GPP than $F_{760,\mathrm{tot}}$.

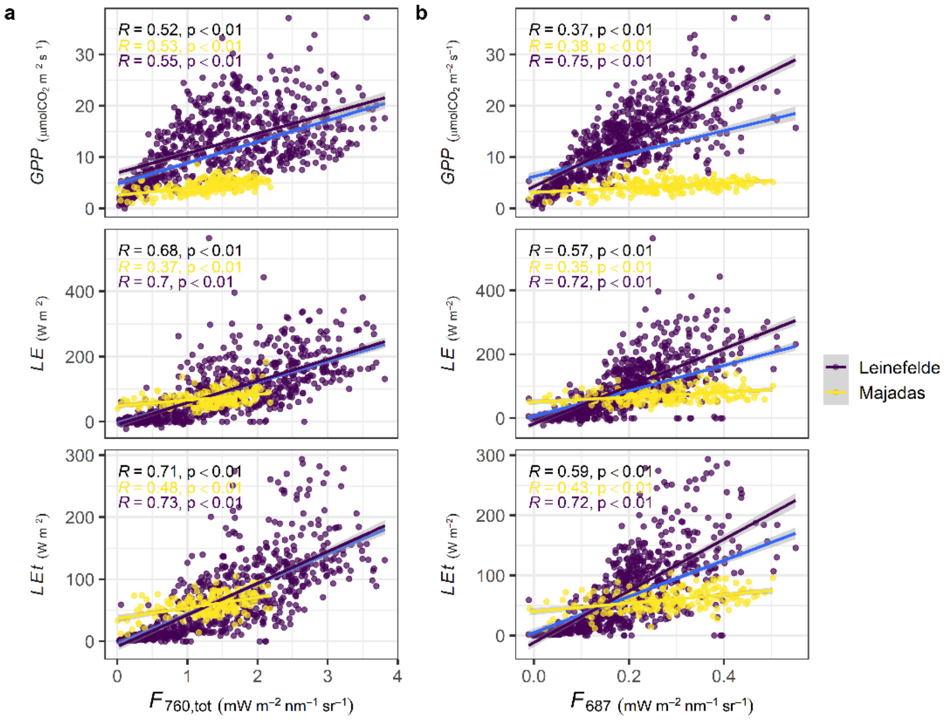

Fig. 4.1. (a) Scatterplot between fluorescence emission at 760 nm ($F_{760,tot}$) (F_{760} / $Fesc$) and gross primary production (GPP), latent heat flux (LE) and laten heat flux of transpiration (LEt). (b) Scatterplot between fluorescence at 687 nm (F_{687}) and GPP, LE and LEt. Violet points are from the Leinefelde site and yellow points are from the Majadas site. In each panel the Spearman's rank correlation coefficient (R) and p value are reported for the Majadas site, Leinefelde site and for the total dataset (in black). The blue line is the overall fit from a linear model. The shaded area represents the 95% confidence interval of the fit.

The relationship between SIF in the A and B band as simulated by SCOPE ($F_{760\ SCOPE}$ and $F_{687\ SCOPE}$ respectively) and the simulated GPP (GPP_{SCOPE}) (Supplementary Fig. S4.10) was quite different among the two sites; in the Leinefelde site the GPP-SIF relationship was very strong (R = 0.91, $p < 0.01$ and R = 0.92, $p < 0.01$ for the GPP_{SCOPE}-$F_{760\ SCOPE}$ and for GPP_{SCOPE}-$F_{687\ SCOPE}$ respectively) (Fig. 4.2a,b). On the contrary, Majadas reported non-significant relationship for both GPP_{SCOPE}-$F_{760\ SCOPE}$ and for GPP_{SCOPE}-$F_{687\ SCOPE}$ ($p = 0.55$ and $p = 0.24$ respectively). The relationship between the latent heat flux from SCOPE (LE_{SCOPE}) and SIF was quite comparable among sites for both $F_{760\ SCOPE}$ (R= 0.78, $p < 0.01$ and R = 0.79, $p < 0.01$ for Majadas and Leinefelde respectively) and for $F_{687\ SCOPE}$ (R= 0.83, $p < 0.01$ and R = 0.76, $p < 0.01$ for Majadas and Leinefelde respectively). Finally, the LEt-SIF

relationship was comparable with *LE-SIF* for Leinefelde (R= 0.8, $p < 0.01$ and R = 0.78, $p < 0.01$ for LEt_{SCOPE}-$F_{760\ \mathrm{SCOPE}}$ and LEt_{SCOPE}-$F_{687\ \mathrm{SCOPE}}$ respectively), but not for Majadas, that showed weaker relationships between *LEt-SIF* than in *LE-SIF* (R= 0.24, $p < 0.01$ and R = 0.15, $p < 0.01$ for LEt_{SCOPE}-$F_{760\ \mathrm{SCOPE}}$ and LEt_{SCOPE}-$F_{687\ \mathrm{SCOPE}}$ respectively) (Fig. 4.2a,b).
In summary, according to SCOPE simulations, in the Leinefelde site the *GPP-SIF* (irrespectively of wavelength) was the one that exhibited the higher correlation, followed by *LEt-SIF* and *LE-SIF*. Instead, in Majadas the *GPP-SIF* relationship was surprisingly not significant, and the *LE-SIF* had the higher correlation coefficient, followed by *LEt-SIF*.

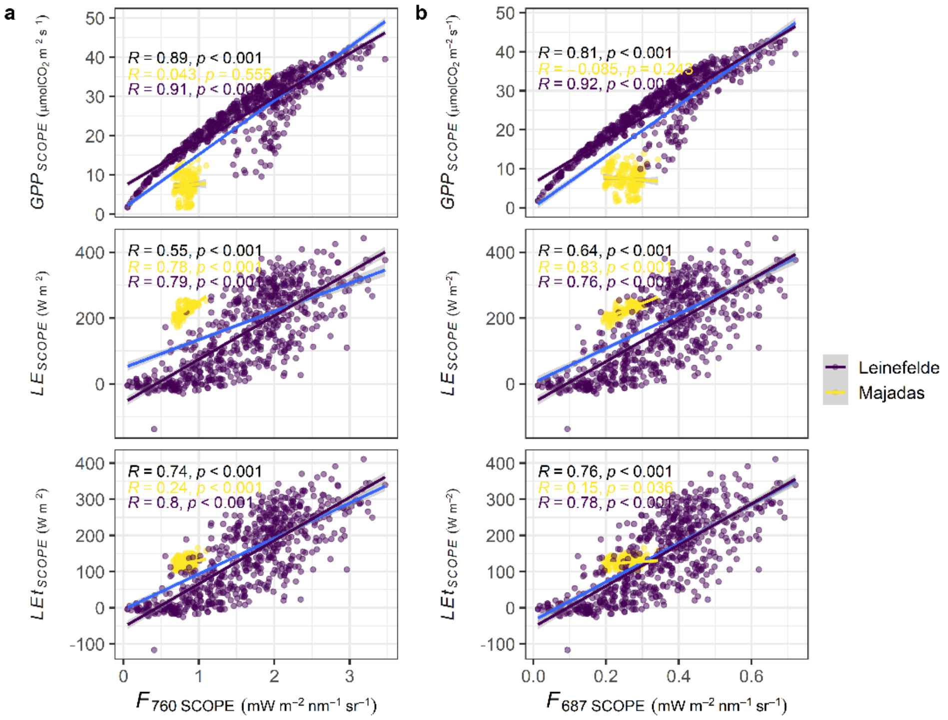

Fig. 4.2. (a) Scatterplot between sun-induced fluorescence at 760 nm as simulated from the SCOPE model ($F_{760\ \mathrm{SCOPE}}$) and gross primary production from SCOPE (GPP_{SCOPE}), latent heat flux from SCOPE (LE_{SCOPE}) and latent heat flux of transpiration from SCOPE (LEt_{SCOPE}). (b) Scatterplot between fluorescence at 687 nm from SCOPE ($F_{687\ \mathrm{SCOPE}}$) and GPP_{SCOPE}, LE_{SCOPE} and LEt_{SCOPE}. Violet points are from the Leinefelde site and yellow points are from the Majadas site. In each panel the Spearman's rank correlation coefficient (R) and p value are reported for the Majadas site, Leinefelde site and for the total dataset (in black). The blue line is the overall fit from a linear model. The shaded area represents the 95% confidence interval of the fit.

Fig. 4.3a shows that $APAR_{\mathrm{SCOPE}}$ and $F_{760\ \mathrm{SCOPE}}$ track LEt_{SCOPE} (R = 0.73, $p < 0.01$ and R = 0.71, $p < 0.01$ respectively) better than GPP_{SCOPE} (R = 0.51, $p < 0.01$). A similar result is observed with the measured data, with $F_{760,\mathrm{tot}}$ and *APAR* showing a stronger correlation with *LEt* (R = 0.71, $p < 0.01$ and R = 0.63, $p < 0.01$ respectively) than *GPP* (R = 0.48, $p < 0.01$) (Fig. 4.3b).

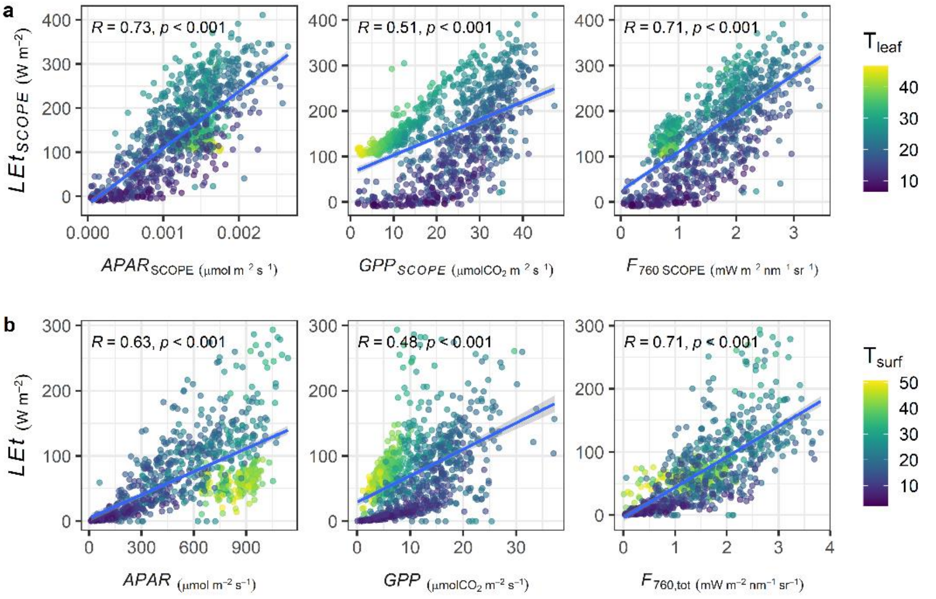

Fig. 4.3. (a) scatterplot between the latent heat flux of transpiration as modelled by SCOPE LEt_{SCOPE} and the absorbed photosynthetic active radiation from SCOPE ($APAR_{\mathrm{SCOPE}}$), gross primary production from SCOPE (GPP_{SCOPE}) and sun-induced fluorescence at 760 nm from SCOPE ($F_{760\ \mathrm{SCOPE}}$). (b) scatterplot between the latent heat flux of transpiration (*LEt*) and the absorbed photosynthetic active radiation (*APAR*), the gross primary production (*GPP*), and the total sun-induced fluorescence at 760 nm ($F_{760,\mathrm{tot}}$). For each panel the correlation coefficient (R) and the p value of the linear regression are reported. Both the Majadas site and the Leinefelde site are considered together. Points are colored by leaf temperature as modelled by SCOPE (T_{leaf}) in (a) and radiometric surface temperature (T_{surf}) in (b).

The relationship between *ETR* measured by PAM and F_{760} was positive, but quite different among sites, with much higher correlation in the Leinefelde site (R = 0.7, $p < 0.01$), than in the Majadas site (R = 0.37, $p < 0.01$) (Fig. 4.4). In contrast, a much higher correlation was observed between *ETR* and *APAR* (R = 0.88, $p < 0.01$). *LEt* and *ETR* showed quite divergent relationship among sites (Fig. 4.4); if in the Leinfelde site the relationship was positive and significant (R = 0.76, $p < 0.01$), the Majadas site presented a non-significant relationship (R = 0.16, p = *0.21*), suggesting how the *LEt* flux is likely much more energy driven in the deciduous Beech forest (Leinfelde), rather than in a Mediterranean Savannah (Majadas) where are more driven by water availability. Finally *ETR* and *NPQ* presented a linear relationship at both sites, but positive in Leinefelde (R = 0.77, $p < 0.01$) and negative at Majadas (R = -0.62, $p < 0.01$). Overall, the highly non-linear relationship suggests that at high levels of stress, such as those experienced in the Majadas site, *ETR* starts to decrease and *NPQ* becomes the more prominent dissipation pathway.

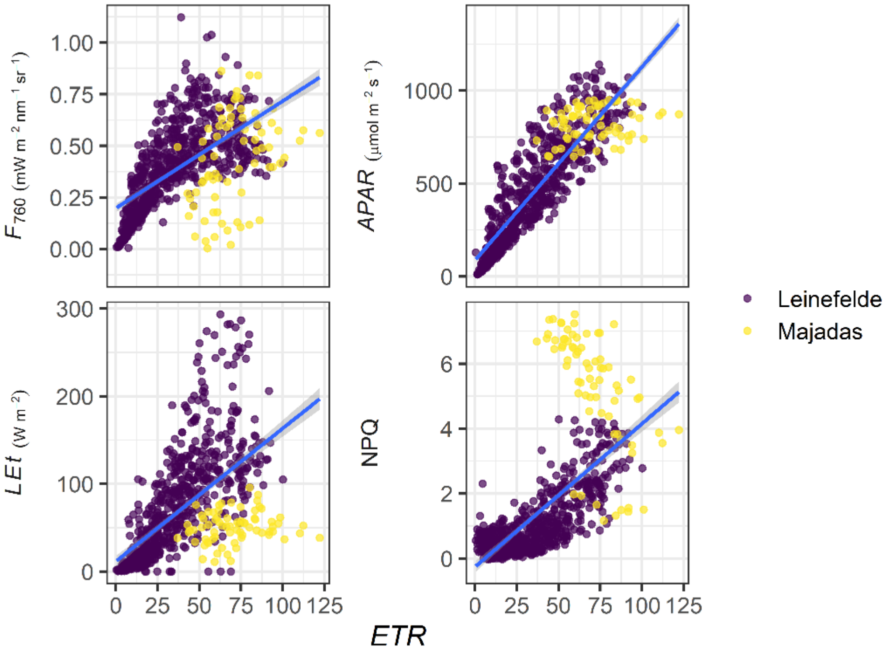

Fig. 4.4. (a) Scatterplot between fluorescence at 760 nm (F_{760}) and electron transport rate (ETR). (b) scatterplot between absorbed photosynthetic active radiation (*APAR*) and *ETR*. (c) scatterplot between the latent heat flux of transpiration (*LEt*) and *ETR*. (d) scatterplot between nonphotochemical quenching (*NPQ*) and *ETR*. Violet points are from the Leinefelde site and yellow points are from the Majadas site. In each panel the Spearman's rank correlation coefficient (R) and p value are reported for the total dataset (in black). The blue line is the overall fit from a linear model. The shaded area represents the 95% confidence interval of the fit.

The relationship between the simulated electron transport rate (Ja_{SCOPE}) and $F_{760\ \text{SCOPE}}$ was significant only in the Leinefelde site (R = 0.95, $p < 0.01$), while not-significant in the Majadas site ($p = 0.06$) (Supplementary Fig. S 4.9a). The absorbed photosynthetic active radiation from chlorophyll molecules as simulated by SCOPE ($APAR_{\text{cab SCOPE}}$), which is frequently well correlated with F_{760}, had in Leinefelde a strong and positive relationship with Ja_{SCOPE} (R = 0.88, $p < 0.01$), but a negative relationship in Majadas (R = -0.27, $p < 0.01$) (Supplementary Fig. S 4.9). The LEt_{SCOPE}-Ja_{SCOPE} relationship had a similar correlation among sites (R= 0.81, $p < 0.01$ for Majadas and R = 0.75, $p < 0.01$ for Leinefelde), but significant different slopes and intercepts ($p < 0.01$ in both cases) (Supplementary Fig. S 4.9c). Finally, similarly to the measured data in (Fig. 4.4d), the simulated NPQ (NPQ_{SCOPE}) showed a negative relationship with Ja_{SCOPE} in Majadas (R = -0.47, $p < 0.01$), but a positive relationship in Leinefelde (R = 0.72, $p < 0.01$) (Supplementary Fig. S 4.9d).

The most important variables from the VIP when predicting T resulted to be $F_{760,\mathrm{tot}}$ (VIP = 100), *APAR* (VIP = 84 for RS and VIP = 79 for RS + PAM) and *ETR* (VIP = 66.4) (Fig. 4.5a). When considering only a limited range of *gc* that corresponds to significant metabolic limitation to photosynthesis, the most important predictors changed, with T_{surf}, *APAR* and *NPQ* being selected as the three most important (Supplementary Fig. S4.3). In terms of predictions (Table 1), using all the variables (RS + PAM) did not result in a large increase in R^2 (R^2 = 0.79 for RS + PAM and R^2 = 0.77 for RS) or normalized root mean square (NRMSE) (NRMSE = 0.31 for RS + PAM and NRMSE = 0.37 for RS) (Fig. 4.5b,c) (Fig. 4.14a,b).

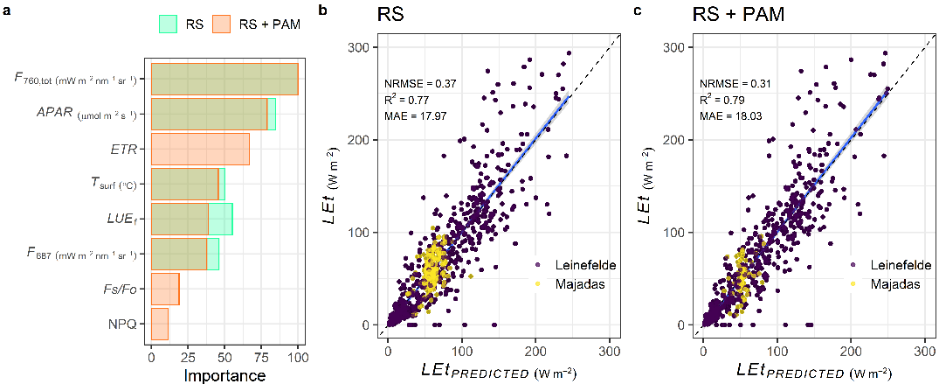

Fig. 4.5. (a) Permutation random forest feature importance for the latent heat flux of transpiration (*LEt*), with two sets of predictors; remote sensing only (RS), in light blue, and RS and pulse amplitude modulation data (PAM), in red. RS predictors include $F_{760,\mathrm{tot}}$, *APAR*, LUE_f, F_{760}, T_{surf} and F_{687}. PAM predictors include *ETR*, *Fs/Fo* and *NPQ*. (b) scatterplot between observed *LEt* and *LEt* predicted by random forest with only RS predictors for the Majadas site (in yellow) and Leinefelde site (in violet) together. (c) scatterplot between observed *T* and *T* predicted by random forest with RS and PAM predictors for the Majadas site (in yellow) and Leinefelde site (in violet) together. Normalized root mean square error (NRMSE), coefficient of

determination (R^2) and mean absolute errors (MAE) are calculated through 10-fold cross validation for both (b) and (c).

A partial dependence plot (pdp) of the *LEt* prediction model allows to understand the marginal effect (yhat) of multiple predictors on the predicted outcome of the random forest model (Cutler *et al.*, 2007) (Fig. 4.6). It is for example possible to discern whether the relationship between a predictor and the predicted variable is linear or non-linear. Both *APAR* and F_{760tot} showed a similar marginal contribution (Fig. 4.6a), with *APAR* being overall more marginally important (higher yhat values) in Leinefelde and with F_{760tot} clearly showing higher importance in Majadas. The relationship of the predictors to the predicted outcome of *LEt* is not strictly linear in Majadas, with F_{760tot} showing a saturation around 2 mW m^2 nm^{-1} s^{-1}. LUE_f and *ETR* showed opposite patterns in their contribution, with higher contribution at low values of LUE_f and higher values of *ETR* (Fig. 4.6b). In Majadas the LUE_f clearly contributed more to the overall *T* prediction as shown by the higher yhat values (Fig. 4.6b).

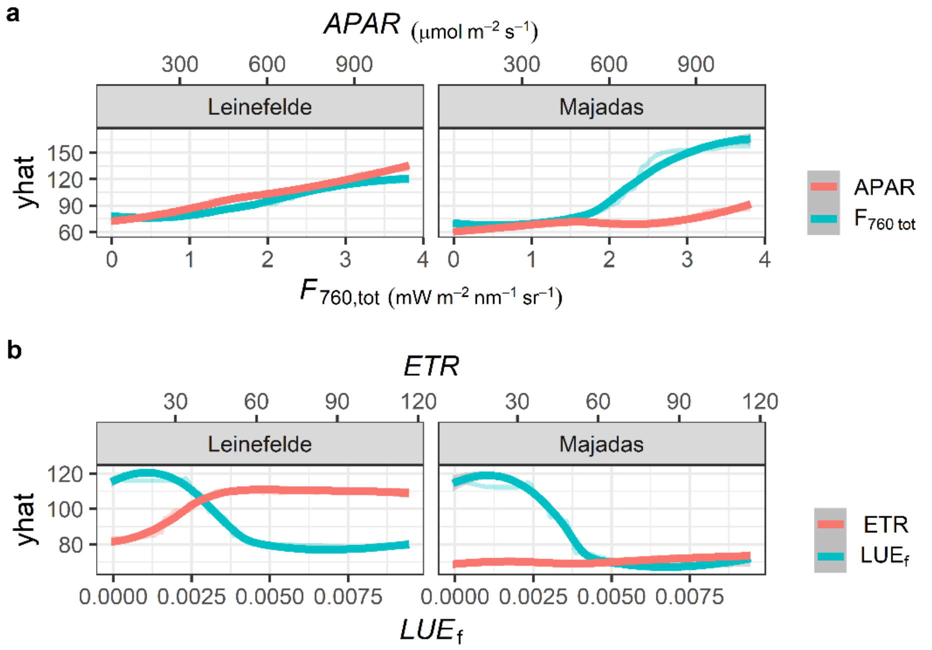

Fig. 4.6. Partial dependence plot (pdp) for the Transpiration (*T*) prediction model. (a) marginal effect (yhat) of fluorescence emission at 760 nm ($F_{760,tot}$) and absorbed photosynthetic active radiation (*APAR*) on the predicted outcome of *T*. (b) marginal effect (yhat) of light use efficiency of fluorescence emission at 760 nm (LUE_f) and electron transport rate (*ETR*) on the predicted outcome of *T*. In both panels the pdp is divided between the Majadas and Leinefelde site.

LE presented a very strong similarity in terms of variable importance in comparison with *LEt*. Indeed, the same predictors were selected with $F_{760,tot}$ (VIP = 100), *APAR* (VIP = 79 for RS; and VIP = 82 for RS + PAM), *ETR* (VIP = 62) and F_{687} (VIP = 53 for RS; and VIP = 67 for RS + PAM) (Fig. 4.7a). Also, the cross-validation metrics were similar to the one obtained from *LEt* (R^2 = 0.74 for RS + PAM; and R^2 = 0.76), although the normalized root mean square error was generally higher for *LE* (NRMSE = 0.36 for RS + PAM; and NRMSE = 0.44 for RS) (Fig. 4.7b,c) (Fig. 4.14c,d).

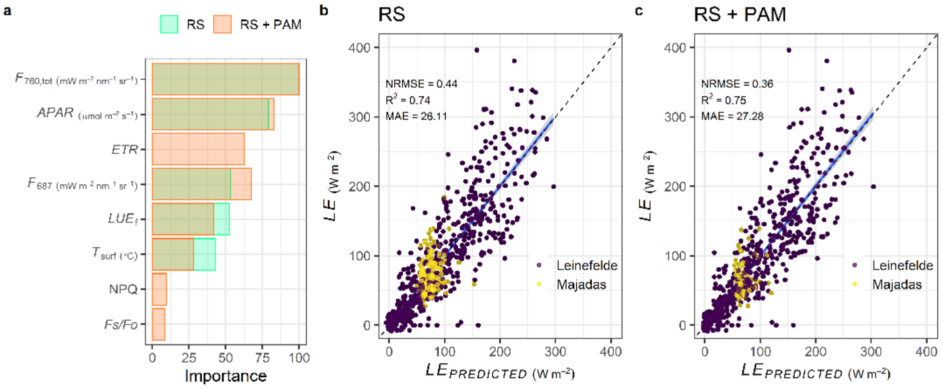

Fig. 4.7. (a) Permutation random forest feature importance for latent heat flux (*LE*), with two sets of predictors; remote sensing only (RS), in light blue, and RS and pulse amplitude modulation data (PAM), in red. RS predictors include $F_{760,tot}$, *APAR*, LUE_f, F_{760}, T_{surf} and F_{687}. PAM predictors include *ETR*, *Fs/Fo* and *NPQ*. (b) scatterplot between observed *LE* and *LE* predicted by random forest with only RS predictors for the Majadas site (in yellow) and Leinefelde site (in violet) together. (c) scatterplot between observed *LE* and *LE* predicted by random forest with RS and PAM predictors for the Majadas site (in yellow) and Leinefelde site (in violet) together. Normalized root mean square error (NRMSE), coefficient of determination (R^2) and mean absolute errors (MAE) are calculated through 10-fold cross validation for both (b) and (c).

The relationship between RS and PAM related variables with *gc* resulted to be highly dependent on the level of photosynthetic limitation (Fig. 4.8). The relationship between *gc* and *APAR* showed a low determination coefficient (R^2 = 0.11, $p < 0.01$) (Fig. 4.8a), whereas T_{surf} presented the best overall determination coefficient (R^2 = 0.61) (Fig. 4.8b), with a pronounced negative relationship during periods of only metabolic limitations and both stomatal and metabolic limitation to photosynthesis. Both passive fluorescence, in particular $F_{760,tot}$, and active fluorescence such as *Fs/Fo* presented a similar relationship with *gc* with both R^2 = 0.25 ($p < 0.01$) (Fig. 4.8c,d). Especially at low values of *gc* both fluorescence metrics had a steeper relationship which then tended to saturate especially for *Fs/Fo*. *ETR* did not show a significant relationship with *gc* (R^2 = 0.01, *p* = 0.63) (Fig. 4.8e). *NPQ* in contrast presented a steep negative relationship with *gc* during periods of stress, and saturation at higher levels of *gc*, with total R^2 = 0.33 (Fig. 4.8f).

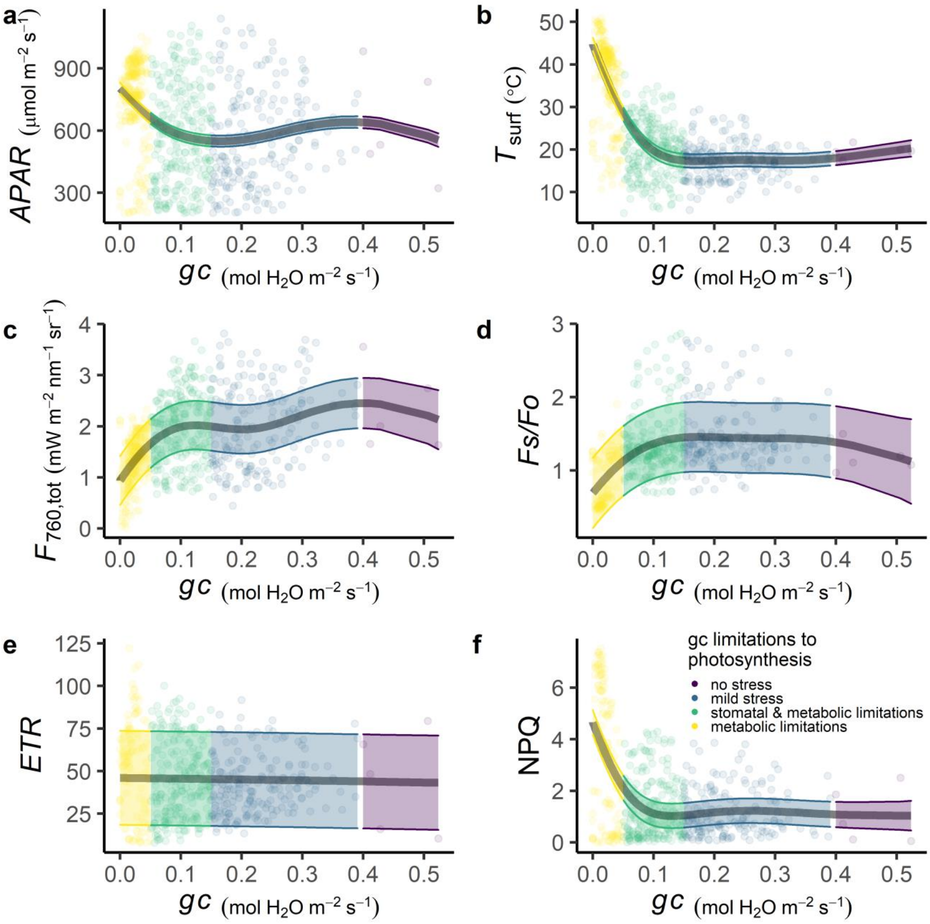

Fig. 4.8. (a) Scatterplot between absorbed photosynthetic active radiation (*APAR*) and canopy conductance (*gc*). (b) Scatterplot between surface temperature (T_{surf}) and *gc*. (c) Scatterplot between total fluorescence at 760 nm ($F_{760,tot}$, F_{760} / *Fesc*) and *gc*. (d) scatterplot between normalized steady state fluorescence (*Fs/Fo*) and *gc*. (e) scatterplot between electron transport rate (*ETR*) and *gc*. (f) scatterplot between nonphotochemical quenching (*NPQ*) and *gc*. Both the Majadas site and Leinefelde site are considered together. Colors represent different photosynthetic limitations; yellow represent metabolic limitations to photosynthesis, green represents stomatal and metabolic limitations to photosynthesis, blue represents mild stress and violet represents period of no stress. Lines are regression from a Gaussian

process model and shaded areas represent 95% confidence interval of the Gaussian process.

Unlike *LEt* or *LE*, variables importance for the *gc* variables showed a clear dominant predictor: T_{surf} was by far the most important predictor of *gc* (VIP = 100 for both RS and RS + PAM) (Fig. 4.9a). The second predictor was F_{687} (VIP = 40.6 for RS and VIP = 45.6 for RS + PAM) and the third was *Fs/Fo* (VIP = 36.6). When plants' photosynthesis is metabolically limited the most important predictors shift to $F_{760,tot}$, T_{surf} and *Fs/Fo* (Supplementary Fig. S4.5). This change in predictors indicates the dynamic natures of *gc*, which appears to be more physiologically controlled during periods of stress. In terms of predictive power (Table 1), reconstructing *LEt* from *gc* through the Penman-Monteith approach yielded very similar results to predicting *LEt* directly. Using only RS predictors resulted in NRMSE = 0.38 and R^2 = 0.76, whereas the RS + PAM approach lead to slightly lower NRMSE (NRMSE = 0.32) and R^2 = 0.79 (Fig. 4.9b,c) (Fig. 4.14e,f).

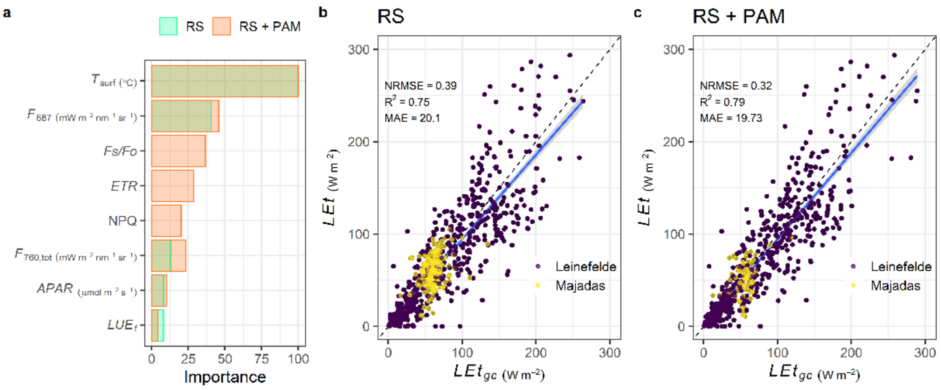

Fig. 4.9. (a) Permutation random forest feature importance for canopy conductance (*gc*), with two sets of predictors; remote sensing only (RS), in light blue, and RS and pulse amplitude modulation data (PAM), in red. RS predictors include $F_{760,tot}$, *APAR*, LUE_f, F_{760}, T_{surf} and F_{687}. PAM predictors include *ETR*, *Fs/Fo* and *NPQ*. (b) scatterplot between observed *LEt* and *LEt* calculated from predicted *gc* through the Penman-Monteith approach (LEt_{gc}). *gc* is predicted by random forest with only RS predictors for the Majadas site (in yellow) and Leinefelde site (in violet) together. (c) scatterplot between observed *LEt* and *LEt* calculated from predicted *gc* through the Penman-Monteith approach. *gc* is predicted by random forest with RS and PAM predictors for the Majadas site (in yellow) and Leinefelde site (in violet) together. Normalized root mean square error (NRMSE), coefficient of determination (R^2) and mean absolute errors (MAE) are calculated through 10-fold cross validation for both (b) and (c).

The pdp of the *gc* prediction model shows a somewhat linear relationship between the predictors F_{687}, T_{surf} and the predicted outcome of *gc* in Leinefelde, where higher values of F_{687} and lower values of T_{surf} had higher marginal contribution to the random-forest model (Fig. 4.10a). In Majadas T_{surf} resulted to be much more important than F_{687} (Fig. 4.10a). *ETR* and *NPQ* in Leinefelde showed a positive relationship (higher values correspond to higher marginal contribution to the prediction), whereas in Majadas *ETR* showed a strongly nonlinear and marginal contribution, with *NPQ*, especially at lower values, being much more important for *gc* prediction (Fig. 4.10b).

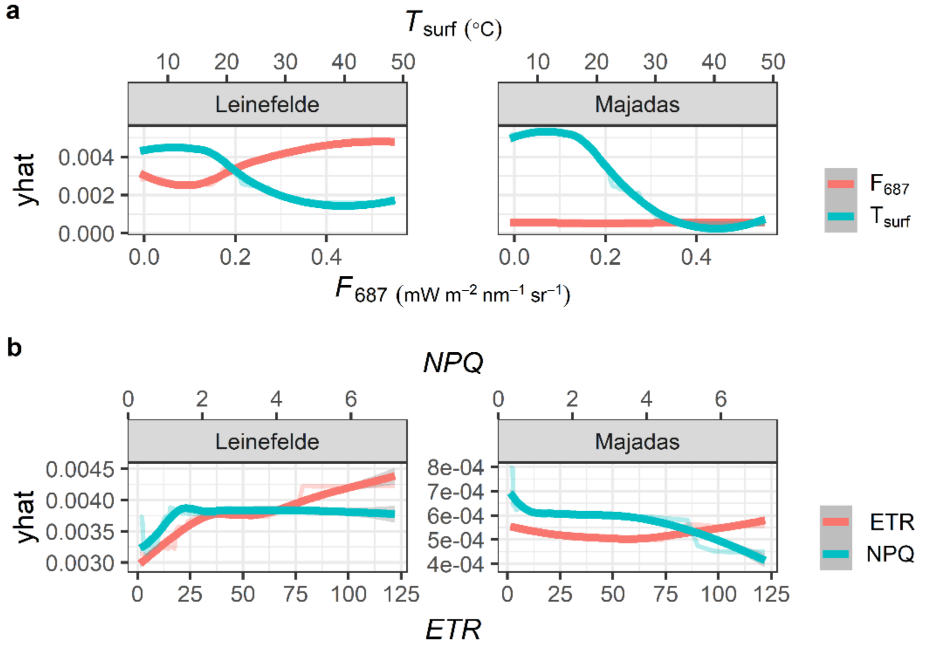

Fig. 4.10. Partial dependence plot (pdp) for the canopy conductance (*gc*) prediction model. (a) marginal effect (yhat) of sun-induced fluorescence at 687 nm (F_{687}) and surface temperature (T_{surf}) on the predicted outcome of *gc*. (b) marginal effect (yhat) of electron transport rate (*ETR*) and nonphotochemical quenching (*NPQ*) on the predicted outcome of *gc*. In both panels the pdp is divided between the Majadas and Leinefelde site.

gs, which was obtained by inverting the Penman-Monteith equation using the total *LE*, instead of the partitioned *LEt*, had as similar sets of predictors selected by the variable importance, but with some key differences. The most important variable was again T_{surf} (VIP = 100 for RS and VIP = 100 for RS + PAM) (Fig. 4.11a). Second was F_{687} (VIP = 65.1 for RS and VIP = 100 for RS + PAM). Finally *ETR* was also selected (VIP = 66). In contrast with *gc*, LE reconstructed from predicted *gs* had a very poor fit with measured *LE*, as shown by NMRSE (NRMSE = 1.02 for RS and NRMSE = 0.89 for RS + PAM) and R^2 ($R^2 = 0.01$ for RS and $R^2 = 0.06$) (Fig. 4.11b,c) (Fig. 4.14g,h). Individual relationship within site are mostly significant (in Leinefelde $R^2 = 0.29$, $p < 0.01$ and $R^2 = 0.28$, $p < 0.01$ for RS and RS + PAM respectively and for Majadas $R^2 = 0.05$, $p < 0.01$ and $p = 0.328$ for RS and RS + PAM respectively), but the overall fit is very poor ($R^2 = 0.01$, $p < 0.01$ and $R^2 = 0.05$, $p < 0.01$ for RS and RS + PAM respectively). This result confirms the importance of partitioning water fluxes when estimating canopy conductance.

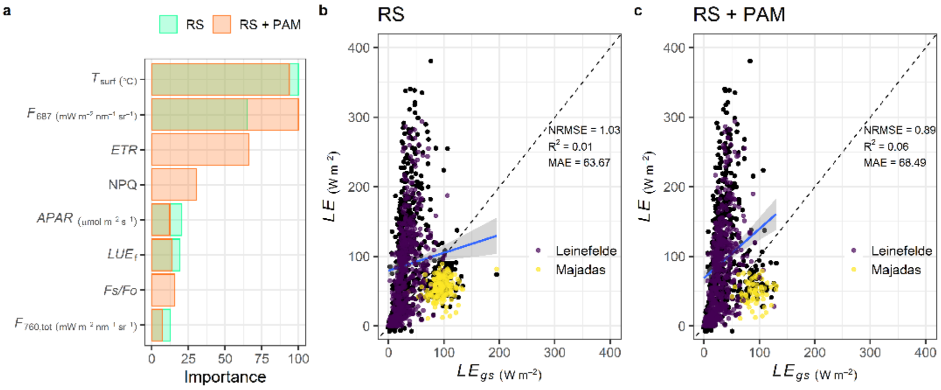

Fig. 4.11. (a) Permutation random forest feature importance for surface conductance (*gs*), with two sets of predictors; remote sensing only (RS), in light blue, and RS and pulse amplitude modulation data (PAM), in red. RS predictors include $F_{760,tot}$, *APAR*, LUE_f, F_{760}, T_{surf} and F_{687}. PAM predictors include *ETR*, *Fs/Fo* and *NPQ*. (b) scatterplot between observed *LE* and *LE* calculated from predicted *gs* through the Penman-Monteith approach. *gs* is predicted by random forest with only RS predictors for the Majadas site (in yellow) and Leinefelde site (in violet) together. (c) scatterplot between observed *LE* and *LE* calculated from predicted *gs* through the Penman-Monteith approach. *gs* is predicted by random forest with RS and PAM predictors for the Majadas site (in yellow) and Leinefelde site (in violet) together. Normalized root mean square error (NRMSE), coefficient of determination (R^2) and mean absolute errors (MAE) are calculated through 10-fold cross validation for both (b) and (c).

uWUE presented 3 different predictors that seemed to contribute to similar extent to the variable importance. *ETR* was the most important predictor of *uWUE* (VIP = 100). *APAR* was the second one (VIP = 100 for RS and VIP = 87.6 for RS + PAM), and third T_{surf} (VIP = 77.8 for RS and VIP = 99.5 for RS + PAM) (Fig. 4.12a). When considering periods of metabolic limitations to photosynthesis we observed a change in the predictors being selected, with $F_{760,tot}$, T_{surf} and *ETR* as the three most important (Supplementary Fig. S4.7). Predicting *uWUE* (Table 1) and using it to reconstruct *LEt* showed to be the worst approach of the three in terms of predictive power. Indeed, *LEt* recalculated from predicted *uWUE* in relation to measured *LEt* showed quite high error (NRMSE = 0.73 for RS and NRMSE = 0.52 for RS + PAM) and large scatter (R^2 = 0.45 for RS and R^2 = 0.59 for RS + PAM), especially at high values of *LEt* (Fig. 4.12b,c) (Fig. 4.14i,l).

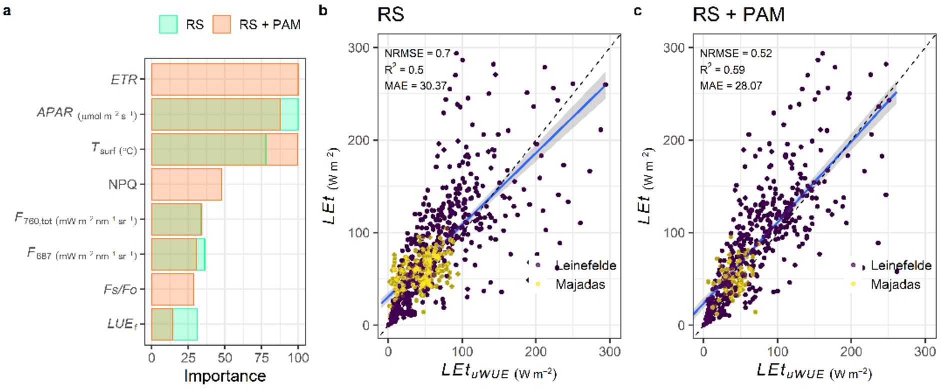

Fig. 4.12. (a) Permutation random forest feature importance for underlying water use efficiency (*uWUE*), with two sets of predictors; remote sensing only (RS), in light blue, and RS and pulse amplitude modulation data (PAM), in red. RS predictors include $F_{760,tot}$, *APAR*, LUE_f, F_{760}, T_{surf} and F_{687}. PAM predictors include *ETR*, *Fs/Fo* and *NPQ*. (b) scatterplot between observed *LEt* and *LEt* calculated from predicted *uWUE*. *uWUE* is predicted by random forest with only RS predictors for the Majadas site (in yellow) and Leinefelde site (in violet) together. (c) scatterplot between observed *LEt* and *LEt* calculated from predicted *uWUE* (LEt_{uWUE}). *uWUE* is predicted by random forest with RS and PAM predictors for the Majadas site (in yellow) and Leinefelde site (in violet) together. Normalized root mean square error (NRMSE), coefficient of determination (R^2) and mean absolute errors (MAE) are calculated through 10-fold cross validation for both (b) and (c).

The pdp for the *uWUE* prediction model shows that lower values of *ETR* and *APAR* contributed more to the predicted outcome of *uWUE* (Fig. 4.13a), unlike in the case of pdp of *LEt* (Fig. 4.6), and *gc* (Fig. 4.10). The *NPQ* and T_{surf} marginal contribution to the prediction of *uWUE* was highly nonlinear, with high values of *NPQ* and T_{surf} ($NPQ > 2$ and $T_{surf} > 25$°C) having very limited contribution to the predicted *uWUE* in both Leinefelde and Majadas (Fig. 4.13a).

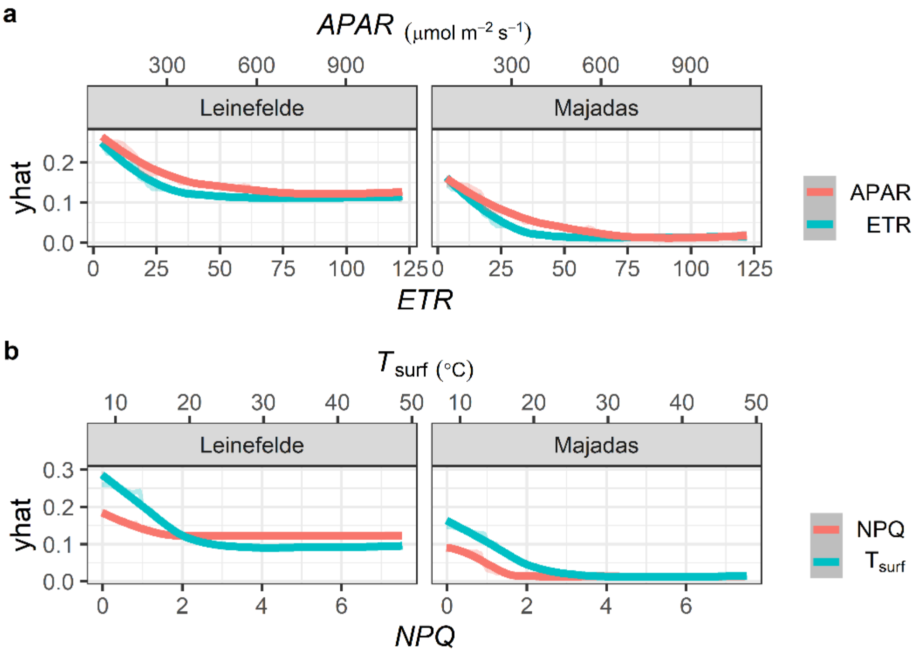

Fig. 4.13. Partial dependence plot (pdp) for the underlying water use efficiency (*uWUE*) prediction model. (a) marginal effect (yhat) of electron transport rate (*ETR*) and absorbed photosynthetic active radiation (*APAR*) on the predicted outcome of *uWUE*. (b) marginal effect (yhat) of nonphotochemical quenching (*NPQ*) and surface temperature (T_{surf}) on the predicted outcome of *uWUE*. In both panels the pdp is divided between the Majadas and Leinefelde site.

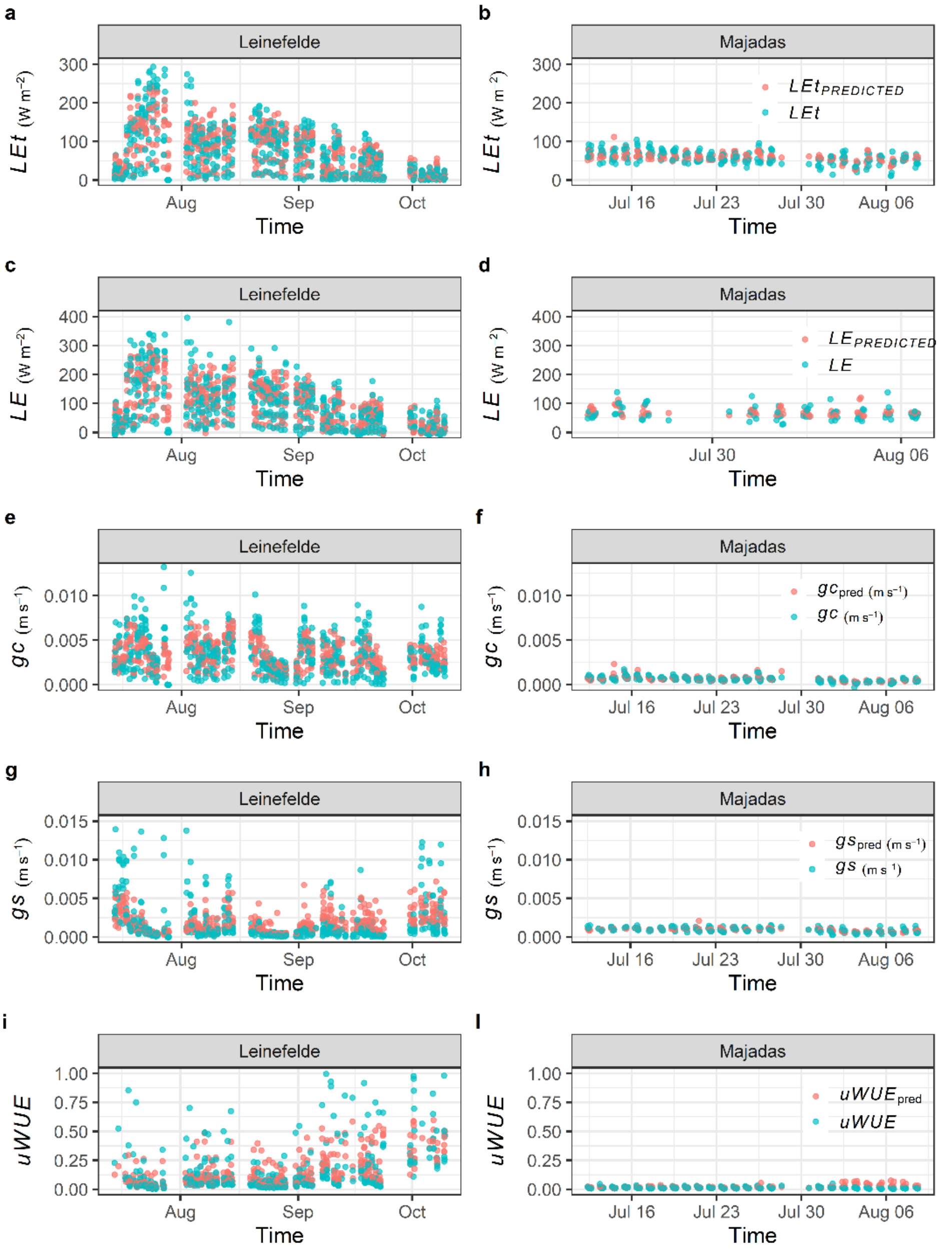

Fig. 4.14. Time series of latent heat flux of transpiration (*LEt*), in blue, and predicted *LEt*, in red, divided for the Leinefelde site (a) and Majadas site (b). Time series of transpiration (*LE*), in blue, and predicted *LE*, in red, divided for the Leinefelde site (c) and Majadas site (d). Time series of canopy conductance (*gc*), in blue, and predicted *gc*, in red, divided for the Leinefelde site (e) and Majadas site (f). Time series of surface conductance (*gs*), in blue,

and predicted *gs*, in red, divided for the Leinefelde site (g) and Majadas site h). Time series of underlying water use efficiency (*uWUE*), in blue, and predicted *uWUE*, in red, divided for the Leinefelde site (e) and Majadas site (f). All predictions are performed though 10-fold cross validation random forest using only remote sensing predictors. Predictions are calculated for the two sites together and not on a separate basis.

Table 1. Metrics for predicted variables (Outcome) from 10-fold cross-validation random forest, using remote sensing (RS) variables and RS and variables derived from pulse amplitude modulation (PAM) at both the Majadas site and Leinefelde site. The predicted variables are latent heat flux of transpiration (*LEt*), latent heat flux (*LE*), canopy conductance (*gc*), surface conductance (*gs*) and underlying water use efficiency (*uWUE*). Metrics include normalized root mean square error (NRMSE), coefficient of determination (R^2), and mean absolute error (MAE).

Outcome	**Predictors**	**NRMSE**	**R^2**	**MAE**
LEt	RS	0.37	0.75	18.89 W m^{-2}
LEt	RS + PAM	0.31	0.77	18.75 W m^{-2}
LE	RS	0.44	0.74	26.11 W m^{-2}
LE	RS + PAM	0.36	0.76	27.30 W m^{-2}
gc	RS	0.38	0.49	0.0011 m s^{-1}
gc	RS + PAM	0.32	0.51	0.0011 m s^{-1}
gs	RS	1.02	0.20	0.0011 m s^{-1}
gs	RS + PAM	0.89	0.32	0.0011 m s^{-1}
uWUE	RS	0.73	0.59	0.06
uWUE	RS + PAM	0.52	0.61	0.07

4.5 Discussion

Although *SIF* has been proposed as a good predictor of *LEt*, either directly or through the ingestion of *SIF* into PM or WUE approaches, not enough is known about the possible mechanistic link between *SIF* and *LEt*, *gc* or *WUE* *(Damm et al., 2021)*. Previous research has suggested that in order to predict *LEt*, *SIF* should be coupled with other Earth observation data to produce robust predictions (Damm *et al.*, 2021). Our study examined the relation of *SIF*, coupled with additional RS predictor such as *APAR* and T_{surf} on *LEt*, *gc* and *uWUE* in a Beech forest and a Mediterranean Savannah. We also include variables obtained at leaf scale with the PAM approach to further improve our understanding of the physiological link between *SIF* and *LEt*.

Passive and active fluorescence as a tool to understand carbon and water dynamics

Although *SIF* has been traditionally linked with *GPP*, in this study we find that $F_{760,\mathrm{tot}}$ predicts *LEt* better than *GPP* across sites (Fig. 4.1), confirming therefore the recent literature that explores the potential of using *SIF* to predict *LEt* (Jonard *et al.*, 2020). A similar result is obtained from SCOPE simulations, with (especially for Majadas) $F_{760\ \mathrm{SCOPE}}$ having very strong relationship with LE_{SCOPE}, and to a lesser extent with LEt_{SCOPE}, and a not significant relationship with GPP_{SCOPE} (Fig. 4.2) demonstrating that the *SIF-LEt* relationship emerges not only from empirical observations, but also from process-based modelling. The reason for this is illustrated in (Fig. 4.3), where both in measured data and in SCOPE simulations the *LEt-APAR* and *LEt*-F_{760} have higher correlation than *LEt-GPP*. Both *LEt* and F_{760} seem to be largely driven by *APAR*, as already reported in previous research (Yang *et al.*, 2018). Instead, *LEt-GPP* is influenced to a larger extent by T_{surf} as well. At high temperatures a decoupling of the *LEt-GPP* seems to occur (Kauwe *et al.*, 2019), caused by a decrease in *WUE*. F_{760}'s inability to properly track *GPP* when *GPP-LEt* decoupling occurs seems to be an asset when using F_{760} to predict *LEt*.

We also find that the choice of wavelength when using *SIF* for *LEt* predictions matters. Indeed, $F_{760,\mathrm{tot}}$ predicts *LEt* better than F_{687}, likely because F_{687} is strongly affected by canopy reabsorption and $F_{760,\mathrm{tot}}$ is quite related to *APAR*, a critical driver of water fluxes. Still we found F_{687} to be the best predictor of *GPP*, especially in the Leinefelde site (Fig. 4.4). Red *SIF* has not been explored enough as a proxy for GPP, as usually far-red *SIF* was preferred, but it seems to effectively track photosynthesis especially in deciduous vegetation types (Liu *et al.*, 2020).

PAM fluorescence has also been used to constrain estimates of water fluxes, more frequently in relation to stomatal conductance (Flexas & Medrano, 2002; Medrano *et al.*, 2002), but recently also at canopy scale by linking *ETR* and *gc* through the use of optimal stomatal theory (Shan *et al.*, 2021). In this work we find *ETR* to be strongly energy driven and to have an excellent relationship with *APAR* across sites (Fig. 4.4). In contrast, the F_{760}-*ETR* presents a strong saturation and differs across sites; this brings into question approaches that estimates plant functioning from SIF that rely on the linear relationship between F_{760}-*ETR.* For instance*,* (Shan *et al.*, 2021) used F_{760} as a proxy for *ETR* (obtained through SCOPE simulations), which was then ingested in a photosynthesis-transpiration model to obtain *LEt*. Such approach would probably require an ecosystem-specific or climate-specific *SIF-ETR* parametrization to be accurately used across scale and might be therefore challenging to generalize.

NPQ and normalized steady state fluorescence (*Fs/Fo*) have been suggested by multiple authors to be mechanistically linked to stomata closure during stress (Flexas & Medrano, 2002; Medrano *et al.*, 2002). In our study *ETR* and

NPQ are linearly and positively related during periods of low stress, but their relationship becomes negative at high levels of T_{air} and *VPD*, as the light reaction of photosynthesis are bottlenecked by the dark reaction (Porcar-Castell, 2011) and *ETR* has to decrease in response to *NPQ* increase (Fig. 4.4, Supplementary Fig. S 4.9). This would suggest that approaches that rely on *ETR* to estimate *LEt* might work only under low stress conditions, and we anticipate their predictive power to deteriorate under stress.

Direct prediction of T and LE

Direct *SIF* based predictions of *LEt* have been proven to be successful at global scale (Maes *et al.*, 2020). However, it is not clear if their relationship is mechanistic in nature, or rather caused by co-variation of external variables such as net radiation and *LAI* (Damm *et al.*, 2021). In this work we try to move beyond an empirical-only approach, by analyzing possible confounding variables and implementing process-based simulations with the SCOPE model. With our random forest modelling approach we are able not only to perform predictions, but we also assess the importance and the marginal contribution of predictors. It should be noted that we do not make the distinction between what might be defined as a mechanistic driver of *LEt* (such as *VPD* or soil moisture) and state variables that correlate with *LEt* (such as $F_{760,\mathrm{tot}}$ or *ETR*). Here, we confirm *LEt* to be largely energy driven as *APAR* and $F_{760,\mathrm{tot}}$ are both selected as important predictors of *LEt* (Fig. 4.5). *ETR,* which is strongly driven by PAR (as *PAR* is required for the calculation of *ETR*) is also selected as an important predictor. This further confirms our hypothesis that especially in energy driven ecosystems (such as Leinefelde) the incoming and absorbed *PAR* are the variables that drive both F_{760} and *LEt* and therefore causing the correlation between the two (Fig. 4.3). Interestingly, T_{surf} is not selected as an important predictor, as most of the *LEt* variability is captured by variables related to absorbed energy (*APAR*) and photosynthetic activity ($F_{760,\mathrm{tot}}$, LUE_{f}). From a purely predictive point of view it seems that the inclusion of PAM related metrics does not improve the *LEt* prediction and that only RS variables are sufficient to directly estimate *LEt*. This can have three explanations. First, the remote sensing measurements already include all the driver of the processes; second, scaling issues from leaf to canopy (LAI sunlit/shaded, different field of view) cause a certain mismatch between the active and the passive measurements, despite the PAM measurements and passive RS measurements showing a good temporal agreement; the third, nonlinearity in the predictor space. The pdp allows to observe the marginal contribution of the different predictors to the prediction model. For example, a pdp of a linear model would always result in a linear relationship between the predictor and yhat. The pdp of the *LEt* random forest prediction model shows a plateau in the contribution of $F_{760,\mathrm{tot}}$ (at 2 mW m^{-2} sr^{-1} nm^{-1}) only in the Majadas site. This suggests that the inclusion of sites with different climatic conditions might introduce nonlinearity in the predictor space and potentially complicating the interpretation of the prediction.

LE predictions with RS or RS + PAM have slightly higher normalized root mean square error (NRMSE), but do not significantly differ from *LEt* predictions (Fig. 4.7). It seems therefore that the inclusion of non-physiologically regulated water fluxes such as soil evaporation do not significantly worsen the ability of RS to predict *LE*. As soil evaporation is only energy driven, this result confirms our assumption and previous research (Damm *et al.*, 2021) that *SIF* related metrics are able to predict *LEt* or *LE* by capturing their dependence to energy availability.

Prediction of gc and gs

Stomatal conductance influences both transpiration and carbon assimilation and has therefore been considered to be the key to understand the process behind the correlations between *LEt* and *SIF*. There is however much more literature on the link between *gc* and PAM related metrics (Flexas & Medrano, 2002; Medrano *et al.*, 2002; Omasa & Takayama, 2003), than on the link between *gc* and passive fluorescence (Shan *et al.*, 2019) which has only been employed in recent years to estimate *gc*. Also, typically active measurements are correlated with stomatal conductance estimated with leaf gas exchange measurements. Here we try to do a step forward and look at the relationship between multiple leaf level measurements and canopy scale gc derived from the eddy covariance measurements. Clearly we should acknowledge the scale mismatch between these measurements (i.e. leaf level measurements have a much smaller spatial scale than eddy covariance measurements), but postulate to be of minimal impact for the understanding of the predictors of the temporal variability of *gc*. The flat *gc-APAR* relationship reported in Fig. 4.8 is indicative of the fact that we are not observing the part of the *gc* response that is only light-limited (Wong *et al.*, 1979) (due to filtering for SZA < 50°), but rather the range in which gc is co-limited by *VPD* as well. It has been proposed that the relationship between *gc* and PAM derived metrics (such as *NPQ* or *Fs/Fo*) is affected by stomatal and non-stomatal limitations to photosynthesis (Fig. 4.8) (Medrano *et al.*, 2002). Even experiments in which stomatal conductance is artificially suppressed show changes in PAM derived metrics such as the quantum yield of PSII (*ΦPSII*), but curiously not in *SIF* (Marrs *et al.*, 2020). Under stress-induced stomatal closure leaf CO_2 concentration (*Ci*) decreases, causing an increase in photorespiration and in the Mehler reaction. As less ATP is consumed by other processes than photosynthesis, the trans-thylakoid pH will surge (Osmond et al., 1197b), activating the xanthophyll cycle and therefore causing an increase in *NPQ* and a decrease in fluorescence emission (*SIF* or *Fs*).

This theoretical framework seems to be confirmed by our data. When photosynthesis is metabolically limited i.e., because of photorespiration, Mehler reaction, cyclical electron transport or xanthophyll cycle activity, the best predictors of *gc* are $F_{760,\mathrm{tot}}$, T_{surf}, *Fs/Fo* and *NPQ* (Supplementary Fig. S4.5). In contrast, when we consider the whole range of *gc*, the best predictor is T_{surf}, followed by *Fs/Fo* (Fig. 4.9). As stomata regulate *LEt*, they also control the amount of evaporative cooling (Inoue et al. 1990), therefore explaining why T_{surf} is selected as the best predictor of *gc*. T_{surf} also shows to be linearly related to *gc* at both sites, unlike *ETR* and *NPQ* (Fig. 4.10), suggesting a robust T_{surf}-*gc* relationship that holds across climates. The upcoming fluorescence explorer satellite (FLEX) will fly in tandem with Sentinel 3, which is equipped with the Sea and Land Surface Temperature Radiometer (SLSTR) instrument. The combined use of *SIF* (in the red and far-red region) and surface temperature will ensure accurate predictions of *gc* for *LEt* calculations.

This work does not explicitly take into account the effect of the plant's water strategies and stomatal regulation behavior on the RS prediction of *gc*. Isohydric plants maintain a constant leaf water potential by strongly regulating stomatal conductance, while anisohydric plants continue to transpire during periods of water stress, therefore lowering their leaf water potential (Sade *et al.*, 2012). This strategy allows anisohydric plants to keep both transpiration and carbon assimilation high during periods of mild water stress. Previous research has shown that *NPQ*, *ETR* and fluorescence emission are more strongly related to *gc* than leaf water potential (Medrano *et al.*, 2002). We therefore assume that different plant's water management strategies might not significantly influence the ability to estimate *gc* with RS or PAM variables, but further research is needed to confirm this assumption.

The predictive power of *LEt* estimates through predicted *gc* is not superior to direct prediction of *LEt* through RS or RS + PAM approaches. As re-computing *LEt* from *gc* requires knowledge of aerodynamic resistance and meteorological conditions it would seem that from a purely predictive standpoint RS prediction of *LEt* with *SIF* would be the most viable option. Although we found that predictions of *LEt* are not significantly better than *LE*, when it comes to predicting stomatal conductance *ET* partitioning plays a very important role. In fact, *gs,* which is estimated from total LE, could not be predicted across sites (Fig. 4.11). The poor prediction does not seem to berelated with the hybrid-modelling approach. It is possible in certain cases to successfully predict a parameter, but not the variable of interest (in this case *LE*) due to equifinality in the estimated parameters (Efstratiadis & Koutsoyiannis, 2010). In this case *gs* is the only parameter being estimated and the accuracy of prediction is much lower than *gc* (Table 1). This calls into question previous approaches that attempted to estimate *LEt* by predicting *LE*-derived canopy conductance (Shan *et al.*, 2019) or that validate *LEt* estimates against *LE* (Shan *et al.*, 2021). These methods are likely to not perform well across diverse ecosystems, which might have different ratios of *LEt*/*LE*.

Prediction of WUE

Previous research has suggested that the relationship between *SIF* and transpiration is regulated by *WUE* (Maes *et al.*, 2020), but has not provided a convincing theoretical basis for the proposed link. Here we find that u*WUE* is mostly energy driven and temperature driven, as APAR, T_{surf} and *ETR* are selected as important predictors for *uWUE*. *uWUE* presents an exponential negative relationship to these three variables (Supplementary Fig. S4.8) and is not predicted well by $F_{760,\mathrm{tot}}$ across sites when all the data is considered. Only when metabolic limitations to photosynthesis are present $F_{760,\mathrm{tot}}$ becomes an important predictor. Overall, *uWUE* appears to be mostly energy and temperature limited and not regulated by *gc* (Supplementary Fig. S4.8), with higher marginal contribution of the predictors at low values of APAR (Fig. 4.13). We had hypothesized that because *uWUE* reflects *VPD* driven changes in *Ci/Ca*, *uWUE* could be driven partially by *NPQ*. However, our results do not support this hypothesis. We rather find that *uWUE* is mostly driven by and negatively related to *APAR* and *ETR*. The diurnal cycle of *uWUE* is generally inverse to the one of *PAR*, with *uWUE* showing a peak in the morning and in the afternoon, but a drop during midday (Niu *et al.*, 2003). The drop in *uWUE* is likely caused by higher *VPD* values (and therefore the evaporative demand) and midday depression in *GPP*. The development of RS based proxies of WUE is one of the outstanding challenges in earth observation (El Masri *et al.*, 2021) and our empirical study represent a step stone to understand the interlinks between WUE and different processes that can picked up by remote sensing observations.

Concluding remarks

In order to advance the mechanistic understanding regarding the *LEt*-fluorescence relationship it appears important to differentiate between periods of stomatal or metabolic limitation to photosynthesis and periods characterized by low stress. Overall, when considering the entire dataset, energy and temperature (*APAR*, T_{surf}) have a more prominent role in all the approaches presented, whereas when only periods of high stress are considered more physiological indicators ($F_{760,\mathrm{tot}}$, *NPQ*, *Fs/Fo*) are selected. We show that F_{760} is better at predicting *LEt* than *GPP* because during periods of photosynthesis-transpiration decoupling $F_{760,\mathrm{tot}}$ still tracks *APAR* well, whereas *GPP* is strongly downregulated. Traditionally PAM fluorimetry and *SIF* have been used separately to investigate transpiration and stomatal conductance, but a combined approach of active and passive fluorescence might be required to better understand and constraint water fluxes.

Acknowledgments

The project received funding from the European Union’s Horizon 2020 research and innovation program under the Marie Sklodowska-Curie grant agreement No. 721995. The authors acknowledge the Alexander von

Humboldt Foundation for supporting this research with the Max-Planck Prize to Markus Reichstein. We also acknowledge the European Space Agency (ESA) in the frame of the FLEXSense campaign (ESA Contract No. 4000125402/18/NL/NA) and the Photoproxy campaign (ESA contract No. 4000125731/19/NL/LF).
MMigliavacca and GWohlfart acknowledge funding from D-A-CH-DFG project "Verbesserte Abschätztung der Brüttoprimarproduktion”.

SUPPLEMENTARY MATERIAL

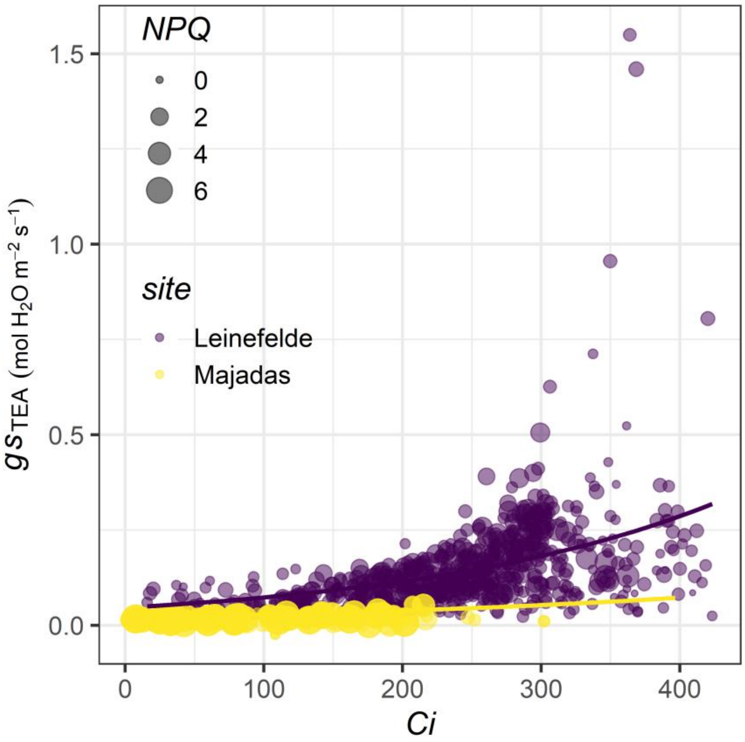

Supplementary Fig. S4.1. Scatterplot between canopy conductance (*gc*) and leaf internal CO_2 concentration (*Ci*). Yellow points are from the majadas site and violet points are from the Leinefelde site. The size of the points is proportional to the nonphotochemical quenching (*NPQ*). Lines are regression from a second degree polynomial. Shaded areas represent the 95% confidence interval.

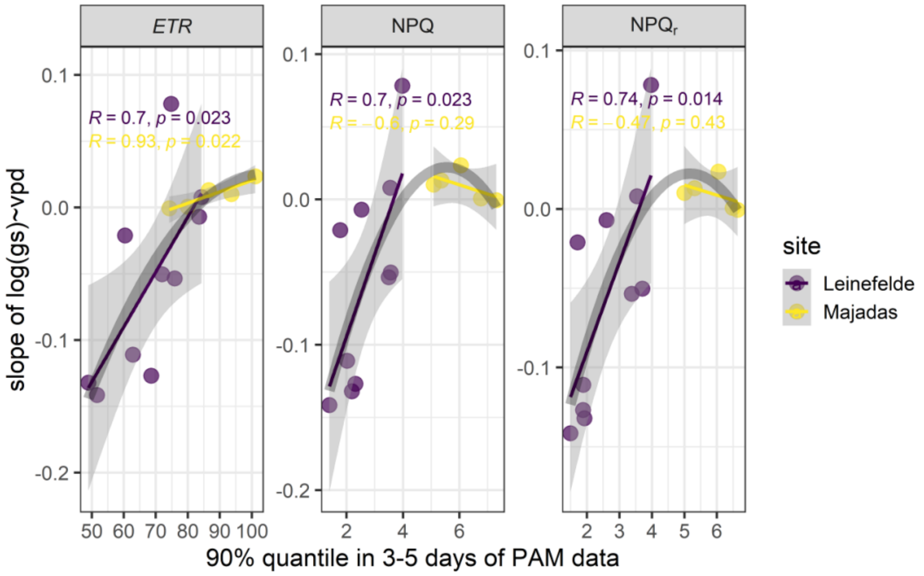

Supplementary Fig. S4.2. Scatterplot between the slope of surface conductance (*gs*) and vapor pressure deficit (*VPD*) during a window of 5 days for the Leinefelde site (violet points) and 3 days for the Majadas site (yellow points) and the 90% quantile of electron transport rate (*ETR*), nonphotochemical quenching (*NPQ*) and reversible nonphotochemical quenching (NPQ_r). Black and yellow lines are regressions from linear models from the Leinefelde site and Majadas site respectively. Gray lines are regressions from second degree polynomials for the whole data. Shaded areas represent the 95% confidence interval.

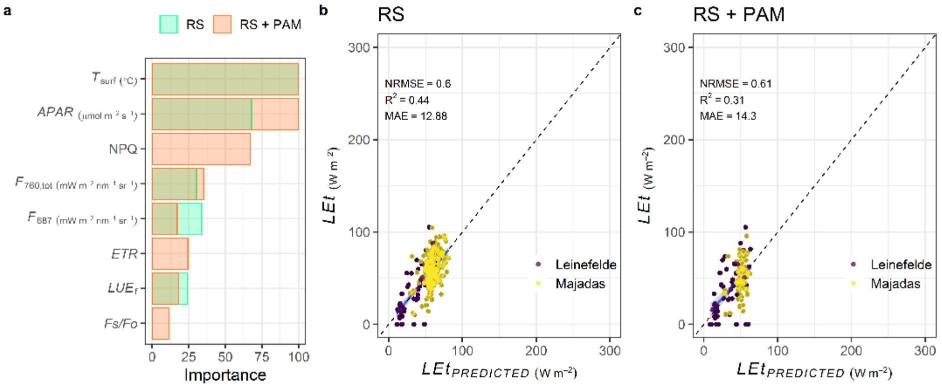

Supplementary Fig. S4.3. (a) Permutation random forest feature importance for latent heat flux of transpiration (*LEt*), with two sets of predictors; remote sensing only (RS), in light blue, and RS and pulse amplitude modulation data (PAM), in red. RS predictors include $F_{760,tot}$, *APAR*, LUE_f, F_{760}, T_{surf} and F_{687}. PAM predictors include *ETR*, *Fs/Fo* and *NPQ*. (b) scatterplot between observed *LEt* and *LEt* predicted by random forest with only RS predictors for the Majadas site (in yellow) and Leinefelde site (in violet) together. (c) scatterplot between observed *LEt* and *LEt* predicted by random forest with RS and PAM predictors for the Majadas site (in yellow) and Leinefelde site (in violet) together. Normalized root mean square error (NRMSE), coefficient of determination (R^2) and mean absolute errors (MAE) are calculated through 10-fold cross validation for both (b) and (c). Only data that present metabolic limitations to photosynthesis are considered.

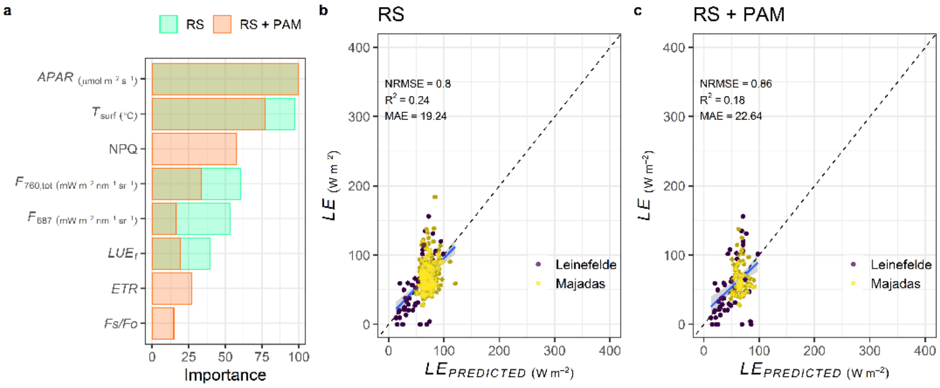

Supplementary Fig. S4.4. (a) Permutation random forest feature importance for latent heat flux (*LE*), with two sets of predictors; remote sensing only (RS), in light blue, and RS and pulse amplitude modulation data (PAM), in red. RS predictors include $F_{760,tot}$, *APAR*, LUE_f, F_{760}, T_{surf} and F_{687}. PAM predictors include *ETR*, *Fs/Fo* and *NPQ*. (b) scatterplot between observed *LE* and *LE* predicted by random forest with only RS predictors for the Majadas site (in yellow) and Leinefelde site (in violet) together. (c) scatterplot between observed *LE* and *LE* predicted by random forest with RS and PAM predictors for the Majadas site (in yellow) and Leinefelde site (in violet) together. Normalized root mean square error (NRMSE), coefficient of determination (R^2) and mean absolute errors (MAE) are calculated through 10-fold cross validation for both (b) and (c). Only data that present metabolic limitations to photosynthesis are considered.

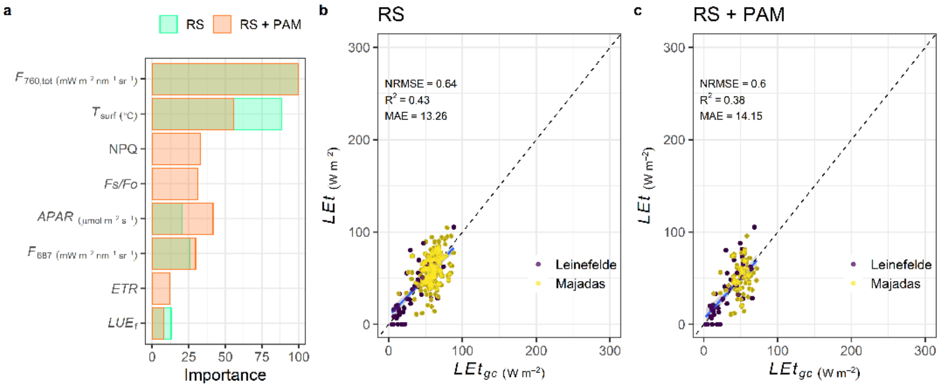

Supplementary Fig. S4.5. (a) Permutation random forest feature importance for canopy conductance (*gc*), with two sets of predictors; remote sensing only (RS), in light blue, and RS and pulse amplitude modulation data (PAM), in red. RS predictors include $F_{760,tot}$, *APAR*, LUE_f, F_{760}, T_{surf} and F_{687}. PAM predictors include *ETR*, *Fs/Fo* and *NPQ*. (b) scatterplot between observed latent heat flux of transpiration *(LEt)* and *LEt* calculated from predicted *gc* through the Penman-Monteith approach. *gc* is predicted by random forest with only RS predictors for the Majadas site (in yellow) and Leinefelde site (in violet) together. (c) scatterplot between observed *LEt* and *LEt* calculated from predicted *gc* through the Penman-Monteith approach. *gc* is predicted by random forest with RS and PAM predictors for the Majadas site (in yellow) and Leinefelde site (in violet) together. Normalized root mean square error (NRMSE), coefficient of determination (R^2) and mean absolute errors (MAE) are calculated through 10-fold cross validation for both (b) and (c). Only data that present metabolic limitations to photosynthesis are considered.

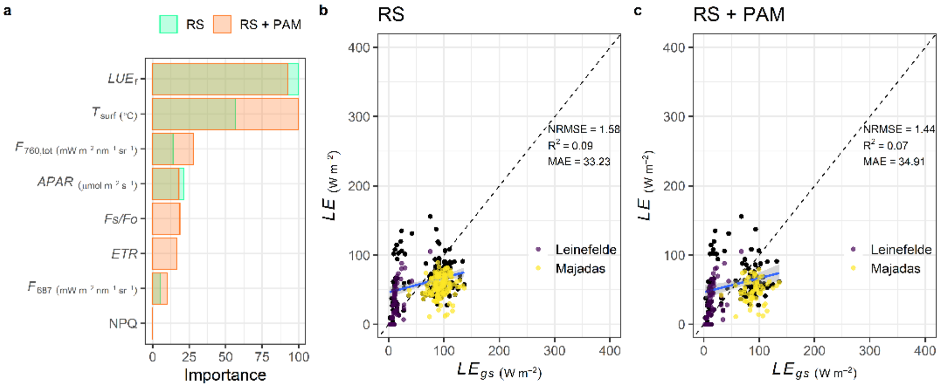

Supplementary Fig. S4.6. (a) Permutation random forest feature importance for surface conductance (*gs*), with two sets of predictors; remote sensing only (RS), in light blue, and RS and pulse amplitude modulation data (PAM), in red. RS predictors include $F_{760,tot}$, *APAR*, LUE_f, F_{760}, T_{surf} and F_{687}. PAM predictors include *ETR*, *Fs/Fo* and *NPQ*. (b) scatterplot between observed latent heat flux (*LE)* and *LE* calculated from predicted *gs* through the Penman-Monteith approach. *gs* is predicted by random forest with only RS predictors for the Majadas site (in yellow) and Leinefelde site (in violet) together. (c) scatterplot between observed *LE* and *LE* calculated from predicted *gs* through the Penman-Monteith approach. *gs* is predicted by random forest with RS and PAM predictors for the Majadas site (in yellow) and Leinefelde site (in violet) together. Normalized root mean square error (NRMSE), coefficient of determination (R^2) and mean absolute errors (MAE) are calculated through 10-fold cross validation for both (b) and (c). Only data that present metabolic limitations to photosynthesis are considered.

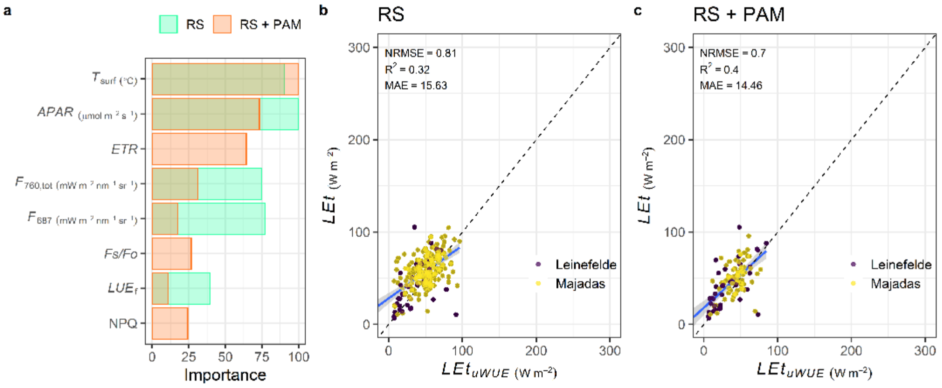

Supplementary Fig. S4.7. (a) Permutation random forest feature importance for underlying water use efficiency (*uWUE*), with two sets of predictors; remote sensing only (RS), in light blue, and RS and pulse amplitude modulation data (PAM), in red. RS predictors include $F_{760,tot}$, *APAR*, LUE_f, F_{760}, T_{surf} and F_{687}. PAM predictors include *ETR*, *Fs/Fo* and *NPQ*. (b) scatterplot between observed latent heat flux of transpiration (*LEt)* and *LEt* calculated from predicted *uWUE*. *uWUE* is predicted by random forest with only RS predictors for the Majadas site (in yellow) and Leinefelde site (in violet) together. (c) scatterplot between observed *LEt* and *LEt* calculated from predicted *uWUE*. *uWUE* is predicted by random forest with RS and PAM predictors for the Majadas site (in yellow) and Leinefelde site (in violet) together. Normalized root mean square error (NRMSE), coefficient of determination (R^2) and mean absolute errors (MAE) are calculated through 10-fold cross validation for both (b) and (c). Only data that present metabolic limitations to photosynthesis are considered.

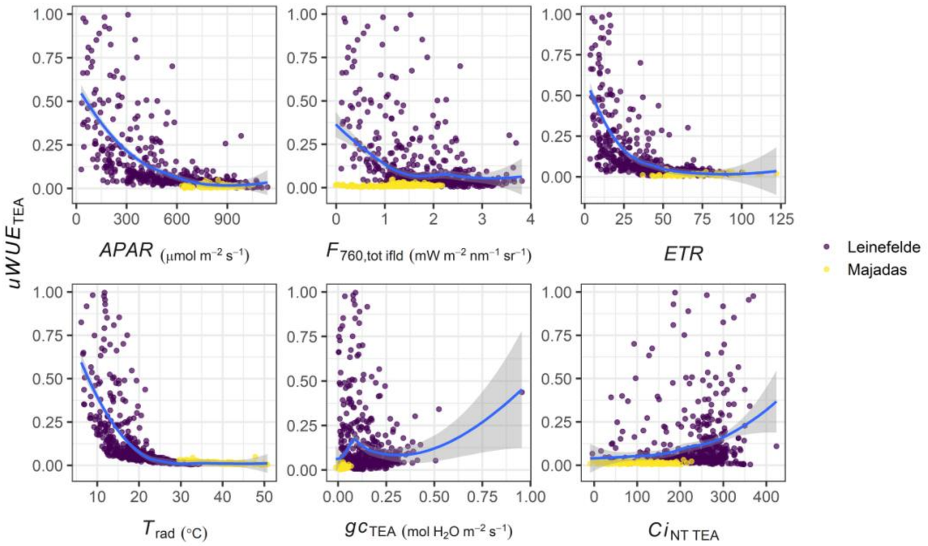

Supplementary Fig. S4.8. (a) scatterplot between underlying water use efficiency (*uWUE*) and a absorbed photosynthetic active radiation (*APAR*). (b) scatterplot between *uWUE* and total fluorescence at 760 nm ($F_{760,\mathrm{tot}}$: F_{760} / *Fesc*). (c) scatterplot between *uWUE* and electron transport rate (*ETR*). (d) scatterplot between *uWUE* and surface temperature (T_{surf}). (e) scatterplot *uWUE* and canopy conductance (*gc*). (f) scatterplot between *uWUE* and leaf internal CO_2 concentration (*Ci*). Yellow points refer to the Majadas site and violet points to the Leinefelde site. Blue lines are locally polynomial regression (LOESS). Shaded areas refer to the 95% confidence interval.

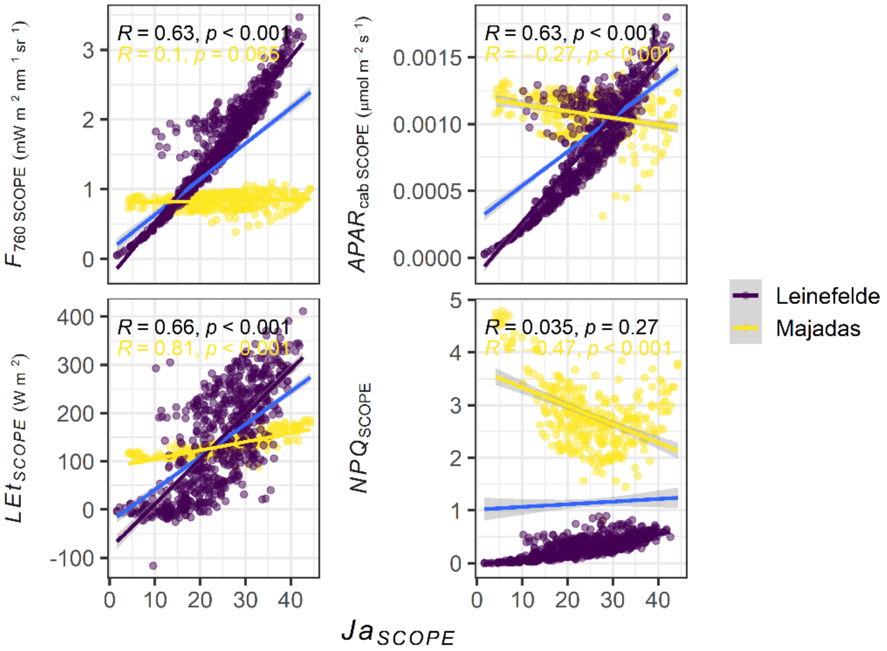

Supplementary Fig. S 4.9. (a) Scatterplot between fluorescence at 760 nm from the SCOPE model ($F_{760\ \mathrm{SCOPE}}$) and actual electron transport rate from SCOPE ($\mathrm{Ja}_{\mathrm{SCOPE}}$). (b) scatterplot between absorbed photosynthetic active radiation by chlorophylls from SCOPE ($APAR_{cab\ \ SCOPE}$) and $\mathrm{Ja}_{\mathrm{SCOPE}}$. (c) scatterplot between latent heat flux of transpiration from SCOPE (LEt_{SCOPE}) and $\mathrm{Ja}_{\mathrm{SCOPE}}$. (d) scatterplot between nonphotochemical quenching from SCOPE (NPQ_{SCOPE}) and $\mathrm{Ja}_{\mathrm{SCOPE}}$. Violet points are from the Leinefelde site and yellow points are from the Majadas site. In each panel the Spearman's rank correlation coefficient (R) and p value are reported for the total dataset (in black) and for each site. The blue line is the overall fit from a linear model. The shaded area represents the 95% confidence interval of the fit.

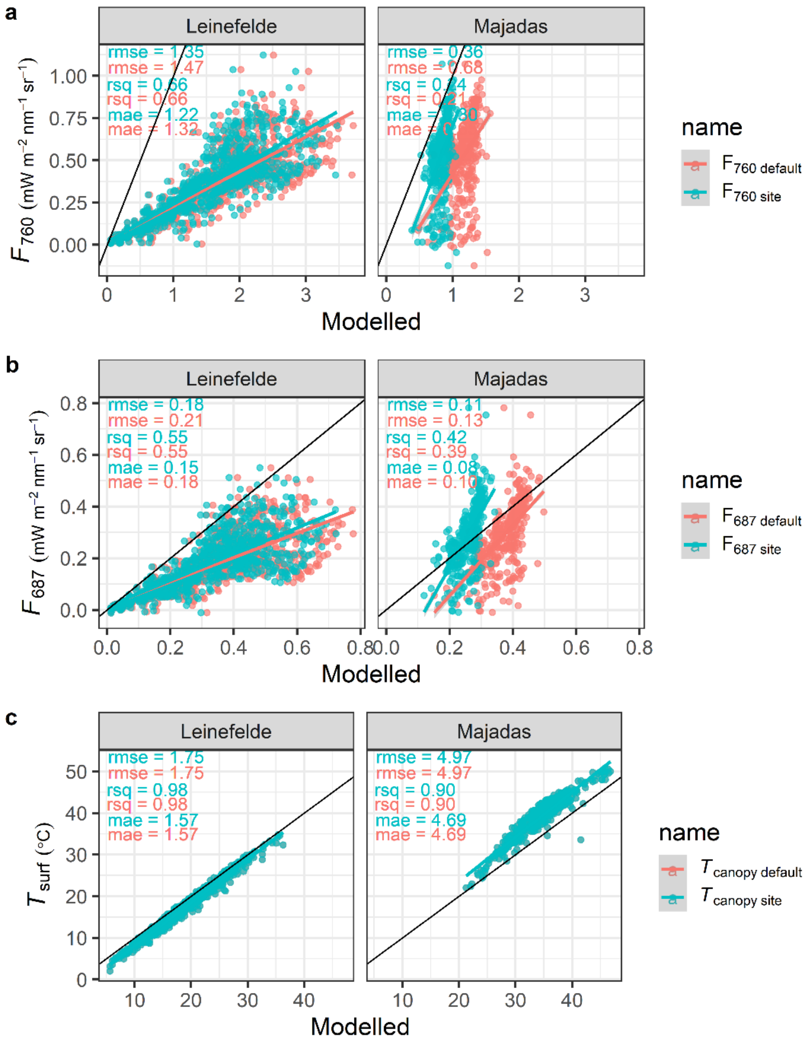

Supplementary Fig. S4.10. (a) scatterplot between sun-induced fluorescence at 760 nm F_{760} and F_{760} modelled by the SCOPE model. (b) scatterplot between sun-induced fluorescence at F_{687} and modelled F_{687}. (c) scatterplot between surface temperature (T_{surf}) and modelled canopy temperature (T_{canopy}). In each panel the plots are divided between the Leinefelde and Majadas site. The suffix "default" refers to variable simulated with SCOPE with the default parametrization of *NPQ*. The suffix "site" refers to variables simulated with SCOPE with the site calibrated parametrization of *NPQ*. In each panel the root mean square error (rmse), the coefficient of determination (rsq), and the mean annual error (mae) are reported.

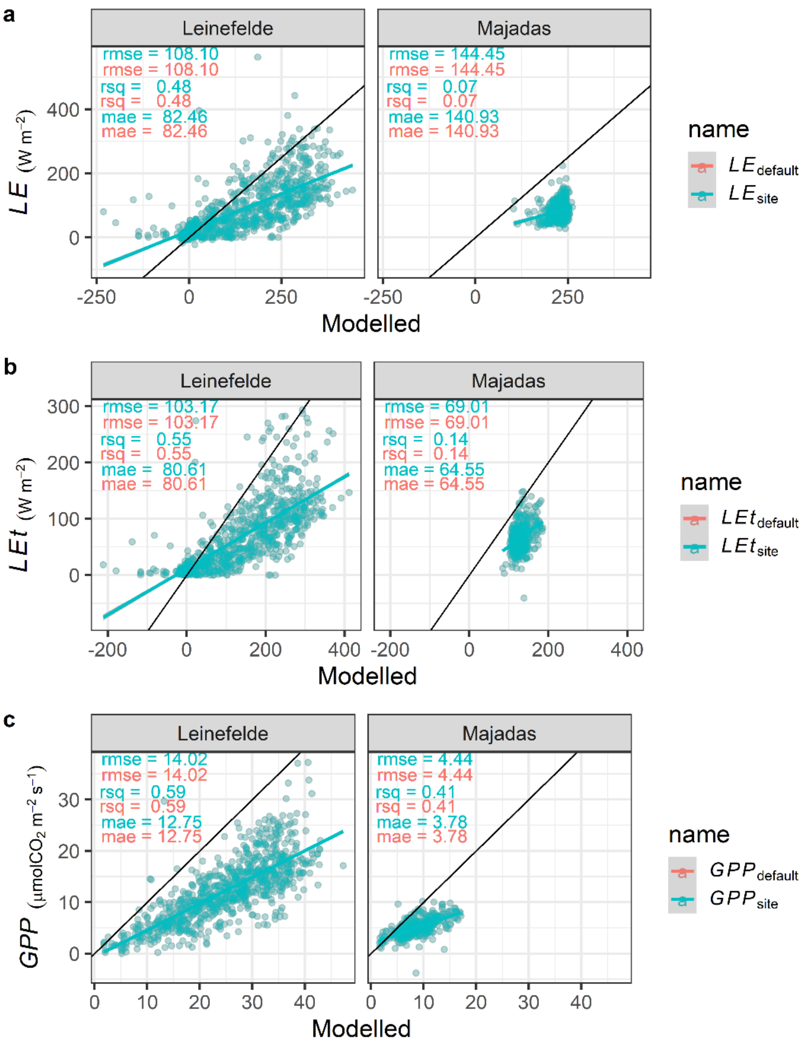

Supplementary Fig. S4.11. (a) scatterplot between latent heat flux (*LE*) and *LE* modelled by the SCOPE model. (b) scatterplot between latent heat flux of transpiration (*LEt*) and modelled *LEt*. (c) scatterplot between gross primary production (*GPP*) and modelled *GPP*. In each panel the plots are divided between the Leinefelde and Majadas site. The suffix "default" refers to variable simulated with SCOPE with the default parametrization of *NPQ*. The suffix "site" refers to variables simulated with SCOPE with the site calibrated parametrization of *NPQ*. In each panel the root mean square error (rmse), the coefficient of determination (rsq), and the mean annual error (mae) are reported.

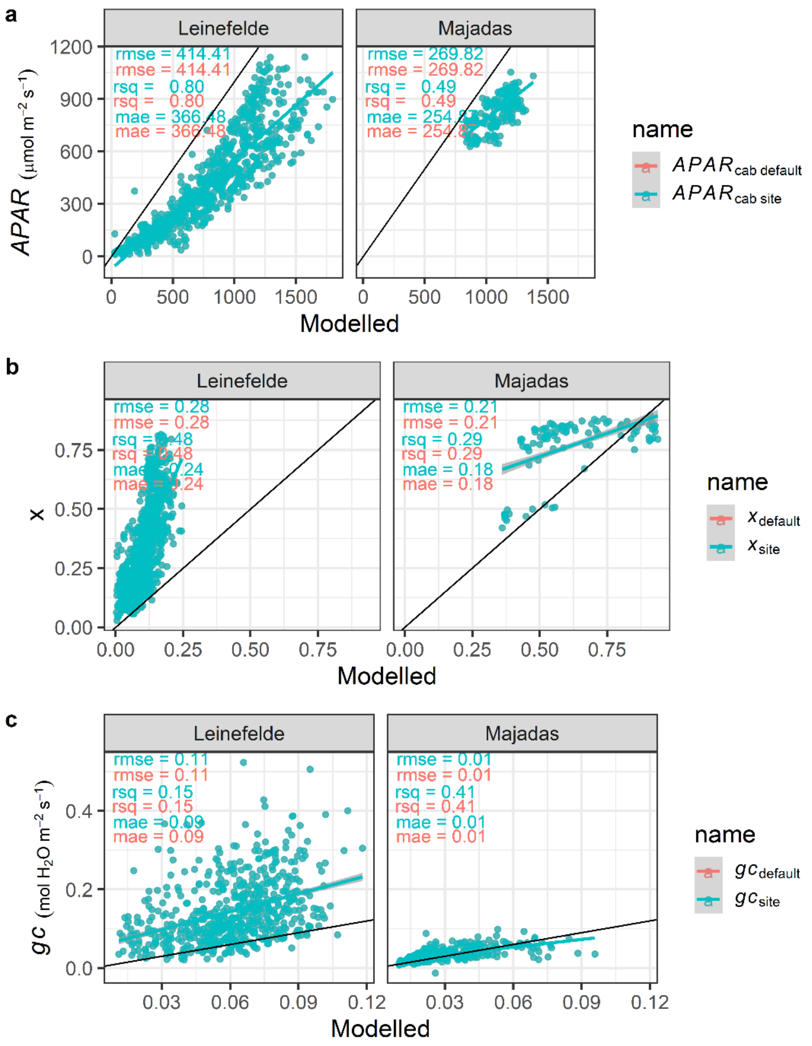

Supplementary Fig. S4.12. (a) scatterplot between absorbed photosynthetic active radiation (*APAR*) and *APAR* modelled by the SCOPE model. (b) scatterplot between relative light saturation of photosynthesis (*x*) and modelled *x*. (c) scatterplot between canopy conductance (*gc*) and modelled *gc*. In each panel the plots are divided between the Leinefelde and Majadas site. The suffix "default" refers to variable simulated with SCOPE with the default parametrization of *NPQ*. The suffix "site" refers to variables simulated with SCOPE with the site calibrated parametrization of *NPQ*. In each panel the root mean square error (rmse), the coefficient of determination (rsq), and the mean annual error (mae) are reported.

`

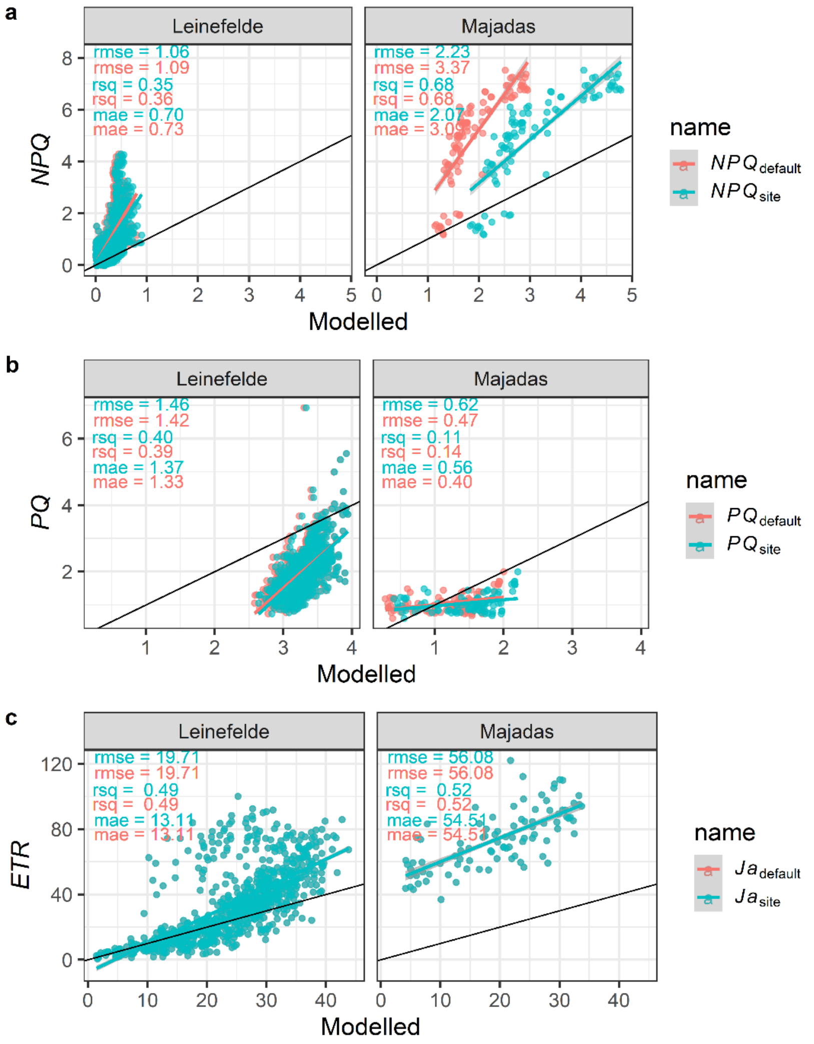

Supplementary Fig. S4.13. scatterplot between nonphotochemical quenching (*NPQ*) and *NPQ* modelled by the SCOPE model. (b) scatterplot between photochemical quenching (*PQ*) and *PQ* modelled by the SCOPE model. (c) scatterplot between electron transport rate (*ETR*) and modelled *ETR (Ja)*. In each panel the plots are divided between the Leinefelde and Majadas site. The suffix "default" refers to variable simulated with SCOPE with the default parametrization of *NPQ*. The suffix "site" refers to variables simulated with SCOPE with the site calibrated parametrization of *NPQ*. In each panel the root mean square error (rmse), the coefficient of determination (rsq), and the mean annual error (mae) are reported.

5 Synthesis

The ability of *SIF* to predict *GPP* and *T* across temporal and spatial scales can be exploited to better constrain and improve the understanding of the carbon and water cycle. The monitoring of *SIF* can therefore indirectly contribute to human welfare in several ways; first, *SIF* can improve estimates of global carbon assimilation, which can benefit policy making. Second, *SIF* can be used as a tool to assess extreme events, which are becoming more severe and frequent in a changing climate. Lastly, *SIF* may be used to predict *WUE*, which is set to increase due to higher atmospheric CO_2 concentration. In this thesis I improve the mechanistic understanding of *SIF* based monitoring of *GPP* and *T* with three contributions; 1) first I show which factors are responsible for the nutrient induced changes in the *GPP*-*SIF* relationship. I show that N influences *GPP-SIF* in two major ways; first by modifying canopy structure, and therefore *APAR* and *Fesc*, and secondly by lowering T_{surf} (due to increases in Albedo) which has a positively effect on fluorescence emission. P together with N had mainly the physiological effect of increasing LUE_{f}. This type of analysis are relevant for questions about the effect of fertilization, either intentional (as in agriculture) or unintentional (nitrogen and phosphorus deposition) on vegetation activity. 2) the second contribution is on the effect of extreme events on *GPP-SIF*. I show that under extreme levels of temperature and *VPD* a saturation of the *NPQ* pathway occurs, leading to an inversion of the *GPP-SIF* relationship during the heatwave and overall to large nonlinearities in *GPP-SIF*. This analysis is particularly important because nonlinear photosynthesis-fluorescence relationships have been observed at leaf scale with the PAM technique and theorized to occur at canopy scale as well, but I empirically show for the first time that these type of nonlinearities can be observed at canopy scale as well, even in the absence of changes in canopy structure. This analysis advances the understanding of the interplay of *GPP-SIF-NPQ* and is relevant for questions related to climate change, as well as questions related to effect of extreme events on vegetation. 3) the third contribution is related to *SIF* based *T* predictions. I show that *SIF* can be used to predict *T*, but its link is mostly related to the fact that both *SIF* and *T* co-vary with *APAR*. Under conditions of metabolic or stomatal limitations to photosynthesis I find that variables which are physiologically regulated (such as LUE_{f} and *NPQ*) are more important for *T* or stomatal conductance predictions. This research is relevant for questions related to water fluxes and water-carbon relationship.

This thesis also opens up new possible research lines that may answer some of the questions that it was not possible to answer. In chapter 3 I show how *NPQ* saturation might cause nonlinearities in the *GPP-SIF* relationship, but it is unclear how often this deviation from linearity occurs under stress. More research is needed to investigate how heatwaves affect *GPP-SIF* in different ecosystems. In chapter 4 I show that *SIF* may be used to predict *T* mostly because of covariation with *APAR*. It still unclear if *SIF* can track *T* when there are *APAR* independent changes in *T*, and how these relationship scales across space and time.

In this conclusion I also want to reflect on three cross-cutting themes that emerged from the overall body of work in this thesis and that advance our understanding of the relationship between *SIF* and *GPP* and between *SIF* and *T*; 1) the importance of *APAR*. 2) energy allocation as a key mechanism to understand *GPP-SIF*. 3) The role of surface temperature.

There is a current debate on the information content of F_{760} and the GPP-SIF relationship with two different positions (Dechant *et al.*, 2020): the first is that F_{760} contains both information about canopy structure but also physiological modulation of photosynthesis (due to changes in allocation of absorbed energy), the second is that F_{760} and *GPP-SIF* is mainly determined by *APAR* (Yang *et al.*, 2018). In this dissertation I find evidence of both cases. In chapter 2 I quantify through a path analysis the strength of the link between *APAR* and $F_{760,\mathrm{tot}}$ (considering as well all other relevant drivers) and find it to be highly robust. In the case of N and P fertilization *APAR* is influenced mostly by N. The positive effect of N on APAR is mediated by higher chlorophyll content and changes in species composition and therefore canopy structure (evidenced by significant changes in *Fesc*). In chapter 3 I instead come to the contradicting conclusion that even in absence of large changes in *APAR* it is possible to have drastic changes in F_{760} and *GPP*. This seeming inconsistency, can be resolved by acknowledging that in most cases F_{760} is mostly driven by *APAR*, but in others, especially under stress conditions and when canopy structure does not change quickly, F_{760} can be strongly regulated by the physiological modulation of *PQ* and *NPQ* (the other dissipation pathways).

When it comes however, to the *SIF* based prediction of *T* (as shown in the third chapter) it is clear that *APAR* plays a large role in driving both. From extensive measurements, SCOPE simulations and variable importance analysis I can conclude that in the study sites analyzed *APAR* acts as a "third variable", which influences both the independent variable (in this case $F_{760,\mathrm{tot}}$) and the dependent variable (*T*). This claim is further confirmed by the fact that *SIF* based predictions of *LE* (which include non-physiologically regulated soil evaporation) have a very similar fit to the *T* prediction. It is important to acknowledge that this specific conclusion is based on only two sites, and that the majority of the $F_{760,\mathrm{tot}}$-*T* correlation was driven by the Leinefelde site, which is light limited. More research is therefore needed to confirm the role of *APAR* in *SIF* based predictions of *T*.

Despite the very important role of *APAR*, *SIF* emission is also the result of how this energy is allocated by the three main dissipation pathways; photochemical quenching, fluorescence emission and nonphotochemical quenching. I find clear evidence of the role of energy allocation (in chapter 3) in shaping the *GPP-SIF* relationship. It is known that there are three main phases that drive the relationship between the *ΦP* and *ΦF*; a) the "*PQ* phase", which occurs at low levels of solar irradiance and is generally not observed with remote sensing due to high solar zenith angle. b) the "*NPQ* phase", where due to progressively higher solar irradiance *NPQ* drives both *ΦP* and *ΦF* down. In this phase we observe a positive *ΦP* and *ΦF* relationship (also reflected on *GPP*-F_{760}). This phase is what is generally observed in most studies that correlate *GPP* with F_{760}. c) the "*NPQ* saturation phase", which has been theorized and observed at leaf scale with PAM fluorimetry, but observed for the first time at canopy scale in this work as described in chapter 2. During the "*NPQ* saturation phase" I observe strong nonlinearities in the *GPP*-$F_{760,\mathrm{tot}}$ relationship caused by increases in LUE_{f}. In this phase, *NPQ* saturates early in the day (Fig. 3.5C), leaving the photosystems without sufficient protection to cope with excess energy. I propose that the mechanisms responsible for the observed *GPP*-F_{760} nonlinearity under high heat stress are shifts in energy allocation towards fluorescence emission.

These results highlight the need to use combined passive and active fluorescence methods. PAM represents an invaluable tool that provides several variables (such as *NPQ* and *ETR*) which are necessary to understand the mechanistic processes behind the *GPP-SIF* relationship.

The final cross-cutting theme highlighted here relates to the importance of T_{surf} for *SIF* based *GPP* and *T* predictions. In chapter 2 I find T_{surf} to be the most important predictor of LUE_{p}. I also find T_{surf} to negatively correlate with LUE_{f}, which generally decreases with temperature (but can increase under extreme temperature as explained in chapter 3). I also find that T_{surf} change can be driven by changes in Albedo. An increase in NIR reflectance can therefore indirectly affect LUE_{f}, highlighting the varied and complex mechanisms that can have an influence on *GPP-SIF*. T_{surf}, in combination with *VPD*, can strongly affect *GPP-SIF* dynamics, as seen in chapter 3, likely because of its ability to track *NPQ*. In fact, the tight relationship between *NPQ* and *VPD* and T_{surf} obtained in chapter 3 validates the assumption made in chapter 2 to use T_{surf} as a proxy for *NPQ*. Finally in chapter 4 I found T_{surf} to be the most important predictor of gc. As stomata regulate *T*, they also control the amount of evaporative cooling (Inoue et al. 1990), therefore explaining why T_{surf} is selected as the best predictor of *gc*. The upcoming fluorescence explorer satellite (FLEX) will fly in tandem with Sentinel 3, which is equipped with the Sea and Land Surface Temperature Radiometer (SLSTR) instrument. The combined use of *SIF* (in the red and far-red region) and surface temperature will ensure accurate predictions of *gc* for *T* calculations. Furthermore, the ability of $\mathrm{T}_{\mathrm{surf}}$ to track LUE_{p} and LUE_{f} clearly shows that $\mathrm{T}_{\mathrm{surf}}$ should be used in combination with *SIF* as additional input of LUE models aimed at the prediction of GPP (Sims *et al.*, 2008).

In conclusion, this thesis highlights the most important factors responsible for the mechanistic link between *GPP* and *SIF*, analyzes the effect of nutrients, extreme events on the *GPP-SIF* relationship and provides a framework for understanding how *SIF* can be used to track *T*. The increase use of high temporal resolution proximal sensing of *SIF* has vastly expanded the understanding of *SIF* in the last decade. With the upcoming FLEX satellite it is going to be possible to observe at relatively high spatial resolution *SIF* from areas that have been so far understudied, such as the tropical regions of the Americas and Africa, but that contribute to a large extent to the global carbon and water cycle.

6 Bibliography

Ač A, Malenovský Z, Olejníčková J, Gallé A, Rascher U, Mohammed G. 2015. Meta-analysis assessing potential of steady-state chlorophyll fluorescence for remote sensing detection of plant water, temperature and nitrogen stress. *Remote Sensing of Environment* **168**: 420-436.

Alonso L, Van Wittenberghe S, Amorós-López J, Vila-Francés J, Gómez-Chova L, Moreno J. 2017. Diurnal cycle relationships between passive fluorescence, PRI and NPQ of vegetation in a controlled stress experiment. *Remote Sensing* **9**(8): 770.

Antal TK, Kovalenko IB, Rubin AB, Tyystjärvi E. 2013. Photosynthesis-related quantities for education and modeling. *Photosynthesis Research* **117**(1): 1-30.

Anthoni P, Knohl A, Rebmann C, Freibauer A, Mund M, Ziegler W, Kolle O, Schulze ED. 2004. Forest and agricultural land-use-dependent CO2 exchange in Thuringia, Germany. *Global Change Biology* **10**(12): 2005-2019.

Asada K. 2000. The water-water cycle as alternative photon and electron sinks. *Philosophical Transactions of the Royal Society of London Series B-Biological Sciences* **355**(1402): 1419-1430.

Atherton J, Liu W, Porcar-Castell A. 2019. Nocturnal Light Emitting Diode Induced Fluorescence (LEDIF): A new technique to measure the chlorophyll a fluorescence emission spectral distribution of plant canopies in situ. *Remote Sensing of Environment* **231**: 111137.

Badgley G, Field CB, Berry JA. 2017. Canopy near-infrared reflectance and terrestrial photosynthesis. *Science Advances* **3**(3): e1602244.

Barriopedro D, Sousa PM, Trigo RM, Garcia-Herrera R, Ramos AM. 2020. The Exceptional Iberian Heatwave of Summer 2018. *Bulletin of the American Meteorological Society* **101**(1): S29-S33.

Bastos A, Ciais P, Friedlingstein P, Sitch S, Pongratz J, Fan L, Wigneron J, Weber U, Reichstein M, Fu Z. 2020. Direct and seasonal legacy effects of the 2018 heat wave and drought on European ecosystem productivity. *Science Advances* **6**(24): eaba2724.

Beer C, Reichstein M, Tomelleri E, Ciais P, Jung M, Carvalhais N, Rodenbeck C, Arain MA, Baldocchi D, Bonan GB, et al. 2010. Terrestrial Gross Carbon Dioxide Uptake: Global Distribution and Covariation with Climate. *Science* **329**(5993): 834-838.

Bernstein L, Bosch P, Canziani O, Chen Z, Christ R, Riahi K 2008. IPCC, 2007: Climate Change 2007: Synthesis Report.

Contribution of Working Groups I, II and III to the Fourth Assessment Report of the Intergovernmental Panel on Climate Chang. Geneva, Switzerland: IPCC. 151.

Beven K. 1979. A sensitivity analysis of the Penman-Monteith actual evapotranspiration estimates. *Journal of Hydrology* **44**(3-4): 169-190.

Bilger W, Bjorkman O. 1991. Temperature-Dependence of Violaxanthin Deepoxidation and Nonphotochemical Fluorescence Quenching in Intact Leaves of Gossypium-Hirsutum L and Malva-Parviflora L. *Planta* **184**(2): 226-234.

Bindoff NL, Stott PA, AchutaRao KM, Allen MR, Gillett N, Gutzler D, Hansingo K, Hegerl G, Hu YY, Jain S, et al. 2014. IPCC; Climate Change 2013: The Physical Science Basis. IPCC Working Group I Contribution to AR5. 867-952.

Bonan G, Williams M, Fisher R, Oleson K. 2014. Modeling stomatal conductance in the earth system: linking leaf water-use efficiency and water transport along the soil–plant–atmosphere continuum. *Geoscientific Model Development* **7**(5): 2193-2222.

Boulet G, Chehbouni A, Gentine P, Duchemin B, Ezzahar J, Hadria R. 2007. Monitoring water stress using time series of observed to unstressed surface temperature difference. *Agricultural and Forest Meteorology* **146**(3-4): 159-172.

Brand WA, Coplen TB. 2012. Stable isotope deltas: tiny, yet robust signatures in nature. *Isotopes in Environmental and Health Studies* **48**(3): 393-409.

Burchard-Levine V, Nieto H, Riaño D, Migliavacca M, El-Madany TS, Perez-Priego O, Carrara A, Martín MP. 2020. Seasonal adaptation of the thermal-based two-source energy balance model for estimating evapotranspiration in a semiarid tree-grass ecosystem. *Remote Sensing* **12**(6): 904.

Buschmann C. 2007. Variability and application of the chlorophyll fluorescence emission ratio red/far-red of leaves. *Photosynthesis Research* **92**(2): 261-271.

Butler WL. 1978. Energy distribution in the photochemical apparatus of photosynthesis. *Annual Review of Plant Physiology* **29**(1): 345-378.

Cailly A. 1996. Fate of excitation at PS II in leaves. The non-photochemical side. *Plant Physiol. Biochem.*: 86.

Cendrero-Mateo MP, Moran MS, Papuga SA, Thorp K, Alonso L, Moreno J, Ponce-Campos G, Rascher U, Wang G. 2015. Plant chlorophyll fluorescence: active and passive measurements at canopy and leaf scales with different nitrogen treatments. *Journal of Experimental Botany* **67**(1): 275-286.

Cendrero-Mateo MP, Wieneke S, Damm A, Alonso L, Pinto F, Moreno J, Guanter L, Celesti M, Rossini M, Sabater N, et al. 2019. Sun-Induced Chlorophyll Fluorescence III: Benchmarking Retrieval Methods and Sensor Characteristics for Proximal Sensing. *Remote Sensing* **11**(8): 962.

Coplen TB. 2011. Guidelines and recommended terms for expression of stable-isotope-ratio and gas-ratio measurement results. *Rapid communications in mass spectrometry* **25**(17): 2538-2560.

Cutler DR, Edwards Jr TC, Beard KH, Cutler A, Hess KT, Gibson J, Lawler JJ. 2007. Random forests for classification in ecology. *Ecology* **88**(11): 2783-2792.

Damm A, Elbers J, Erler A, Gioli B, Hamdi K, Hutjes R, Kosvancova M, Meroni M, Miglietta F, Moersch A. 2010. Remote sensing of sun-induced fluorescence to improve modeling of diurnal courses of gross primary production (GPP). *Global Change Biology* **16**(1): 171-186.

Damm A, Guanter L, Paul-Limoges E, van der Tol C, Hueni A, Buchmann N, Eugster W, Ammann C, Schaepman ME. 2015. Far-red sun-induced chlorophyll fluorescence shows ecosystem-specific relationships to gross primary production: An assessment based on observational and modeling approaches. *Remote Sensing of Environment* **166**: 91-105.

Damm A, Haghighi E, Paul-Limoges E, van der Tol C. 2021. On the seasonal relation of sun-induced chlorophyll fluorescence and transpiration in a temperate mixed forest. *Agricultural and Forest Meteorology* **304**: 108386.

Dechant B, Ryu Y, Badgley G, Zeng Y, Berry JA, Zhang Y, Goulas Y, Li Z, Zhang Q, Kang M. 2020. Canopy structure explains the relationship between photosynthesis and sun-induced chlorophyll fluorescence in crops. *Remote Sensing of Environment* **241**: 111733.

Demmig B, Winter K, Kruger A, Czygan FC. 1988. Zeaxanthin and the Heat Dissipation of Excess Light Energy in Nerium-Oleander Exposed to a Combination of High Light and Water-Stress. *Plant Physiology* **87**(1): 17-24.

Diaz M, de Haro V, Munoz R, Quiles MJ. 2007. Chlororespiration is involved in the adaptation of Brassica plants to heat and high light intensity. *Plant, cell & environment* **30**(12): 1578-1585.

Drake JE, Tjoelker MG, Varhammar A, Medlyn BE, Reich PB, Leigh A, Pfautsch S, Blackman CJ, Lopez R, Aspinwall MJ, et al. 2018. Trees tolerate an extreme heatwave via sustained transpirational cooling and increased leaf thermal tolerance. *Global Change Biology* **24**(6): 2390-2402.

Efstratiadis A, Koutsoyiannis D. 2010. One decade of multi-objective calibration approaches in hydrological modelling: a review. *Hydrological Sciences Journal–Journal Des Sciences Hydrologiques* **55**(1): 58-78.

El-Madany. in preparation.

El-Madany TS, Carrara A, Martin MP, Moreno G, Kolle O, Pacheco-Labrador J, Weber U, Wutzler T, Reichstein M, Migliavacca M. 2020. Drought and heatwave impacts on semi-arid ecosystems' carbon fluxes along a precipitation gradient. *Philosophical Transactions of the Royal Society B-Biological Sciences* **375**(1810): 20190519.

El-Madany TS, Reichstein M, Perez-Priego O, Carrara A, Moreno G, Martin MP, Pacheco-Labrador J, Wohlfahrt G, Nieto H, Weber U, et al. 2018. Drivers of spatio-temporal variability of carbon dioxide and energy fluxes in a Mediterranean savanna ecosystem. *Agricultural and Forest Meteorology* **262**: 258-278.

El Masri B, Stinchcomb GE, Cetin H, Ferguson B, Kim SL, Xiao J, Fisher JB. 2021. Linking Remotely Sensed Carbon and Water Use Efficiencies with In Situ Soil Properties. *Remote Sensing* **13**(13): 2593.

Evans JR. 1989. Photosynthesis and nitrogen relationships in leaves of C 3 plants. *Oecologia* **78**(1): 9-19.

Falge E, Baldocchi D, Olson R, Anthoni P, Aubinet M, Bernhofer C, Burba G, Ceulemans R, Clement R, Dolman H, et al. 2001. Gap filling strategies for defensible annual sums of net ecosystem exchange. *Agricultural and Forest Meteorology* **107**(1): 43-69.

Farquhar GD, Lloyd J, Taylor JA, Flanagan LB, Syvertsen JP, Hubick KT, Wong SC, Ehleringer JR. 1993. Vegetation effects on the isotope composition of oxygen in atmospheric CO 2. *Nature* **363**(6428): 439-443.

Farquhar GD, von Caemmerer Sv, Berry J. 1980. A biochemical model of photosynthetic CO 2 assimilation in leaves of C 3 species. *Planta* **149**(1): 78-90.

Feng XH, Dietze M. 2013. Scale dependence in the effects of leaf ecophysiological traits on photosynthesis: Bayesian parameterization of photosynthesis models. *New Phytologist* **200**(4): 1132-1144.

Flexas J, Escalona JM, Evain S, Gulías J, Moya I, Osmond CB, Medrano H. 2002. Steady-state chlorophyll fluorescence (Fs) measurements as a tool to follow variations of net CO2 assimilation and stomatal conductance during water-stress in C3 plants. *Physiologia Plantarum* **114**(2): 231-240.

Flexas J, Medrano H. 2002. Energy dissipation in C-3 plants under drought. *Functional Plant Biology* **29**(10): 1209-1215.

Frankenberg C, Berry J. 2018. Solar Induced Chlorophyll Fluorescence: Origins, Relation to Photosynthesis and Retrieval.

Fratini G, Mauder M. 2014. Towards a consistent eddy-covariance processing: an intercomparison of EddyPro and TK3. *Atmospheric Measurement Techniques* **7**(7): 2273-2281.

Galmés J, Ribas-Carbó M, Medrano H, Flexas J. 2007. Response of leaf respiration to water stress in Mediterranean species with different growth forms. *Journal of Arid Environments* **68**(2): 206-222.

Games PA, Howell JF. 1976. Pairwise multiple comparison procedures with unequal n's and/or variances: a Monte Carlo study. *Journal of Educational Statistics* **1**(2): 113-125.

Gamon JA, Serrano L, Surfus JS. 1997. The photochemical reflectance index: an optical indicator of photosynthetic radiation use efficiency across species, functional types, and nutrient levels. *Oecologia* **112**(4): 492-501.

Garcia-Plazaola JI, Esteban R, Hormaetxe K, Fernandez-Marin B, Becerril JM. 2008. Photoprotective responses of Mediterranean and Atlantic trees to the extreme heat-wave of summer 2003 in Southwestern Europe. *Trees-Structure and Function* **22**(3): 385-392.

Genty B, Briantais J-M, Baker NR. 1989. The relationship between the quantum yield of photosynthetic electron transport and quenching of chlorophyll fluorescence. *Biochimica et Biophysica Acta (BBA)-General Subjects* **990**(1): 87-92.

Genty B, Harbinson J, Baker N. 1990. Relative quantum efficiencies of the two photosystems of leaves in photorespiratory and non-respiratory conditions. *Plant Physiology and Biochemistry (Paris)* **28**(1): 1-10.

Georgieva K, Yordanov I. 1994. Temperature dependence of photochemical and non-photochemical fluorescence quenching in intact pea leaves. *Journal of Plant Physiology* **144**(6): 754-759.

Gibson J, Edwards T. 2002. Regional water balance trends and evaporation-transpiration partitioning from a stable isotope survey of lakes in northern Canada. *Global Biogeochemical Cycles* **16**(2): 10-11-10-14.

Girden ER. 1992. *ANOVA: Repeated measures*. Newbury Park, CA, USA: Sage.

Gitelson AA, Buschmann C, Lichtenthaler HK. 1998. Leaf chlorophyll fluorescence corrected for re-absorption by means of absorption and reflectance measurements. *Journal of Plant Physiology* **152**(2-3): 283-296.

Gonzalez-Cascon R, Jiménez-Fenoy L, Verdú-Fillola I, Martín MP. 2017. Aqueous-acetone extraction improves the drawbacks of using dimethylsulfoxide as solvent for photometric pigment quantification in *Quercus ilex* leaves. *Forest Systems* **26**(2): eSC04--eSC04.

Govindjee. 1995. 63 Years since Kautsky - Chlorophyll-a Fluorescence. *Australian Journal of Plant Physiology* **22**(2): 131-160.

Gratani L, Bombelli A. 2000. Correlation between leaf age and other leaf traits in three Mediterranean maquis shrub species: *Quercus ilex, Phillyrea latifolia* and *Cistus incanus*. *Environmental and Experimental Botany* **43**(2): 141-153.

Grime JP. 2006. Trait convergence and trait divergence in herbaceous plant communities: Mechanisms and consequences. *Journal of Vegetation Science* **17**(2): 255-260.

Groemping U, Matthias L. 2006. Relaimpo: relative importance of regressors in linear models. *R package version*: 1.1-1.

Guan K, Berry JA, Zhang Y, Joiner J, Guanter L, Badgley G, Lobell DB. 2016. Improving the monitoring of crop productivity using spaceborne solar-induced fluorescence. *Global Change Biology* **22**(2): 716-726.

Guanter L, Zhang YG, Jung M, Joiner J, Voigt M, Berry JA, Frankenberg C, Huete AR, Zarco-Tejada P, Lee JE, et al. 2014. Global and time-resolved monitoring of crop photosynthesis with chlorophyll fluorescence. *Proceedings of the National Academy of Sciences of the United States of America* **111**(14): E1327-E1333.

Heimann M, Reichstein M. 2008. Terrestrial ecosystem carbon dynamics and climate feedbacks. *Nature* **451**(7176): 289-292.

Hilker T, Coops NC, Hall FG, Black TA, Wulder MA, Nesic Z, Krishnan P. 2008. Separating physiologically and directionally induced changes in PRI using BRDF models. *Remote Sensing of Environment* **112**(6): 2777-2788.

Holmberg M, Aalto T, Akujarvi A, Arslan AN, Bergstrom I, Bottcher K, Lahtinen I, Makela A, Markkanen T, Minunno F, et al. 2019. Ecosystem Services Related to Carbon Cycling - Modeling Present and Future Impacts in Boreal Forests. *Frontiers in Plant Science* **10**: 343.

Houborg R, Cescatti A, Migliavacca M, Kustas W. 2013. Satellite retrievals of leaf chlorophyll and photosynthetic capacity for improved modeling of GPP. *Agricultural and Forest Meteorology* **177**: 10-23.

Hu Lt, Bentler PM. 1999. Cutoff criteria for fit indexes in covariance structure analysis: Conventional criteria versus new alternatives. *Structural equation modeling: a multidisciplinary journal* **6**(1): 1-55.

Iacobucci D. 2010. Structural equations modeling: Fit indices, sample size, and advanced topics. *Journal of consumer psychology* **20**(1): 90-98.

Jackson RD, Idso S, Reginato R, Pinter P. 1981. Canopy temperature as a crop water stress indicator. *Water resources research* **17**(4): 1133-1138.

Jahns P, Holzwarth AR. 2012. The role of the xanthophyll cycle and of lutein in photoprotection of photosystem II. *Biochimica Et Biophysica Acta-Bioenergetics* **1817**(1): 182-193.

Jasechko S, Sharp ZD, Gibson JJ, Birks SJ, Yi Y, Fawcett PJ. 2013. Terrestrial water fluxes dominated by transpiration. *Nature* **496**(7445): 347-350.

Jiang M, Caldararu S, Zaehle S, Ellsworth DS, Medlyn BE. 2019. Towards a more physiological representation of vegetation phosphorus processes in land surface models. *New Phytologist*.

Johnson J, Berry J. 2021. The role of Cytochrome $$\text {b} _ {6}\text {f} $$ b 6 f in the control of steady-state photosynthesis: a conceptual and quantitative model. *Photosynthesis Research*: 1-36.

Jonard F, De Canniere S, Brüggemann N, Gentine P, Gianotti DS, Lobet G, Miralles DG, Montzka C, Pagán BR, Rascher U. 2020. Value of sun-induced chlorophyll fluorescence for quantifying hydrological states and fluxes: Current status and challenges. *Agricultural and Forest Meteorology* **291**: 108088.

Julitta T, Burkart A, Colombo R, Rossini M, Schickling A, Migliavacca M, Cogliati S, Wutzler T, Rascher U 2017. Accurate measurements of fluorescence in the O2A and O2B band using the FloX spectroscopy system—Results and prospects. *Proceedings of the Potsdam GHG Flux Workshop: From Photosystems to Ecosystems, Potsdam, Germany*. 24-26.

Julitta T, Corp LA, Rossini M, Burkart A, Cogliati S, Davies N, Hom M, Mac Arthur A, Middleton EM, Rascher U, et al. 2016. Comparison of Sun-Induced Chlorophyll Fluorescence Estimates Obtained from Four Portable Field Spectroradiometers. *Remote Sensing* **8**(2): 122.

Jung M, Koirala S, Weber U, Ichii K, Gans F, Camps-Valls G, Papale D, Schwalm C, Tramontana G, Reichstein M. 2019. The FLUXCOM ensemble of global land-atmosphere energy fluxes. *Scientific data* **6**(1): 1-14.

Katul GG, Palmroth S, Oren R. 2009. Leaf stomatal responses to vapour pressure deficit under current and CO2-enriched atmosphere explained by the economics of gas exchange. *Plant, cell & environment* **32**(8): 968-979.

Kauwe MGD, Medlyn BE, Pitman AJ, Drake JE, Ukkola A, Griebel A, Pendall E, Prober S, Roderick M. 2019. Examining the evidence for decoupling between photosynthesis and transpiration during heat extremes. *Biogeosciences* **16**(4): 903-916.

Kitajima M, Butler WL. 1975. Quenching of Chlorophyll Fluorescence and Primary Photochemistry in Chloroplasts by Dibromothymoquinone. *Biochimica Et Biophysica Acta* **376**(1): 105-115.

Knauer J, El-Madany TS, Zaehle S, Migliavacca M. 2018. Bigleaf—An R package for the calculation of physical and physiological ecosystem properties from eddy covariance data. *Plos One* **13**(8): e0201114.

Knohl A, Schulze E-D, Kolle O, Buchmann N. 2003. Large carbon uptake by an unmanaged 250-year-old deciduous forest in Central Germany. *Agricultural and Forest Meteorology* **118**(3-4): 151-167.

Knyazikhin Y, Schull MA, Stenberg P, Mõttus M, Rautiainen M, Yang Y, Marshak A, Carmona PL, Kaufmann RK, Lewis P. 2013. Hyperspectral remote sensing of foliar nitrogen content. *Proceedings of the National Academy of Sciences* **110**(3): E185-E192.

Kramer DM, Johnson G, Kiirats O, Edwards GE. 2004. New fluorescence parameters for the determination of Q A redox state and excitation energy fluxes. *Photosynthesis Research* **79**(2): 209.

Lasslop G, Reichstein M, Papale D, Richardson AD, Arneth A, Barr A, Stoy P, Wohlfahrt G. 2010. Separation of net ecosystem exchange into assimilation and respiration using a light response curve approach: critical issues and global evaluation. *Global Change Biology* **16**(1): 187-208.

Lee J-E, Frankenberg C, van der Tol C, Berry JA, Guanter L, Boyce CK, Fisher JB, Morrow E, Worden JR, Asefi S. 2013. Forest productivity and water stress in Amazonia: Observations from GOSAT chlorophyll fluorescence. *Proceedings of the Royal Society B: Biological Sciences* **280**(1761): 20130171.

Li J, Malley JD, Andrew AS, Karagas MR, Moore JH. 2016. Detecting gene-gene interactions using a permutation-based random forest method. *BioData mining* **9**(1): 1-17.

Li Z, Moreau L. 1996. A new approach for remote sensing of canopy-absorbed photosynthetically active radiation. I: Total surface absorption. *Remote Sensing of Environment* **55**(3): 175-191.

Liu X, Guanter L, Liu L, Damm A, Malenovský Z, Rascher U, Peng D, Du S, Gastellu-Etchegorry J-P. 2018. Downscaling of solar-induced chlorophyll fluorescence from canopy level to photosystem level using a random forest model. *Remote Sensing of Environment*.

Liu X, Liu L, Hu J, Guo J, Du S. 2020. Improving the potential of red SIF for estimating GPP by downscaling from the canopy level to the photosystem level. *Agricultural and Forest Meteorology* **281**: 107846.

Lommen PW, Smith SK, Yocum CS, Gates DM 1975. Photosynthetic model. *Perspectives of Biophysical Ecology*: Springer, 33-43.

Lu, Liu ZQ, An SQ, Miralles DG, Maes WH, Liu YL, Tang JW. 2018. Potential of solar-induced chlorophyll fluorescence to estimate transpiration in a temperate forest. *Agricultural and Forest Meteorology* **252**: 75-+.

Lu X, Liu Z, Zhou Y, Liu Y, Tang J. 2018. Performance of Solar-Induced Chlorophyll Fluorescence in Estimating Water-Use Efficiency in a Temperate Forest. *Remote Sensing* **10**(5): 796.

Luo Y, El-Madany T, Filippa G, Ma X, Ahrens B, Carrara A, Gonzalez-Cascon R, Cremonese E, Galvagno M, Hammer T. 2018a. Using near-infrared-enabled digital repeat photography to track structural and physiological phenology in mediterranean tree–grass ecosystems. *Remote Sensing* **10**(8): 1293.

Luo Y, El-Madany TS, Filippa G, Ma X, Ahrens B, Carrara A, Gonzalez-Cascon R, Cremonese E, Galvagno M, Hammer TW. 2018b. Using near-infrared-enabled digital repeat photography to track structural and physiological phenology in mediterranean tree–grass ecosystems. *Remote Sensing* **10**(8): 1293.

Luo Y, El-Madany T, Ma X, Nair R, Jung M, Weber U, Filippa G, Bucher SF, Moreno G, Cremonese E. 2020. Nutrients and water availability constrain the seasonality of vegetation activity in a Mediterranean ecosystem. *Global Change Biology* **26**(8): 4379--4400.

Maes WH, Pagán BR, Martens B, Gentine P, Guanter L, Steppe K, Verhoest NE, Dorigo W, Li X, Xiao J. 2020. Sun-induced fluorescence closely linked to ecosystem transpiration as evidenced by satellite data and radiative transfer models. *Remote Sensing of Environment* **249**: 112030.

Magney TS, Barnes ML, Yang X. 2020. On the covariation of chlorophyll fluorescence and photosynthesis across scales. *Geophysical Research Letters* **47**(23): e2020GL091098.

Magney TS, Bowling DR, Logan BA, Grossmann K, Stutz J, Blanken PD, Burns SP, Cheng R, Garcia MA, Kohler P, et al. 2019. Mechanistic evidence for tracking the seasonality of photosynthesis with solar-induced fluorescence. *Proceedings of the National Academy of Sciences of the United States of America* **116**(24): 11640-11645.

Magney TS, Frankenberg C, Fisher JB, Sun Y, North GB, Davis TS, Kornfeld A, Siebke K. 2017. Connecting active to passive fluorescence with photosynthesis: a method for evaluating remote sensing measurements of Chl fluorescence. *New Phytologist* **215**(4): 1594-1608.

Maksymiuk S, Gosiewska A, Biecek P. 2020. Landscape of R packages for eXplainable Artificial Intelligence. *arXiv preprint arXiv:2009.13248*.

Marrs J, Reblin J, Logan B, Allen D, Reinmann A, Bombard D, Tabachnik D, Hutyra L. 2020. Solar-induced fluorescence does not track photosynthetic carbon assimilation following induced stomatal closure. *Geophysical Research Letters* **47**(15): e2020GL087956.

Mauder M, Foken T. 2011. Documentation and instruction manual of the eddy-covariance software package TK3. **https://epub.uni-bayreuth.de/342/1/ARBERG046.pdf, last accessed on 06/12/2021**.

Medrano H, Escalona JM, Bota J, Gulías J, Flexas J. 2002. Regulation of photosynthesis of C3 plants in response to progressive drought: stomatal conductance as a reference parameter. *Annals of Botany* **89**(7): 895-905.

Meinzer FC, Smith DD, Woodruff DR, Marias DE, McCulloh KA, Howard AR, Magedman AL. 2017. Stomatal kinetics and photosynthetic gas exchange along a continuum of isohydric to anisohydric regulation of plant water status. *Plant Cell and Environment* **40**(8): 1618-1628.

Meroni M, Colombo R. 2006. Leaf level detection of solar induced chlorophyll fluorescence by means of a subnanometer resolution spectroradiometer. *Remote Sensing of Environment* **103**(4): 438-448.

Meroni M, Rossini M, Guanter L, Alonso L, Rascher U, Colombo R, Moreno J. 2009. Remote sensing of solar-induced chlorophyll fluorescence: Review of methods and applications. *Remote Sensing of Environment* **113**(10): 2037-2051.

Migliavacca M, Perez-Priego O, Rossini M, El-Madany TS, Moreno G, van der Tol C, Rascher U, Berninger A,

Bessenbacher V, Burkart A, et al. 2017. Plant functional traits and canopy structure control the relationship between photosynthetic CO_2 uptake and far-red sun-induced fluorescence in a Mediterranean grassland under different nutrient availability. *New Phytologist* **214**(3): 1078--1091.

Moder K. 2010. Alternatives to F-test in one way ANOVA in case of heterogeneity of variances (a simulation study). *Psychological Test and Assessment Modeling* **52**(4): 343-353.

Mohammed GH, Colombo R, Middleton EM, Rascher U, van der Tol C, Nedbal L, Goulas Y, Pérez-Priego O, Damm A, Meroni M. 2019. Remote sensing of solar-induced chlorophyll fluorescence (SIF) in vegetation: 50 years of progress. *Remote Sensing of Environment* **231**: 111177.

Monteith J. 1972. Solar radiation and productivity in tropical ecosystems. *Journal of applied ecology* **9**(3): 747-766.

Moreau L, Li Z. 1996. A new approach for remote sensing of canopy absorbed photosynthetically active radiation. II: Proportion of canopy absorption. *Remote Sensing of Environment* **55**(3): 192-204.

Moreno J, Goulas Y, Huth A, Middleton E, Miglietta F, Mohammed G, Nedbal L, Rascher U, Verhoef W, Drusch M. 2015. Report for mission selection: FLEX. *ESA SP* **1330**(2).

Nelson JA, Carvalhais N, Cuntz M, Delpierre N, Knauer J, Ogée J, Migliavacca M, Reichstein M, Jung M. 2018. Coupling water and carbon fluxes to constrain estimates of transpiration: The TEA algorithm. *Journal of Geophysical Research: Biogeosciences* **123**(12): 3617-3632.

Niinemets Ü, Kull O, Tenhunen JD. 1999. Variability in leaf morphology and chemical composition as a function of canopy light environment in coexisting deciduous trees. *International Journal of Plant Sciences* **160**(5): 837-848.

Niu S, Jiang G, Li Y, Gao L, Liu M. 2003. Diurnal gas exchange and superior resources use efficiency of typical C 4 species in Hunshandak Sandland, China. *Photosynthetica* **41**(2): 221-226.

Nixon PJ. 2000. Chlororespiration. *Philosophical Transactions of the Royal Society of London. Series B: Biological Sciences* **355**(1402): 1541-1547.

Ogaya R, Peñuelas J. 2003. Comparative seasonal gas exchange and chlorophyll fluorescence of two dominant woody species in a Holm Oak Forest. *Flora-Morphology, Distribution, Functional Ecology of Plants* **198**(2): 132-141.

Ollinger S, Frolking S, Richardson A, Martin M, Hollinger D, Reich P, Plourde L. 2009. Reply to Fisher: Nitrogen–albedo relationship in forests remains robust and thought-provoking. *Proceedings of the National Academy of Sciences* **106**(7): E17-E17.

Ollinger SV, Richardson AD, Martin ME, Hollinger DY, Frolking SE, Reich PB, Plourde LC, Katul GG, Munger JW, Oren R. 2008. Canopy nitrogen, carbon assimilation, and albedo in temperate and boreal forests: Functional relations and potential climate feedbacks. *Proceedings of the National Academy of Sciences* **105**(49): 19336-19341.

Omasa K, Takayama K. 2003. Simultaneous measurement of stomatal conductance, non-photochemical quenching, and photochemical yield of photosystem II in intact leaves by thermal and chlorophyll fluorescence imaging. *Plant and Cell Physiology* **44**(12): 1290-1300.

Pacheco-Labrador J, Hueni A, Mihai L, Sakowska K, Julitta T, Kuusk J, Sporea D, Alonso L, Burkart A, Cendrero-Mateo MP. 2019a. Sun-induced chlorophyll fluorescence I: Instrumental considerations for proximal spectroradiometers. *Remote Sensing* **11**(8): 960.

Pacheco-Labrador J, Perez-Priego O, El-Madany TS, Julitta T, Rossini M, Guan J, Moreno G, Carvalhais N, Martín MP, Gonzalez-Cascon R. 2019b. Multiple-constraint inversion of SCOPE. Evaluating the potential of GPP and SIF for the retrieval of plant functional traits. *Remote Sensing of Environment* **234**: 111362.

Pacheco-Labrador Javier OP-P, Tarek S. El-Madany, Tommaso Julitta, Micol Rossini, Jinhong Guan, Gerardo Moreno, Nuno Carvalhais, M. Pilar Martín, Rosario González-Cascón, Olaf Kolle, Markus Reischtein, Christiaan van der Tol, Arnaud Carra, David Martini, Tiana W. Hammer, Heiko Moosen, Mirco Migliavacca. 2019. MULTIPLE-CONSTRAINT INVERSION OF SCOPE. EVALUATING THE POTENTIAL OF GPP AND SIF FOR THE 2 RETRIEVAL OF PLANT FUNCTIONAL TRAITS. *Remote sensing of Environment (In press)*.

Pagán BR, Maes WH, Gentine P, Martens B, Miralles DG. 2019. Exploring the potential of satellite solar-induced fluorescence to constrain global transpiration estimates. *Remote Sensing* **11**(4): 413.

Papale D, Reichstein M, Aubinet M, Canfora E, Bernhofer C, Kutsch W, Longdoz B, Rambal S, Valentini R, Vesala T, et al. 2006. Towards a standardized processing of Net Ecosystem Exchange measured with eddy covariance technique: algorithms and uncertainty estimation. *Biogeosciences* **3**(4): 571-583.

Parazoo NC, Bowman K, Fisher JB, Frankenberg C, Jones DB, Cescatti A, Pérez-Priego Ó, Wohlfahrt G, Montagnani L. 2014. Terrestrial gross primary production inferred from satellite fluorescence and vegetation models. *Global Change Biology* **20**(10): 3103-3121.

Peng Y, Gitelson AA, Keydan G, Rundquist DC, Moses W. 2011. Remote estimation of gross primary production in maize and support for a new paradigm based on total crop chlorophyll content. *Remote Sensing of Environment* **115**(4): 978-989.

Perez-Priego O, El-Madany TS, Migliavacca M, Kowalski AS, Jung M, Carrara A, Kolle O, Martin MP, Pacheco-Labrador J, Moreno G, et al. 2017. Evaluation of eddy covariance latent heat fluxes with independent lysimeter and sapflow estimates in a Mediterranean savannah ecosystem. *Agricultural and Forest Meteorology* **236**: 87-99.

Perez-Priego O, Guan J, Rossini M, Fava F, Wutzler T, Moreno G, Carvalhais N, Carrara A, Kolle O, Julitta T, et al. 2015. Sun-induced chlorophyll fluorescence and photochemical reflectance index improve remote-sensing gross primary production estimates under varying nutrient availability in a typical Mediterranean savanna ecosystem. *Biogeosciences* **12**(21): 6351-6367.

Perez-Priego O, Katul G, Reichstein M, El-Madany TS, Ahrens B, Carrara A, Scanlon TM, Migliavacca M. 2018. Partitioning eddy covariance water flux components using physiological and micrometeorological approaches. *Journal of Geophysical Research: Biogeosciences* **123**(10): 3353-3370.

Porcar-Castell A. 2011. A high-resolution portrait of the annual dynamics of photochemical and non-photochemical quenching in needles of *Pinus sylvestris*. *Physiologia Plantarum* **143**(2): 139-153.

Porcar-Castell A, Juurola E, Ensminger I, Berninger F, Hari P, Nikinmaa E. 2008. Seasonal acclimation of photosystem II in *Pinus sylvestris*. II. Using the rate constants of sustained thermal energy dissipation and photochemistry to study the effect of the light environment. *Tree Physiology* **28**(10): 1483-1491.

Porcar-Castell A, Tyystjarvi E, Atherton J, van der Tol C, Flexas J, Pfundel EE, Moreno J, Frankenberg C, Berry JA. 2014. Linking chlorophyll a fluorescence to photosynthesis for remote sensing applications: mechanisms and challenges. *Journal of Experimental Botany* **65**(15): 4065-4095.

Reichstein M, Bahn M, Ciais P, Frank D, Mahecha MD, Seneviratne SI, Zscheischler J, Beer C, Buchmann N,

Frank DC, et al. 2013. Climate extremes and the carbon cycle. *Nature* **500**(7462): 287-295.

Reichstein M, Camps-Valls G, Stevens B, Jung M, Denzler J, Carvalhais N. 2019. Deep learning and process understanding for data-driven Earth system science. *Nature* **566**(7743): 195-204.

Reichstein M, Falge E, Baldocchi D, Papale D, Aubinet M, Berbigier P, Bernhofer C, Buchmann N, Gilmanov T, Granier A, et al. 2005. On the separation of net ecosystem exchange into assimilation and ecosystem respiration: review and improved algorithm. *Global Change Biology* **11**(9): 1424-1439.

Rosseel Y. 2012. Lavaan: An R package for structural equation modeling and more. Version 0.5–12 (BETA). *Journal of statistical software* **48**(2): 1-36.

Rossini M, Meroni M, Migliavacca M, Manca G, Cogliati S, Busetto L, Picchi V, Cescatti A, Seufert G, Colombo R. 2010. High resolution field spectroscopy measurements for estimating gross ecosystem production in a rice field. *Agricultural and Forest Meteorology* **150**(9): 1283-1296.

Rutherford A. 2001. *Introducing ANOVA and ANCOVA: a GLM approach*: Sage.

Sade N, Gebremedhin A, Moshelion M. 2012. Risk-taking plants: anisohydric behavior as a stress-resistance trait. *Plant signaling & behavior* **7**(7): 767-770.

Sager J, McFarlane J. 1997. Plant growth chamber handbook.

Seibt U, Rajabi A, Griffiths H, Berry JA. 2008. Carbon isotopes and water use efficiency: sense and sensitivity. *Oecologia* **155**(3): 441-454.

Shan N, Ju W, Migliavacca M, Martini D, Guanter L, Chen J, Goulas Y, Zhang Y. 2019. Modeling canopy conductance and transpiration from solar-induced chlorophyll fluorescence. *Agricultural and Forest Meteorology* **268**: 189-201.

Shan N, Zhang Y, Chen JM, Ju W, Migliavacca M, Peñuelas J, Yang X, Zhang Z, Nelson JA, Goulas Y. 2021. A model for estimating transpiration from remotely sensed solar-induced chlorophyll fluorescence. *Remote Sensing of Environment* **252**: 112134.

Sims DA, Rahman AF, Cordova VD, El-Masri BZ, Baldocchi DD, Bolstad PV, Flanagan LB, Goldstein AH, Hollinger DY, Misson L. 2008. A new model of gross primary productivity for North American ecosystems based solely on the enhanced vegetation index and land surface temperature from MODIS. *Remote Sensing of Environment* **112**(4): 1633-1646.

Singh S, Reddy V, Fleisher D, Timlin D. 2017. Relationship between photosynthetic pigments and chlorophyll fluorescence in soybean under varying phosphorus nutrition at ambient and elevated CO 2. *Photosynthetica* **55**(3): 421-433.

Singh SK, Reddy VR. 2014. Combined effects of phosphorus nutrition and elevated carbon dioxide concentration on chlorophyll fluorescence, photosynthesis, and nutrient efficiency of cotton. *Journal of Plant Nutrition and Soil Science* **177**(6): 892-902.

Sousa PM, Barriopedro D, Ramos AM, Garcia-Herrera R, Espirito-Santo F, Trigo RM. 2019. Saharan air intrusions as a relevant mechanism for Iberian heatwaves: The record breaking events of August 2018 and June 2019. *Weather and Climate Extremes* **26**: 100224.

Spellerberg IF, Fedor PJ. 2003. A tribute to Claude Shannon (1916-2001) and a plea for more rigorous use of species richness, species diversity and the 'Shannon-Wiener' Index. *Global Ecology and Biogeography* **12**(3): 177-179.

Sterling TM. 2005. Transpiration: Water movement through plants. *Journal of Natural Resources and Life Sciences Education* **34**(1): 123-123.

Suárez L, Zarco-Tejada PJ, Sepulcre-Cantó G, Pérez-Priego O, Miller J, Jiménez-Muñoz J, Sobrino J. 2008. Assessing canopy PRI for water stress detection with diurnal airborne imagery. *Remote Sensing of Environment* **112**(2): 560-575.

Sullivan FB, Ollinger SV, Martin ME, Ducey MJ, Lepine LC, Wicklein HF. 2012. Foliar nitrogen in relation to plant traits and reflectance properties of New Hampshire forests. *Canadian Journal of Forest Research* **43**(1): 18-27.

Sumayao C, Kanemasu E, Brakke T. 1980. Using leaf temperature to assess evapotranspiration and advection. *Agricultural Meteorology* **22**(2): 153-166.

Sun Z, Livingston N, Guy R, Ethier G. 1996. Stable carbon isotopes as indicators of increased water use efficiency and productivity in white spruce (Picea glauca (Moench) Voss) seedlings. *Plant, cell & environment* **19**(7): 887-894.

Tatarko AR, Knops JMH. 2018. Nitrogen addition and ecosystem functioning: Both species abundances and traits alter community structure and function. *Ecosphere* **9**(1).

Teskey R, Wertin T, Bauweraerts I, Ameye M, McGuire MA, Steppe K. 2015. Responses of tree species to heat waves and extreme heat events. *Plant Cell and Environment* **38**(9): 1699-1712.

Thom A. 1972. Momentum, mass and heat exchange of vegetation. *Quarterly Journal of the Royal Meteorological Society* **98**(415): 124-134.

van der Tol C, Berry JA, Campbell PKE, Rascher U. 2014. Models of fluorescence and photosynthesis for interpreting measurements of solar-induced chlorophyll fluorescence. *Journal of Geophysical Research-Biogeosciences* **119**(12): 2312-2327.

van der Tol C, Verhoef W, Rosema A. 2009a. A model for chlorophyll fluorescence and photosynthesis at leaf scale. *Agricultural and Forest Meteorology* **149**(1): 96-105.

van der Tol C, Verhoef W, Timmermans J, Verhoef A, Su Z. 2009b. An integrated model of soil-canopy spectral radiances, photosynthesis, fluorescence, temperature and energy balance. *Biogeosciences* **6**(12): 3109-3129.

Van Wittenberghe S, Alonso L, Malenovsky Z, Moreno J. 2019. In vivo photoprotection mechanisms observed from leaf spectral absorbance changes showing VIS-NIR slow-induced conformational pigment bed changes. *Photosynthesis Research* **142**(3): 283-305.

Verhoeven AS, Demmig-Adams B, Adams III WW. 1997. Enhanced employment of the xanthophyll cycle and thermal energy dissipation in spinach exposed to high light and N stress. *Plant Physiology* **113**(3): 817-824.

Vilfan N, van der Tol C, Verhoef W. 2019. Estimating photosynthetic capacity from leaf reflectance and chlorophyll fluorescence by coupling radiative transfer to a model for photosynthesis. *New Phytologist*.

Vina A, Gitelson AA. 2005. New developments in the remote estimation of the fraction of absorbed photosynthetically active radiation in crops. *Geophysical Research Letters* **32**(17).

Weis E, Berry JA 1988. Plants and high temperature stress. *Symposia of the Society for Experimental Biology*. 329-346.

Weisser WW, Roscher C, Meyer ST, Ebeling A, Luo G, Allan E, Beßler H, Barnard RL, Buchmann N, Buscot F. 2017. Biodiversity effects on ecosystem functioning in a 15-year grassland experiment: patterns, mechanisms, and open questions. *Basic and Applied Ecology* **23**: 1-73.

Wieneke S, Ahrends H, Damm A, Pinto F, Stadler A, Rossini M, Rascher U. 2016. Airborne based spectroscopy of red and far-red sun-induced chlorophyll fluorescence: Implications for improved estimates of gross primary productivity. *Remote Sensing of Environment* **184**: 654-667.

Wohlfahrt G, Bahn M, Tappeiner U, Cernusca A. 2001. A multi-component, multi-species model of vegetation-atmosphere CO2 and energy exchange for mountain grasslands. *Agricultural and Forest Meteorology* **106**(4): 261-287.

Wohlfahrt G, Gerdel K, Migliavacca M, Rotenberg E, Tatarinov F, Muller J, Hammerle A, Julitta T, Spielmann FM, Yakir D. 2018. Sun-induced fluorescence and gross primary productivity during a heat wave. *Scientific Reports* **8**: 1--9.

Wong S, Cowan I, Farquhar G. 1979. Stomatal conductance correlates with photosynthetic capacity. *Nature* **282**(5737): 424-426.

Wutzler T, Lucas-Moffat A, Migliavacca M, Knauer J, Sickel K, Sigut L, Menzer O, Reichstein M. 2018. Basic and extensible post-processing of eddy covariance flux data with REddyProc. *Biogeosciences* **15**(16): 5015-5030.

Yang JC, Magney TS, Yan D, Knowles JF, Smith WK, Scott RL, Barron-Gafford GA. 2020. The photochemical reflectance index (PRI) captures the ecohydrologic sensitivity of a semiarid mixed conifer forest. *Journal of Geophysical Research: Biogeosciences* **125**(11): e2019JG005624.

Yang K, Ryu Y, Dechant B, Berry JA, Hwang Y, Jiang C, Kang M, Min J, Kimm H, Kornfeld A, et al. 2018. Sun-induced chlorophyll fluorescence is more strongly related to absorbed light than to photosynthesis at half-hourly resolution in a rice paddy. *Remote Sensing of Environment* **216**: 658-673.

Yang P, van der Tol C, Campbell PK, Middleton EM. 2020. Fluorescence Correction Vegetation Index (FCVI): A physically based reflectance index to separate physiological and non-physiological information in far-red sun-induced chlorophyll fluorescence. *Remote Sensing of Environment* **240**: 111676.

Yang PQ, van der Tol C. 2018. Linking canopy scattering of far-red sun-induced chlorophyll fluorescence with reflectance. *Remote Sensing of Environment* **209**: 456-467.

Yang X, Tang J, Mustard JF, Lee JE, Rossini M, Joiner J, Munger JW, Kornfeld A, Richardson AD. 2015. Solar-induced chlorophyll fluorescence that correlates with canopy photosynthesis on diurnal and seasonal scales in a temperate deciduous forest. *Geophysical Research Letters* **42**(8): 2977-2987.

Zeng Y, Badgley G, Dechant B, Ryu Y, Chen M, Berry JA. 2019. A practical approach for estimating the escape ratio of near-infrared solar-induced chlorophyll fluorescence. *Remote Sensing of Environment* **232**: 111209.

Zhang Y, Guanter L, Berry JA, Joiner J, van der Tol C, Huete A, Gitelson A, Voigt M, Köhler P. 2014. Estimation of vegetation photosynthetic capacity from space-based measurements of chlorophyll fluorescence for terrestrial biosphere models. *Global Change Biology* **20**(12): 3727-3742.

Zhou S, Yu B, Huang Y, Wang G. 2014. The effect of vapor pressure deficit on water use efficiency at the subdaily time scale. *Geophysical Research Letters* **41**(14): 5005-5013.

7 Summary

Photosynthetic organism slowly transformed Earth from a rocky and bare landscape to a lush, diverse collection of thriving ecosystems. The photosynthetic process also altered the atmosphere by lowering atmospheric CO_2 and increasing O_2 levels, thus permitting animal life. The synthesis of the organic compounds through photosynthesis (gross primary production, *GPP*), by terrestrial plants is today the largest global carbon flux and supports human welfare as it is the basis for food, wood and fibers. *GPP* also provides several critical ecosystem services such as the offsetting of anthropogenic CO_2 emissions. The photosynthetic process is mediated by stomata; small openings on plant's leaves that allow the exchange of CO_2 and water vapor. The movement of water through plants and its evaporation from stomata (Transpiration, *T*) plays a pivotal role in the global water cycle and land-surface energy balance and represents a large fraction of evapotranspiration. Accurate estimations of *GPP* and *T* are therefore critical to monitor ecosystems and to quantify the amount of CO_2 sequestered from the atmosphere. Remote and proximal sensing techniques offer the possibility to estimate *GPP* and *T* in an unintrusive way, while also allowing for high temporal or high spatial resolution measurements. Sun-induced fluorescence (*SIF*), the radiation emitted by plant's upon sun's exposure, is a promising remote sensing tool to estimate *GPP* and *T*. *SIF* contains information on the amount of photosynthetic active radiation absorbed by plants and the efficiency with which it is used to drive photosynthesis. It has also been recently related to *T*, although the mechanistic link between the two is still unclear. As *SIF* has been progressively used more extensively in the last decade to estimate *GPP*, and more recently *T*, much as been learned on the way *SIF* may be used to constrain carbon and water fluxes. Still, many research gaps have yet to be investigated, such as: 1) the role of nutrients (such as nitrogen (N) and phosphorus (P)) in shaping the *GPP*-*SIF* relationship, 2) how extreme event such as heatwaves can affect *GPP*-*SIF* and 3) improving the understanding of how *SIF* may be used to predict *T*. This dissertation examines the first objective by investigating a nutrient manipulation experiment (with N and P) where simultaneous *GPP* and *SIF* measurements were conducted in a Mediterranean grassland. I uncover the mechanisms that link the fertilization-driven changes in canopy nitrogen and phosphorus concentration to the observed changes in *SIF* and *GPP*. Specifically, I find that N addition changed plant community structure and increased canopy chlorophyll content, which jointly lead to changes in absorbed photosynthetic active radiation (*APAR*), which ultimately affected both *GPP* and *SIF*. The changes in plant type abundance driven by N addition lead to changes in structural properties of the canopy such as leaf angles, which ultimately influenced observed *SIF* by controlling the escape probability of *SIF* (*Fesc*). Additionally, the N addition induced changes in the biophysical properties of the canopy that lead to a trade-off between surface temperature, which decreased, and *SIF* at leaf scale that increased. The P addition lead to a statistically significant increase in light use efficiency of fluorescence emission (LUE_f), in particular in plots with also N addition, suggesting a co-limitation of LUE_f by N and P. In regard to the second objective I analyzed how the 2018 heatwave, which was characterized by temperatures up to 45 °C, affected the *GPP-SIF* relationship in a Mediterranean tree-grass ecosystem. I combine canopy scale passive fluorescence (*SIF*) with leaf scale active fluorimetry, which allows to obtain the amount of heat dissipation (nonphotochemical quenching, *NPQ*) which is a major dissipation pathway of absorbed energy and an important driver of *SIF*. I find that the heatwave caused an inversion of the photosynthesis-fluorescence relationship at both canopy and leaf scale. The highly nonlinear relationship was strongly shaped by *NPQ*. During the extreme heat stress, plants experienced a saturation of *NPQ* causing a change in the allocation of energy dissipation pathways towards *SIF*. These innovative results showed that the relationship between *GPP* and *SIF* (which has been broadly considered to be linear) can depart from linearity under extreme stress due to physiological regulations. Additionally I show the complex modulation of the relationship *NPQ-SIF-GPP* at an extreme level of heat stress, which is not fully represented in state-of-the-art coupled radiative transfer and photosynthesis models. Finally for the third objective I predict *T* using passive and active fluorescence in two sites; a Mediterranean tree-grass ecosystem and a deciduous beech forest. I test the three different methods that have been used so far to relate *SIF* and *T*; a) fully empirical, b) hybrid modeling approach and c) water use efficiency (WUE) based approach in order to establish a framework for *SIF* based *T* predictions. I find that total *SIF* had a stronger correlation with *T* than *GPP* across sites, as both total *SIF* and *T* are driven to larger extent by *APAR* than *GPP*. Additionally, I found approach (a) and (b) to have similar predictive power across sites. Finally, the WUE approach had the lowest performance out of the three. In order to better understand the mechanistic relationship between *SIF* and *T* I highlight the importance of separating periods in which photosynthesis is stomatal or non-stomatically (i.e. carboxylation) limited from periods of low or no stress. During periods of photosynthetic limitations *T* was mostly predicted by variables that can be physiologically modulated by plants, such as *NPQ* and *SIF*, whereas during periods of no stress I found *T* to be more energy driven and therefore more strongly predicted by *APAR* or surface temperature. This thesis advances the understanding of *SIF* based *GPP* and *T* prediction by analyzing the most important factors able to affect the *GPP-SIF* relationship and by testing *SIF* based *T* prediction with different methodologies. *SIF* is a powerful, yet complex predictor of *GPP* and *T* which has the potential to be used to accurately constrain carbon and water fluxes in a changing climate. Future studies should focus on understanding in which ecosystems and under which conditions *SIF* can be used to predict *T*, as the link between the two, although increasing more clear, remains understudied.

8 Samenvatting

Fotosynthetiserende organismen veranderden de aarde langzaam van een rotsachtig en kaal landschap in een weelderige, gevarieerde verzameling van bloeiende ecosystemen. Fotosynthese veranderde tevens de atmosfeer door het CO_2-gehalte in de atmosfeer te verlagen en het O_2-gehalte te verhogen, waardoor dierlijk leven mogelijk werd. De synthese van organische verbindingen door fotosynthese (bruto primaire productie, *GPP*) door terrestrische planten is vandaag de dag de grootste globale koolstofstroom en ondersteunt het menselijk welzijn, aangezien het de basis vormt voor voedsel, hout en vezels. *GPP* levert ook verschillende cruciale ecosysteemdiensten zoals de compensatie van antropogene CO_2-emissies. Fotosynthese wordt geregeld door huidmondjes; kleine openingen op de bladeren van planten die de uitwisseling van CO_2 en waterdamp mogelijk maken. De beweging van water door planten en de verdamping door huidmondjes (Transpiratie, T) speelt een centrale rol in de globale watercyclus en de energiebalans van het landoppervlak en vertegenwoordigt een groot deel van de evapotranspiratie. Nauwkeurige schattingen van *GPP* en T zijn daarom van het hoogste belang om ecosystemen en de hoeveelheid CO_2 die uit de atmosfeer wordt vastgelegd gade te slaan. Remote en proximal sensing technieken bieden de mogelijkheid om *GPP* en *T* te schatten op een niet-intrusieve manier, terwijl ze ook metingen met hoge temporele of ruimtelijke resolutie mogelijk maken. Door de zon geïnduceerde fluorescentie (*SIF*), de straling die door planten wordt uitgezonden wanneer zij aan de zon worden blootgesteld, is een veelbelovend teledetectie-instrument om *GPP* en *T* te kunnen schatten. *SIF* bevat informatie over de hoeveelheid fotosynthetisch actieve straling die door planten wordt geabsorbeerd en de efficiëntie waarmee deze wordt gebruikt om de fotosynthese aan te drijven. Recentelijk is er ook een verband gelegd met *T*, hoewel het mechanistische verband tussen beide nog onduidelijk is. Aangezien *SIF* de afgelopen tien jaar steeds vaker is gebruikt om *GPP*, en recentelijk ook *T*, te schatten, is veel bekend geworden over de manier waarop *SIF* kan worden gebruikt om de koolstof- en waterstromen aan banden te leggen. Toch zijn er nog onbeantwoorde onderzoeksvragen, zoals 1) de rol van nutriënten (zoals stikstof (N) en fosfor (P)) in de vorming van de *GPP-SIF* relatie, 2) hoe weer extremen zoals hittegolven *GPP-SIF* kunnen beïnvloeden en 3) het verbeteren van het begrip van hoe *SIF* kan worden gebruikt om *T* te voorspellen. Dit proefschrift onderzoekt de eerste doelstelling door een experiment met nutriëntenmanipulatie (met N en P) te onderzoeken waarbij simultaan *GPP* en *SIF* metingen werden uitgevoerd in een mediterraan grasland. Ik leg de mechanismen bloot die de door bemesting veroorzaakte veranderingen in de stikstof- en fosforconcentratie in het bladerdak verbinden met de waargenomen veranderingen in *SIF* en *GPP*. In het bijzonder ontdekte ik dat de toevoeging van stikstof de structuur van de plantengemeenschap wijzigde en het chlorofylgehalte van het bladerdak verhoogde, wat samen leidde tot veranderingen in de geabsorbeerde fotosynthetische actieve straling (*APAR*), die uiteindelijk zowel *GPP* als *SIF* beïnvloedden. De door de N-toevoeging veroorzaakte veranderingen in de overvloed aan plantensoorten leidden tot veranderingen in de structurele eigenschappen van het bladerdak, zoals de hoeken van bladeren, die uiteindelijk de waargenomen *SIF* beïnvloedden doordat ze de ontsnappingskans van *SIF* (*Fesc*) controleerden. Bovendien leidde de N-toevoeging tot veranderingen in de biofysische eigenschappen van het bladerdak die leidden tot een wisselwerking tussen de oppervlaktetemperatuur, die daalde, en de *SIF* op bladschaal, die steeg. De P-toevoeging leidde tot een statistisch significante toename van de lichtgebruiksefficiëntie van fluorescentie-emissie (LUE_f), in het bijzonder in percelen met ook N-toevoeging, wat een co-limitatie van LUE_f door N en P suggereert. Met betrekking tot de tweede doelstelling analyseerde ik hoe de hittegolf van 2018, die werd gekenmerkt door temperaturen tot 45 °C, de GPP-*SIF* relatie in een mediterraan boom-gras ecosysteem beïnvloedde. Ik combineer passieve fluorescentie (*SIF*) op boomkruinschaal met actieve fluorimetrie op bladschaal, wat toelaat om de hoeveelheid warmte dissipatie (niet-fotochemische quenching, *NPQ*) te verkrijgen, wat een belangrijke dissipatie route is van geabsorbeerde energie en een belangrijke motor van *SIF*. Ik ontdekte dat de hittegolf een inversie veroorzaakte van de fotosynthese-fluorescentie relatie zowel op kroonblad- als op bladschaal. De zeer niet-lineaire relatie werd sterk bepaald door *NPQ*. Tijdens de extreme hittestress ondervonden de planten een verzadiging van *NPQ*, wat leidde tot een verandering in de toewijzing van energie dissipatiewegen naar *SIF*. Deze innovatieve resultaten toonden aan dat de relatie tussen *GPP* en *SIF* (die in het algemeen als lineair wordt beschouwd) onder extreme stress kan afwijken van lineariteit als gevolg van fysiologische regulaties. Bovendien toon ik de complexe modulatie van de relatie *NPQ-SIF-GPP* bij extreme hittestress, die niet volledig wordt weergegeven in de modernste gekoppelde modellen voor stralingsoverdracht en fotosynthese. Ten slotte voor de derde doelstelling voorspel ik *T* met behulp van passieve en actieve fluorescentie in twee sites; een mediterraan boom-gras ecosysteem en een bladverliezend beukenbos. Ik test de drie verschillende methoden die tot nu toe gebruikt zijn om *SIF* en *T* in verband te brengen; a) volledig empirisch, b) hybride modelbenadering en c) op watergebruiksefficiëntie (WUE) gebaseerde benadering om een kader te creëren voor op *SIF* gebaseerde *T*-voorspellingen. Ik vond dat de totale *SIF* een sterkere correlatie met *T* vertoonde dan *GPP* over alle sites, aangezien zowel de totale *SIF* als *T* in grotere mate door *APAR* worden bepaald dan *GPP*. Bovendien bleken de benaderingen (a) en (b) een vergelijkbaar voorspellend vermogen te hebben voor de verschillende locaties. Ten slotte was de WUE-benadering de slechtste van de drie. Om de mechanistische relatie tussen *SIF* en *T* beter te begrijpen, benadruk ik dat het belangrijk is om periodes waarin de fotosynthese stomatisch of niet-stomatisch (d.w.z. carboxylatie) beperkt is, te scheiden van periodes met weinig of geen stress. Tijdens periodes van fotosynthesebeperking werd *T* vooral voorspeld door variabelen die fysiologisch gemoduleerd kunnen worden door planten, zoals *NPQ* en *SIF*, terwijl tijdens periodes van geen stress *T* meer energiegedreven bleek te zijn en daarom sterker voorspeld werd door *APAR* of oppervlaktetemperatuur. Deze dissertatie bevordert het begrip van *SIF*-gebaseerde *GPP* en *T*-voorspelling door de belangrijkste factoren te analyseren die de *GPP-SIF* relatie kunnen beïnvloeden en door *SIF*-gebaseerde *T*-voorspelling te testen met verschillende methodologieën. *SIF* is een krachtige, maar complexe voorspeller van *GPP* en *T*, die het potentieel heeft om gebruikt te worden om nauwkeurig de koolstof- en waterfluxen te beperken in een veranderend klimaat. Toekomstige studies doen zich er goed aan zich toe te spitsen op de vraag in welke ecosystemen en onder welke omstandigheden *SIF* kan worden gebruikt om *T* te voorspellen, aangezien het verband tussen beide, hoewel het steeds duidelijker wordt, nog steeds onvoldoende bestudeerd is.

9 Author’s biography and publications

David Martini was born in 1990 in Moncalieri, Italy. He received a BA in Forest and Environmental Science at the University of Turin, Italy in 2013 and a MSc in Forest and Nature Conservation at Wageningen University, The Netherlands in 2016. In 2017 he received a grant within the Marie Sklodowska-Curie Innovative Training Network (Grant Agreement no 721995) and started a PhD at Max Planck Institute for Biogeochemistry. He later enrolled at the Faculty of Geo-Information Science and Earth Observation (ITC), University of Twente.

Martini, D., Sakowska, K., Wohlfahrt, G., Pacheco-Labrador, J., van der Tol, C., Porcar-Castell, A., ... & Migliavacca, M. (2021). Heatwave breaks down the linearity between sun-induced fluorescence and gross primary production. *New Phytologist*.

David Martini, Karolina Sakowska, Georg Wohlfahrt, Javier Pacheco-Labrador, Christiaan van der Tol, Albert Porcar-Castell, Troy S Magney, Arnaud Carrara, Roberto Colombo, Tarek El-Madanay, Rosario Gonzalez-Cascon, M. Pilar Martín, Tommaso Julitta, Gerardo Moreno, Uwe Rascher, Markus Reichstein, Micol Rossini, & Mirco Migliavacca. (2021). Heatwave breaks down the linearity between sun-induced fluorescence and gross primary production. Reproducible workflow [**Data set**]. Zenodo. https://doi.org/10.5281/zenodo.5773208

Martini, D., Pacheco-Labrador, J., Perez-Priego, O., Van der Tol, C., El-Madany, T. S., Julitta, T., ... & Migliavacca, M. (2019). Nitrogen and phosphorus effect on sun-induced fluorescence and gross primary productivity in mediterranean grassland. *Remote sensing*, *11*(21), 2562.

Migliavacca, Mirco, **et al.** "The three major axes of terrestrial ecosystem function." Nature 598.7881 (2021): 468-472.

Zhang, Z., Zhang, Y., Porcar-Castell, A., Joiner, J., Guanter, L., Yang, X., ... & **Martini, D.** (2020). Reduction of structural impacts and distinction of photosynthetic pathways in a global estimation of GPP from space-borne solar-induced chlorophyll fluorescence. Remote Sensing of Environment, 240, 111722.

Boonman, C. C., van Langevelde, F., Oliveras, I., Couédon, J., Luijken, N., **Martini, D**., & Veenendaal, E. M. (2020). On the importance of root traits in seedlings of tropical tree species. *New Phytologist*, *227*(1), 156-167.

JavierPacheco-Labrador, OscarPerez-Priego, Tarek S.El-Madany, Tommaso Julitta, Micol Rossini, Jinhong Guan, Gerardo Moreno, Nuno Carvalhais, M. Pilar Martín, Rosario Gonzalez-Cascon, Olaf Kolle, Markus Reischtein, Christiaan van der Tol, Arnaud Carrara, **David Martini**, Tiana W.Hammer, Heiko Moossen, Mirco Migliavacca "Multiple-constraint inversion of SCOPE. Evaluating the potential of GPP and SIF for the retrieval of plant functional traits." Remote Sensing of Environment 234 (2019): 111362.

Shan, N., Ju, W., Migliavacca, M., **Martini, D.**, Guanter, L., Chen, J., ... & Zhang, Y. (2019). Modeling canopy conductance and transpiration from solar-induced chlorophyll fluorescence. *Agricultural and Forest Meteorology*, *268*, 189-201.